frontiers | Research Topics

Resource utilization of agricultural waste through bioprocess engineering for environmental sustainability

Edited by
Junting Pan, Benyamin Khoshnevisan and Li Yeqing

Published in
Frontiers in Bioengineering and Biotechnology
Frontiers in Environmental Science

ISSN 1664-8714
ISBN 978-2-83252-166-3
DOI 10.3389/978-2-83252-166-3

About Frontiers

Frontiers is more than just an open access publisher of scholarly articles: it is a pioneering approach to the world of academia, radically improving the way scholarly research is managed. The grand vision of Frontiers is a world where all people have an equal opportunity to seek, share and generate knowledge. Frontiers provides immediate and permanent online open access to all its publications, but this alone is not enough to realize our grand goals.

Frontiers journal series

The Frontiers journal series is a multi-tier and interdisciplinary set of open-access, online journals, promising a paradigm shift from the current review, selection and dissemination processes in academic publishing. All Frontiers journals are driven by researchers for researchers; therefore, they constitute a service to the scholarly community. At the same time, the *Frontiers journal series* operates on a revolutionary invention, the tiered publishing system, initially addressing specific communities of scholars, and gradually climbing up to broader public understanding, thus serving the interests of the lay society, too.

Dedication to quality

Each Frontiers article is a landmark of the highest quality, thanks to genuinely collaborative interactions between authors and review editors, who include some of the world's best academicians. Research must be certified by peers before entering a stream of knowledge that may eventually reach the public - and shape society; therefore, Frontiers only applies the most rigorous and unbiased reviews. Frontiers revolutionizes research publishing by freely delivering the most outstanding research, evaluated with no bias from both the academic and social point of view. By applying the most advanced information technologies, Frontiers is catapulting scholarly publishing into a new generation.

What are Frontiers Research Topics?

Frontiers Research Topics are very popular trademarks of the *Frontiers journals series*: they are collections of at least ten articles, all centered on a particular subject. With their unique mix of varied contributions from Original Research to Review Articles, Frontiers Research Topics unify the most influential researchers, the latest key findings and historical advances in a hot research area.

Find out more on how to host your own Frontiers Research Topic or contribute to one as an author by contacting the Frontiers editorial office: frontiersin.org/about/contact

Resource utilization of agricultural waste through bioprocess engineering for environmental sustainability

Topic editors

Junting Pan — Institute of Agricultural Resources and Regional Planning, Chinese Academy of Agricultural Sciences, China

Benyamin Khoshnevisan — University of Southern Denmark, Denmark

Li Yeqing — China University of Petroleum, Beijing, China

Citation

Pan, J., Khoshnevisan, B., Yeqing, L., eds. (2023). *Resource utilization of agricultural waste through bioprocess engineering for environmental sustainability*. Lausanne: Frontiers Media SA. doi: 10.3389/978-2-83252-166-3

Table of contents

frontiers | Frontiers in Bioengineering and Biotechnology

TYPE Editorial
PUBLISHED 30 March 2023
DOI 10.3389/fbioe.2023.1147748

OPEN ACCESS

EDITED AND REVIEWED BY
Manfred Zinn,
HES-SO Valais-Wallis, Switzerland

*CORRESPONDENCE
Junting Pan,
panjunting@caas.cn
Yeqing Li,
liyeqing@cup.edu.cn
Benyamin Khoshnevisan,
bekh@igt.sdu.dk

SPECIALTY SECTION
This article was submitted to Bioprocess Engineering, a section of the journal Frontiers in Bioengineering and Biotechnology

RECEIVED 19 January 2023
ACCEPTED 22 March 2023
PUBLISHED 30 March 2023

CITATION
Pan J, Li Y and Khoshnevisan B (2023), Editorial: Resource utilization of agricultural waste through bioprocess engineering for environmental sustainability.
Front. Bioeng. Biotechnol. 11:1147748.
doi: 10.3389/fbioe.2023.1147748

Editorial: Resource utilization of agricultural waste through bioprocess engineering for environmental sustainability

Junting Pan[1]*, Yeqing Li[2]* and Benyamin Khoshnevisan[3]*

[1]Institute of Agricultural Resources and Regional Planning, Chinese Academy of Agricultural Sciences, Beijing, China, [2]State Key Laboratory of Heavy Oil Processing, Beijing Key Laboratory of Biogas Upgrading Utilization, College of New Energy and Materials, China University of Petroleum Beijing (CUPB), Beijing, China, [3]Institute of Chemical Engineering, Biotechnology and Environmental Technology, University of Southern Denmark, Odense, Denmark

KEYWORDS

agricultural waste, bioconversation, high efficiency, anaerobic digestion (AD), composting

Editorial on the Research Topic
Resource utilization of agricultural waste through bioprocess engineering for environmental sustainability

The purpose of this paper is to put together an overview of the recent development of bioconversion processes and their related technology. Its scope is wide so as to cover various aspects of the field, including the high-value conversion of agricultural waste, gas emission reduction, and agricultural waste utilization. Eleven articles were accepted and published in 2022.

Ai et al., from Henan Agricultural University, proposed a method of immobilization of sodium alginate to prepare "slurry capsules" for fermentative biohydrogen production. Not only does this method make biohydrogen slurry a harmless treatment, but it also addresses the problem of producing clean hydrogen energy. Shang et al. team found a strong positive correlation between the increase of N_2O concentration in biological filter and the elimination ability of NH_3. According to the authors, reducing the retention time of empty beds could help to prevent greenhouse gases from being produced by biofilters. Gao et al. and his team conducted a comprehensive evaluation of large-scale, multi-component and aerobic composting of rural refuse, which is an extension of the optimization of the previous multi-component mixed compost theory. The co-composting method proposed in this study is strong operable, complies with product standards, and aids in the reduction of waste and the rational utilization of resources. Wang et al., from Yunnan Normal University, used steel slag as a raw material to synthesize a hydrothermally carbonized steel slag. This method innovatively used solid waste-derived environmentally functional materials for heavy metal remediation. This material showed good removal efficiencies for Hg^{2+} and $Cr_2O_7^{2-}$. Shi et al. studied the characteristics and bacterial communities of static compost in low temperature and cold areas. Their results suggest that early spring or late fall is suitable for composting and, interestingly, amino acid and carbohydrate metabolism function genes indicate the changes of nitrogen and organic acids. Li et al. studied the effect of heat pre-treatment on the thermophilic anaerobic digestion of high-solid manure. The result shows that the increase of

heat treatment biogas could reasonably cover the energy consumption of the pre-treatment itself, and therefore, combining heat pre-treatment with the high-load anaerobic digestion of pig manure is appropriate. Chen et al., through field experiments, provided ideas for improving the soil micro-ecology environment and improving the yield and chemical quality of tobacco. Luo et al. prepared modified biochar from agricultural and industrial by-products. It was found that their modified prepared biochar is a feasible candidate and has a good effect on the removal of selenite from wastewater. Zhang et al. described a variety of technical methods for the improvement of *Saccharomyces cerevisiae* and their industrial applications. The methods to improve the cell surface display efficiency were also discussed. Zhou et al. studied the influence of inorganic and organic fertilizers on crop yield, fauna feeding efficiency, and soil quality. The experimental results suggested that the combination of inorganic fertilizer and organic fertilizer had good effects, such as improving the activity of the soil organic carbon and enzymes and improving the efficiency of the feeding of animals. Heredia Salgado et al. evaluated the transformation of agricultural residues from quinoa and lupin into biochar for soil improvement.

Eleven articles have been published in the journal, which cover a wide range of areas in waste valorization, including garbage, steel slag, and animal feces. The design field is diverse, including clean energy production, reactor research, and the development of biofuel production. This Research Topic may provide new solutions and ideas for future research.

Author contributions

JP: Formal analysis; writing–review and editing. YL: Formal analysis; writing–review and editing. BK: Formal analysis; writing–review and editing.

Conflict of interest

The authors declare that the research was conducted in the absence of any commercial or financial relationships that could be construed as a potential conflict of interest.

Publisher's note

frontiers | Frontiers in Bioengineering and Biotechnology

ORIGINAL RESEARCH
published: 16 May 2022
doi: 10.3389/fbioe.2022.906968

Clean Style Recovery and Utilization of Residual Nutrients in Effluents From Biohydrogen Production: *In Situ* Immobilization Based on Sodium Alginate

*Fuke Ai[1,2], Yang Zhang[1], Xiaoni Fan[1], Yameng Li[1], Haorui Zhang[1,2], Yinggang Jiao[1], Quanguo Zhang[1], Cheng Yong[2], Jinfei Zhao[3], Francesco Petracchini[4], Valerio Paolini[4] and Zhiping Zhang[1]**

[1]Key Laboratory of New Materials and Facilities for Rural Renewable Energy, MOA of China, Henan Agricultural University, Zhengzhou, China, [2]Institute of Agricultural Resources and Environment, Jiangsu Academy of Agricultural Sciences, Nanjing, China, [3]Key Laboratory of Modern Agricultural Engineering of Xinjiang Higher Education Institutions, Alar, China, [4]National Research Council of Italy- Institute of Atmospheric Pollution Research, Rome, Italy

Clean- and high-value recovery and reuse of the residue of biohydrogen production (biohydrogen slurry) is an urgent problem to be solved. In this study, sodium alginate (SA) gel was used to concentrate nutrients quickly *in situ* from biohydrogen slurry, which was prepared into gel microspheres (GMs), just like "capsule." The immobilization and release efficiency of conventional and reverse spherification were investigated. Better immobilization and release efficiency were detected under the conventional spherification method. The effect of GM sizes and concentrations of SA and calcium chloride ($CaCl_2$) was further studied in terms of sphericity factor, nutrient release, yield, encapsulation efficiency, and loading capacity. The best immobilization effect was obtained with a 1.6-mm syringe needle, 3.0 wt% SA, and 6 wt% $CaCl_2$, in which the sphericity factor, nitrogen release, yield, nitrogen encapsulation efficiency, and nitrogen loading capacity reached to 0.047, 96.20, 77.68, 38.37, and 0.0476%, respectively. This process not only avoids environmental pollution from biohydrogen slurry but also uses them at a high value as a fertilizer to nourish the soil. The feasibility of "slurry capsule" preparation will realize the clean recovery and reuse of biohydrogen slurry, which provides a new idea for ecological protection and carbon neutral goals and has important significance for sustainable development.

Keywords: sodium alginate, slurry capsule, fermentative biohydrogen production, immobilization effect, fertilizer

OPEN ACCESS

Edited by:
Junting Pan,
Institute of Agricultural Resources and Regional Planning (CAAS), China

Reviewed by:
Kunlin Song,
University of Washington, United States
Ping Ai,
Huazhong Agricultural University, China
Hongqiong Zhang,
Northeast Agricultural University, China
Jiabao Li,
Chengdu Institute of Biology (CAS), China

****Correspondence:***
Zhiping Zhang
zhangzhiping715@163.com

Specialty section:
This article was submitted to Bioprocess Engineering, a section of the journal Frontiers in Bioengineering and Biotechnology

Received: *29 March 2022*
Accepted: *18 April 2022*
Published: *16 May 2022*

Citation:
Ai F, Zhang Y, Fan X, Li Y, Zhang H, Jiao Y, Zhang Q, Yong C, Zhao J, Petracchini F, Paolini V and Zhang Z (2022) Clean Style Recovery and Utilization of Residual Nutrients in Effluents From Biohydrogen Production: In Situ Immobilization Based on Sodium Alginate. Front. Bioeng. Biotechnol. 10:906968. doi: 10.3389/fbioe.2022.906968

1 INTRODUCTION

The resource utilization of biomass is an important measure to promote the green and sustainable development and reduce carbon emissions (Hameed et al., 2021). Agricultural waste recycling combined with green hydrogen production has become an important scientific innovation exploration (Lepage et al., 2021). Among several green hydrogen production pathways, fermentative biohydrogen production (FHP) is a promising one, which has a wide range of raw materials, high substrate utilization efficiency, and low energy consumption (Anwar et al., 2019). A

large amount of fermentation wastewater (biohydrogen slurry) will be produced after the process of hydrogen production by fermentation. The biohydrogen slurry after hydrogen production is rich in not only nitrogen, phosphorus, potassium, and other mineral nutrients needed for plant growth but also some beneficial amino acids (Akhlaghi and Najafpour-Darzi, 2020). Some of the nutrients are obtained from the addition in the process of hydrogen production but not fully utilized, and the other part is obtained from the degradation of raw materials (Wang Y. et al., 2021). The process and composition of biohydrogen slurry and biogas slurry are similar. It has been reported that biogas slurry could be used as a liquid fertilizer to irrigate land, which can significantly promote nitrogen absorption by plants, increase crop yield, and improve soil structure (Zeng et al., 2022). But there are no reports about the utilization of biohydrogen slurry; instead, many researchers focused on the optimization and enhancement of the hydrogen production process (Zhu et al., 2021).

Compared with biogas slurry, biohydrogen slurry has higher VFAs and lower pH. From the angle of economy, discharging the tail liquid directly into the field seems to be most beneficial, but the absorption capacity of soil is limited and excessive biohydrogen slurry returning to the field may cause soil acidification and groundwater pollution, posing direct and indirect risks to human health (Li et al., 2021). The concentration of biohydrogen slurry is low, the water content is high, and excessive water content limits the direct return of biohydrogen slurry to the field. In addition, providing a large amount of nutrient elements for the plant at one time cannot achieve the maximum effect of nutrient elements because the demand for nutrient elements is different in different growth stages of the plant (Zhang et al., 2022). Therefore, it is necessary to explore a technology that can concentrate nutrients from the biohydrogen slurry and release nutrients slowly. By concentrating nutrients from the biohydrogen slurry, the storage and transportation of biohydrogen slurry can be reduced. *In situ* immobilization is the focus of recent research to immobilize the nutrients on the carrier in a special form by ion exchange, electrostatic attraction, physical adsorption, and carbonate precipitation, which is mainly used for the remediation of extensive contamination with heavy metals (Wang G. et al., 2021; Xie et al., 2022) and rapid *in situ* removal of residual antibiotics in aquaculture systems (Sha et al., 2022). Biochar, metal oxides, phosphate compounds, and silicon fertilizer are common immobilized carriers and show better fixation and sealing effect (Huang et al., 2020), preventing the fixed target precipitation from fixed carriers. But for the nutrients in biohydrogen slurry, the immobilized carrier should meet the requirement, which not only can concentrate nutrients from the biohydrogen slurry but also release nutrients slowly.

Recently, sodium alginate (SA) gel, as an environmentally friendly material, has been used in the field of environmental remediation because of its hydrophilicity and stability (Thakur et al., 2018). SA was used to fix magnesium-loaded bentonite to produce beads, which could effectively adsorb phosphate in water, and the beads could be used as slow-release fertilizer for the growth of mint (Xi et al., 2021). At present, there is no unified evaluation standard for slow-release fertilizer, and the method of comparison with the chemical fertilizer is generally used to evaluate its slow-release performance. The composite hydrogel modified by polyacrylamide with sodium alginate had higher pesticide-loading efficiency and sustained release performance and had a positive effect on the clean utilization of pesticides (Wang et al., 2019). Specifically, the environmental remediation mechanism of SA is mainly adsorption and slow release, that is, using the characteristics of SA to provide a stable condition for the inclusion so as to realize the ecological environment management *via* the character of the inclusion (Fernando et al., 2020; Gao et al., 2020).

Hence, considering the physicochemical characters of biohydrogen slurry and nutrient release requirement, the SA immobilization method, which is not only a conventional fix method but also a novel utilization pathway for fixing the beneficial substances in the biohydrogen slurry produced from the FHP process, was discussed. Using SA as the carrier, gel microspheres (GMs) are rapidly formed by combining with polyvalent cations under extremely mild conditions (Tokarev and Minko, 2010). The production of GMs can realize the clean utilization of biohydrogen slurry. For its fixation of biohydrogen slurry, active substances, such as nutrients, proteins, and amino acids, can be embedded by SA, and the composition retention and effectiveness can be maximized. Moreover, the GMs are easier to store and transport and have the effect of slow release of nutrients, just like the "slurry capsule" that can be used for soil remediation, nutrient control, and treatment of other soil problems (Bennacef et al., 2021). This process not only avoids environmental pollution from biohydrogen slurry but also uses them at a high value as a fertilizer to nourish the soil.

2 MATERIAL AND METHODS

2.1 Chemicals and Materials

Five types of biohydrogen slurry were collected from the following experiments, dark-fermentative biohydrogen production from alfalfa (ADF), dark-fermentative biohydrogen production from corn straw (SCDF), photo-fermentative biohydrogen production from corncob (CLF), photo-fermentative biohydrogen production from co-digestion of cow dung and corn straw (CCLF), and photo-fermentative biohydrogen production from corn straw with the biochar additive (CBLF). The procedures of the FHP process are mentioned in the previous literature (Garcia-Depraect et al., 2021; Zhang et al., 2021). The composition of the five biohydrogen slurries and mock biohydrogen slurry (MBS) is shown in **Table 1**.

SA is obtained from Fuchen (Tianjin) Chemical Reagent Co., LTD. Anhydrous calcium chloride ($CaCl_2$) is obtained from Kemiou (Tianjin) Chemical Reagent Co., LTD.

2.2 The *In Situ* Immobilization Method of Biohydrogen Slurry

Two immobilization methods, the conventional spherification method and inverse spherification method, were conducted in this work to compare its immobilization effect and releasing property (Bennacef et al., 2021). In the conventional

TABLE 1 | Composition of the five biohydrogen slurries.

Biohydrogen slurry	Nutritive element (mg/L)					Amino acid (mg/L)		
	N	P	K	Mg	Ca	Phe	Pro	Arg
ADF	2057.840	70.339	2636.114	74.258	255.463	6.661	2.370	2.772
CCLF	71.543	68.939	154.689	49.008	99.138	0.329	0.141	0.037
CBLF	148.683	39.889	1028.864	22.525	55.288	0.428	0.173	0.269
SCDF	628.430	286.114	740.614	83.733	157.388	3.388	0.996	2.913
CLF	104.893	27.189	1274.864	27.658	87.488	0.496	0.489	0.485
MBS	2000.000	100.000	2200.000	——	——	7.000	3.000	3.000

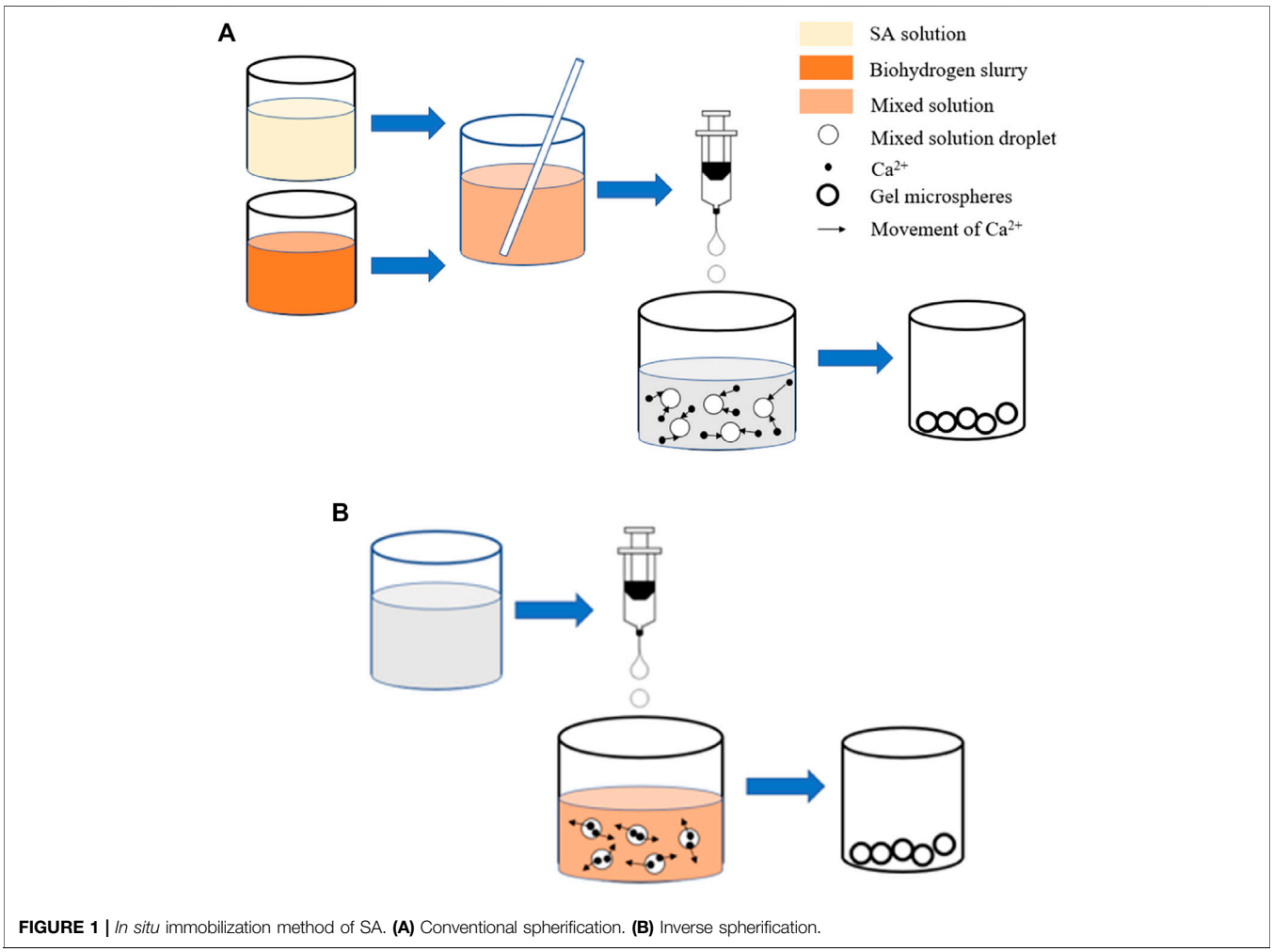

FIGURE 1 | *In situ* immobilization method of SA. **(A)** Conventional spherification. **(B)** Inverse spherification.

spherification method, SA and biohydrogen slurry are directly mixed and dropped into an aqueous solution containing Ca^{2+}. Ca^{2+} penetrates from the outside to the inside, and the outer layer of the "capsule" has a high crosslinking density. In the inverse spherification method, an aqueous solution containing Ca^{2+} is dropped into the mixed solution of sodium alginate and biohydrogen slurry. Ca^{2+} penetrates from the inside to the outside, and the inner layer of the "capsule" has a high crosslinking density (Tsai et al., 2017).

Three mL biohydrogen slurry and 7 ml 3.0 wt% SA solution were injected into a 50-ml beaker with a pipette, shaken and oscillated so that the solution was fully mixed. Then, the 10 ml uniform solution was extracted by a 10-ml hypodermic needle and uniformly dropped into a sufficient amount of 10 wt% $CaCl_2$ solution. After 2 h, the GMs were filtered out and placed in reserve (**Figure 1A**); this differs from the conventional spherification method. During the inverse spherification, 10 wt% $CaCl_2$ solution was injected into the mixed solution of 3 ml biohydrogen slurry and 7 ml 3.0 wt% SA, and then

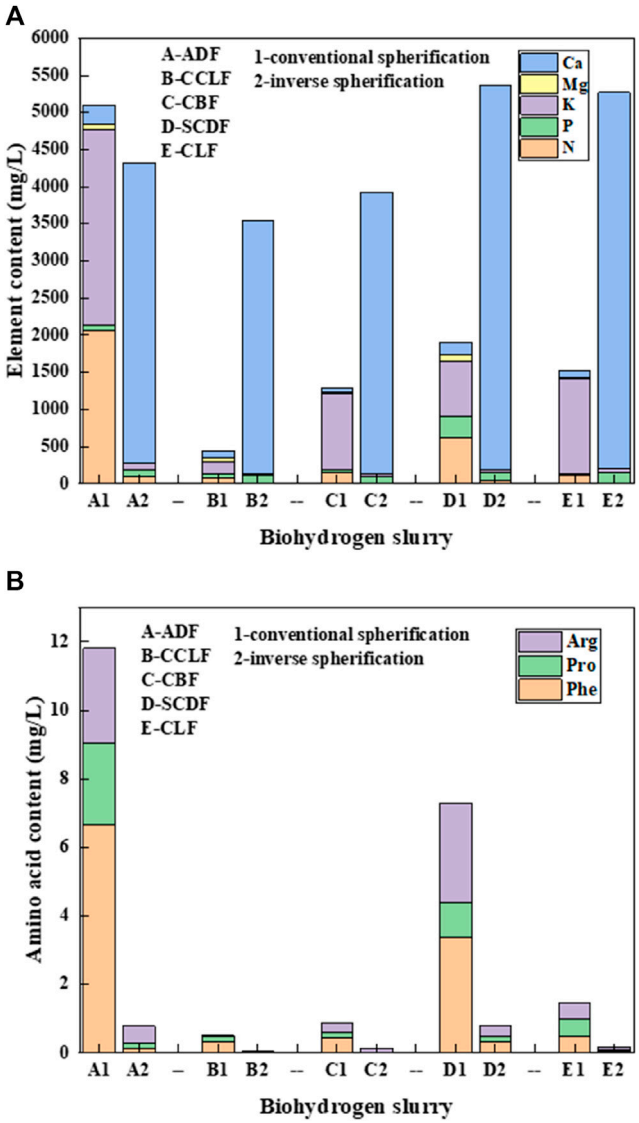

FIGURE 2 | Release effect of nutrients in five kinds of biohydrogen slurry. **(A)** Release effect of nutrient elements. **(B)** Release effect of amino acids.

the next steps were the same as those in the conventional spherification method (**Figure 1B**).

2.3 Immersion Experiment Design

The element release effect and immobilization effect of GM were evaluated by the single-factor experiment. Using the effective volume, a 150-ml cone bottle was used as the release experimental reactor, 12 g GMs were accurately placed in the reactor, and 100 ml deionized water was added to the reactor, sealed with the fresh-keeping film, and the water sample was extracted after static 24 h. In the single-factor experiments, the conditions were changed one by one according to the following levels. Different syringe needle sizes (0.3, 0.7, 1.6, and 3.0 mm), SA concentration (1.0, 1.5, 2.0, 2.5, 3.0, 3.5, and 4.0 wt%), and $CaCl_2$ concentration (2, 4, 6, 8, 10, and 12 wt%) were set separately to observe the effect.

2.4 Analytical Methods

2.4.1 Immobilization Effect

The molding effect of GM was observed and the number, mass, particle size, and sphericity factor (SF) were also observed. The diameter of the GM was measured with a spiral micrometer. The mass of GM was measured by an electronic balance. The sphericity was calculated according to the following equation (**Eq 1**):

$$SF = \frac{d_{max} - d_{min}}{d_{max} + d_{min}}, \quad (1)$$

TABLE 2 | Effects of GM with different sizes on the immobilization of nutrients.

Syringe needle size (mm)	GM size (mm)<	SF	EE% (N)	LC% (N)	EE% (K)	LC% (K)	Y%
0.3	2.096 ±0.044	0.078	34.65 ±0.15	0.0545	29.29 ±0.07	0.0507	60.87
0.7	2.482 ±0.089	0.062	34.32 ±0.18	0.0491	30.30 ±0.06	0.0477	66.96
1.6	3.182 ±0.010	0.045	34.56 ±0.06	0.0472	30.30 ±0.11	0.0455	70.16
3.0	3.505 ±0.075	0.057	34.51 ±0.07	0.0502	27.27 ±0.03	0.0419	68.59

where $d_{\max}$ (mm) refers to the maximum diameter of the GM and $d_{\min}$ (mm) refers to the minimum diameter of the same GM (Benavides et al., 2016). When SF ≤ 0.05, it can be considered to be a standard sphere.

2.4.2 Nutrient Detection

The content of each element is determined by ICP-AES/MS, adding 5 ml nitric acid and 1 ml hydrochloric acid to the bottom of the polytetrafluoroethylene digestion tank for microwave digestion and then the ratio of acid and digestion time was adjusted on the basis of different sample conditions. After digestion, the volume can be fixed to 50 ml. The potassium content was measured by using a flame photometer. The total nitrogen content of the biohydrogen slurry and water sample was determined by a TOC organic carbon total nitrogen analyzer (Jena, N3-1082/AQ, Germany), using oxygen as the carrier gas, control detector temperature was 800 ˚C, and the sample was 200.0uL per injection. Amino acids were determined by HPLC (Agilent, 1260, United States).

2.4.3 GM Yield (*Y*%) Refers to the Ratio Between GM Output and Liquid Input; *Y*% Is Expressed by the Following Expression (Eq 2) (Chan, 2011)

$$Y\% = \frac{M_{out}}{M_{in}} \times 100, \tag{2}$$

where M_{out} is the weight of the GM obtained and M_{in} is the weight of liquid used.

2.4.4 Encapsulation Efficiency (*EE*%) Refers to the Ratio of the Weight of Elements in GM to the Total Weight of Elements Invested (Eq 3) (Yari et al., 2020):

$$EE\% = \frac{M_a - M_b}{M_a} \times 100, \tag{3}$$

where M_a is the weight of the elements added and M_b is the weight of elements lost during immobilization.

2.4.5 Loading Capacity (*LC%)* Refers to the Ratio of the Weight of Elements in GM to the Total Weight of GM (Eq 4) (Gong et al., 2011)

$$LC\% = \frac{M_a - M_b}{M_C} \times 100, \tag{4}$$

where M_c is the weight of GM.

2.5 Statistical Analysis

All data collation and mapping were performed by using OriginPro 2018C and Excel software. Three groups of parallel experiments were set for all samples, and the immobilization effect of each factor on the biohydrogen slurry and nutrient release effect of GM was analyzed by single-factor standard deviation (Markowski, 1990).

3 RESULTS AND DISCUSSION

3.1 Comparison of the Nutrient Release Effect Between Conventional and Inverse Spherification

As shown in **Figure 2A**, the nitrogen content in the sustained release nutrient solution prepared by conventional spherification is 10–20 times higher than that of inverse spherification, while the phosphorus content is basically similar. The potassium content is 20–30 times higher than that of inverse spherification, and the magnesium content is 5–15 times higher than that of inverse spherification. When using the inverse spherification method, nutrients need to enter the inside of the droplet and then be fixed, while the sodium alginate gel process is very fast, resulting in a large number of nutrients lost in the external solution, making it less nutrient-embedded. The content of calcium in the nutrient solution prepared by inverse spherification is about 60 times higher than that by conventional spherification, but only a fraction of the calcium is released from the anerobic biohydrogen slurry, and most are released by decomposition of the GM's shell. The faster the calcium release, more volatile the gel forming. It can prove that the GMs prepared by conventional spherification have better a release effect than the glue block formed by inverse spherification.

The contents of main amino acids in the five biohydrogen slurries after slow release are shown in **Figure 2B**. The content of Phe in conventional spherification was 10–60 times higher than that in inverse spherification. The release of Phe in conventional spherification of the alfalfa biohydrogen slurry even reached 6.661 mg/L, and the content of Pro in conventional

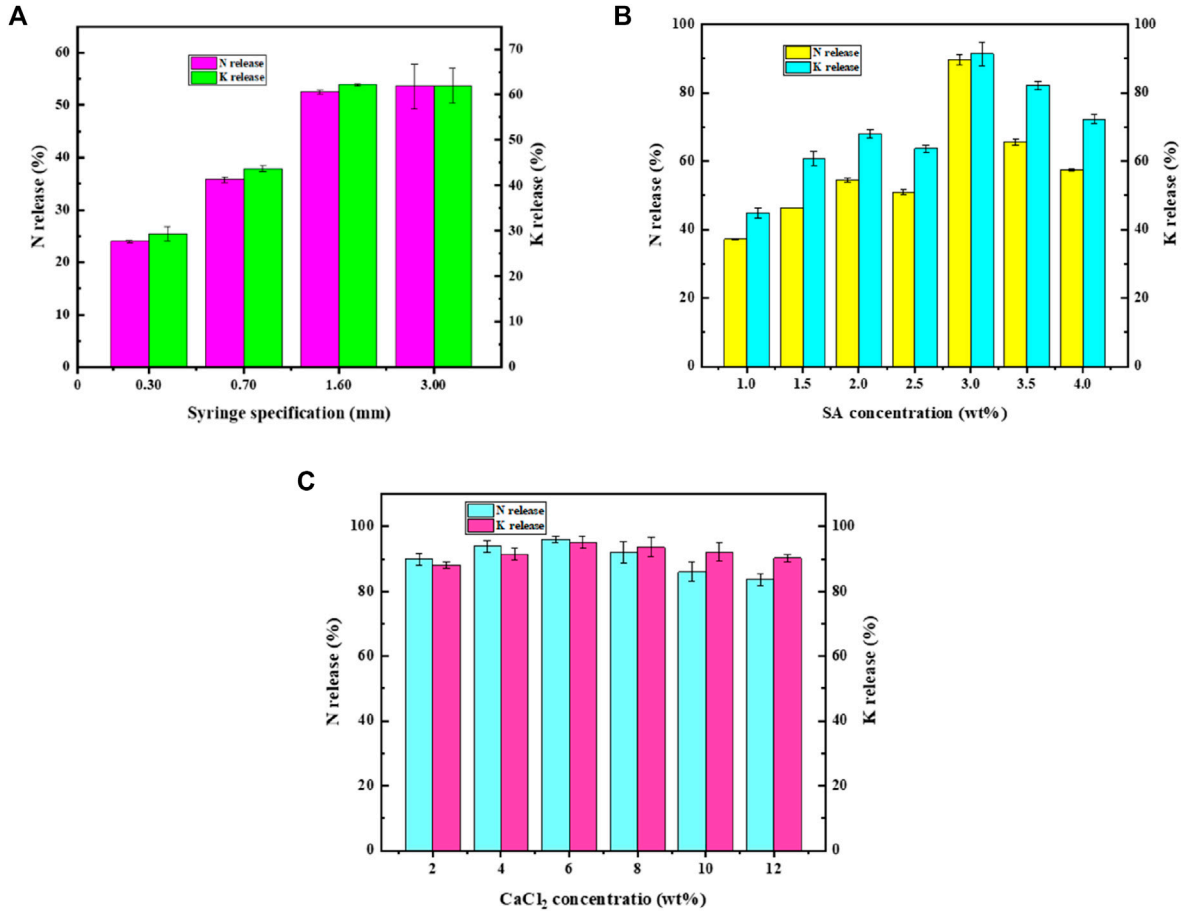

FIGURE 3 | Effects of different factors on the release of nutrients. **(A)** Sizes of GM. **(B)** SA concentration. **(C)** $CaCl_2$ concentration.

TABLE 3 | Effects of SA concentration on the immobilization of nutrients.

SA wt%	SF	EE% (N)	LC% (N)	EE% (K)	LC% (K)	Y%
1.0	0.141	37.84 ±0.11	0.0653	31.31 ±0.15	0.0595	55.44
1.5	0.073	36.91 ±0.17	0.0502	30.81 ±0.27	0.0461	70.39
2.0	0.055	35.39 ±0.03	0.0476	29.29 ±0.31	0.0433	71.21
2.5	0.053	36.38 ±0.04	0.0496	30.81 ±0.07	0.0462	70.28
3.0	0.049	34.96 ±0.14	0.0420	28.79 ±0.12	0.0380	79.74
3.5	0.018	35.99 ±0.07	0.0434	27.27 ±0.00	0.0362	79.38
4.0	0.017	36.83 ±0.10	0.0463	27.78 ±0.27	0.0384	76.19

TABLE 4 | Effects of $CaCl_2$ concentration on the immobilization of nutrients.

$CaCl_2$ wt%	SF	EE% (N)	LC% (N)	EE% (K)	LC% (K)	Y%
2	0.038	35.44 ±0.01	0.0493	30.55 ±0.02	0.0479	76.61
4	0.044	36.09 ±0.94	0.0463	30.81 ±0.25	0.0434	74.71
6	0.047	38.37 ±0.59	0.0476	32.32 ±0.15	0.0438	77.68
8	0.061	38.43 ±0.27	0.0482	32.82 ±0.12	0.0439	76.28
10	0.062	40.81 ±0.16	0.0486	33.33 ±0.01	0.0437	80.33
12	0.068	42.42 ±0.90	0.0512	33.84 ±0.31	0.0449	79.29

spherification was more than 10 times higher than that in inverse spherification. The content of Arg was 2–10 times higher in conventional spherification than in the inverse method. It can be clearly seen that the GMs produced by the conventional spherification had much higher amino acid content in the nutrient solution that is released than the glue block produced by the inverse spherification.

The utilization rate of nutrient elements and amino acids in biohydrogen slurry was significantly improved by conventional spherification ($p = 0.02542 < 0.05$), and the high value

immobilized treatment means would provide some positive significance for the clean utilization of biohydrogen slurry. The conventional spherification method was used for the subsequent optimization experiments.

3.2 Effects of GM Sizes on the Immobilization and Release of Nutrients

Generally, the immobilization effect of GM was evaluated by sphericity, EE%, LC%, and Y%, and the release effect of GM was evaluated by the release rate of nutrients. The size of the GM was adjusted by changing the syringe needle size, as shown in **Table 2**. Four syringe needles correspond to four particle sizes. It can be clearly seen that only when the syringe needle size was 1.6 mm, the SF of GM is <0.05, which was more similar to spheres than other kinds. This may be because the liquid dropped faster when the syringe needle was small, and the impact force was too large when it came in contact with the $CaCl_2$ solution, resulting in irregular GM formation; when the syringe needle was too large, the droplet volume and gravity became larger and the antideformation ability was weak, which increased SF. GM size had little influence on the EE% and LC % of N and K. When the needle was 1.6 mm, Y% was the highest. When GM size was small, the specific surface area increased, then the proportion of the gel shell increased, and the water loss was too much, leading to the decrease of GM total mass; when GM size was large, the amount of GM produced by a certain amount of biohydrogen slurry decreased and the total mass decreased.

As shown in **Figure 3A**, the cumulative release of N and K for GM prepared with 0.3 and 0.7 mm needles was much lower than that prepared with 1.6 and 3.0 mm needles. The cumulative release of N and K of GM prepared with 1.6 and 3.0 mm needles was about 53 and 62%, respectively, showing no significant difference (P_N = 0.06759 > 0.05 and P_K = 0.07090 > 0.05). Therefore, it is a good choice to use a 1.6-mm syringe needle to prepare GM.

3.3 Effect of SA Concentration on Immobilization and Nutrient Release of GM

As the material is directly carrying biohydrogen slurry, SA concentration plays an important role in GM molding. As shown in **Table 3**, with the increase of SA concentration, the sphericity of GM gradually decreased. When the SA concentration reached 3.0 wt% SA, GM had approximated to a sphere. When SA concentration was high in the droplet, the egg-box structure formed by crosslinking with Ca^{2+} was more stable and had stronger impact resistance. The EE% and LC % of GM prepared by 1% and 1.5% SA were slightly higher than those of other concentrations, but there was no significant difference ($P_{EE\%}$ = 0.14458 > 0.05 and $P_{LC\%}$ = 0.23465 > 0.05). The Y% of 3, 3.5, and 4.0 wt% SA was obviously higher than that of low concentration SA.

The cumulative release of N and K increased gradually in the low concentration of SA and reached a peak at 3.0 wt%, and then the cumulative release gradually decreased (**Figure 3B**). Combined with the experimental process, the result was caused by the slow gel forming process of SA with low concentration and excessive loss of nutrients. When the SA concentration is too high, the egg-box structure proportion in GM is too large and the porosity decreases, resulting in insufficient release of nutrients. Hence, the SA concentration of 3.0 wt% is more suitable for embedding the biohydrogen slurry.

3.4 Effect of $CaCl_2$ Concentration on Immobilization and Nutrient Release of GM

$CaCl_2$ concentration is also an important factor affecting *in situ* immobilization of the biohydrogen slurry (**Table 4**). With the increase of $CaCl_2$ concentration, the SF of GM increased, but when the concentration is 8 wt%, SF had exceeded 0.05. This was because with the increase of $CaCl_2$ concentration, the surface tension of the aqueous solution would also increase, and the resistance of the droplet when falling to the water surface would increase, resulting in serious deformation of GM. EE% of N and K also increased with increasing $CaCl_2$ concentration, but the range of change was not large. This may be because when the concentration of Ca^{2+} in the solution was high, the external osmotic pressure increased, and the loss of nutrients in GM would be reduced. The variation of LC% and Y% was relatively small. These phenomena indicate that the increase of $CaCl_2$ concentration had a slight positive effect on the immobilization effect of GM.

As can be seen from **Figure 3C**, with the change of $CaCl_2$ concentration, the cumulative release of N was maintained between 83.62 and 96.02%, and the cumulative release of K was maintained between 88.13 and 95.08%, with the change range within 15%. There was an inflection point at 6 wt%, and the cumulative release was the largest at this time. Considering the immobilization effect and release effect, 6 wt% $CaCl_2$ is suitable as the embedding carrier.

4 CONCLUSION

Previous research on the treatment of biological mud does not have a very good effect; this study will use biological mud with higher efficiency. In this work, the SA immobilization method was proposed to prepare the "slurry capsule" by biohydrogen slurry produced from FHP. Good pellet immobilization ability and the release level of nutrient elements are shown. It not only realized the harmless treatment of biohydrogen slurry and protected the environment but also achieved the purpose of resource utilization of biohydrogen slurry and solved an issue concerning the clean production of hydrogen energy.

The immobilization effect of conventional spherification is obviously better than that of the inverse spherification. The mixture (3.0 wt% SA/biohydrogen slurry) dropped into 6 wt% $CaCl_2$ solution by a 1.6-mm syringe needle, which was found to be the optimal immobilization condition. The sphericity factor, nitrogen release, yield, nitrogen encapsulation efficiency, and nitrogen loading capacity reached to 0.047, 96.20, 77.68, 38.37, and 0.0476%, respectively.

Compared with previous studies, this is a cleaner immobilization method of biohydrogen slurry, which can ensure the utilization value of fermentation tail liquid and provide some favorable directions for environmental protection and waste resource utilization research. This study provides new ideas for ecological conservation and carbon neutrality, which is of great significance for sustainable development.

DATA AVAILABILITY STATEMENT

The raw data supporting the conclusion of this article will be made available by the authors, without undue reservation.

AUTHOR CONTRIBUTIONS

FA: writing the original draft. YZ: methodology. XF: visualization. YL: resources. HZ: software. YJ: application of statistical analysis. QZ: validation. CY: editing. FP: validation. VP: validation. ZZ: corresponding author, responsible for ensuring that the description is accurate and agreed by all authors.

FUNDING

This work was financially supported by the National Key R and D Program of China (2018YFE0206600) and Key Scientific Research Projects of colleges and universities of Henan Province (22A416006).

REFERENCES

Akhlaghi, N., and Najafpour-Darzi, G. (2020). A Comprehensive Review on Biological Hydrogen Production. *Int. J. Hydrogen Energy* 45 (43), 22492–22512. doi:10.1016/j.ijhydene.2020.06.182

Anwar, M., Lou, S., Chen, L., Li, H., and Hu, Z. (2019). Recent Advancement and Strategy on Bio-Hydrogen Production from Photosynthetic Microalgae. *Bioresour. Technol.* 292, 121972. doi:10.1016/j.biortech.2019.121972

Benavides, S., Cortés, P., Parada, J., and Franco, W. (2016). Development of Alginate Microspheres Containing Thyme Essential Oil Using Ionic Gelation. *Food Chem.* 204, 77–83. doi:10.1016/j.foodchem.2016.02.104

Bennacef, C., Desobry-Banon, S., Probst, L., and Desobry, S. (2021). Advances on Alginate Use for Spherification to Encapsulate Biomolecules. *Food Hydrocoll.* 118, 106782. doi:10.1016/j.foodhyd.2021.106782

Chan, E.-S. (2011). Preparation of Ca-Alginate Beads Containing High Oil Content: Influence of Process Variables on Encapsulation Efficiency and Bead Properties. *Carbohydr. Polym.* 84 (4), 1267–1275. doi:10.1016/j.carbpol.2011.01.015

Fernando, I. P. S., Lee, W., Han, E. J., and Ahn, G. (2020). Alginate-based Nanomaterials: Fabrication Techniques, Properties, and Applications. *Chem. Eng. J.* 391, 123823. doi:10.1016/j.cej.2019.123823

Gao, X., Guo, C., Hao, J., Zhao, Z., Long, H., and Li, M. (2020). Adsorption of Heavy Metal Ions by Sodium Alginate Based Adsorbent-A Review and New Perspectives. *Int. J. Biol. Macromol.* 164, 4423–4434. doi:10.1016/j.ijbiomac.2020.09.046

García-Depraect, O., Muñoz, R., Rodríguez, E., Rene, E. R., and León-Becerril, E. (2021). Microbial Ecology of a Lactate-Driven Dark Fermentation Process Producing Hydrogen under Carbohydrate-Limiting Conditions. *Int. J. Hydrogen Energy* 46 (20), 11284–11296. doi:10.1016/j.ijhydene.2020.08.209

Gong, R., Li, C., Zhu, S., Zhang, Y., Du, Y., and Jiang, J. (2011). A Novel pH-Sensitive Hydrogel Based on Dual Crosslinked alginate/N-α-Glutaric Acid Chitosan for Oral Delivery of Protein. *Carbohydr. Polym.* 85 (4), 869–874. doi:10.1016/j.carbpol.2011.04.011

Hameed, Z., Aslam, M., Khan, Z., Maqsood, K., Atabani, A. E., Ghauri, M., et al. (2021). Gasification of Municipal Solid Waste Blends with Biomass for Energy Production and Resources Recovery: Current Status, Hybrid Technologies and Innovative Prospects. *Renew. Sustain. Energy Rev.* 136, 110375. doi:10.1016/j.rser.2020.110375

Huang, F., Li, K., Wu, R.-R., Yan, Y.-J., and Xiao, R.-B. (2020). Insight into the Cd2+ Biosorption by Viable Bacillus Cereus RC-1 Immobilized on Different Biochars: Roles of Bacterial Cell and Biochar Matrix. *J. Clean. Prod.* 272, 122743. doi:10.1016/j.jclepro.2020.122743

Lepage, T., Kammoun, M., Schmetz, Q., and Richel, A. (2021). Biomass-to-hydrogen: A Review of Main Routes Production, Processes Evaluation and Techno-Economical Assessment. *Biomass Bioenergy* 144, 105920. doi:10.1016/j.biombioe.2020.105920

Li, D., Liu, R., Cui, X., He, M., Zheng, S., Du, W., et al. (2021). Co-culture of Bacteria and Microalgae for Treatment of High Concentration Biogas Slurry. *J. Water Process Eng.* 41, 102014. doi:10.1016/j.jwpe.2021.102014

Markowski, C. A., and Markowski, E. P. (1990). Conditions for the Effectiveness of a Preliminary Test of Variance. *Am. Statistician* 44 (4), 322–326. doi:10.1080/00031305.1990.10475752

Sha, S., Dong, Z., Gao, Y., Hashim, H., Lee, C. T., and Li, C. (2022). *In-situ* Removal of Residual Antibiotics (Enrofloxacin) in Recirculating Aquaculture System: Effect of Ultraviolet Photolysis Plus Biodegradation Using Immobilized Microbial Granules. *J. Clean. Prod.* 333, 130190. doi:10.1016/j.jclepro.2021.130190

Thakur, S., Sharma, B., Verma, A., Chaudhary, J., Tamulevicius, S., and Thakur, V. K. (2018). Recent Progress in Sodium Alginate Based Sustainable Hydrogels for Environmental Applications. *J. Clean. Prod.* 198, 143–159. doi:10.1016/j.jclepro.2018.06.259

Tokarev, I., and Minko, S. (2010). Stimuli-Responsive Porous Hydrogels at Interfaces for Molecular Filtration, Separation, Controlled Release, and Gating in Capsules and Membranes. *Adv. Mat.* 22 (31), 3446–3462. doi:10.1002/adma.201000165

Tsai, F.-H., Kitamura, Y., and Kokawa, M. (2017). Liquid-core Alginate Hydrogel Beads Loaded with Functional Compounds of Radish By-Products by Reverse Spherification: Optimization by Response Surface Methodology. *Int. J. Biol. Macromol.* 96, 600–610. doi:10.1016/j.ijbiomac.2016.12.056

Wang, G., Zhang, Q., Du, W., Lin, R., Li, J., Ai, F., et al. (2021). *In-situ* Immobilization of Cadmium-Polluted Upland Soil: A Ten-Year Field Study. *Ecotoxicol. Environ. Saf.* 207, 111275. doi:10.1016/j.ecoenv.2020.111275

Wang, L., Yu, G., Li, J., Feng, Y., Peng, Y., Zhao, X., et al. (2019). Stretchable Hydrophobic Modified Alginate Double-Network Nanocomposite Hydrogels for Sustained Release of Water-Insoluble Pesticides. *J. Clean. Prod.* 226, 122–132. doi:10.1016/j.jclepro.2019.03.341

Wang, Y., Jing, Y., Lu, C., Kongjan, P., Wang, J., Awasthi, M. K., et al. (2021). A Syntrophic Co-fermentation Model for Bio-Hydrogen Production. *J. Clean. Prod.* 317, 128288. doi:10.1016/j.jclepro.2021.128288

Xi, H., Jiang, H., Zhao, D., Zhang, A. H., Fan, B., Yang, Y., et al. (2021). Highly Selective Adsorption of Phosphate from High-Salinity Water Environment Using MgO-Loaded and Sodium Alginate-Immobilized Bentonite Beads. *J. Clean. Prod.* 313, 127773. doi:10.1016/j.jclepro.2021.127773

Xie, X., Zhang, Z., Chen, Z., Wu, J., Li, Z., Zhong, S., et al. (2022). *In-situ* Preparation of Zinc Sulfide Adsorbent Using Local Materials for Elemental Mercury Immobilization and Recovery from Zinc Smelting Flue Gas. *Chem. Eng. J.* 429, 132115. doi:10.1016/j.cej.2021.132115

Yari, K., Akbari, I., and Yazdi, S. A. V. (2020). Development and Evaluation of Sodium Alginate-Basil Seeds Mucilage Beads as a Suitable Carrier for Controlled Release of Metformin. *Int. J. Biol. Macromol.* 159, 1–10. doi:10.1016/j.ijbiomac.2020.04.111

Zeng, W., Qiu, J., Wang, D., Wu, Z., and He, L. (2022). Ultrafiltration Concentrated Biogas Slurry Can Reduce the Organic Pollution of Groundwater in Fertigation. *Sci. Total Environ.* 810, 151294. doi:10.1016/j.scitotenv.2021.151294

Zhang, K., Liang, X., Zhang, Y., Liu, X., Tian, Y., Zhu, Y., et al. (2022). Optimizing Spikelet Fertilizer Input in Irrigated Rice System Can Reduce Nitrous Oxide Emission while Increase Grain Yield. *Agric. Ecosyst. Environ.* 324, 107737. doi:10.1016/j.agee.2021.107737

Zhang, Q., Zhu, S., Zhang, Z., Zhang, H., and Xia, C. (2021). Enhancement Strategies for Photo-Fermentative Biohydrogen Production: A Review. *Bioresour. Technol.* 340, 125601. doi:10.1016/j.biortech.2021.125601

Zhu, S., Yang, X., Zhang, Z., Zhang, H., Li, Y., Zhang, Y., et al. (2021). Tolerance of Photo-Fermentative Biohydrogen Production System Amended with Biochar and Nanoscale Zero-Valent Iron to Acidic Environment. *Bioresour. Technol.* 338, 125512. doi:10.1016/j.biortech.2021.125512

Conflict of Interest: The authors declare that the research was conducted in the absence of any commercial or financial relationships that could be construed as a potential conflict of interest.

Publisher's Note: All claims expressed in this article are solely those of the authors and do not necessarily represent those of their affiliated organizations, or those of the publisher, the editors, and the reviewers. Any product that may be evaluated in this article, or claim that may be made by its manufacturer, is not guaranteed or endorsed by the publisher.

frontiers | Frontiers in Bioengineering and Biotechnology

ORIGINAL RESEARCH
published: 15 June 2022
doi: 10.3389/fbioe.2022.918365

Greenhouse Gas Emissions From Biofilters for Composting Exhaust Ammonia Removal

Bin Shang, Tanlong Zhou, Xiuping Tao and Yongxing Chen*

Key Laboratory of Energy Conservation and Waste Management of Agricultural Structures, MARA, Institute of Environment and Sustainable Development in Agriculture, Chinese Academy of Agricultural Sciences, Beijing, China

Emissions of odorous compounds, such as ammonia (NH_3), from composting have negative agronomic and environmental impacts. A biofilter is widely used for NH_3 removal, with one of its potential detrimental by-products being nitrous oxide (N_2O), which is a higher warming potential greenhouse gas (GHG). The aim of the study was to evaluate the effect of empty bed retention time (EBRT) on GHG emissions from biofilters for removing NH_3 from composting. Composting experimental trials lasted 6 weeks, and composting materials were mixtures of dead pigs and manure. Three groups of biofilters with 1.2 m-height, 0.3 m-inner diameter, and 1.0 m media depth were conducted with EBRT of 30, 60, and 100s, respectively. Each treatment was performed in triplicate, and the gas was monitored using the dynamic emission vessel method. The Spearman's correlation analysis showed a significantly positive correlation between inlet concentrations (ICs) of NH_3 and increased N_2O concentrations: ρ = 0.707, 0.762, and 0.607 with $p \leq 0.0001$ for biofilters with EBRT of 30, 60, and 100s, respectively. The fraction of NH_3-N denitrified into N_2O-N in biofilters with EBRT of 60 and 100s was higher than that with EBRT of 30s. The total global warming potential (GWP) increased by 126%, 162%, and 144% for biofilters with EBRT of 30, 60, and 100s, respectively. These results indicated that biofilters with longer EBRT will lead to higher GWP production. Future research on odorous mitigation for composting with biofilters should focus more on greenhouse gas emissions.

Keywords: empty bed retention time, ammonia biofilter, greenhouse gases, nitrous oxide, waste management

OPEN ACCESS

Edited by:
Junting Pan,
Institute of Agricultural Resources and Regional Planning (CAAS), China

Reviewed by:
Zengqiang Zhang,
Northwest A & F University, China
Guodi Zheng,
Institute of Geographic Sciences and Natural Resources Research (CAS), China

****Correspondence:***
Bin Shang
shangbin@caas.cn

Specialty section:
This article was submitted to Bioprocess Engineering, a section of the journal Frontiers in Bioengineering and Biotechnology

Received: *12 April 2022*
Accepted: *04 May 2022*
Published: *15 June 2022*

Citation:
Shang B, Zhou T, Tao X and Chen Y (2022) Greenhouse Gas Emissions From Biofilters for Composting Exhaust Ammonia Removal. Front. Bioeng. Biotechnol. 10:918365. doi: 10.3389/fbioe.2022.918365

INTRODUCTION

Composting has been applied worldwide as an environmentally friendly and cost-effective method for sanitation and recycling animal waste (Loyon, 2017; Zheng et al., 2020). However, one major complication during composting is the odor emission (Cheng and Hu, 2010; Huang et al., 2012; Paulot, et al., 2014), which not only poses a problem to the general public and environmental health but also causes adverse effects on vegetation surrounding the composting plants (Han et al., 2019). Ammonia (NH_3) is considered the major contributor to odor from composting (Zhang et al., 2016; Zhu et al., 2016), and the precursors of particulate matter can be produced by the reactions of NH_3 with sulfuric and nitric acid aerosols (Pinder, et al., 2007; Renner and Wolke, 2010; Kong et al., 2020).

Biofilters are widely used to reduce NH_3 emissions from composting (Turan et al., 2009; Mudliar et al., 2010; Janni et al., 2014). Many studies have focused on the physical, chemical, and biological

TABLE 1 | Experimental performance of biofilters.

Treatment	Biofilter	Volume per biofilter (m^3)	Empty bed retention time (EBRT, s)
1	1,2, and 3	0.071	30
2	4,5, and 6	0.071	60
3	7,8, and 9	0.071	100

parameters influencing the biofiltration process (Park, et al., 2002; Yuan et al., 2019). A number of studies have shown that nitrous oxide (N_2O) generation in biofilters is often accompanied by NH_3 removal (Maia et al., 2012b; Yang et al., 2014a; Kong et al., 2020). Akdeniz and Janni (2012) observed that N_2O generation ranged from −29.2% to 4.0% for a flat-bed biofilter with an empty bed retention time (EBRT) of 5s. Clemens and Cuhls (2003) observed that approximately 26% of NH_3-N entered in the biofilters is converted into N_2O-N. N_2O emissions from biofilters can be affected by several factors, such as inlet NH_3 concentration, temperature, moisture content, and pH value (Maia et al., 2012b; Yang et al., 2014a; Yang et al., 2014b; Dumont et al., 2014). High moisture content can cause regional anaerobic zones and increase the microbial activity, which favors N_2O emission (Yang et al., 2014a). Compared to a high pH value (8.0–9.5), a low pH value (4.5–6.0) of the media can inhibit the generation of N_2O reductase and reduce the emission of N_2O (Yang et al., 2014b). N_2O from biofilters was correlated significantly with the NH_3 in the biofilters (Clemens and Cuhls, 2003). EBRT can affect microorganism absorption and the conversion process of NH_3 in the biofilters (Shang et al., 2020). Shorter EBRT means faster gas flow velocity, which can change the oxygen (O_2) gradients in the biofilter media and can lead to changes in denitrification (Maia, et al., 2012b). In addition, higher air flow can increase the emission rate of gas from composting. EBRT is one of the key parameters of biofilters for NH_3 removal (Liu et al., 2017); however, few studies have investigated the effects of EBRT on emissions of N_2O. A better understanding of the effects of EBRT on the generation and emission of N_2O needs to be elucidated. In this study, the effects of EBRT on greenhouse gas (N_2O and methane, CH_4) emissions from pilot-scale biofilter systems were studied. The results can provide a promising tool for greenhouse gas reduction from full-scale biofilters.

CH_4 is another important greenhouse gas emitted during composting (Zhu-Barker, et al., 2017). Biofilters also can be used to reduce CH_4 emissions (Haubrichs and Widmann, 2006). Many studies performed on CH_4 biofiltration utilized an EBRT of at least 4 min (La et al., 2018), which posed obstacles to the biofilter application. Little information is available in the literature about CH_4 reduction capabilities during NH_3 biofiltration.

Global warming potential for N_2O and CH_4 is 296 and 23 times higher than that of carbon dioxide (CO_2), respectively (Pachauri et al., 2014). It is very important to examine the generation of greenhouse gas due to odor treatment by biofilters. Thus, the objectives of this study were 1) to investigate the emissions of N_2O from biofilters with different EBRT and 2) to assess the greenhouse gas (N_2O and CH_4) emissions from biofilters for composting NH_3 removal.

MATERIALS AND METHODS

Experiment Materials

This study was conducted in the Beijng Anding pig farm, located in Daxing District, Beijing, China (39°62′N, 116°50′E). The composting materials and composting process have been described by Shang et al. (2020).

The mature compost, composted for about 4 months, was used as the medium material. Before the experiment, the mature compost was inoculated with activated sludge from the aerobic fermentation plant for wastewater treatment in the pig farm, and the water content of packing materials at the beginning of composting was adjusted to 57.4 ± 2.5%, according to Akdeniz and Janni (2012). The mature compost used for biofilter media had total carbon (C) and nitrogen (N) contents of 30.8 ± 2.8% and 2.9 ± 0.7%, respectively, with a pH of 7.0.

Biofilter Design and Operations, Gas Sampling, and Analytical Method

The biofilters were constructed with circular unplasticized polyvinyl chloride (UPVC) pipes. The dimensions were 1.2 m (height) and 0.3 m (inner diameter), with a 1.0 m depth of media (corresponding to a bed material volume $V = 0.07\ m^3$). Nine biofilters were divided into three treatments, and different EBRT (30s, 60s, and 100s) were set according to previous studies (Pagans et al., 2005). Each treatment was conducted with three replicates. EBRT = V/Q, where Q is the air flow rate in $m^3 \cdot s^{-1}$. The experimental arrangements are shown in **Table 1**. NH_3, CH_4, and N_2O concentrations of air outside (1 sampling point), a gas inlet of biofilters (3 sampling points), and a gas outlet of biofilters (9 sampling points) were measured continuously and simultaneously using a photoacoustic multigas analyzer (model Innova 1412i, LumaSense Technologies, Ballerup, Denmark) every day. The deodorization system was constructed, as previously described (Shang et al., 2020), and the schematic is shown in **Figure 1**. The experiment corresponding to the composting period was carried out for 42 days. During the experiment, no water was supplied to the media of biofilters.

Data Analyses

All data were analyzed by Microsoft Excel 2016 and SPSS 22. The variables were tested for significance using Spearman's correlation coefficient. The rations of gas concentrations in outlet and inlet biofilters were calculated (Dumont, 2018). A ration >1 indicates gas formation in the biofilter, and a ration <1 indicates gas depletion in the biofilters. The t-test (one side $p < 0.05$) was used to determine if there was a significant deviation from 1.

Global Warming Potential Calculations

Global warming potential (GWP) was quantified as CO_2 equivalent with a 100-year timescale: 1 kg CH_4 and N_2O emitted are equivalent to 23 and 298 kg CO_2, respectively (Pachauri et al., 2014). The CH_4, N_2O, and GHG emissions (in kg $eqCO_2$) were calculated by multiplying the aerobic rates, the concentration, and the GWP factor during the whole experiment which lasted for 42 days. In this study, the GWP of

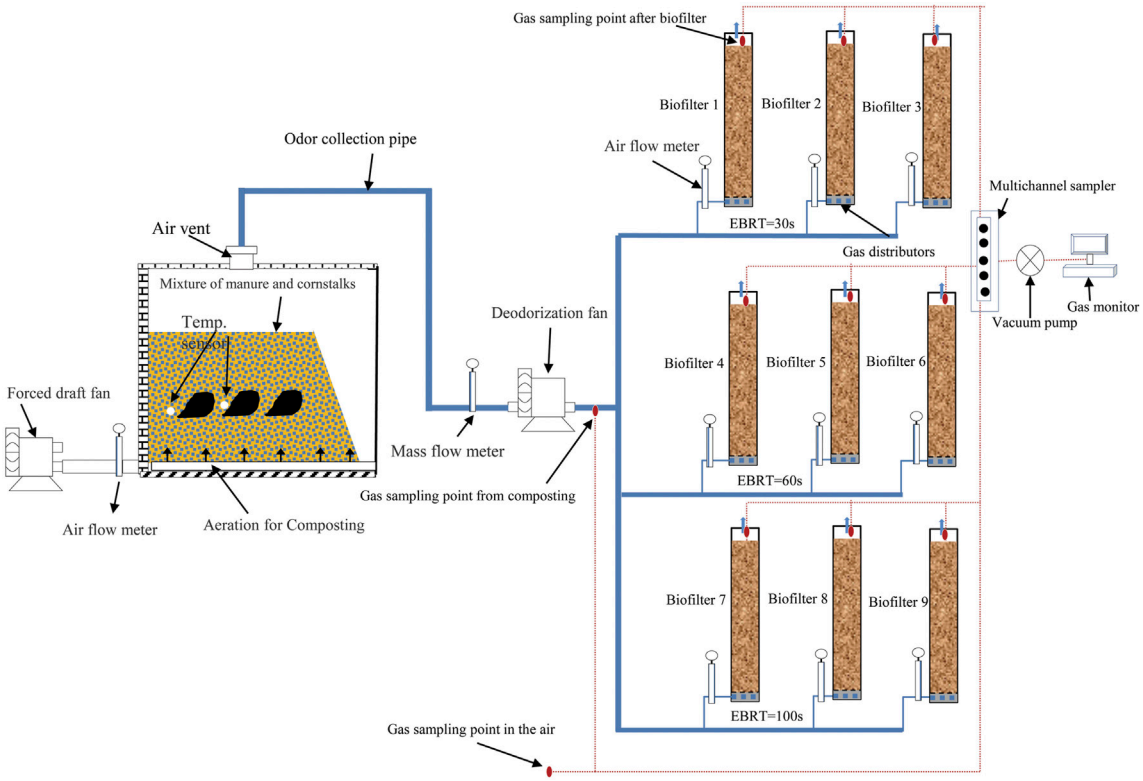

FIGURE 1 | Schematic representation of the composting and the biofiltration system.

CO_2 was not included because it is not considered GHG of agriculture (Buendia et al., 2019).

RESULTS AND DISCUSSION

Emission of Nitrous Oxide From Biofilters

NH_3, N_2O, and CH_4 concentrations in the air during the composting period were 5.6 ± 2.5, 1.0 ± 1.6, and 3.2 ± 1.6 mg m^{-3}, respectively. The NH_3 removal efficiencies have been described by Shang et al. (2020). The daily mean concentration of N_2O from composting ranged between 1.5 and 11.5 mg m^{-3}, while the daily mean N_2O concentrations from biofilters were about around 1.0 mg m^{-3} (**Figure 2**). The large variation in N_2O production was due to the different concentrations of NH_3 and N_2O from composting. The N_2O concentrations at the biofilters' outlet were in the range of 20%–1250%, 23%–1652%, and 3–1352% higher than those at the biofilters' inlet for EBRT of 30, 60, and 100s. The outlet concentrations of N_2O of biofilters with EBRT of 100 and 60s were higher than those with EBRT of 30s (**Figure 3**). But there are no significant differences between the biofilters with different EBRT.

With biofiltration systems, about half of the inlet NH_3 is converted to nitrites or nitrates, and the other half is absorbed into the water as ammonium (Ottosen et al., 2011; Yasuda et al., 2017). Both ammonia oxidizer and denitrifier can produce N_2O in a biofilter, but the majority of N_2O was generated from denitrification (Kong et al., 2020). Maia et al. (2012a) pointed that higher EBRT may result in non-uniform oxygen distribution, which favors conditions for denitrification to generate N_2O. In this study, the higher EBRT means a slower air flow rate, and the increasing N_2O concentration from biofilters with increasing EBRT may result from more denitrification. In addition, when the air continuously goes through media in the biofilter, the higher EBRT implies that there is more content time of air and media, which can lead to high NH_3-sorption, which favors the occurrence of nitrification–denitrification (Maia et al., 2012a). In this study, N_2O concentrations were found to be higher, up to 16 times, than inlet concentrations, which may be due to the longer EBRT and higher inlet concentrations of NH_3 (Dumont et al., 2014; Liu et al., 2017).

The inlet concentrations, inlet loads, and elimination capacities of NH_3 may affect N_2O generation. The Spearman's correlation analysis showed a strong positive correlation between inlet NH_3 concentrations and increased N_2O concentrations: ρ = 0.707, 0.762, and 0.607 with ($p \leq 0.0001$) for EBRT of 30, 60s and 100s, respectively. Inlet loads of NH_3 and increased N_2O concentrations were positively correlated: ρ = 0.685, 0.750, and 0.579 ($p \leq 0.0001$) for EBRT of 30, 60s, and 100s, respectively. Elimination capacities of NH_3 and increased N_2O concentrations were also positively correlated: ρ = 0.706, 0.761, and 0.602 with $p \leq 0.0001$ for EBRT 30, 60, and 100s, respectively. In this study, the inlet NH_3 concentrations were between 12 and 447 mg m^{-3}

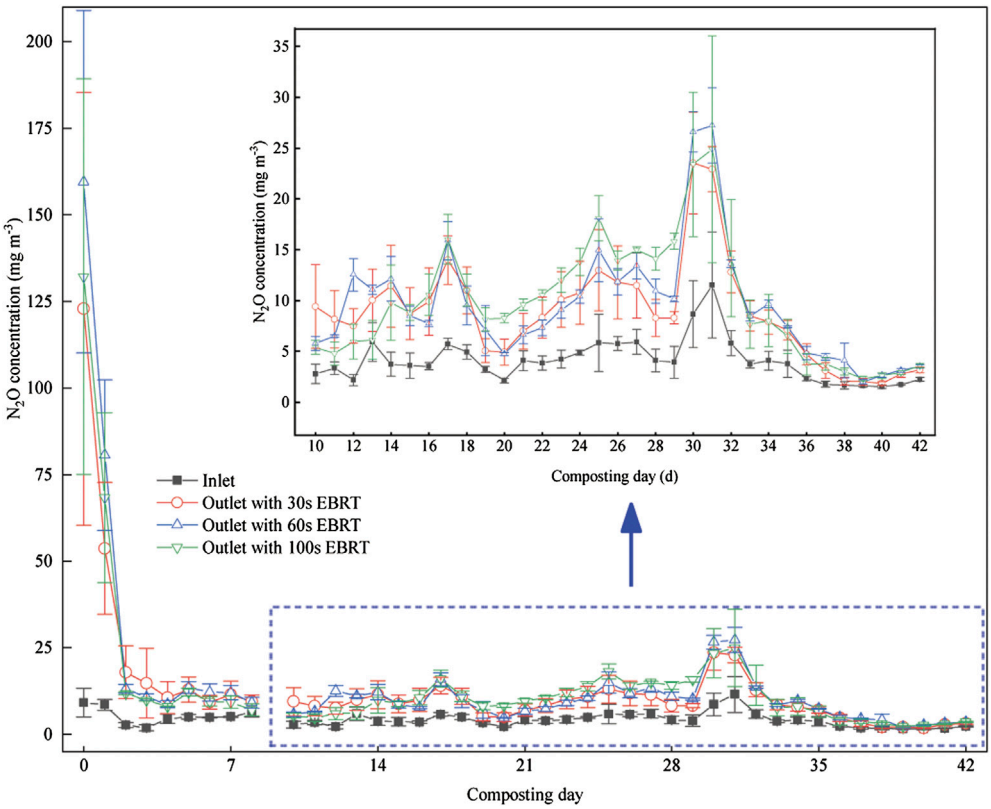

FIGURE 2 | Daily N_2O concentrations (mean ± SE) at the biofilter inlet (IC) and outlet (OC).

due to different composting processes, while the overall removal efficiencies were 85.4%, 88.7%, and 89.0% for EBRTs of 30, 60, and 100s, respectively. The elimination capacities of NH_3 have been discussed by Shang et al. (2020). NH_3 removal was considered the net source of N_2O in biofilters (Maia et al., 2012a). N_2O is considered normal at biofilters treating NH_3-containing air, being a byproduct of nitrification and denitrification, and the pathways of N_2O formation reported in the literature, however, are complex. Kong et al. (2020) found that the inlet NH_3 concentration can affect the nitrification process and the substrate availability for denitrification. In the present study, high inlet loads of NH_3 promoted N_2O generation, which were consistent with the other study (Kong, et al., 2020); the denitrification is the main pathway for N_2O formation.

Fraction of NH_3-N Denitrified Into N_2O-N

In the present study, there were significant differences in N_2O emissions between biofilters with different EBRT due to different inlet loads of NH_3 resulting from different EBRT. The fractions of NH_3-N converted into N_2O-N were 4.6%, 5.6%, and 5.1% for biofilters with EBRT of 30, 60, and 100s, respectively. The results were consistent with other studies (**Table 2**). Denitrification is considered the main source of N_2O emission while nitrification is a trigger (Yang et al., 2014a; Dumont et al., 2014; Kong et al., 2020), and the presence of oxygen can inhibit the denitrification process. In this study, low EBRT means high gas flow rate, which results in more oxygen penetration into the media of the biofilter, further reducing the denitrification rates. Except for the EBRT, some other factors, such as the kind of media and moisture content may also affect N_2O generation in biofilters. In Maia et al. (2012a), the compost of horse manure, cattle manure, chicken waste, woodchips, sawdust, and other materials were used as media for NH_3 removal, fraction of NH_3-N denitrified into N_2O-N was 14% and 19% for one biofilter and two other biofilters, respectively. The results of Yasuda et al. (2009) confirmed that NH_3 could be treated by biofilter with rockwool mixture without an extra increase of N_2O. The percentage of N_2O reduction efficiency ranging from 0.13 to 0.73% was found by Akdeniz (et al., 2011), who studied the removal of NH_3 and N_2O using biofilters with lava rock as media at 5s EBRT. The part of NH_3-N converted into N_2O was estimated to range from 10% to 40% (Dumont et al., 2014). Yang et al. (2014a) found that there was a slight increase in N_2O when the media moisture content increased from 35 to 55%, but further increasing the moisture content to 63% triggered N_2O generation rapidly. Yasuda et al. (2009) observed a higher N_2O generation when the moisture content ranged from 65% to 52%; when the moisture content decreased to 48%, the N_2O net generation decreased to nearly zero; when the moisture content decreased from 44% to 13%, N_2O generation decreased. A moisture content of about 50% is recommended for efficient NH_3 removal and less N_2O generation. Yang et al.

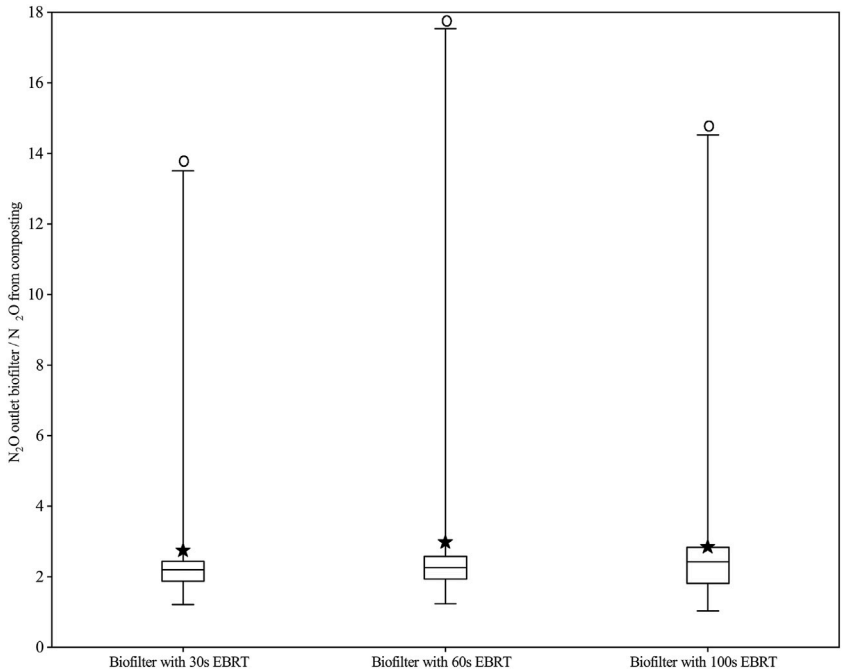

FIGURE 3 | Boxplot: Ratio of N_2O concentration of the outlet and inlet at different biofilters (Box border means 25 and 75% percentile, the solid line in the box means the median value, the solid pentacle means the mean value, whisker means the maximum and minimum values, and the white circle means significant differences between the inlet and outlet).

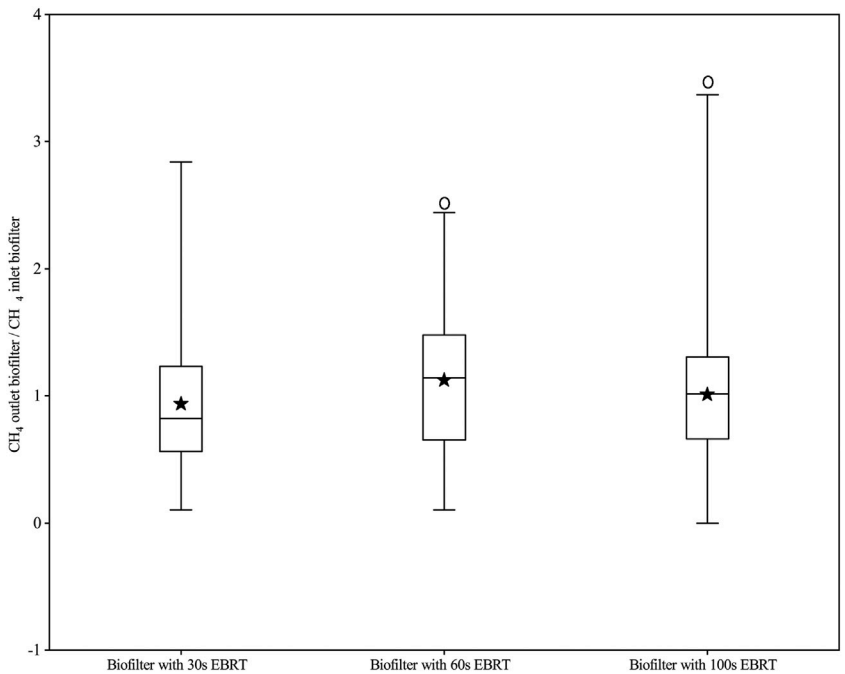

FIGURE 4 | Boxplot: Ratio of CH4 concentrations of the outlet and inlet at different biofilters (Box border means 25 and 75% percentile, the solid line in the box means the median value, a solid pentacle means the mean value, a whisker means the maximum and the minimum values, and the white circle means significant differences between the inlet and outlet).

TABLE 2 | Literature overview of N_2O generations in biofilters.

Biofilter media material	Empty bed retention time (s)	Experiment periods (d)	Inlet NH_3 load ($g.m^{-3}.h^{-1}$)	Inlet NH_3 concentration ($mg.m^{-3}$)	N_2O-N emission ($g.m^{-3}.h^{-1}$)	Inlet NH_3-N to N_2O-N (%)	Reference
Woodchips inoculated with activated sludge	12	124	2.4–3.0	8–12	Maximum was around 1	10–40	Dumont, et al. (2014)
Compost (mixture of horse manure, cattle manure, chicken waste, woodchips, sawdust, and others)	25	100	0.99	17.5	0.2	/[a]	Maia, et al. (2012b)
Compost (mixture of horse manure, cattle manure, chicken waste, woodchips, sawdust, and others)	20	21	0.47	11.2	/	14–19	Maia, et al. (2012a)
Mixture of wood chip and compost	34	22–35	5.24	31	/	1.9–2.3	Yang, et al. (2014a)
Mixture of pine wood chips and peat soil	42	/	1.5–3	13.7–26.6	/	5.2–14.8	Kong, et al. (2020)
Woodchips	1.4–3.3	/	8.7–67	19–86	0.2–0.5	1.3–21	Melse and Hol, (2017)
Mature compost	30–100	42	0.5–53.6	13–447	0.3–1.6	4.6–5.6	The present study

[a]*"/" means no data.*

TABLE 3 | Cumulative nitrous oxide (N_2O) and methane (CH_4) emissions from biofilters used for composting exhaust ammonia (NH_3) removal (values are means ± SE, $n = 3$)[a].

	Biofilter inlet			Biofilter outlet		
	CH_4 ($kg.m^{-3}$ biofilter)	N_2O ($kg.m^{-3}$ biofilter)	Total GWP [kg (CO_2 eq.) m^{-3} biofilter][b]	CH_4 ($kg.m^{-3}$ biofilter)	N_2O ($kg.m^{-3}$ biofilter)	Total GWP [kg (CO_2 eq.) m^{-3} biofilter]
Biofilter with EBRT 30s	3.8 (0.5)	0.52 (0.09)	240 (40)	3.2 (0.6)	1.6 (0.4)	544 (131)
Biofilter with EBRT 60s	1.9 (0.5)	0.26 (0.05)	120 (20)	2.0 (0.1)	0.9 (0.1)	314 (33)
Biofilter with EBRT 100s	1.1 (0.2)	0.16 (0.03)	72 (12)	1.1 (0.3)	0.5 (0.1)	176 (39)

[a]*The nitrous oxide (N_2O) and methane (CH_4) emissions were the cumulative amount emitted from biofilters during the whole experiment which lasted for 42 days.*
[b]*GWP_{CH4} = 23 and GWP_{N2O} = 296 (Pachauri et al., 2014).*

(2014b) showed that N_2O concentrations ranged from 0.1 to 0.4 ppm with a pH of 8.0, and the acidified biofilters showed higher N_2O concentrations than alkalized biofilters. In the present study, the values of the moisture content and pH of media change very little through the experiment. During the experiment, the pH of media was maintained at around seven for all biofilters, while the average moisture contents of media (mean ± SE, n = 12) were 48.3 ± 0.4, 48.5 ± 0.5, and 49.1 ± 0.4 for the biofilters with EBRT of 30, 60, and 100s, respectively.

Emissions of CH_4 From Biofilters

The daily mean concentrations of CH_4 from composting ranged between 5 and 149 mg m^{-3}, while the concentrations from biofilters ranged between 2 and 241 mg m^{-3}. The average daily REs of CH_4 were 6.5%, −10.5%, and −6.0% for EBRT 30, 60s, and 100s, respectively. Lim et al. (2012) reported the CH_4 reductions ranged from 0.1% to 1.9% in biofilters with 0.3s–0.6s EBRT. Fedrizzi et al. (2018) attained nearly 100% CH_4 100% removal efficiencies with 756s EBRT, so enough EBRT is needed for CH_4 removal. Akdeniz et al. (2011) achieved the removal efficiencies of 6.9%–25% for CH_4 by using the pilot-scale biofilters with lava rock media at the high moisture levels and low inlet CH_4 concentrations (90% moisture content and average of 31.0 ppm of inlet CH_4 concentration), while the EBRT was just 5s. Melse and van der Werf (2005) reported that the biological conversion of CH_4 in a biofilter is a slow process due to the low water solubility of methane (Henry's law constant = 1.5×10^{-3} M atm^{-1}). Biofilters with EBRT of 83–199s cannot reduce concentrations of CH_4 emitted from municipal solid waste composting, which has been reported by Clemens and Chuls (2003). Yasuda et al. (2009) also pointed out that several microbial CH_4 production and consumption reactions occurred, but a large portion of the CH_4 seemed to pass straightly through the biofilter with the EBRT of 100–200s 2014; Devinny, et al., 1999). In the present study, negligible CH_4 removal and no significant difference were found among three EBRTs, (**Figure 4**) and the result was similar to that of Akdeniz et al. (2011), Yasuda et al. (2009), and Lim et al. (2012). The possible reason is that the EBRT in this study is not enough for the transfer of CH_4 from the gas phase to the biofilm phase (Melse and Van der Werf, 2005). On the other hand, although the anaerobic methanogens were not tested in this study, the retention time for anaerobic suspended growth in

biofilters was about 50 days (Maia et al., 2012b); the slow acclimation of methanogens in the biofilter will lead to low CH_4 removal efficiency.

Global Warming Potential Emissions

Based on the measurements, the total global warming potential (GWP) emissions were calculated. **Table 3** shows the GWP loading rate before and after passing through the biofilter for all the biofilters. The total GWP emission increased by 126%, 162%, and 144% for biofilters with EBRT values of 30, 60, and 100s, respectively. Significant differences were found in the total CO_2-eq emissions from the biofilters. A lower percentage of GWP was emitted from the biofilter with 30s EBRT than in biofilters with 60 and 100s EBRT because the fraction of NH_3-N denitrified into N_2O-N is lower for the biofilter with 30s EBRT than that of 60 and 100s EBRT. These results showed that prolonged EBRT can improve RE of NH_3 but increase the GWP emissions accordingly. Melse and Hol (2017) evaluated three kinds of biofiltration of exhaust air from animal houses in which the total GWP emissions increased by 60%, 45%, and 0 in biofilters with EBRT of 1.4, 2.6, and 3.3s, respectively. In their experiment, the average inlet concentrations of NH_3 were 66, 10, and 15 ppm, respectively, and the removal efficiencies were 74%, 42%, and 38%, respectively. In the present study, the average inlet NH_3 concentrations were 124–163 mg m^{-3}, and the removal efficiencies were 82%–89%; both average inlet NH_3 concentrations and removal efficiencies of biofilters were higher than Melse and Hol (2017).

With regard to GHG emissions, it can be concluded that the lower EBRT is more suitable for biofilter systems of composting, and the parameters of the control process, such as pH, temperature, dissolved oxygen, and water content, will be useful to prevent N_2O formation and guarantee a good NH_3 removal efficiency.

CONCLUSION

The increased N_2O concentrations from the biofilter were strongly and positively correlated with the elimination capacities of NH_3. The total GWP emission increased by 54%, 62%, and 61% for biofilters with 30, 60, and 100s EBRT, respectively. The total GWP emission from biofilters increases by over 50% compared to a composting system without biofilters. More NH_3 converted into N_2O due to higher EBRT suggested that lower EBRT is useful to prevent GHG from biofilters.

DATA AVAILABILITY STATEMENT

The original contributions presented in the study are included in the article/**Supplementary Material**; further inquiries can be directed to the corresponding author.

AUTHOR CONTRIBUTIONS

BS: conceptualization, data curation, formal analysis, funding acquisition, writing—original draft, and writing—review and editing. TZ: conceptualization, data curation, formal analysis, and writing—review and editing. XT: formal analysis, investigation, methodology, and writing—review and editing. YC: investigation, validation, and writing—review and editing.

FUNDING

The study was supported by the National Natural Science Foundation of China (grant number: 32072784) and the National Key Research and Development Program (grant number: 2016YFD0501400).

SUPPLEMENTARY MATERIAL

The Supplementary Material for this article can be found online at: https://www.frontiersin.org/articles/10.3389/fbioe.2022.918365/full#supplementary-material

REFERENCES

Akdeniz, N., and Janni, K. A. (2012). Full-scale Biofilter Reduction Efficiencies Assessed Using Portable 24-hour Sampling Units. *J. Air & Waste Manag. Assoc.* 62, 170–182. doi:10.1080/10473289.2011.639479

Akdeniz, N., Janni, K. A., and Salnikov, I. A. (2011). Biofilter Performance of Pine Nuggets and Lava Rock as Media. *Bioresour. Technol.* 102, 4974–4980. doi:10.1016/j.biortech.2011.01.058

C E. Buendia, K. Tanabe, A. Kranjc, J. Baasansuren, M. Fukuda, and S. Ngarize (Editors) (2019). "2019Refinement to the 2006 IPCC Guidelines for National Greenhouse Gas Inventories," in *Agriculture Forestry and Other Land Use* (Switzerland: IPCC), Volume 4.

Cheng, H., and Hu, Y. (2010). Municipal Solid Waste (MSW) as a Renewable Source of Energy: Current and Future Practices in china. *Bioresour. Technol.* 101, 3816–3824. doi:10.1016/j.biortech.2010.01.040

Clemens, J., and Cuhls, C. (2003). Greenhouse Gas Emissions from Mechanical and Biological Waste Treatment of Municipal Waste. *Environ. Technol.* 24, 745–754. doi:10.1080/09593330309385611

Devinny, J. S., Deshusses, M. A., and Webster, T. S. (1999). *Biofiltration for Air Pollution Control*. Boca Raton: Lewis Publishers. ISBN1-56670-289-5.

Dumont, É. (2018). Impact of the Treatment of NH3 Emissions from Pig Farms on Greenhouse Gas Emissions. Quantitative Assessment from the Literature Data. *New Biotechnol.* 46, 31–37. doi:10.1016/j.nbt.2018.06.001

Dumont, E., Lagadec, S., Landrain, P., Landrain, B., and Andrès, Y. (2014). N_2O Generation Resulting from Piggery Air Biofiltration. *Chem. Eng. J.* 248, 337–341. doi:10.1016/j.cej.2014.03.058

Fedrizzi, F., Cabana, H., Ndanga, É. M., and Cabral, A. R. (2018). Biofiltration of Methane from Cow Barns: Effects of Climatic Conditions and Packing Bed Media Acclimatization. *Waste Manag.* 78, 669–676. doi:10.1016/j.wasman.2018.06.038

Han, Z., Qi, F., Wang, H., Li, R., and Sun, D. (2019). Odor Assessment of NH3 and Volatile Sulfide Compounds in a Full-Scale Municipal Sludge Aerobic Composting Plant. *Bioresour. Technol.* 282, 447–455. doi:10.1016/j.biortech.2019.03.062

Haubrichs, R., and Widmann, R. (2006). Evaluation of Aerated Biofilter Systems for Microbial Methane Oxidation of Poor Landfill Gas. *Waste Manag.* 26, 408–416. doi:10.1016/j.wasman.2005.11.008

Huang, X., Song, Y., Li, M. M., Li, J. F., Huo, Q., Cai, X. H., et al. (2012). A High-Resolution Ammonia Emission Inventory in China. *Glob. Biogeochem. Cycle* 26, 1–14. doi:10.1029/2011gb004161

Janni, K. A., Jacobson, L. D., and Hetchler, B. P. (2014). Sem-icontinuous Air Sampling versus 24-hour Bag Samples to Evaluate Biofilters on a Pig Nursery in Warm Weather. *Trans. ASABE* 57, 1501

Kong, X., Ying, S., Yang, L., Xin, Y., Cai, Z., Zhu, S., et al. (2020). Microbial and Isotopomer Analysis of N2O Generation Pathways in Ammonia Removal Biofilters. *Chemosphere* 251, 126357. doi:10.1016/j.chemosphere.2020.126357

La, H., Hettiaratchi, J. P. A., Achari, G., and Dunfield, P. F. (2018). Biofiltration of Methane. *Bioresour. Technol.* 268, 759–772. doi:10.1016/j.biortech.2018.07.043

Lim, T.-T., Jin, Y., Ni, J.-Q., and Heber, A. J. (2012). Field Evaluation of Biofilters in Reducing Aerial Pollutant Emissions from a Commercial Pig Finishing Building. *Biosyst. Eng.* 112, 192–201. doi:10.1016/j.biosystemseng.2012.04.001

Liu, T., Dong, H., Zhu, Z., Shang, B., Yin, F., Zhang, W., et al. (2017). Effects of Biofilter Media Depth and Moisture Content on Removal of Gases from a Swine Barn. *J. Air & Waste Manag. Assoc.* 67 (12), 1288–1297. doi:10.1080/10962247.2017.1321591

Loyon, L. (2017). Overview of Manure Treatment in France. *Waste Manag.* 61, 516–520. doi:10.1016/j.wasman.2016.11.040

Maia, G. D. N., Day V, G. B., Gates, R. S., and Taraba, J. L. (2012a). Ammonia Biofiltration and Nitrous Oxide Generation during the Start-Up of Gas-phase Compost Biofilters. *Atmos. Environ.* 46, 659–664. doi:10.1016/j.atmosenv.2011.10.019

Maia, G. D. N., Day V, G. B., Gates, R. S., Taraba, J. L., and Coyne, M. S. (2012b). Moisture Effects on Greenhouse Gases Generation in Nitrifying Gas-phase Compost Biofilters. *Water Res.* 46, 3023–3031. doi:10.1016/j.watres.2012.03.007

Melse, R. W., and Hol, J. M. G. (2017). Biofiltration of Exhaust Air from Animal Houses: Evaluation of Removal Efficiencies and Practical Experiences with Biobeds at Three Field Sites. *Biosyst. Eng.* 159, 59–69. doi:10.1016/j.biosystemseng.2017.04.007

Melse, R. W., and Van der Werf, A. W. (2005). Biofiltration for Mitigation of Methane Emission From Animal Husbandry. *Environ. Sci. Technol.* 39, 5460–5468. doi:10.2166/wst.2013.82610.1021/es048048q

Mudliar, S., Giri, B., Padoley, K., Satpute, D., Dixit, R., Bhatt, P., et al. (2010). Bioreactors for Treatment of VOCs and Odours - A Review. *J. Environ. Manag.* 91, 1039–1054. doi:10.1016/j.jenvman.2010.01.006

Ottosen, L. D. M., Juhler, S., Guldberg, L. B., Feilberg, A., Revsbech, N. P., and Nielsen, L. P. (2011). Regulation of Ammonia Oxidation in Biotrickling Airfilters with High Ammonium Load. *Chem. Eng. J.* 167, 198–205. doi:10.1016/j.cej.2010.12.022

Pachauri, R. K., Allen, M. R., Barros, V. R., Broome, J., and Cramer, W. (2014). *Climate Change 2014: Synthesis Report Contribution of Working Groups I, II and III to the Fifth Assessment Report of the Intergovernmental Panel on Climate Change*. Geneva, Switzerland: IPCC.

Pagans, E. l., Font, X., and Sánchez, A. (2005). Biofiltration for Ammonia Removal from Composting Exhaust Gases. *Chem. Eng. J.* 113, 105–110. doi:10.1016/j.cej.2005.03.004

Park, K. J., Choi, M. H., and Hong, J. H. (2002). Control of Composting Odor Using Biofiltration. *Compost Sci. Util.* 10, 356–362. doi:10.1080/1065657X.2002.10702098

Paulot, F., Jacob, D. J., Pinder, R. W., Bash, J. O., Travis, K., and Henze, D. K. (2014). Ammonia Emissions in the United States, European Union, and China Derived by High-Resolution Inversion of Ammonium Wet Deposition Data: Interpretation with a New Agricultural Emissions Inventory (MASAGE_NH_3). *J. Geophys. Res. Atmos.* 119, 4343–4364. doi:10.1002/2013jd021130

Pinder, R. W., Adams, P. J., and Pandis, S. N. (2007). Ammonia Emission Controls as a Cost-Effective Strategy for Reducing Atmospheric Particulate Matter in the Eastern United States. *Environ. Sci. Technol.* 41, 380–386. doi:10.1021/es060379a

Renner, E., and Wolke, R. (2010). Modelling the Formation and Atmospheric Transport of Secondary Inorganic Aerosols with Special Attention to Regions with High Ammonia Emissions. *Atmos. Environ.* 44, 1904–1912. doi:10.1016/j.atmosenv.2010.02.018

Shang, B., Zhou, T., Tao, X., Chen, Y., and Dong, H. (2020). Simultaneous Removal of Ammonia and Volatile Organic Compounds from Composting of Dead Pigs and Manure Using Pilot-Scale Biofilter. *J. Air & Waste Manag. Assoc.* 71, 378–391. doi:10.1080/10962247.2020.1841040

Turan, N. G., Akdemir, A., and Ergun, O. N. (2009). Removal of Volatile Organic Compounds by Natural Materials during Composting of Poultry Litter. *Bioresour. Technol.* 100, 798–803. doi:10.1016/j.biortech.2008.07.010

Yang, L., Kent, A. D., Wang, X., Funk, T. L., Gates, R. S., and Zhang, Y. (2014a). Moisture Effects on Gas-phase Biofilter Ammonia Removal Efficiency, Nitrous Oxide Generation, and Microbial Communities. *J. Hazard. Mater.* 271, 292–301. doi:10.1016/j.jhazmat.2014.01.058

Yang, L., Wang, X., and Funk, T. L. (2014b). Strong Influence of Medium pH Condition on Gas-phase Biofilter Ammonia Removal, Nitrous Oxide Generation and Microbial Communities. *Bioresour. Technol.* 152, 74–79. doi:10.1016/j.biortech.2013.10.116

Yasuda, T., Kuroda, K., Fukumoto, Y., Hanajima, D., and Suzuki, K. (2009). Evaluation of Full-Scale Biofilter with Rockwool Mixture Treating Ammonia Gas from Livestock Manure Composting. *Bioresour. Technol.* 100, 1568–1572. doi:10.1016/j.biortech.2008.09.033

Yasuda, T., Waki, M., Fukumoto, Y., Hanajima, D., Kuroda, K., and Suzuki, K. (2017). Characterization of the Denitrifying Bacterial Community in a Full-Scale Rockwool Biofilter for Compost Waste-Gas Treatment. *Appl. Microbiol. Biotechnol.* 101, 6779–6792. doi:10.1007/s00253-017-8398-y

Yuan, J., Du, L. L., Li, S., Yang, F., Zhang, Z., Li, G. X., et al. (2019). Use of Mature Compost as Filter Media and the Effect of Packing Depth on Hydrogen Sulfide Removal from Composting Exhaust Gases by Biofiltration. *Environ. Sci. Pollut. Res.* 26, 3762–3770. doi:10.1007/s00253-017-8398-y

Zhang, H., Li, G., Gu, J., Wang, G., Li, Y., and Zhang, D. (2016). Influence of Aeration on Volatile Sulfur Compounds (VSCs) and NH_3 Emissions during Aerobic Composting of Kitchen Waste. *Waste Manag.* 58, 369–375. doi:10.1016/j.wasman.2016.08.022

Zheng, J., Liu, J., Han, S., Wang, Y., and Wei, Y. (2020). N_2O Emission Factors of Full-Scale Animal Manure Windrow Composting in Cold and Warm Seasons. *Bioresour. Technol.* 316, 123905. doi:10.1016/j.biortech.2020.123905

Zhu, Y.-l., Zheng, G.-d., Gao, D., Chen, T.-b., Wu, F.-k., Niu, M.-j., et al. (2016). Odor Composition Analysis and Odor Indicator Selection during Sewage Sludge Composting. *J. Air. Waste Manag. Assoc.* 66, 930–940. doi:10.1080/10962247.2016.1188865

Zhu-Barker, X., Bailey, S. K., Paw U, K. T., Burger, M., and Horwath, W. R. (2017). Greenhouse Gas Emissions from Green Waste Composting Windrow. *Waste Manag.* 59, 70–79. doi:10.1016/j.wasman.2016.10.004

Conflict of Interest: The authors declare that the research was conducted in the absence of any commercial or financial relationships that could be construed as a potential conflict of interest.

Publisher's Note: All claims expressed in this article are solely those of the authors and do not necessarily represent those of their affiliated organizations, or those of the publisher, the editors, and the reviewers. Any product that may be evaluated in this article, or claim that may be made by its manufacturer, is not guaranteed or endorsed by the publisher.

frontiers | Frontiers in Bioengineering and Biotechnology

ORIGINAL RESEARCH
published: 01 July 2022
doi: 10.3389/fbioe.2022.928032

Full-Scale of a Compost Process Using Swine Manure, Human Feces, and Rice Straw as Feedstock

Yi Gao†, Chunxue Zhang†, Lu Tan, Xiaocheng Wei, Qian Li, Xiangqun Zheng, Fang Liu, Jiarui Wang and Yan Xu**

Agro-Environmental Protection Institute, Ministry of Agriculture and Rural Affairs, Tianjin, China

Regarding the composting of rural waste, numerous studies either addressed the composting of a single waste component or were conducted at a laboratory/pilot scale. However, far less is known about the mixed composting effect of multi-component rural waste on a large scale. Here, we examined nutrient transformation, maturity degree of decomposition, and succession of microbial communities in large-scale (1,000 kg mixed waste) compost of multi-component wastes previously optimized by response models. The results showed that multi-component compost can achieve the requirement of maturity and exhibit a higher nutritional value in actual compost. It is worth noting that the mixed compost effectively removed pathogenic fungi, in which almost no pathogenic fungi were detected, and only two pathogenic bacteria regrown in the cooling and maturation stages. Structural equation models revealed that the maturity (germination index and the ratio of ammonium to nitrate) of the product was directly influenced by compost properties (electrical conductivity, pH, total organic carbon, moisture, temperature, and total nitrogen) compared with enzymes (cellulase, urease, and polyphenol oxidase) and microbial communities. Moreover, higher contents of total phosphorus, nitrate-nitrogen, and total potassium were conducive to improving compost maturity, whereas relatively lower values of moisture and pH were more advantageous. In addition, compost properties manifested a remarkable indirect effect on maturity by affecting the fungal community (*Penicillium* and *Mycothermus*). Collectively, this evidence implies that mixed compost of multi-component rural waste is feasible, and its efficacy can be applied in practical applications. This study provides a solution for the comprehensive treatment and utilization of rural waste.

Keywords: rural waste, mixed compost, compost maturity, microbial succession, composting effect

OPEN ACCESS

Edited by:
Benyamin Khoshnevisan, University of Southern Denmark, Denmark

Reviewed by:
Farinaz Ebrahimian, Isfahan University of Technology, Iran
Adekunle Adeleke, Nigerian Turkish Nile University, Nigeria
Armaghan Kosari Moghaddam, Ferdowsi University of Mashhad, Iran

***Correspondence:**
Xiangqun Zheng
zhengxiangqun@126.com
Yan Xu
xuyan@aepi.org.cn

†These authors have contributed equally to this work and share first authorship

Specialty section:
This article was submitted to Bioprocess Engineering, a section of the journal Frontiers in Bioengineering and Biotechnology

Received: *25 April 2022*
Accepted: *26 May 2022*
Published: *01 July 2022*

Citation:
Gao Y, Zhang C, Tan L, Wei X, Li Q, Zheng X, Liu F, Wang J and Xu Y (2022) Full-Scale of a Compost Process Using Swine Manure, Human Feces, and Rice Straw as Feedstock. Front. Bioeng. Biotechnol. 10:928032. doi: 10.3389/fbioe.2022.928032

1 INTRODUCTION

According to statistics, global rural waste generation reached 9.05 billion tons as of 2018, at least one-third of which is not properly treated (Qu et al., 2020). Solid waste pollution poses a serious threat to the environment and human health, as a result of either direct emission or inappropriate treatment (Diener et al., 2011). Moreover, rural waste often cannot be not completely treated, which causes secondary pollution in the receiving environment. At present, the cases of compost used in the treatment of livestock manure, domestic waste, and straw, etc. have been widely documented (Wang et al., 2020; Wang et al., 2021). As previously reported, single component compost presented a series

of drawbacks, such as high moisture content, low degradation rate, low carbon-to-nitrogen ratio, small particle size, and high viscosity, etc. (Zhu, 2007; Bernal et al., 2009). Then, an increasing number of studies have been conducted on co-composting to improve composting quality by adding amendments. For instance, the addition of straw and tail vegetables can effectively reduce the pathogenic factors in pure manure compost (Li H. et al., 2021). Hence, the mixed composting of rural wastes has gradually developed into a solution that cannot just increase the waste disposal rate but also improve the treatment effect. In addition, the Chinese government announced the "*Five-Year Action Plan for Elevating Improvement of Rural Living Environment (2021–2025)*" in 2021, which clearly noted the need to promote the resource treatment and use of rural domestic waste, human feces, and agricultural production of organic waste.

Even so, most studies have been confined to the co-processing of up to two components. Qian et al. (2014) performed a pilot-scale study to determine the effects of the mixed composting process of poultry manure and rice straw. Wang et al. (2020) explored the functionality of the fungal community during the large scale aerobic co-composting process of swine manure and rice straw. However, little information is available on composting with multi-component rural waste. Previously, we optimized the best proportion of swine manure, human feces, rice straw, and kitchen waste through small-scale tests and mixed models, acquiring an optimal mixed compost proportion of 41.4% swine manure, 13.7% human feces, and 44.9% rice straw (Gao et al., 2021). Regrettably, the optimal composite composting ratio was determined using only NI (NH_4^+-N/NO_3^--N), seed germination index (GI), and T (the final C/N ratio/the initial C/N ratio) as response parameters, without large-scale verification. Therefore, the actual effect of composting remains unknown. As is well known, there are differences in the effect between small-scale experiments and pilot-scale trials. Semitela et al. (2019) found that a volume change in the micro-composting experiments occurred much faster than that in the pilot-scale, with a volume reduction rate approximately four times higher during the first 3 weeks. As previously stated, it was corroborated that pH, temperature, and C/N ratio had an influence on the effect of mixed composting (Zhou et al., 2019), still, most of them were in reliance on the properties of compost products or simply subjective judgment to evaluate the overall effect of the compost. The trait of substance transformation in the process of mixed composting is still vague. This will lead to the inability to optimize the effect of mixed composting in a targeted manner at a later stage. Thus, it is necessary to systematically examine the changes in biotic and abiotic factors in the whole process of mixed composting.

We developed a mixed compost of rural multi-component wastes based on a previously obtained compost ratio. The study aimed to 1) investigate the effect of large-scale mixed compost, 2) understand the dynamic changes in biotic factors, mainly enzyme activities and the microbial community during composting, and 3) dissect the key drivers of mixed compost maturity. The outcome can provide a practical technology for the efficient co-processing of rural waste.

TABLE 1 | Physicochemical characteristics of the composting materials.

Parameter	Swine manure	Human feces	Rice straw
pH	8.8 ± 0.86	8.1 ± 1.25	6.5 ± 0.58
Organic matter (%)	56.8 ± 2.12	10.2 ± 1.36	94.3 ± 5.69
Moisture content (%)	80.52 ± 1.69	60.56 ± 4.12	60.24 ± 2.58
Total organic carbon (%)	21.56 ± 2.34	6.31 ± 1.28	51.28 ± 0.59
Nitrogen content (%)	2.64 ± 0.69	0.59 ± 0.08	1.08 ± 0.36

2 METHODS AND MATERIALS

2.1 Composting Process and Sampling

Composting tests were carried out at the same place where raw materials were obtained (the resource utilization center of livestock and poultry manure in Yangjiapo Town, Tianjin Binhai New area) (**Supplementary Figure S1**). The physicochemical properties of the raw materials are listed in **Table 1**. Composting was conducted in triplicate, and the dimension of each composting pile was 1.8 m × 1.2 m × 1.5 m (length × width × height). Before each test, dried straw was mechanically shredded into small particles of sizes smaller than a 25-mesh. The raw material ratio of compost referred to the optimal ratio in the previous study (Gao et al., 2021), in which the ratio of swine manure, human feces, and rice straw were 0.40: 0.15: 0.45. The initial moisture content of the mixed raw material is set at about 60 wt% and the turning frequency of compost is referred to in the study by Xu et al. (2022).

The entire composting process lasted for 102 days, which was divided into three phases according to the temperature changes during composting, namely, the mesophilic phase (MEP: 0–7 days), thermophilic phase (THP: 8–40 days), and cooling phase (COP: 41–101 days). The samples were collected at 0 (the initial mixed compost raw material), 3, 6, 12, 25, 38, 44, 63, 82, and 101 days. One aliquot was dry-preserved at −80 ˚C for subsequent DNA extraction and the others were stored at 4 ˚C for analyzing composting properties.

2.2 Physicochemical Analysis

The extracts of the fresh composting samples (1:10, w/v, sample/deionized water) were used to determine the electrical conductivity (EC) by using a conductometer (DJS-1C, Shanghai, China). The total phosphorus (TP) was measured using a chemical analyzer (CleverChem 380) and total potassium (TK) was determined by using an atomic absorption spectroscope (Agilent AA240). The elemental analyzer (VARIO EL III) was used to quantify the total carbon (TC) and total nitrogen (TN) concentration. Moisture and organic matter (OM) depend on drying at 105˚C (24 h) and combustion at 500˚C (5 h) to determine final values, respectively. Seed germination (GI) tests were conducted using extract solutions prepared by extraction of the compost in H_2O (1:10, w/v), centrifugation at 4500 rpm for 10 min, followed by filtration through a 0.45 μm membrane. GI was calculated according to the equation [GI (%) = (A1 × A2)/(B1 × B2) × 100%], where A1 and B1 represent the germinated seed numbers in extract-treated and control dishes, respectively, and A2 and B2 represent the average root

lengths of extract-treated and control seeds, respectively. The samples for the measurement of ammonium (NH_4^+-N) and nitrate (NO_3^--N) were extracted with 0.01 M $CaCl_2$ solution, then shaken at 150 rpm for 1 h, and finally determined by using the flow-injection analyzer (SEAL Analytical, Germany) (Li et al., 2022).

2.3 Enzyme Activities

The kit used 3,5-dinitrosalicylic acid to react with the end product reducing sugar to produce a brownish-red substance with a characteristic absorption peak at 540 nm, which leads to cellulase activity. The urease was analyzed by the colorimetric method of indophenol blue, which has the maximum light absorption at 578 nm, and its color depth was proportional to the ammonium nitrogen content in the solution, and then the sample urease activity size was calculated. The enzyme activity of polyphenol oxidase was determined following the protocols described in the studies by Zeng et al. (2010). Three kits were purchased from Suzhou Grace Biotechnology Co., Ltd. (Suzhou, China).

2.4 Microbial Community Analysis

Total genomic DNA samples were extracted using the OMEGA Soil DNA Kit (M5635-02) (Omega Bio-Tek, Norcross, GA, United States), according to the manufacturer's instructions. The quantity and quality of the extracted DNAs were measured by using a NanoDrop NC2000 spectrophotometer (Thermo Fisher Scientific, Waltham, MA, United States) and by agarose gel electrophoresis, respectively. The primers 338F (5′-ACTCCTACGGGAGGCAGCA-3′) and 806R (5′-GGACTACHVGGGTWTCTAAT-3′) were used to amplify the V3-V4 region of the bacterial 16SrRNA, and the ITS-V1 primer was used to amplify the fungal ITS region (sample-specific 7-bp barcodes were incorporated into the primers for multiplex sequencing). Vazyme V AHTSTM DNA Clean Beads (Vazyme, Nanjing, China) and Quant-iT PicoGreen dsDNA Assay Kit (Invitrogen, Carlsbad, CA, United States) were used to purify and quantify the PCR amplicons. Subsequently, equal amounts of amplicons were combined, and paired-end 2 × 250 bp sequencing was performed using the Illumina MiSeq platform with a MiSeq Reagent Kit V3 at Shanghai Personal Biotechnology Co., Ltd. (Shanghai, China).

2.5 Statistical Analysis

All statistical analyses and mapping were performed using Excel 2016 and Origin 2020 software packages. One-way analysis of variance was carried out to analyze the physicochemical data as the means of three replicates, and the Duncan test assisted in separating the means ($p < 0.05$). Gephi software was used for network visualization with a calculation of topological properties. We generated structural equation models (SEMs) to evaluate the contribution of composting properties, enzyme activity, bacterial community, and fungal community to the compost maturity with the smart PLS 3 software.

3 RESULTS AND DISCUSSION

3.1 The Trait of Abiotic Factors During Composting

3.1.1 Physical Properties: Temperature, pH, and Electrical Conductivity

Temperature is deemed as a primary indicator of compost since it is closely related to organic matter decomposition and microorganism growth and microbial communities (Wei et al., 2022). It was observed that the mixed composting temperature rose rapidly in the first 2 days and reached the maximum temperature of 74.5°C on the 7th day (**Figure 1A**), moreover, can last for 33 days with the temperature of more than 70°C. It was demonstrated that multi-component composting enabled the rapid increase in the temperature and prolong the thermophilic phase, as compared to single-component or two-component compost (Wang et al., 2020). This implied that mixed composting could present higher fermentation efficiency with a more adequate fermentation process. As is known, the high temperature can effectively eliminate pathogens and weed seeds in the compost. After 41 days, the compost temperature gradually declined, such a fluctuation was primarily owed to the more sufficient mixing of microorganisms and materials after turning the pile, thereby enhancing the biochemical degradation of materials.

pH is an important condition in relation to the success of composting, which is associated with the growth, reproduction, and physiological metabolism of microorganisms in the compost. Here, pH manifested an alkaline with a range of 7.32–8.48 in composting. Previous studies noted that the pH in the range of 6.7–9.0 well supported microbial activity during composting (Meng et al., 2020). As a result, the pH of the whole process was appropriate. When the composting entered the thermophilic stage, the pH showed a descending trend, mainly owing to the high temperature caused by NH_4^+-N volatilizing to NH_3, while thermophilic microbes work diligently to decompose organic matter and produce small molecule acids. That was also supported by previous studies (Wang et al., 2020). The pH dropped to 7.74 at the cooling phase, probably due to the degradation of organic matter which led to the release of CO_2 and organic acids; similarly, the study by Wang et al. (2021) also rendered a similar observation.

The EC as an essential index can reflect the change in soluble salt contents upon the composting process. Admittedly, high EC in the compost is not advisable since salt is phytotoxic and negatively affects crop production (Meng et al., 2020). It can be seen here that after 6 days of composting, the EC rapidly rose to 3.04 mS/cm **(Figure 1B)**, which was attributed to water loss caused by evaporation and a net loss of dry matter caused by the decomposition of organic matter, which was similar to previous studies (Silva et al., 2009). After that, the EC declined slightly, as a result of the loss of some salt ions in the leachate. In the cooling phase, the organic matter was further decomposed, resulting in a decrease in the total weight, while the salt was residual in the compost, resulting in the gradual increase of the EC content, and eventually stabilized at 3 mS/cm. It is worth affirming that the safe

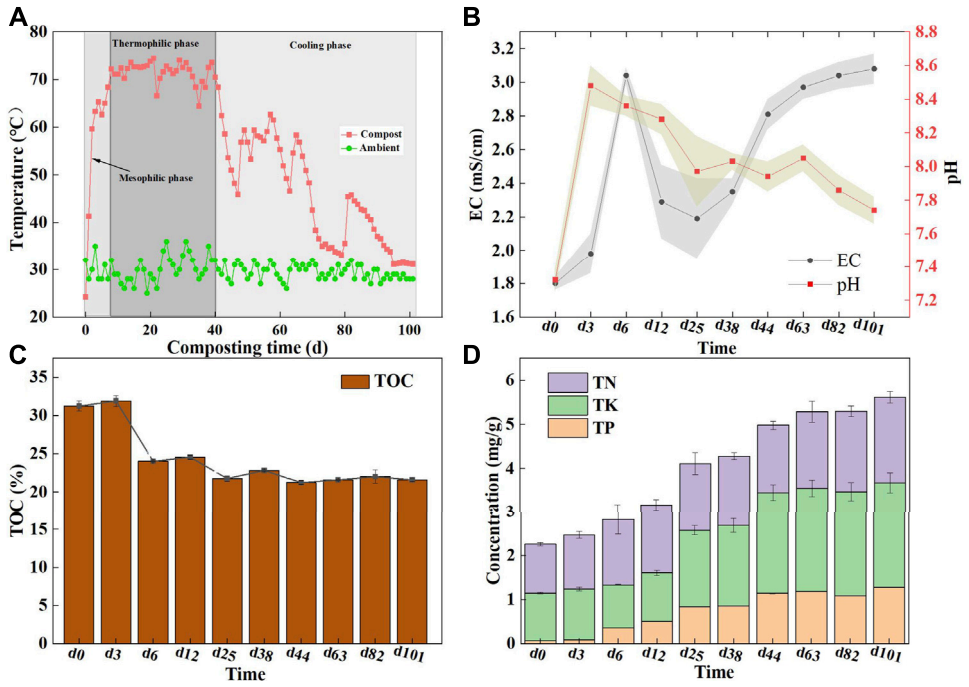

FIGURE 1 | Changes of physicochemical parameters during composting; **(A)** Temperature during co-compost process; **(B)** pH and EC, the stripe represents the standard deviation; **(C)** The concentration of total organic carbon (TOC) and **(D)** The concentrations of TN, TP and TK.

threshold of 4 mS/cm has never been exceeded throughout the composting process (Awasthi et al., 2018).

3.1.2 Chemical Properties: Nutrients

Changes in the TOC, TN, TP, and TK concentrations were tracked to reflect nutrient conversion across the mixed composting process. As an extremely important carbon and energy source for microorganisms, the TOC is involved in several complex microbial metabolic processes to the extent which reflects the quality of the compost. As shown in **Figure 1C**, the decline in the TOC content mainly occurred in the initial stage of composting with a decrease of 7.23%. This loss was higher than that in a previous report showing a TOC loss of approximately 4% during the initial 5–6 days in livestock manure composting (Li M.-X. et al., 2021), potentially owing to the high availability of easily degradable organics in a multi-component compost, which accelerated the decomposition rate of the TOC. After composting, the organic matter content was uncovered at 37.24%, which was higher than the Chinese national organic fertilizer standard of 30% (NY 525/T-2021). It is thus believed that the mixed compost of rural multi-component wastes can yield high-quality organic fertilizer. As composting progressed, the relative content of the TN gradually increased from 1.11 to 1.95%, which may have been caused by the massive degradation of carbon-containing compounds (Castaldi et al., 2008). Similar to the TN variance, the TP exhibited an ascending trend from 0.07 to 1.28% during composting, which was consistent with the result of Wei et al. (2015), who showed that the proportion of phosphorus in the final product was higher than that in the early stages of composting. Similarly, the TK content showed an overall upward trend, with a minimum of 0.93% on the 6th day and a peak of 2.39% on the 101st day (**Figure 1D**). The increase in the TP and TK was attributed to the "concentration effect," in which the organic matter was lost in the form of CO_2, NH_3, and H_2O, while the TP and TK were still retained in the compost (Wei et al., 2022). As the aforementioned evidence, the fermentation and decomposition capacity of the mixed compost is superior to that of one- or two-component compost. This may be ascribed to the high bioavailability of organic matter in the composite raw materials. Also, multi-component compost can preserve more nutrient elements that enable the production of higher-quality organic fertilizer products. This will be an advantage of multi-component composting.

3.2 Comprehensive Evaluation of Composting Effects

The quality of final products under large-scale composting should be systematically evaluated using the aforementioned characteristics, and the maturity indexes including the germination index (GI) and NI (NH_4^+-N/NO_3^--N), both of which were commonly used to assess compost safety (Gao et al., 2021). There was a remarkable increase in the GI, ranging from 10.90–95.80% during composting (**Figure 2A**). The compost was considered phytotoxin-free when the GI value exceed 80% (Zhou et al., 2019); thus, it was determined

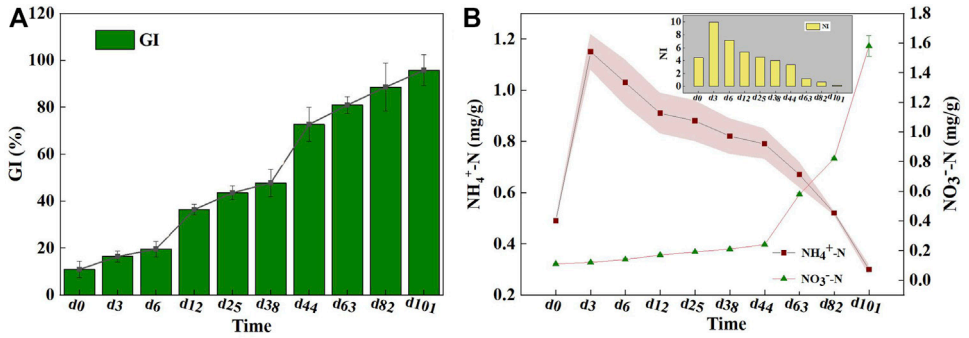

FIGURE 2 | The changes of **(A)** GI and **(B)** NH_4^+-N/NO_3^--N and NI during composting. The stripe represents the standard deviation.

TABLE 2 | Quality analysis of compost products.

Substrate	Index					Composting technology	Reference
	Organic matter (based on dry weight), %	Total nutrient contents (based on dry weight), %	Moisture mass fraction (fresh sample), %	pH	GI (%)		
-	≥30	≥4.0	≤30	5.5–8.5	≥70	-	NY 525/ T-2021
Swine manure, human feces, and rice straw	37.24	5.62	28.82	7.74	95.8	Windrow composting	This study
Swine manure, saw dust, and rice husk	62.51	9.59	21.92	8.32	-	A 40-m^3 composting reactor	Liu et al. (2020)
Blue-green algae sludge, livestock feces, and straw	57.91	6.59	28.36	8.00	114.5	The device included a main composting vessel, feeding and discharge conveyors, and a gas removal biofilter system	Zhang et al. (2021)
Fresh swine manure, composted swine manure, and maize straw	49.48	8.4	32	8.22	71	A patent compost tray	Wei et al. (2022)

-: unknown.

that the mixed compost product met the requirement of maturity according to the organic fertilizer standard.

Figure 2B showed the dynamic changes in NH_4^+-N, NO_3^--N, and the NI during the composting process. In the early period of composting, the NH_4^+-N content increased rapidly from 0.49 to 4.25 g/kg, probably because of the conversion of organic-N into NH_4^+-N by ammonification (Meng et al., 2020). Still, the NO_3^--N amounts remained relatively low during the first 44 days of composting. Indeed, NO_3^--N formation from nitrification was confined as a result of the activity and growth of ammonia oxidizers, which were likely to be inhibited by the higher temperature and paucity of dissolved oxygen caused by intensive organic matter degradation (Gao et al., 2010). A marked increase in the NO_3^--N content was observed as the cooling phase started. Compared with NH_4^+-N, NO_3^--N is more easily absorbed and used by plants, which denoted that the high-quality compost organic fertilizer should yield sufficient NO_3^--N (Gross et al., 2011). Also, the highest NI was acquired in the first 3 days of composting, then it gradually dropped to 0.19 until the end of composting. Referring to the relevant standards of the California Compost Quality Council, NI lower than 0.5 after composting can be regarded as very mature, whereas 0.5–3.0 is considered mature (Dahiya et al., 2018). It is thus considered that the end-product was mature, meaning that the mixed compost can accord to the availability of organic products.

Overall, the indexes required by the Organic Fertilizer Standard (NY 525/T-2021) involving pH, moisture content, organic matter, and total nutrient (listed in **Table 2**) should all be met as a prerequisite. It can be seen here that, multi-component compost products had achieved complete maturity and possessed a higher nutritional level. As previously reported, although composting of rural household waste alone can meet the maturity requirement, it showed lower nutrient levels and higher relative abundances of pathogenic bacteria in the final product (Muscolo et al., 2018). The multi-component composts in other studies albeit meet the standard requirements, had complex composting processes, and large investments (**Table 2**). Collectively, this

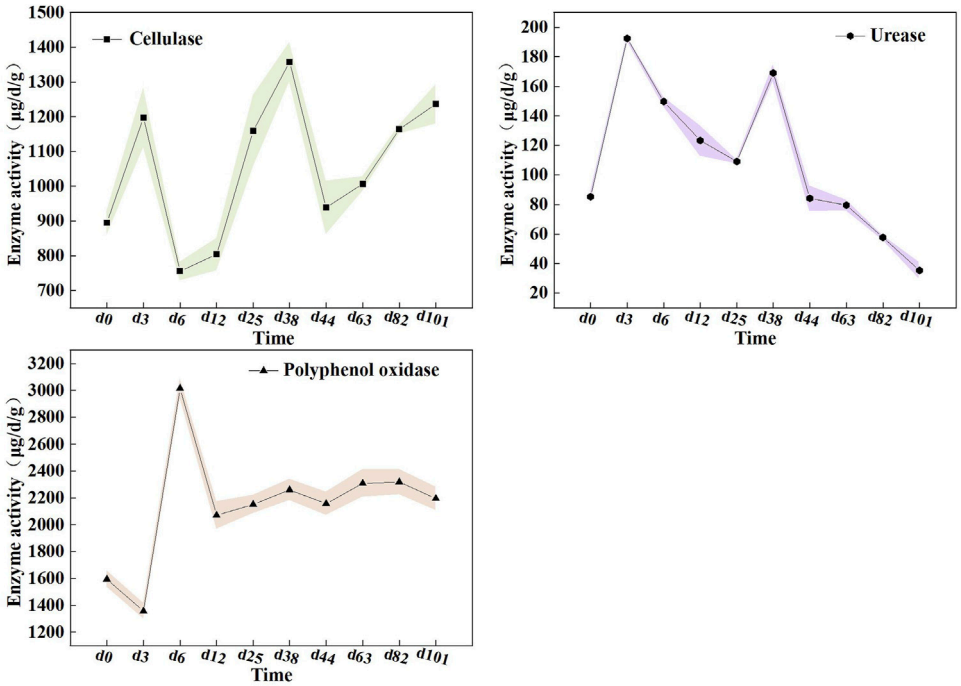

FIGURE 3 | The activities of emzymes during composting. (a) cellulase, (b) urease and (c) polyphenol oxidase.

large-scale mixed composting can be used in practice as a solution to improve rural waste disposal.

3.3 The Biotic Factors Involved in Composting

3.3.1 Enzymatic Activities

Microorganisms metabolize insoluble components by secreting various enzymes, which can characterize the degrading capacity of the substrates (Kong et al., 2018). Herein, we tracked enzyme changes to reflect the transformation of organic matter during the composting process (**Figure 3**). The cellulase activity is often used to indicate the degradation of cellulose in a material during composting (Zhang and Sun, 2014). It was observed that the cellulase activity peaked during the thermophilic phase, up to 1,357.71 μg/d/g, which was in agreement with previous results about co-composting of pig manure and straw (Li et al., 2020). Unexpectedly, the cellulase activity remained at a high level during the cooling phase of the compost, which was different from the traditional compost that exhibited a lower cellulase activity during this phase. As Du et al. (2019) reported, in the heating and thermophilic stages, it generally decomposes easily degraded organic matter, whereas the cooling stage mainly tackled cellulose, which is difficult to degrade by microorganisms. Hence, we consider that the mixed compost can promote the decomposition of cellulose, as evidenced by the high cellulose enzyme activity across the composting process, especially in the presence of high cellulose substances, such as straw. This will be conducive for improving the efficiency of aerobic fermentation.

In addition, the results showed that urease activity peaked on the 3rd day with a maximum level of 192.43 μg/d/g. This observation was similar to the profile reported by Wang et al. (2020). As is known, urease catalyzes the conversion of urea into ammonia, which plays an important role in waste decomposition. Lower urease activity was potentially related to the degradation of available nitrogen compounds, which was also the primary cause of the persisting declination of the ammonia nitrogen content in the later stage of composting. Nevertheless, urease activity exhibited a remarkable upward trend in the thermophilic period, unlike previous studies showing a consistent decline from the peak (Li et al., 2020). Theoretically, multi-component compost was endowed with a high microbial metabolism that was resistant to high temperatures, which can accelerate the mineralization and decomposition rate of nitrogen-containing organic matter. This can partly explain the elevated urease activity in the mixed compost system.

Here, we also examined polyphenol oxidase which was capable of catalyzing lignin disintegration and condensing quinines and amino acids formed in lignin oxidation into humic acids, to state the process of humification (Guo et al., 2012). The results showed that the activity of polyphenol oxidase decreased in the early stage of composting and then increased rapidly, attaining a maximum value of 3015.99 μg/d/g on the 6th day. Of note, the activity of polyphenol oxidase was maintained in a high and stable range until the end of composting compared with the observation of the previous study (Zhang and Sun, 2018). It suggested that this mixed compost can develop more abundant humification.

These evidences indicated that multi-component composting could effectively improve the activities of cellulase, urease, and

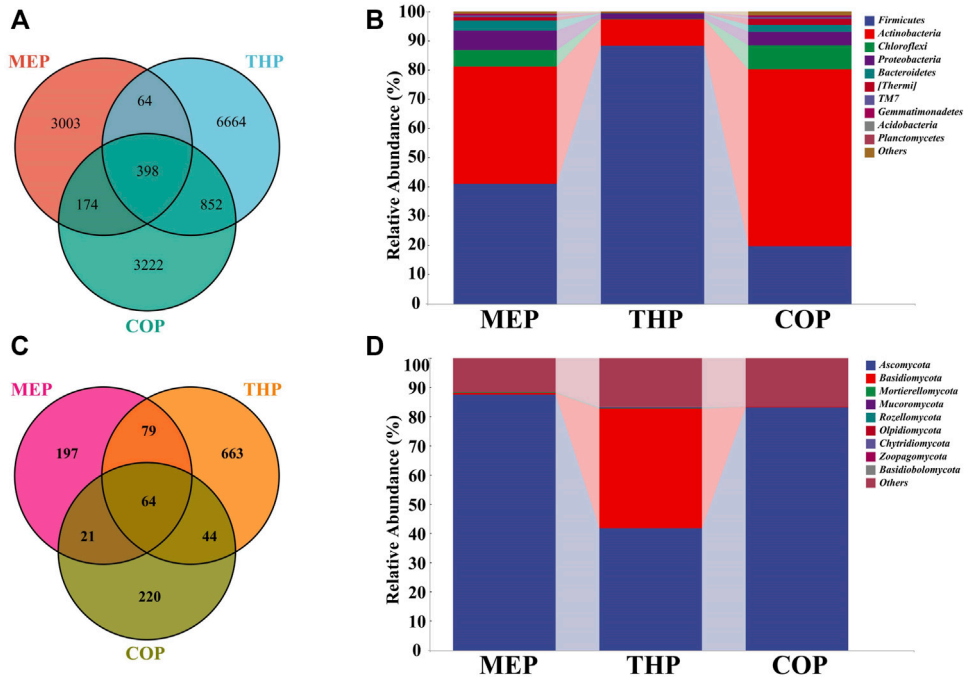

FIGURE 4 | The microbiome composition during composting. **(A)** Bacterial and **(C)** fungal Venn diagram of different phases; **(B,D)** are compositions of bacterial and fungal communities during composting at the phylum-level, respectively.

polyphenol oxidase enzymes which are involved in fermentation. It is speculated that the key reason was that multi-component composting presented a high microbial diversity, which can accelerate microbial metabolism to yield enzymes. To be sure, these enzymes play a critical role in the mixed composting system as they regulate the degradation of multiple components.

3.3.2 Microbial Community

Figure 4A showed the compositions of bacterial communities in the different composting phases. A total of 3,639, 7,978, and 4,646 OTUs were retrieved at MEP, THP, and COP, respectively. Apparently, the richness of the bacterial community in the multi-component compost was significantly higher than that of the two-component compost ($p < 0.01$) (Jiang et al., 2019). Also, unique OTUs, that is, non-shared OTUs were observed in each stage, especially THP, where unique OTUs accounted for 46.35% of the total OTUs, suggesting that the blooms of some specific bacteria may get involved in degrading organic matter which occurred in the thermophilic phase. To explore temporal changes in community composition, the relative abundances of bacterial taxa were compared at the phylum level. *Firmicutes*, *Actinobacteria*, *Chloroflexi*, and *Proteobacteria* were the four dominant phyla in composting **(Figure 4B)**. These phyla accounted for more than 90% of the total identified sequences, which was consistent with the results of other studies (Jiang et al., 2019; Zhang et al., 2021). In the MEP of the compost, *Firmicutes* (41.03%) and *Actinobacteria* (40.21%) dominated, whereas the relative abundance of *Actinobacteria* showed a descending trend to 8.96% in the THP, and the relative abundance of *Firmicutes* increased by 88.06%. In fact, *Firmicutes* can form endospores that are highly tolerant to unfavorable conditions, allowing them to survive in unfavorable environments (Liu et al., 2018). This provided a plausible explanation for the massive proliferation of *Firmicutes* in the THP emerged. In the cooling and mature phases, *Actinobacteria* accounted for 60.47% on average, replacing *Firmicutes* as the dominant phylum, which is far higher than the 15.62% of single straw composting and 31.1% of co-composting (pig manure and straw) (Li et al., 2019; Chang et al., 2021). This benefit is reflected in the fact that more *Actinobacteria* could secrete more antibiotics to inhibit and kill pathogens during composting (Tian et al., 2013). Moreover, the abundance of *Proteobacteria* was relatively higher, up to 4.61% more than that of other conventional composts. This phylum contains diverse members, most of which exerted important roles in the carbon, sulfur, and nitrogen cycles of the compost (Zhang et al., 2021). Briefly, the relative abundances of *Firmicutes* and *Actinobacteria* in the multi-component compost were markedly higher, compared with previous compost cases, especially *Actinobacteria* which was often used as a marker for compost maturity (Jurado et al., 2014). As a consequence, multi-component composting can facilitate compost efficiency and improve maturity by increasing bacterial diversity and the dominance of functional bacteria in the materials.

The composition of the fungal community in different composting phases is shown in **Figure 4C**. A total of 361, 850, and 349 OTUs were acquired for the MEP, THP, and COP, respectively. This indicated that the richness of the fungal

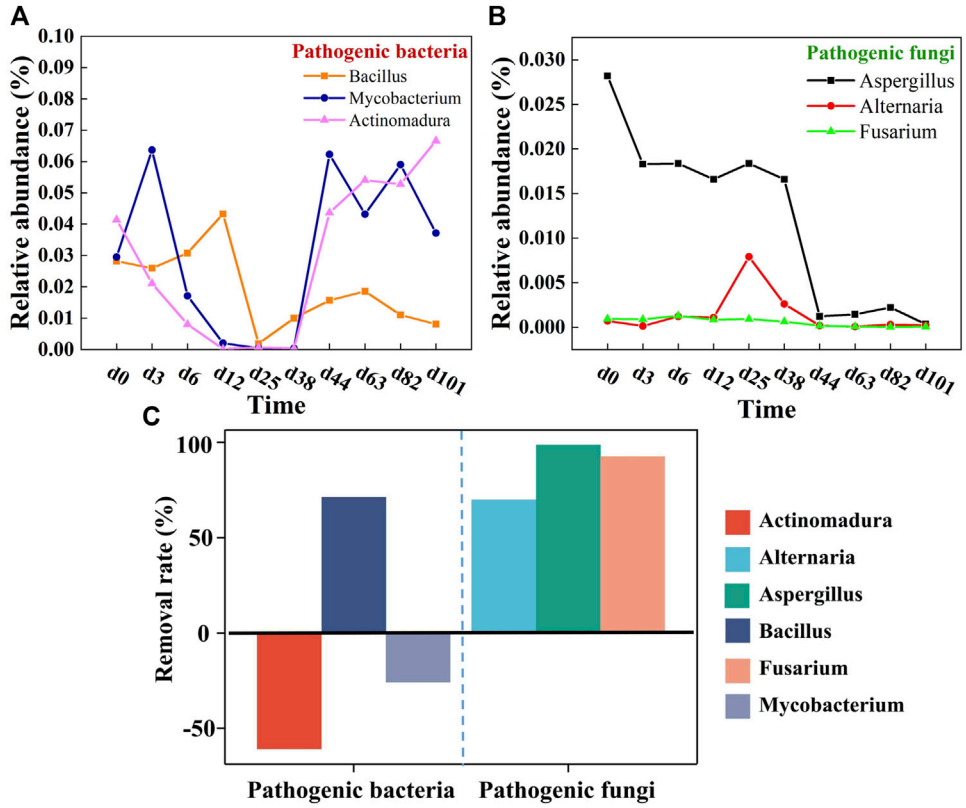

FIGURE 5 | Relative abundance of **(A)** pathogenic bacteria and **(B)** pathogenic fungi in top 20 genus and **(C)** their removal rates.

community in a multi-component compost was significantly higher than that reported in previous studies ($p < 0.01$) (Meng et al., 2018; Wang et al., 2020). As mentioned previously, fungi usually performed an important role in the degradation of lignocellulose because of the special structure of their hyphae, whereby indicating that mixed composting can be more conducive to the degradation of organic waste, as evidenced by the high richness of fungi (Duan et al., 2021). Of these, *Ascomycota* and *Basidiomycota* were recognized as the core fungi, as a result of the higher proportion of abundances in the compost (**Figure 4D**). This is similar to previous results (Chang et al., 2021), mostly, *Ascomycota* was detected to be the major phylum of the fungal community during composting which exerted a critical role in producing enzymes responsible for cellulose degradation (Meng et al., 2018). As well, *Basidiomycota* unveiled dominance in the decomposition and mineralization of lignocelluloses (Abdellah et al., 2021). Accordingly, the multi-component compost had a significant effect on cellulose degradation by increasing the abundance of fungal communities and promoting the activity of associated enzymes.

3.3.3 Pathogens

The removal of pathogenic bacteria in the mixed composting system was more effective than previously reported, where a large number of pathogens still remain after composting (Xu et al., 2022). Apparently, the pathogenic bacteria *Bacillaceae-Bacillus* were significantly reduced by 71.21%. It is reported that *Bacillus* can cause an array of infections, from ear infections to meningitis, and urinary tract infections to septicemia. In most cases, they occur as secondary infections in immuno-deficient hosts or otherwise compromised hosts (Xu et al., 2022). Three pathogenic fungi, *Aspergillus*, *Alternaria,* and *Fusarium* were effectively killed, especially *Aspergillus* with a reduction of 98.76% (**Figure 5**). This may be related to the higher microbial diversity in the multi-component compost. Duan et al. (2021) stated that diversification of raw materials can reshape the composting micro-environment and enhance inter-microbial competitiveness, which is thus detrimental to the small population of pathogens. In addition, multi-component composting can achieve higher composting temperatures and prolong the high temperature time compared with traditional single-component/two-component composting, which in turn eliminates pathogenic bacteria more effectively (Wang et al., 2020). Even so, this system is not perfect because potential pathogens were still detected at the end of the compost. *Mycobacterium* and *Actinomadura* remained recalcitrant, possibly because of their unique cell wall structure and ability to survive some heat or chemical stressors. Once acquiring favorable conditions, it will trigger rapid reproduction (Lepesteur, 2022). Moreover, these two strains are more resistant to high temperature, whereby most of them may just be inhibited

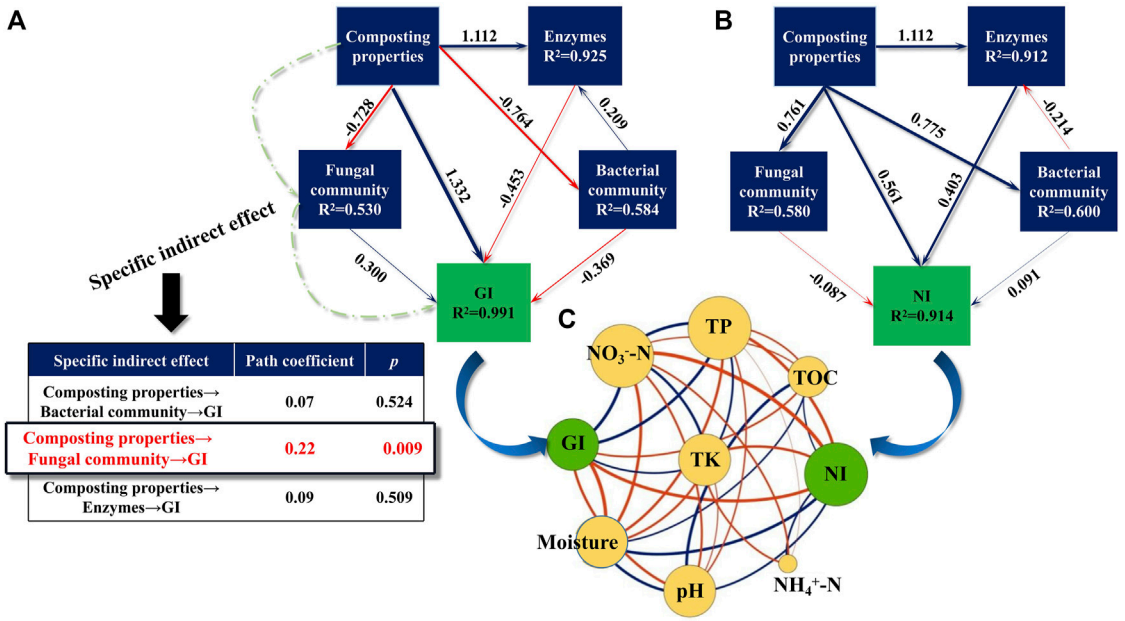

Specific indirect effect	Path coefficient	*p*
Composting properties→ Bacterial community→GI	0.07	0.524
Composting properties→ Fungal community→GI	0.22	0.009
Composting properties→ Enzymes→GI	0.09	0.509

FIGURE 6 | Structural equation models (SEMs) showing the pathways **(A,B)** of the different factors (environmental factors, enzymes and microorganisms) on compost maturity (GI and NI). The path coefficients are adjacent to the arrows. Blue and red lines indicate the positive and negative pathway. Co-occurrence networks between maturity indexes and abiotic factors **(C)**. A connection is observed for strong (Spearman's ρ>|0.6|) and significant ($p < 0.05$) correlations among these variables. The green nodes indicate the parameters of maturity indexes while the orange nodes indicate biotic factors. The size of nodes is proportional to the degree of connectivity. Blue links indicate negative interactions between two individual nodes, while red links indicate positive interactions.

during the high-temperature period, while, with the advent of favorable survival conditions, they will regrow. It is thus considered that the next strive to extend the high-temperature period of composting will assist in the removal of pathogens (Xie et al., 2021). Of course, it is impossible and unnecessary for the compost product to be completely free of pathogenic bacteria. In most environments, such as soil, water, etc., there exist pathogenic bacteria residues. Composting is identified as successful when it effectively reduces pathogenic factors and ultimately produces a hygienic and harmless product. Overall, it can be concluded that multi-component compost features certain advantages over traditional single compost in the removal of pathogens, especially for the removal of pathogenic fungi.

3.4 Key Drivers of Mixed Compost Maturity

Maturity is an important criterion that identifies the effect of composting. Herein, structural equation modeling (SEM) was conducted to assess the contribution of compost properties (EC, pH, NH_4^+-N, NO_3^--N, TOC, moisture, temperature, TN, TP, and TK), enzymes (cellulase, urease, and polyphenol oxidase), and the microbial community to compost maturity. As shown in **Figures 6A,B**, GI and NI changes were well interpreted by all variables, as evidenced by high R^2 values (0.991 and 0.914, respectively). The path coefficients of the compost properties for the GI and NI were highest at 1.332 and 0.561, respectively, implying that compost properties are the main drivers influencing the maturity of the compost. As shown in **Figure 6C**, the GI had a strong positive correlation with the TP, NO_3^--N, and TK ($p < 0.05$), whereas it showed a negative correlation with the moisture content, pH, and TOC ($p < 0.05$), in agreement with the results of Zhang et al. (2021). In contrast, NI was positively correlated with moisture content and pH, but had negative correlations with TOC, TK and NO_3^--N ($p < 0.05$). These pieces of evidence implicated that higher contents of TP, NO_3^--N, and TK were conducive to improving compost maturity, whereas relatively lower values of moisture and pH were more advantageous.

Of note, there was a specific indirect effect of compost properties on the GI (path coefficient = 0.22, $p < 0.01$), as presented by the observation that compost properties had a remarkable correlation with the fungal community, and afterward, the fungal community's impact on the GI. This was supported by previous studies showing that the composting properties regulate the product maturity by shifting fungal communities (Xie et al., 2021). Among the fungal community of the mixed compost, it is unearthed that *Penicillium* and *Mycothermus* exerted an obvious effect on GI changes (**Supplementary Figure S2**). Dehghani et al. (2012) also demonstrated that *Penicillium* was an important fungus for the maturation of domestic waste compost. It has been reported that *Penicillium* degrades a number of toxic exogenous compounds produced by the decomposition of various lignins, thus contributing to a final mature compost (Leitao, 2009). Also, Wang et al. (2020) noted that

Mycothermus was the predominant fungus during the thermophilic phase of swine manure and rice straw co-composting. In a conventional composting environment, it was found that *Mycothermus* is able to produce thermo-stable lignocellulose-degrading enzymes, thus playing an important role in the degradation of lignocellulose. Thus, multi-component composting indirectly affects the GI of compost products by enhancing the relative abundance of particular fungi capable of degrading lignocellulose. Taken together, these pieces of evidence unveiled that the maturity (GI and NI) of the product was most directly influenced by compost properties rather than other drivers (enzymes and microbial community), and that the host properties showed a specific indirect effect on the GI by affecting the fungal community, of which *Penicillium* and *Mycothermus* were key fungi implicated in GI changes.

4 CONCLUSION

This study comprehensively assessed large-scale multi-component rural waste aerobic composting, which is a prolongation of the previous theoretical optimization of multi-component mixed composting. The outcome indicated that the mixed composting with an optimal ratio of 41.4% swine manure, 13.7% human feces, and 44.9% rice straw can not only achieve complete maturity of compost but also furnish relatively high nutrients of organic products. The mixed compost presented to be somewhat surprising in killing pathogenic fungi, that is, almost no potential pathogenic fungi were detected. Still, a few pathogenic bacteria can be revived during the cooling and maturation stages. Furthermore, the product maturity (GI and NI) was mainly influenced directly by compost properties, rather than enzymes and microbial community, while compost properties showed specific indirect effects on the GI by affecting fungal communities, with *Penicillium* and *Mycobacterium* being the key fungi involved in GI variation. In general, the study provided a co-composting method with strong operability and up-to-standard products, which will assist in realizing waste reduction, harmlessness, and resource utilization.

DATA AVAILABILITY STATEMENT

The raw data supporting the conclusion of this article will be made available by the authors, without undue reservation.

AUTHOR CONTRIBUTIONS

YG and CZ designed and conducted the experiments, collected samples, and analyzed data. XZ and YX directed the experimental design and overall concept and provided guidance to YG. LT and XW contributed to investigation. QL, JW, and FL contributed to methodology.

FUNDING

This work was supported by the Fundamental Research Funds for Central Public Welfare Research Institutes (Y2021LM01) and Fundamental Research Funds for Central Public Welfare Research Institutes (2022-jbkyywf-zcx).

SUPPLEMENTARY MATERIAL

The Supplementary Material for this article can be found online at: https://www.frontiersin.org/articles/10.3389/fbioe.2022.928032/full#supplementary-material

REFERENCES

Abdellah, Y. A. Y., Li, T., Chen, X., Cheng, Y., Sun, S., Wang, Y., et al. (2021). Role of Psychrotrophic Fungal Strains in Accelerating and Enhancing the Maturity of Pig Manure Composting under Low-Temperature Conditions. *Bioresour. Technol.* 320, 124402. doi:10.1016/j.biortech.2020.124402

Awasthi, M. K., Chen, H., Wang, Q., Liu, T., Duan, Y., Awasthi, S. K., et al. (2018). Succession of Bacteria Diversity in the Poultry Manure Composted Mixed with Clay: Studies upon its Dynamics and Associations with Physicochemical and Gaseous Parameters. *Bioresour. Technol.* 267, 618–625. doi:10.1016/j.biortech.2018.07.094

Bernal, M. P., Alburquerque, J. A., and Moral, R. (2009). Composting of Animal Manures and Chemical Criteria for Compost Maturity Assessment. A Review. *Bioresour. Technol.* 100 (22), 5444–5453. doi:10.1016/j.biortech.2008.11.027

Castaldi, P., Garau, G., and Melis, P. (2008). Maturity Assessment of Compost from Municipal Solid Waste through the Study of Enzyme Activities and Water-Soluble Fractions. *Waste Manag.* 28 (3), 534–540. doi:10.1016/j.wasman.2007.02.002

Chang, H.-q., Zhu, X.-h., Wu, J., Guo, D.-y., Zhang, L.-h., and Feng, Y. (2021). Dynamics of Microbial Diversity during the Composting of Agricultural Straw. *J. Integr. Agric.* 20 (5), 1121–1136. doi:10.1016/S2095-3119(20)63341-X

Dahiya, S., Kumar, A. N., Shanthi Sravan, J., Chatterjee, S., Sarkar, O., and Mohan, S. V. (2018). Food Waste Biorefinery: Sustainable Strategy for Circular Bioeconomy. *Bioresour. Technol.* 248 (PA), 2–12. doi:10.1016/j.biortech.2017.07.176

Dehghani, R., Asadi, M. A., Charkhloo, E., Mostafaie, G., Saffari, M., Mousavi, G. A., et al. (2012). Identification of Fungal Communities in Producing Compost by Windrow Method. *Jep* 03 (1), 61–67. doi:10.4236/jep.2012.31008

Diener, S., Studt Solano, N. M., Roa Gutiérrez, F., Zurbrügg, C., and Tockner, K. (2011). Biological Treatment of Municipal Organic Waste Using Black Soldier Fly Larvae. *Waste Biomass Valor* 2 (4), 357–363. doi:10.1007/s12649-011-9079-1

Du, J., Zhang, Y., Qu, M., Yin, Y., Fan, K., Hu, B., et al. (2019). Effects of Biochar on the Microbial Activity and Community Structure during Sewage Sludge Composting. *Bioresour. Technol.* 272, 171–179. doi:10.1016/j.biortech.2018.10.020

Duan, H., Ji, M., Chen, A., Zhang, B., Shi, J., Liu, L., et al. (2021). Evaluating the Impact of Rice Husk on Successions of Bacterial and Fungal Communities during Cow Manure Composting. *Environ. Technol. Innovation* 24, 102084. doi:10.1016/j.eti.2021.102084

Gao, M., Liang, F., Yu, A., Li, B., and Yang, L. (2010). Evaluation of Stability and Maturity during Forced-Aeration Composting of Chicken Manure and Sawdust at Different C/N Ratios. *Chemosphere* 78 (5), 614–619. doi:10.1016/j.chemosphere.2009.10.056

Gao, Y., Tan, L., Liu, F., Li, Q., Wei, X., Liu, L., et al. (2021). Optimization of the Proportion of Multi-Component Rural Solid Wastes in Mixed Composting Using a Simplex Centroid Design. *Bioresour. Technol.* 341, 125746. doi:10.1016/j.biortech.2021.125746

Gross, A., Guy, O., Posmanik, R., Fine, P., and Nejidat, A. (2011). A Novel Method for Combined Biowaste Stabilization and Production of Nitrate-Rich Liquid

Fertilizer for Use in Organic Horticulture. *Water Air Soil Pollut.* 223 (3), 1205–1214. doi:10.1007/s11270-011-0938-y

Guo, X., Gu, J., Gao, H., Qin, Q., Chen, Z., Shao, L., et al. (2012). Effects of Cu on Metabolisms and Enzyme Activities of Microbial Communities in the Process of Composting. *Bioresour. Technol.* 108, 140–148. doi:10.1016/j.biortech.2011.12.087

Jiang, Z., Lu, Y., Xu, J., Li, M., Shan, G., and Li, Q. (2019). Exploring the Characteristics of Dissolved Organic Matter and Succession of Bacterial Community during Composting. *Bioresour. Technol.* 292, 121942. doi:10.1016/j.biortech.2019.121942

Jurado, M., López, M. J., Suárez-Estrella, F., Vargas-García, M. C., López-González, J. A., and Moreno, J. (2014). Exploiting Composting Biodiversity: Study of the Persistent and Biotechnologically Relevant Microorganisms from Lignocellulose-Based Composting. *Bioresour. Technol.* 162, 283–293. doi:10.1016/j.biortech.2014.03.145

Kong, Z., Wang, X., Liu, Q., Li, T., Chen, X., Chai, L., et al. (2018). Evolution of Various Fractions during the Windrow Composting of Chicken Manure with Rice Chaff. *J. Environ. Manag.* 207, 366–377. doi:10.1016/j.jenvman.2017.11.023

Leitão, A. L. (2009). Potential of Penicillium Species in the Bioremediation Field. *Ijerph* 6 (4), 1393–1417. doi:10.3390/ijerph6041393

Lepesteur, M. (2022). Human and Livestock Pathogens and Their Control during Composting. *Crit. Rev. Environ. Sci. Technol.* 52 (10), 1639–1683. doi:10.1080/10643389.2020.1862550

Li, C., Li, H., Yao, T., Su, M., Li, J., Liu, Z., et al. (2020). Effects of Microbial Inoculation on Enzyme Activity, Available Nitrogen Content, and Bacterial Succession during Pig Manure Composting. *Bioresour. Technol.* 306, 123167. doi:10.1016/j.biortech.2020.123167

Li, C., Li, H., Yao, T., Su, M., Ran, F., Han, B., et al. (2019). Microbial Inoculation Influences Bacterial Community Succession and Physicochemical Characteristics during Pig Manure Composting with Corn Straw. *Bioresour. Technol.* 289, 121653. doi:10.1016/j.biortech.2019.121653

Li, H., Xu, Y., Zheng, X., Tan, L., Cheng, W., Zhang, C., et al. (2022). Optimising Mixed Aerobic and Anaerobic Composting Process Parameters for Reducing Bacterial Pathogenicity in Compost-Derived Products. *J. Environ. Manag.* 304, 114293. doi:10.1016/j.jenvman.2021.114293

Li, H., Zheng, X., Cao, H., Tan, L., Yang, B., Cheng, W., et al. (2021). Reduction of Antibiotic Resistance Genes under Different Conditions during Composting Process of Aerobic Combined with Anaerobic. *Bioresour. Technol.* 325, 124710. doi:10.1016/j.biortech.2021.124710

Li, M.-X., He, X.-S., Tang, J., Li, X., Zhao, R., Tao, Y.-Q., et al. (2021). Influence of Moisture Content on Chicken Manure Stabilization during Microbial Agent-Enhanced Composting. *Chemosphere* 264, 128549. doi:10.1016/j.chemosphere.2020.128549

Liu, Y., Feng, Y., Cheng, D., Xue, J., Wakelin, S., and Li, Z. (2018). Dynamics of Bacterial Composition and the Fate of Antibiotic Resistance Genes and Mobile Genetic Elements during the Co-composting with Gentamicin Fermentation Residue and Lovastatin Fermentation Residue. *Bioresour. Technol.* 261, 249–256. doi:10.1016/j.biortech.2018.04.008

Liu, Z., Wang, X., Wang, F., Bai, Z., Chadwick, D., Misselbrook, T., et al. (2020). The Progress of Composting Technologies from Static Heap to Intelligent Reactor: Benefits and Limitations. *J. Clean. Prod.* 270, 122328. doi:10.1016/j.jclepro.2020.122328

Meng, X., Liu, B., Xi, C., Luo, X., Yuan, X., Wang, X., et al. (2018). Effect of Pig Manure on the Chemical Composition and Microbial Diversity during Co-composting with Spent Mushroom Substrate and Rice Husks. *Bioresour. Technol.* 251, 22–30. doi:10.1016/j.biortech.2017.09.077

Meng, X., Yan, J., Zuo, B., Wang, Y., Yuan, X., and Cui, Z. (2020). Full-scale of Composting Process of Biogas Residues from Corn Stover Anaerobic Digestion: Physical-Chemical, Biology Parameters and Maturity Indexes during Whole Process. *Bioresour. Technol.* 302, 122742. doi:10.1016/j.biortech.2020.122742

Muscolo, A., Papalia, T., Settineri, G., Mallamaci, C., and Jeske-Kaczanowska, A. (2018). Are Raw Materials or Composting Conditions and Time that Most Influence the Maturity And/or Quality of Composts? Comparison of Obtained Composts on Soil Properties. *J. Clean. Prod.* 195, 93–101. doi:10.1016/j.jclepro.2018.05.204

Qian, X., Shen, G., Wang, Z., Guo, C., Liu, Y., Lei, Z., et al. (2014). Co-Composting of Livestock Manure With Rice Straw: Characterization and Establishment of Maturity Evaluation System. *Waste Manag.* 34 (2), 530–535. doi:10.1016/j.wasman.2013.10.007

Qu, J., Zhang, L., Zhang, X., Gao, L., and Tian, Y. (2020). Biochar Combined with Gypsum Reduces Both Nitrogen and Carbon Losses during Agricultural Waste Composting and Enhances Overall Compost Quality by Regulating Microbial Activities and Functions. *Bioresour. Technol.* 314, 123781. doi:10.1016/j.biortech.2020.123781

Semitela, S., Pirra, A., and Braga, F. G. (2019). Impact of Mesophilic Co-composting Conditions on the Quality of Substrates Produced from Winery Waste Activated Sludge and Grape Stalks: Lab-Scale and Pilot-Scale Studies. *Bioresour. Technol.* 289, 121622. doi:10.1016/j.biortech.2019.121622

Silva, M. E., Lemos, L. T., Cunha-Queda, A. C., and Nunes, O. C. (2009). Co-composting of Poultry Manure with Low Quantities of Carbon-Rich Materials. *Waste Manag. Res.* 27 (2), 119–128. doi:10.1177/0734242X08096693

Tian, W., Sun, Q., Xu, D., Zhang, Z., Chen, D., Li, C., et al. (2013). Succession of Bacterial Communities during Composting Process as Detected by 16S rRNA Clone Libraries Analysis. *Int. Biodeterior. Biodegrad.* 78, 58–66. doi:10.1016/j.ibiod.2012.12.008

Wang, X., Kong, Z., Wang, Y., Wang, M., Liu, D., and Shen, Q. (2020). Insights into the Functionality of Fungal Community during the Large Scale Aerobic Co-composting Process of Swine Manure and Rice Straw. *J. Environ. Manag.* 270, 110958. doi:10.1016/j.jenvman.2020.110958

Wang, X., Wan, J., Jiang, G., Yang, T., Banerjee, S., Wei, Z., et al. (2021). Compositional and Functional Succession of Bacterial and Fungal Communities Is Associated with Changes in Abiotic Properties during Pig Manure Composting. *Waste Manag.* 131, 350–358. doi:10.1016/j.wasman.2021.06.023

Wei, Y., Liang, Z., and Zhang, Y. (2022). Evolution of Physicochemical Properties and Bacterial Community in Aerobic Composting of Swine Manure Based on a Patent Compost Tray. *Bioresour. Technol.* 343, 126136. doi:10.1016/j.biortech.2021.126136

Wei, Y., Zhao, Y., Xi, B., Wei, Z., Li, X., and Cao, Z. (2015). Changes in Phosphorus Fractions during Organic Wastes Composting from Different Sources. *Bioresour. Technol.* 189, 349–356. doi:10.1016/j.biortech.2015.04.031

Xie, G., Kong, X., Kang, J., Su, N., Fei, J., and Luo, G. (2021). Fungal Community Succession Contributes to Product Maturity during the Co-composting of Chicken Manure and Crop Residues. *Bioresour. Technol.* 328, 124845. doi:10.1016/j.biortech.2021.124845

Xu, Y., Gao, Y., Tan, L., Wang, Q., Li, Q., Wei, X., et al. (2022). Exploration of Bacterial Communities in Products after Composting Rural Wastes with Different Components: Core Microbiome and Potential Pathogenicity. *Environ. Technol. innovation.* 25, 102222. doi:10.1016/j.eti.2021.102222

Zeng, G., Yu, M., Chen, Y., Huang, D., Zhang, J., Huang, H., et al. (2010). Effects of Inoculation with Phanerochaete Chrysosporium at Various Time Points on Enzyme Activities during Agricultural Waste Composting. *Bioresour. Technol.* 101 (1), 222–227. doi:10.1016/j.biortech.2009.08.013

Zhang, L., and Sun, X. (2014). Effects of Rhamnolipid and Initial Compost Particle Size on the Two-Stage Composting of Green Waste. *Bioresour. Technol.* 163, 112–122. doi:10.1016/j.biortech.2014.04.041

Zhang, L., and Sun, X. (2018). Influence of Sugar Beet Pulp and Paper Waste as Bulking Agents on Physical, Chemical, and Microbial Properties during Green Waste Composting. *Bioresour. Technol.* 267, 182–191. doi:10.1016/j.biortech.2018.07.040

Zhang, Z., Hu, M., Bian, B., Yang, Z., Yang, W., and Zhang, L. (2021). Full-scale Thermophilic Aerobic Co-composting of Blue-Green Algae Sludge with Livestock Faeces and Straw. *Sci. Total Environ.* 753, 142079. doi:10.1016/j.scitotenv.2020.142079

Zhou, G., Xu, X., Qiu, X., and Zhang, J. (2019). Biochar Influences the Succession of Microbial Communities and the Metabolic Functions during Rice Straw

Composting with Pig Manure. *Bioresour. Technol.* 272, 10–18. doi:10.1016/j.biortech.2018.09.135

Zhu, N. (2007). Effect of Low Initial C/N Ratio on Aerobic Composting of Swine Manure with Rice Straw. *Bioresour. Technol.* 98 (1), 9–13. doi:10.1016/j.biortech.2005.12.003

Conflict of Interest: The authors declare that the research was conducted in the absence of any commercial or financial relationships that could be construed as a potential conflict of interest.

Publisher's Note: All claims expressed in this article are solely those of the authors and do not necessarily represent those of their affiliated organizations, or those of the publisher, the editors, and the reviewers. Any product that may be evaluated in this article, or claim that may be made by its manufacturer, is not guaranteed or endorsed by the publisher.

frontiers | Frontiers in Bioengineering and Biotechnology

TYPE Original Research
PUBLISHED 25 August 2022
DOI 10.3389/fbioe.2022.961907

OPEN ACCESS

EDITED BY
Li Yeqing,
China University of Petroleum, Beijing, China

REVIEWED BY
Yan Dang,
Beijing Forestry University, China
Gang Luo,
Fudan University, China
Chang Chen,
University of Chemical Technology, China

*CORRESPONDENCE
Rui Xu,
ecowatch_xr@163.com
Zhuwei Liao,
liaozhuwei@outlook.com

SPECIALTY SECTION
This article was submitted to Bioprocess Engineering, a section of the journal Frontiers in Bioengineering and Biotechnology

RECEIVED 05 June 2022
ACCEPTED 27 June 2022
PUBLISHED 25 August 2022

CITATION
Wang H, Duan R, Zhou X, Wang J, Liu Y, Xu R and Liao Z (2022), Efficient removal of mercury and chromium from wastewater via biochar fabricated with steel slag: Performance and mechanisms.
Front. Bioeng. Biotechnol. 10:961907.
doi: 10.3389/fbioe.2022.961907

Efficient removal of mercury and chromium from wastewater *via* biochar fabricated with steel slag: Performance and mechanisms

Huabin Wang[1,2], Ran Duan[1], Xinquan Zhou[2,3], Jia Wang[2], Ying Liu[1], Rui Xu[1]* and Zhuwei Liao[2,4]*

[1]School of Energy and Environment Science, Yunnan Normal University, Kunming, China, [2]Department of Environmental Engineering, School of Environmental Science and Engineering, Huazhong University of Science and Technology, Wuhan, China, [3]School of Chemical Engineer and Pharmacy, Henan University of Science and Technology, Luoyang, China, [4]Urban Construction Engineering Division, Wenhua College, Wuhan, China

Biochar derived from biomass is regarded as a promising adsorbent for wastewater treatment, but the high cost of modification is still a challenge for its large-scale practical applications. In this study, we employed steel slag as a low-cost fabricant and synthesized hydrothermally carbonized steel slag (HCSS), as a stable environmentally functional material for heavy metal removal. Typically, positively and negatively charged heavy metal contaminants of Hg^{2+} and $Cr_2O_7^{2-}$ were employed to testify the performance of HCSS as an adsorbent, and good capacities [(283.24 mg/g for Hg (II) and 323.16 mg/g for Cr (VI)] were found. The feasibility of HCSS on real wastewater purification was also evaluated, as the removal efficiency was 94.11% and 88.65% for Hg (II) and Cr (VI), respectively. Mechanism studies revealed that the modification of steel slag on bio-adsorbents offered copious active sites for pollutants. As expected, oxygen-containing functional groups in HCSS acted as the main contributor to adsorption capacity. Moreover, some reactive iron species (i.e., Fe^{2+}) played an essential role in chemical reduction of Cr (VI). The adsorptive reactions were pH-dependent, owing to other more mechanisms, such as coprecipitation, ion-exchange, and electrostatic attraction. This promising recycling approach of biomass waste and the design of agro-industrial byproducts can be highly suggestive of the issues of resource recovery in the application of solid waste-derived environmentally functional materials for heavy metal remediation.

KEYWORDS

biochar, steel slag, mercury, chromium, heavy metals, adsorption, immobilization

1 Introduction

Heavy metal pollution in the aqueous system brought detrimental effects to human beings as well as aquatic lives, which has attracted much attention in recent years. Many approaches were adapted for these water contaminants elimination (Zhang et al., 2018; Zhu et al., 2019), and among these methods, adsorption was regarded as an economic-effective, simple operated, and less-second-pollution one (Lin et al., 2019; Xu et al., 2019; Yang et al., 2019). Hydrothermal carbonization has emerged as a promising method for bio-adsorbents preparation, as this process could simultaneously achieve the targets of resource recovery and environmental protection (Huang et al., 2017). The exceptional adsorptive properties of hydrochar were owing to the copious oxygen-containing functional groups, such as hydroxyl, phenolic, and carbonyl (Xia et al., 2019). However, these carbonaceous fractions were lack of stability in the aqueous system, causing them to partially dissolve into the solution. To solve this problem, some posttreatment was conducted to stabilize them, such as pyrolysis or calcination (Johs et al., 2019).

In addition to heat treatment, various raw materials were applied as carbon support to synthesize hybrid composites with hydrochar components, such as polymers (Ghadikolaei et al., 2019), layered double hydroxides (Zhang et al., 2018), etc., Another category of supporting materials was inorganic metal oxides, the regular structure and abundant surface hydroxyl groups provided sufficient active sites for organic components adherence. Some metal oxides, including manganese oxide (Li et al., 2019) and ferromanganese oxide (Zhou et al., 2018), were employed for the synthesis of metal-organic complexations. Moreover, some solid waste containing metal oxides were also applied as carbon support. Our group attempted to reutilize the sewage sludge, as a carbon support, to capture heavy metals from wastewater (Ngambia et al., 2019), which provided a novel strategy for support design and solid waste reutilization.

Other promising support, such as steel slag, which was often recognized as a solid waste generating from metallurgy, also might be a carbon support as its relatively inert physicochemical property (Gómez-Nubla et al., 2018). Nowadays, the most common treatment of steel slag was landfilling (more than 70 wt.%), which accumulated a large number of metallic elements deposited in fields, leading to the contamination of soil and correspondingly potential risks to public health (Qasrawi, 2018). Many approaches were adapted to reutilize steel slag and its derivatives. Fang et al. (2018) converted slag into porous calcium silica hydrate *via* a simple hydrothermal process and then conducted these slag-derived materials for phosphate immobilization from wastewater. These functional materials demonstrated distinct skeleton structures and abundant active sites which contributed to the pollutants adsorption. Meanwhile, Czech et al. (2018) implemented heat treatment to fabricate calcium silicate-rich slags and then these materials were conducted for cadmium removal from wastewater. Moreover, steel slag was also employed as a support for sodium hydroxide, to enhance the precipitation and coagulation of phosphorus (Park et al., 2017). The sodium hydroxide coated on the surface of steel slag maintained the high pH (>8) of surroundings and subsequently enhanced the removal performance.

Furthermore, hydrothermal treatment was proved as an effective approach to lattice perfection and accelerating crystallization (Zhang et al., 2019). Liu's group applied the hydrothermal method to treat wasted gypsum, and they found this solid waste could be converted and recrystallized, implying hydrothermal treatment could accelerate crystallinity of solid waste (Liu et al., 2018). In addition to structure reconstruction, some chemically active species in steel slag may be also activated after co-hydrothermal process and then reacted with pollutants. Nelson's group proved Fe (II) species in ores or silica surfaces could react with Cr (VI) in solution, as an electron donor for the chemical reduction of Cr (VI) (Nelson et al., 2019). Wang's group also found natural polyphenols system containing Fe (III) could react with Cr (VI), and the *in situ* generated Fe (II) in aqueous media played a vital role for reduction process (Hu et al., 2019b). Hence, in our study, sawdust, as an ordinary biomaterial was applied to represent the biomass feedstock, could be converted into the hydrochar components under the hydrothermal circumstance. Meanwhile, stable inorganic skeleton derived from steel slag might provide the copious active sites for organic components adherence, leading to the large density of surface functional groups, which might play a crucial role in chemisorption and improve the removal performance.

In this study, a novel hydrothermally carbonized steel slag (HCSS) was synthesized *via* a facile one-pot method and conducted for Hg^{2+} and $Cr_2O_7^{2-}$ removal, which was typical positively and negatively charged contaminant, respectively. Batch adsorption experiments were conducted to evaluate the environmental performance of this adsorbent as a function of reaction dosages, contact time, and regeneration test, and this feasibly prepared sorbent exhibited a superior capacity for Hg^{2+} and $Cr_2O_7^{2-}$ removal. In addition, the industrial applicability of HCSS on practical wastewater purification was also evaluated. Elemental analysis, XRD, XRF, SEM, and other approaches were employed and revealed the multiple reaction mechanisms.

2 Materials and methods

2.1 Materials

NaOH, HNO_3 (68.0%), HCl (36.0%–38.0%), $NaHCO_3$, $NaCO_3$, $CaCl_2$, $Cd(NO_3)_2$, $K_2Cr_2O_7$, $HgCl_2$, $MgSO_4$, and NaCl were obtained from Sinopharm Chemical Reagent Co., Ltd. All reagents used in batch experiments were of analytical reagent grade and used as-received without any further purification. Steel

TABLE 1 Chemical composition of steel slag used in this study.

Element	Wt%	Element	Wt%
Ca	25.49	As	0.10
Si	44.78	Cd	0.25
Al	18.76	Pb	0.26
Mg	3.52	C	0.23
Fe	7.91	S	0.45
Cr	0.21	N	0.15
Ni	0.15		

slag (SS) samples were collected from Wuhan Iron and Steel (Group) Company, categorized as basic oxygen slag. SS samples were washed and dried at 50°C overnight and then these slags were smashed and passed through a 0.45-mm sieve. According to relevant literature, steel slag is an alkaline material; the chemical composition of steel slag was determined by XRF. The chemical composition (wt%) of SS is shown in Table 1. Sawdust was collected from a furniture company, located in Wuhan city, and this obtained pinewood sawdust was smashed and crushed through a 0.15-mm sieve. Practical Hg (II)-containing wastewater was collected from a local foundry industry, while polluted water containing Cr (VI) was gathered from an electronic industry in Wuhan city. Deionized water was applied through all the batch experiments, as 18.0 mΩ cm, generated by using a Milli-Q system.

2.2 Characterization

The composition of adsorbents was analyzed by using the X-ray fluorescence method (XRF, EAGLE III, EDAX Inc., United States) and inductively coupled plasma-optical emission spectrometry (ICP-OES, Optima 8,300, PerkinElmer, United States), after digestion by the $HNO_3/H_2O_2/HClO_4$ (2:2:1) mixed solution for 24 h. The compositions of C, N, and S were measured using an elemental analyzer (EA, Vario MICRO cube Elementary, German). The X-ray diffraction spectra were conducted by X'Pert PRO (PANalytical B.V, Holland), with Cu Kα radiation (λ = 0.1542 nm) over a 2Θ collection range of 5–80 with a scanning rate of 5 /min. The surface area and pore size measurements were conducted by a JW-BK low-temperature N_2 adsorption instrument (JWGB Sci. &Tech, China) at −196.15°C, and the Brunauer–Emmett–Teller equation was used to calculate the surface area. Before measurement, the sample was degassed under vacuum and dried at 120°C for 24 h. The pH was adjusted by adding 0.01 mM NaOH or 0.01 mM HCl into the solution. The FT-IR spectrum was detected by using the KBr pellet method, over the wavelength ranging from 4,000 to 400 cm^{-1} by using a Vertex 70 Fourier

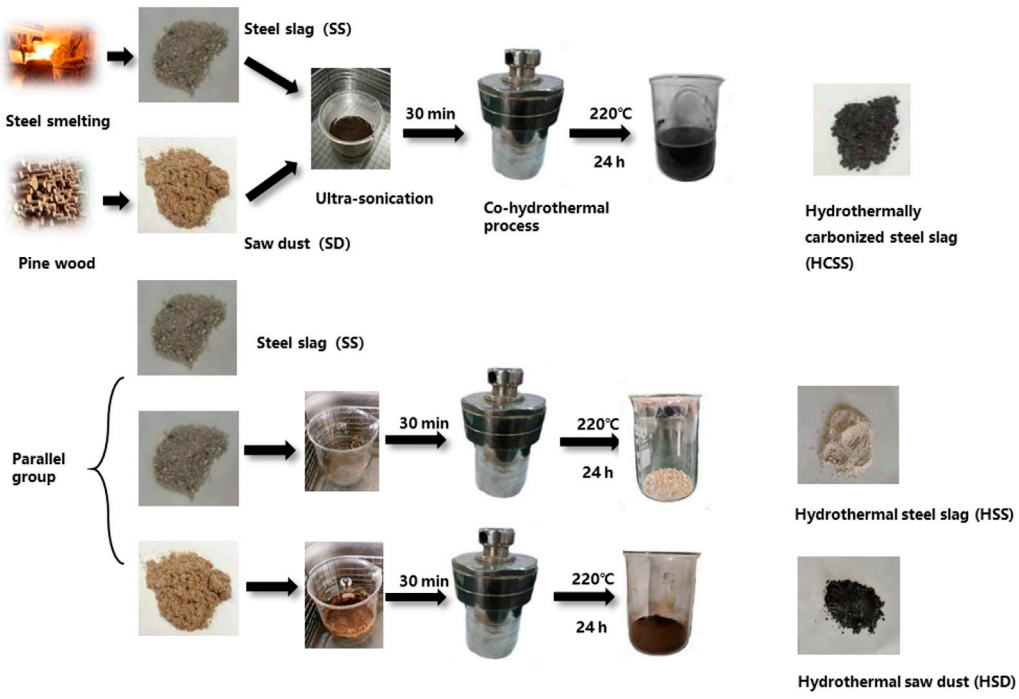

SCHEME 1
Preparation of HCSS and the parallel samples.

transform infrared spectrometer (United States). Quantitative calculation of functional groups was characterized by Boehm titration. In brief, 1.0 g HCSS was added into a 100 ml Erlenmeyer flask containing 25 ml NaOH (0.05 M), shaken for 24 h, filtrated, and then washed with deionized water for three times; the washed water was collected for analysis. For integrity, deionized water without samples was used as blanks. In addition, 0.1 g methyl red was dissolved into 100 ml ethanol as an indicator and added into solution with 0.15 ml for each sample. Furthermore, 0.05 M HCl was used for titration, consumed amount of HCl solution at the equilibrium state was used for calculation, and then the total amount of acidic groups on the surface of adsorbents was calculated. Moreover, $NaHCO_3$ (0.05 M) and Na_2CO_3 (0.05 M) were conducted to test and calculate the amount of carboxyl and hydroxyl with the same former process. A scanning electron microscope (SEM, Quanta 200 ESEM FET, Holland) cooperated with dispersive electron X-ray (EDX) equipment was applied to elucidate the morphology of the adsorbent. X-ray fluorescence (XRF, EAGLE III, EDAX Inc., United States) was applied for characterization of HCSS after reactions. The pH_{PZC} and zeta potentials of HCSS at various pHs were measured by Zetasizer Nano series (Nano-ZS90, Malvern, United Kingdom) under 25°C. First, 150 mg of HCSS was individually added into plastic conical flasks containing 65 ml deionized water. Second, the mixture was mechanically shaken for 24 h. Then the resultant materials were collected for zeta potential determination by applying 0.01 mM NaCl solution as the background.

2.3 Preparation

2.3.1 HCSS

General preparation methods of hydrothermally carbonized steel slag (HCSS) and parallel materials are shown in Scheme 1. Specifically, 3.75 g pinewood sawdust (SD) and 3.75 g steel slag (SS) were soaked in 56 ml aqueous solution (weight ratio of SD: SS = 1:1). A volume of 19 ml NaOH solution (1 M) was slowly added, forming a solution with 10% solid part in weight, and was kept stirring at room temperature (25°C) at 200 rpm for 30 min. Then this mixture was transferred into a 250-ml stainless steel autoclave for the hydrothermal process at 220°C for 24 h. After hydrothermal treatment, the mixture was filtrated, washed with deionized water several times, dried in a vacuum oven at 80°C for 6 h, and stored for further experiments. Additionally, different ratios of SD and steel slag SS were conducted to manipulate the properties of adsorbents. The weight ratio of SD:SS varied from 1: 2, 1:1, and 2:1, which were labeled as HCSS2, HCSS, and HCSS0.5, respectively. Similarly, different heating temperatures were also conducted with the ratio of 1:1, and HCSS300, HCSS, and HCSS500 were prepared under 300°C, 400°C, and 500°C, respectively.

2.3.2 Parallel group

As shown in Scheme 1, other materials were parallelly prepared for comparison. All conditions were identical to the preparation of HCSS. Hydrothermal steel slag (HSS) was prepared with SS without the addition of sawdust, while hydrothermal sawdust (HSD) was prepared with only sawdust but no SS.

2.4 Batch experiments

2.4.1 Adsorption behaviors

The adsorptive capacity of Hg (II) and Cr (VI) by HCSS was determined by metal capacity values (mg/g). The effects of dosages on adsorption performance of Hg (II) and Cr (VI) from the aqueous system on selected adsorbents were investigated. A volume of 2–20 mg of HCSS was added into 10 ml Hg (II) solution (100 ppm) or 10 ml Cr (VI) solution (100 ppm) in vials at room temperature (25°C) for 24 h. The influence of pH (2.0–9.0) tests was conducted by adding 10 mg HCSS to 10 ml of Hg (II) and Cr (VI) solutions (100 ppm) at 25°C, and neglectable volumes of 0.1 M NaOH or HNO_3 was added for adjusting pH to desired values. A kinetics study was performed by adding 10 mg HCSS into 10 ml Hg (II) and Cr (VI) solution (400 ppm) at 25°C for different time intervals (10, 20, and 30 min and 1, 6, 8, 12, 24 h). Correspondingly, isotherm experiment was carried out by mixing 10 mg HCSS with 10 ml solution in the range of 10–1,000 ppm Hg (II) and Cr (VI) at 25°C. Evaluation of leaching performance was also conducted; SS, HSS, and HCSS were leached at a liquid to solid (L/S) ratio of 10 L/kg for 48 h in acid-cleaned 100 ml PRFE vessels, continuously stirred, and kept at a constant temperature of 25°C. The release of the mercury- and chromium-adsorbed HCSS was conducted by adding 0.1 M Na_2EDTA solution as eluent at 25°C with HCSS dose of 2 g/L. The adsorbed HCSS was stirred in Na_2EDTA for 1 h, washed by deionized water three times, and then dried in a vacuum oven at 105°C for next recycle. In order to evaluate the stability of HCSS, residual weight after six cycles was also tested. Once the reaction was experimented thoroughly, the mixtures were filtered through a 0.22-μm pore size nylon filter and the mercury and chromium concentration in samples was detected by inductively coupled plasma-optical emission spectrometry.

The adsorptive capacity (q_e) for Hg (II) and Cr (VI) after the reaction is calculated according to the following equation:

$$q_e = \frac{(C_0 - C_e)V}{m}, \quad (1)$$

where C_0 and C_e are the concentrations of Hg (II) (ppm) and Cr (VI) (ppm) for initial and equilibrium conditions, respectively; V is the volume of solution (L); and m is the mass of adsorbents (g).

TABLE 2 Comparison of the number of surface parameters, functional groups, and residual weight of HSS, HSD, and HCSS with other adsorbents.

Sample	S_{BET} (m^2/g)	Average pore volume[a] (cm^3/g)	Average pore width[b] (Å)	Amount of functional groups (mmol/g)			Residual weight after recycles[c] (%)	Reference
				Carboxyl	Lactone	Hydroxyl		
Blast								Gao et al. (2017)
Furnace slag (BFS)	4.26	0.005	47.00	—	—	—	—	
BFS								
Acid–alkali precipitate	3.46	0.013	154.00	—	—	—	—	
HSS	2.54	0.021	330.07	0.061	0.026	0.087	98.6	This work
HSD	43.29	0.113	101.46	0.340	0.205	0.675	44.3	
HCSS	52.84	0.055	41.63	0.439	0.374	0.322	96.2	

[a]Pore volume determined at $P/P_0 = 0.99$.
[b]Adsorption average pore width (4V/A by BET).
[c]After recycled for six times. Conditions: DI; water volume: 10 ml; initial dosage: 1.0 g/L; reaction time: 24 h; temperature: 25°C, filtrated, and dried for the next cycle.

2.4.2 Modeling

The kinetics of Hg(II) and Cr(VI) removal was assessed using two models, the pseudo-first-order model and pseudo-second-order model, which were conducted for analyzing the mechanisms of the reaction.

The pseudo-first-order model is as follows:

$$ln(q_e - q_t) = ln\, q_e - k_1 t\,. \quad (2)$$

The pseudo-second-order model is as follows:

$$t/q_t = 1/k_2 q_e^2 + (1/q_e)^t\,, \quad (3)$$

where q_t and q_e is the amount of Hg (II) and Cr (VI) captured by HCSS (mg/g) at time t and equilibrium, respectively; the k_1 (min^{-1}) and k_2 (g/mg min^{-1}) are the constants for the pseudo-first-order and pseudo-second-order model, respectively.

The adsorption isotherm was appraised by two models: Langmuir model and Freundlich model.

The Langmuir model is as follows:

$$C_e/Q_e = C_e/Q_m + 1/Q_m K_L\,, \quad (4)$$

where Q_e is the capacity of HCSS on Hg (II) and Cr (VI) elimination (mg/g), C_e is the equilibrium concentration of target pollutants (mg/L), Q_m is the calculated maximum capacity of HCSS (mg/g), K_L is the Langmuir coefficient, and plots of C_e/Q_e plotted versus C_e could be a straight line as the slope was $1/Q_m$ and the intercept was $1/Q_mK_L$.-

The Freundlich model is as follows:

$$log\, Q_e = log\, K_F + 1/n\, log\, C_e\,, \quad (5)$$

where K_F and n is the calculated capacity of HCSS by Freundlich (mg/g) and intensity of reactions, respectively; C_e is the initial concentration of Hg (II) and Cr (VI) in solution (mg/L).

3 Results and discussion

3.1 Characterization

Initial comparison of HSS, HSD, HCSS, and other slags was conducted by evaluating the porous properties, including S_{BET}, average pore volume, or width, as listed in Table 2. Without the incorporation of bioresource of sawdust, S_{BET} values of blast furnace slag, acid- and alkali-treated slag, and HSS were observed extremely limited (4.26, 3.46, and 2.54 m^2/g, respectively), which was due to its inorganic nature (Gao et al., 2017). On the other hand, HSD exhibited satisfying surface area of 101.46 m^2/g due to the mesoporous structure generated by structure recrystallization. Interestingly, the SBET value of HCSS (52.84 m^2/g) was even larger than the sum of HSS (2.54 m^2/g) and HSD (43.29 m^2/g). The significant increase of S_{BET} for HCSS might be explained by the organic components emerged during the transformation of biomass and then anchored onto the surface of slag skeleton, with the function of relatively high temperature and self-generated pressure (Zhu et al., 2019). Correspondingly, the pore volume of HSS (0.021 cm3/g) also increased to 0.055 cm^3/g of HCSS with the incorporation of sawdust. However, the average pore width dropped from 330.07 Å (HSS) to 41.63 Å (HCSS), implying that HCSS possessed a larger surface area and average pore volume but smaller pore widths.

It was widely accepted that the surface functional groups played pivotal roles in the adsorption of heavy metals. Therefore, the quantitative study of functional groups was employed by Boehm titration, and the total number of carboxyl, lactone, and hydroxyl is summarized in Table 2. In terms of carboxyl, HCSS exhibited higher density compared with HSS or HSD (0.439, 0.061, and 0.340 mmol/g for HCSS, HSS, and HSD, respectively). The same trend was observed for lactone (0.374 mmol/g for

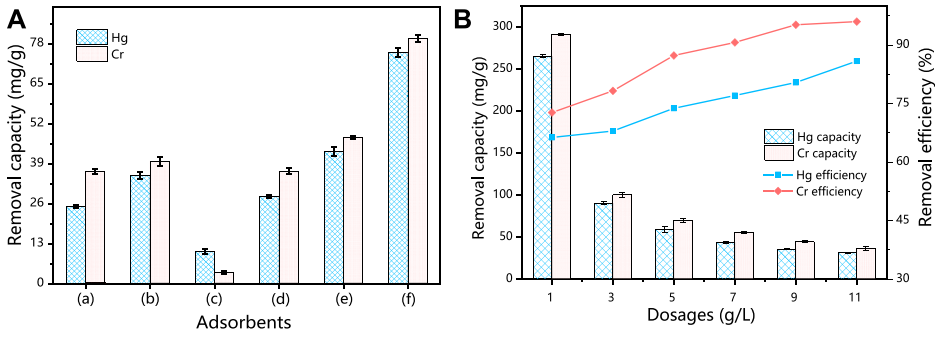

FIGURE 1
(A) Hg(II) and Cr(VI) removal in different systems. **(B)** Influence of different dosages for the capacities and efficiency. Conditions: C0 = 400 ppm; sample volume: 10 ml; reaction time = 24 h; pH 6.5; and temperature: 25°C.

HCSS, 0.096 mmol/g for HSS, and 0 0.005 mmol/g for HSD) and hydroxyl (0.322 mmol/g for HCSS, 0.087 mmol/g for HSS, and 0.675 mmol/g for HSD). The increasing of functional groups on HCSS also demonstrated the successful assembly of the hydrochar component onto the surface of slag skeleton (Yin et al., 2017).

Moreover, the residual weight of these adsorbents after recycling six times was also collected for evaluating the stability (as shown in Table 2). After recycling several times, 98.6% of weight remained for HSS, indicating the stable physicochemical property of this solid waste. Expectedly, after being recycled, the HSD only had 44.3% of the weight left suggesting that the organic component could be partially dissolved in the solution, resulting in the loss of HSD (Ahmad et al., 2019). However, after several recycles, the synthesized HCSS had 96.2% of weight remained, implying the excellent stability of the organic component could be substantially improved after being supported by SS.

3.2 Adsorption behavior

3.2.1 Adsorbent comparison

Initially, the adsorption capacity for Hg (II) and Cr (VI) was compared between SS, HSS, HSD, HCSS, and physical mixture of HSS/HSD and SS/HSD as the parallel samples (Figure 1A). SS alone exhibited a capacity of 25.0 mg/g for Hg (II) and 36.7 mg/g for Cr (VI), and due to the certain porosity and specific surface area of SS, Hg (II) and Cr (VI) can be adsorbed into the steel slag skeleton by an intermolecular force. Meanwhile, the hydroxyl group (OH^-) and other groups also could be involved with the adsorption. These sites can attract pollutants by electrostatic adsorption, so the original steel slag also has a certain adsorption capacity (Duan & Su, 2014; Wang et al., 2018). Also, after being converted from SS into HSS, the capacity increased to 35.1 and 39.9 mg/g for Hg (II) and Cr (VI), respectively. The better performance of HSS could be attributed to the incompletely reformed structure and functional groups on its surface, which complied with Boehm titration. In the case of HSD alone, the removal capacity was 11.4 and 4.4 mg/g for Hg (II) and Cr (VI), respectively, and these unsatisfied values might be assigned to the constrained active cites and low functional group density on the surface of hydrochar (Zhou et al., 2018). Moreover, in the case of HSD alone, after reacting for 24 h, the solution turned into dark brown and still light brown after filtration, indicating that the organic component was partially dissolved and reduced the practicality of HSD alone (Supplementary Figure S1). To further testify the function of biomass feedstock, the mixture of SS and HSD was employed, and the limited increase of capacity compared with SS alone was achieved [from 25.0 to 28.3 mg/g for Hg (II) and from 36.7 to 42.9 mg/g for Cr (VI)]; this could be contributed to the addition of organic functional groups. Same results for the system that mixed HSS with HSD were also obtained, and the capacity was increased from 35.1 to 42.9 mg/g for Hg (II) and from 39.9 to 47.7 mg/g for Cr (VI). However, in the case of HCSS alone, the superior capacity of 75.1 mg/g for Hg (II) and 82.7 mg/g for Cr (VI) was achieved, which was considerably improved compared with other sorbents. This synergetic effect could be explained by the multiple interactions between extra components that emerged during the transformation of co-hydrothermal treatment of both SD and SS in HCSS (Khan et al., 2019). According to the specific affinity between functional groups with surface metal ions, the introduced biomass feedstock could be converted into functional groups, and the regular crystalline structure was also beneficial to pollutants precipitation. On the other hand, the inorganic skeleton as carbon support and provided copious active sites for the functional group adherence increased the density of surface functional groups, which was consistent with aforementioned physicochemical characterizations.

In order to investigate the optimum mass ratio between SS and SD, various adsorbents were prepared in different mass

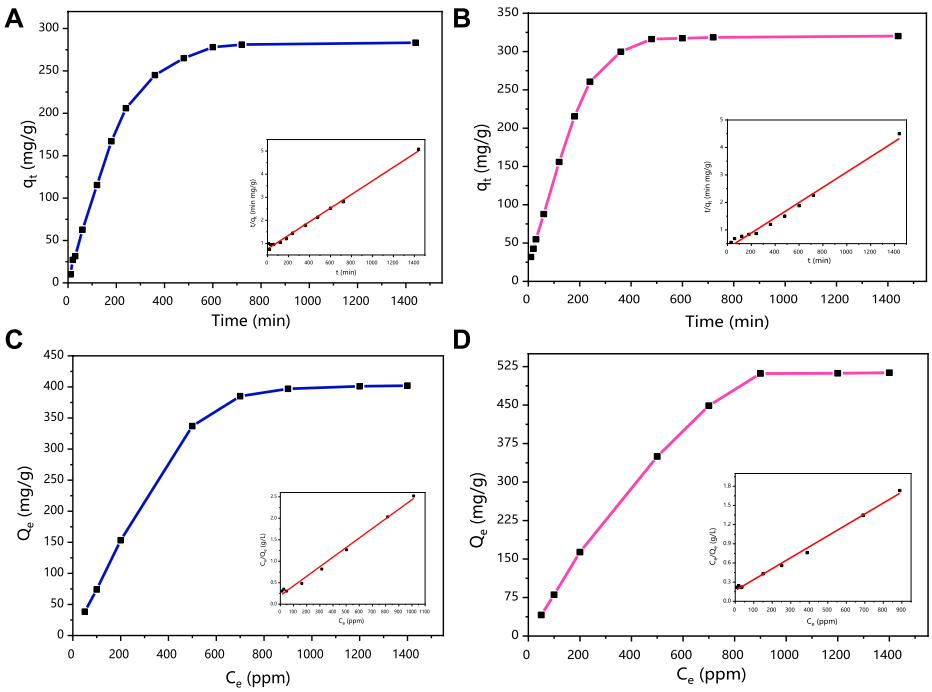

FIGURE 2
(A) Adsorption kinetics curves of HCSS for Hg (II) removal. **(B)** Adsorption kinetics curves for Cr(VI) removal. Inset figure: pseudo-second-order fitting. Conditions: C0 = 400 ppm; sample volume: 10 ml; dosage: 1.0 g/L; pH 6.5; and temperature: 25°C. **(C)** Isotherms of HCSS on Hg (II) removal. **(D)** Isotherms of HCSS on Cr (VI) removal. Inset figure: Langmuir model fitting. Conditions: sample volume: 10 ml; dosage: 1.0 g/L; reaction time: 24 h; pH 6.5; and temperature: 25°C.

ratios as HCSS2 (SD:SS = 1:2), HCSS (SD:SS = 1:1), and HCSS0.5 (SD:SS = 2:1). As shown in Supplementary Figure S2, the capacity increased from 66.98 mg/g and of HCSS2 to 75.12 mg/g of HCSS for Hg (II), indicating the increased amount of organic components could improve the adsorptive performance. After more SD was added during preparation, the SBET of HCSS was increased, and more functional groups were obtained. However, the capacity of HCSS0.5 (50.03 mg/g) was decreased compared to HCSS (75.12 mg/g), this could be attributed to that loading of too many organic ingredients might occupy the active sites on the surface of slag skeleton, decreasing of capacity for heavy metals removal. Same trend was observed for Cr (VI) removal, capacity increased from 49.12 mg/g (HCSS2) to 82.69 mg/g (for HCSS) and then decreased to 65.12 mg/g (for HCSS0.5). Therefore, the mass ratio as SD:SS = 1:1 (HCSS) was selected as the ideal value for adsorbent synthesis.

Furthermore, effects on adsorptive performance by heat treatment temperatures were also evaluated (Supplementary Figure S2B). Adsorbents synthesized with different temperatures were labeled as HCSS300, HCSS, and HCSS500, representing the preparing temperatures were 300°C, 400°C, and 500°C, respectively. In the case of mercury removal, at 300°C, the relatively low temperature made the introduced biomass raw materials not fully carbonized, the pores were not well developed, and they cannot totally react with mercury. The capacity increased from 63.10 mg/g of HCSS300 to 75.12 mg/g of HCSS, which might be attributed to the fact that high

TABLE 3 Parameters of adsorption kinetics and isotherm models for Hg(II) and Cr(VI) removal by HCSS.

	Adsorption	Parameter	Heavy metal	
			Hg (II)	Cr (VI)
Kinetics	Pseudo-first-order	k_1 (min^{-1})	0.004	0.011
		Q_e ($mg{\cdot}g^{-1}$)	238.53	425.98
		R^2	0.870	0.882
	Pseudo-second-order	k_2 ($mg{\cdot}g^{-1}{\cdot}min^{-1}$)	0.003	0.003
		Q_e ($mg{\cdot}g^{-1}$)	276.25	323.155
		R^2	0.996	0.993
Isotherms	Langmuir	k_L ($L{\cdot}mg^{-1}$)	0.012	0.009
		Q_m ($mg{\cdot}g^{-1}$)	281.31	322.18
		R^2	0.997	0.998
		n	0.201	0.101
	Freundlich	K_F ($mg{\cdot}g^{-1}$)	32.17	41.10
		R^2	0.871	0.863

temperature was beneficial for increasing of the aromatic structure and S_{BET} values of adsorbents, thus increasing the contact between biochar and Hg^{2+} (Dai et al., 2019). Meanwhile, HCSS500 exhibited decreased capacity (46.81 mg/g) compared to HCSS300 or HCSS, demonstrating the high temperature was detrimental to the capacity. This phenomenon was ascribed to the loss of biomaterials by calcination under this condition, which led to the reduction of organic functional groups and the destruction of some pore structures, thus reducing the adsorption capacity of mercury. On the another hand, the Cr (VI) removal rates of HCSS300, HCSS, and HCSS500 also showed the same trend, and the capacities were 69.08 mg/g, 82.69 mg/g, and 80.58 mg/g for HCSS300, HCSS, and HCSS500, respectively. There was a neglectable capacity decrease on Cr (VI) removal (from 82.69 of HCSS to 80.58 mg/g of HCSS500) compared to the decreased values for Hg (II) removal, which suggested the limited influence of the organic components on the performance of Cr (VI) removal. It can be seen that the pyrolysis temperature determines the physicochemical properties of the adsorbent and has a significant effect on its adsorption capacity. Therefore, 400°C was selected as the ideal temperature for adsorbents synthesis and prepared HCSS was employed for further adsorption analysis.

3.2.2 Dosage effects

As shown in Figure 1B, the elimination efficiency of Hg (II) was increased from 66% to 79% with the dosage increased from 1 to 9 g/L and then remained higher than 80% when the dosage reached 11 g/L. However, the maximum capacity of 265.3 mg/g was achieved, and the capacity decreased with the increase of dosage. As for Cr (VI) removal, with the increase of dosage of HCSS, the adsorptive capacity was decreased from 290.8 mg/g to 36.4 mg/g, while the removal efficiency increased from 75% to 95% with the dosage increasing from 1 to 11 g/L.

The adsorption kinetics of Hg (II) and Cr (VI) immobilization by HCSS was investigated, and the results are schemed in Figure 2. The reaction reached equilibrium approximately within 480 min for Hg (II), while the adsorption of Cr (VI) attained equilibrium within 360 min. The three-dimensional porous network structure on the surface of HCSS and multiple mechanisms are responsible for the adsorption of Hg (II) and Cr (VI) from the aqueous system (Jung and Sohn, 2014). Here, the pseudo-first-order and pseudo-second-order were employed to analyze the rate-determining step and adsorption mechanism of pollutants removal by HCSS. The corresponding parameters and correlation coefficient of each model are presented in Table 3. The plots of t/qt versus t exhibited excellent linearity in the pseudo-second-order model (Figure 2A inset). The correlation coefficients (R^2) were calculated from equation 2 and equation 3, and the R^2 of the pseudo-first-order model [0.870 and 0.882 for Hg (II) and Cr (VI), respectively] were lower than the pseudo-second-order model [0.996 and 0.993 for Hg (II) and Cr (VI), respectively]. Meanwhile, the calculated q_e in the pseudo-second-order model [276.25 and 323.155 mg/g for Hg (II) and Cr (VI), respectively] fitted well with the experimental data [283.24 and 320.12 mg/g for Hg (II) and Cr (VI), respectively]. Alternatively, the q_e values in the pseudo-first-order model [238.53 and 425.98 mg/g for Hg (II) and Cr (VI), respectively] were far from the experimental data. Hence, the kinetic results of Hg (II) and Cr (VI) removal highly suggested the pseudo-second-order model, which defined the adsorption of mercury and chromium on the HCSS was highly controlled by chemisorption. In literature, the rate-determining steps of chemical sorption involved chemical reduction, inner-sphere complexation, and coprecipitation. In this work, the experimental evidence of chemical reduction, inner-sphere complexation, and coprecipitation was also observed and will be discussed in the mechanism Section 3.4.

In addition to the kinetics, adsorption mechanisms for Hg (II) and Cr (VI) removal were further explored *via* isotherm studies. As revealed, the adsorption capacities (Q_e) increased along with the increasing of initial concentration (C_e), and finally got hold of a plateau and achieved the Q_e of 283.24 and 320.12 mg/g for the adsorption of Hg (II) (Figure 2C) and Cr (VI) (Figure 2D), respectively. A total of two illustrative adsorption models, the Langmuir and Freundlich models, were conducted to pretend the reaction isotherm and reveal the nature of the adsorptive reactions as calculated by Eqs. (4, 5), respectively. Related parameters of Langmuir and Freundlich isotherm models were calculated and are listed in Table 3, while the Langmuir and Freundlich models were referred to the homogeneous monolayer and heterogeneous multilayer reactions of pollutants removal by sorbents, respectively (Rao et al., 2017). The value of Qe calculated by the Langmuir model was 281.31 and 322.18 mg/g for Hg (II) and Cr (VI), correspondingly, which was highly consistent with the experimental data [283.24 and 320.12 mg/g for Hg (II) and Cr (VI), respectively]. While the capacity calculated by the Freundlich model (K_F) was 32.17 and 41.10 mg/g for Hg (II) and Cr (VI), respectively, and this K_F was far lower than that of experimental data. Meanwhile, the correlation coefficients (R^2) calculated by the Langmuir model was 0.997 and 0.998 for Hg (II) and Cr (VI), respectively, which was higher than that of the Freundlich model [0.871 and 0.863 for Hg (II) and Cr (VI), respectively], implying the functional feasibility of the Langmuir model. These results demonstrated the homogeneous surfaces along with monolayer chemical reactions played a pivotal role in the elimination of heavy metals, leading to the superior adsorption capacity for the uptake of Hg (II) and Cr (VI) from aqueous solution.

To sum up, the Hg (II) and Cr (VI) removal by HCSS was mainly on homogeneous surfaces followed with the monolayer sorption. Moreover, after chemisorption of Hg (II) and Cr (VI) onto the surface of HCSS, the surface of sorbents were positively charged, if another heavy metal ion from solution was in contact

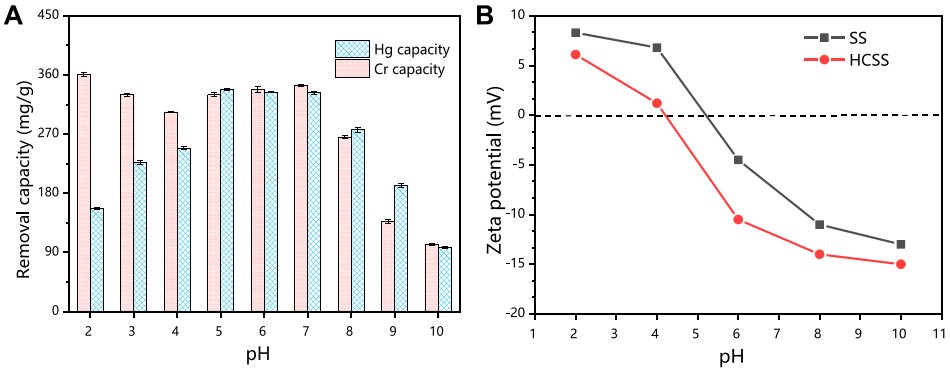

FIGURE 3
(A) Comparison of different pHs. Conditions: C0 = 400 ppm; sample volume: 10 ml; reaction time: 24 h; and temperature: 25°C. **(B)** Comparison of zeta potential of HSS and HCSS.

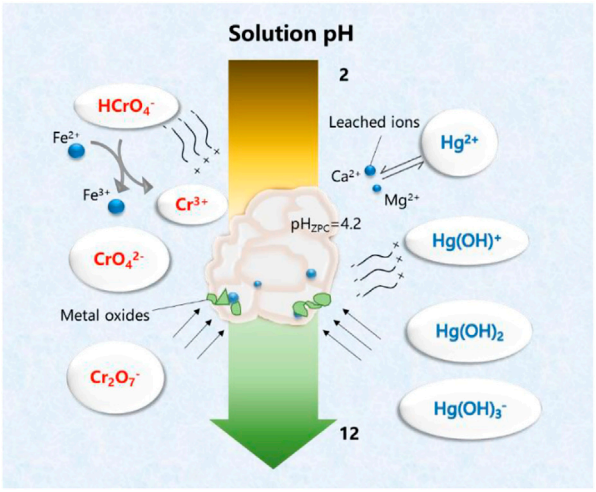

FIGURE 4
Conceptual representation of interactions between HCSS with mercury and chromium species in different solution pHs.

with HCSS surface of positive charge, then repulsion was possible. Hence, it was not applicable for the fitting of multilayer adsorption in the Freundlich model.

3.2.3 Influence of pH

Initial solution pH affects the speciation of heavy metal ions, surface charge, and the ionization degree of the functional groups of the steel slag–derived materials, which in turn may strongly influence the adsorption performance, and also offer insights into the adsorption mechanisms. HCSS was employed for the elimination of Hg (II) and Cr (VI) from aqueous solution, and the determination of pH influence was conducted by varying the initial solution pH from 2 to 10. From Figure 3A, in the case of Hg (II), the capacity increased from 157.1 to 248.9 mg/g with the increase in pH from 2 to 4, and then capacity fluctuated between 338.1 and 332.6 mg/g at pH 5–6. Further increase in pH resulted in a decrease of the capacity from 276.4 mg/g (at pH 8) to 97.7 mg/g (at pH 10). However, as for Cr (VI), the capacity maintained with the increase in pH from 2 to 6 (360.3, 329.7, 303.6, 330.0, and 337.9 mg/g for pH 2, 3, 4, 5, and 6, respectively) and decreased from 344.1 to 102.3 mg/g with the further increase in pH from 7 to 10.

To explain the immobilization of Hg (II) and Cr (VI) by HCSS at various pHs, zeta potential was conducted (Figure 3B). The pH_{ZPC} (point of zero charges) of HCSS was determined to be 4.22, while that value of SS was 5.21, which further confirmed that the organic component was successfully assembled onto the surface of slag skeleton, due to the organic functional groups typically negatively charged (He et al., 2017). Moreover, in the case of Hg (II) adsorption, the surface of HCSS was positively charged at pH 2 ($pH < pH_{ZPC}$); this positively charged surface of adsorbent created the electrostatic repulsion between the HCSS surface sites and cationic Hg (II), and the adsorption of Hg (II) was constrained, since Hg^{2+} is the only dominating species when $pH < 4$. Above this pH, Hg^{2+}, $Hg(OH)^{+}$, $Hg(OH)_2$, and $Hg(OH)_3^{-}$ coexisted in the solution, the electronegative property of HCSS created the electrostatic attraction for mercury ions. Additionally, the functional groups were also deprotonated and formed complexation with mercury ions (such as $COOHg^{+}$ or $COHg^{+}$) (Gong et al., 2014), and all of these resulted in higher removal of Hg (II) ions at pH 5–6. However, when pH kept increasing, the adsorption capacity dropped dramatically, since the dominating species of Hg (II) ions were $Hg(OH)^{+}$, $Hg(OH)_2$, and $Hg(OH)_3^{-}$, and carriage of these species from solutions to the surface of adsorbents may be inhibited as the high molecular weight and large size of these species. Also, the loaded mercury species hindered the further

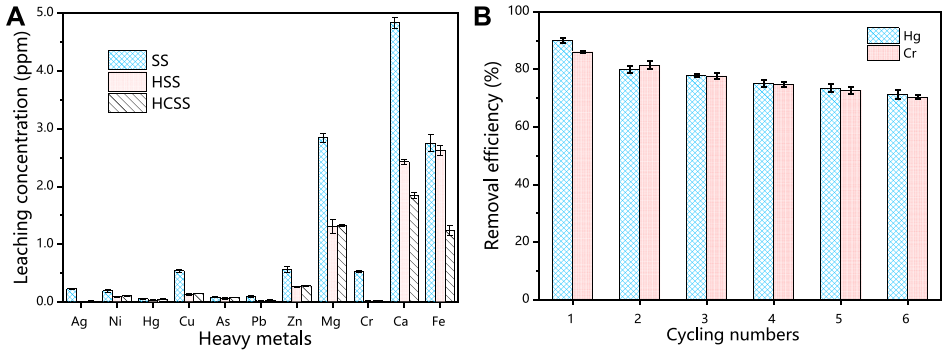

FIGURE 5
(A) Comparison of the different indigenous metal leaching concentration of SS, HSS, and HCSS. Conditions: sample volume: 10 ml; dosage: 100.0 g/L; reaction time: 48 h; pH 6.5; and temperature: 25°C. **(B)** Regeneration of HCSS.

adsorption between mercury ions with active sites on the surface of HCSS.

On the another hand, in the case of Cr (VI) removal, there was no noticeable decrease of capacity at pH 2–6, and this could be attributed to the dominant species of chromium ions were $HCrO_4^-$ and CrO_4^{2-} in this pH environment; as they were negatively charged, they can create electrostatic attraction with HCSS. In addition, there were also more active species leaching from HCSS into solutions under acid conditions, such as calcium and iron, which was evidenced by the aforementioned leaching experiments. These active species could react with chromium ions and are beneficial to the removal of Cr (VI) (Xu et al., 2019), which would be discussed in the following sections. However, at pH > 7, the surface of sorbent was deprotonated and formed an electronegative potential. Thus strong electrostatic repulsion resulted from the electronegative HCSS surface and dominating chromium species, such as $HCrO_4^-$, $Cr_2O_7^{2-}$, and CrO_4^{2-}, thus decreasing the capacity of the adsorbent. The pH dependence of Hg (II) and Cr (VI) adsorption corresponded to the surface charge of HCSS and the metal speciation in different pH environment (Figure 4). Therefore, neutral pH (6.5) was applied for further experiments for the Hg (II) and Cr (VI) removal.

3.3 Real water matrix

3.3.1 Stability and reusability

For the safety concern, we also tested the secondary leaching performance of indigenous metallic from this slag-derived adsorbent. As shown in Figure 5A, for SS, the leaching amount was 3.342, 4.830, and 2.751 ppm for Mg, Ca, and Fe and 1.023, 0.571, and 0.540 ppm for Cr, Zn, and Cu, respectively. These values were similar to other reports (Han et al., 2016). However, after being converted into HSS *via* hydrothermal treatment, the leaching concentration of Mg, Ca, and Fe moderately decreased to 1.280, 2.402, and 2.616 ppm, correspondingly. This phenomenon could be attributed to the heavy metals were partially involved with the reconstruction processes of crystalline structure, as the increased number of network-forming metal oxides units under hydrothermal conditions (Dubey et al., 2017). Moreover, after being incorporated with biomass feedstock provided by SD, the resultant HCSS illustrated the limited leaching concentration as 0.190, 0.311, and 0.961 ppm for Mg, Ca, and Fe, respectively. This decrease in leaching was proposed to the chemical bonding between metals with functional groups on the surface of HCSS followed with the complete reconstruction of the crystalline structure, which was in a good agreement with the XRD analysis in the following sections. Compared with the original steel slag, the hydrochar component has a non-uniform surface, large specific surface area, numerous pores, rich organic functional groups, and the steel slag has a stable skeleton, inorganic adhesive for organic functional groups provide a rich active site, both firmly anchored in the process of heat and water together, and appear to have multiple interactions between the additional components, Therefore, HCSS has a stable structure and can inhibit metal leaching. Meanwhile, for the other metallic elements, such as Ag, Ni, Hg, Cu, As, Pb, Zn, and Cr, the leaching was only 0.023, 0.062, 0.001, 0.007, 0.024, 0.027, 0.023, and 0.015 ppm, respectively. These values were all lower than the recommended limitations by the World Health Organization (Ahmed and Ahmaruzzaman, 2016), implying the neglectable environmental negative impacts on water bodies.

A promising and competitive adsorbent should exhibit excellent recycling ability for practical applications. After six regeneration cycles, the removal efficiency was 71.2% for Hg (II) and 70.3% for Cr (VI), implying the excellent recoverable abilities for HCSS (Figure 5B). It should be mentioned that, in recent studies, the dominant mechanism for pollutants removal by slag-

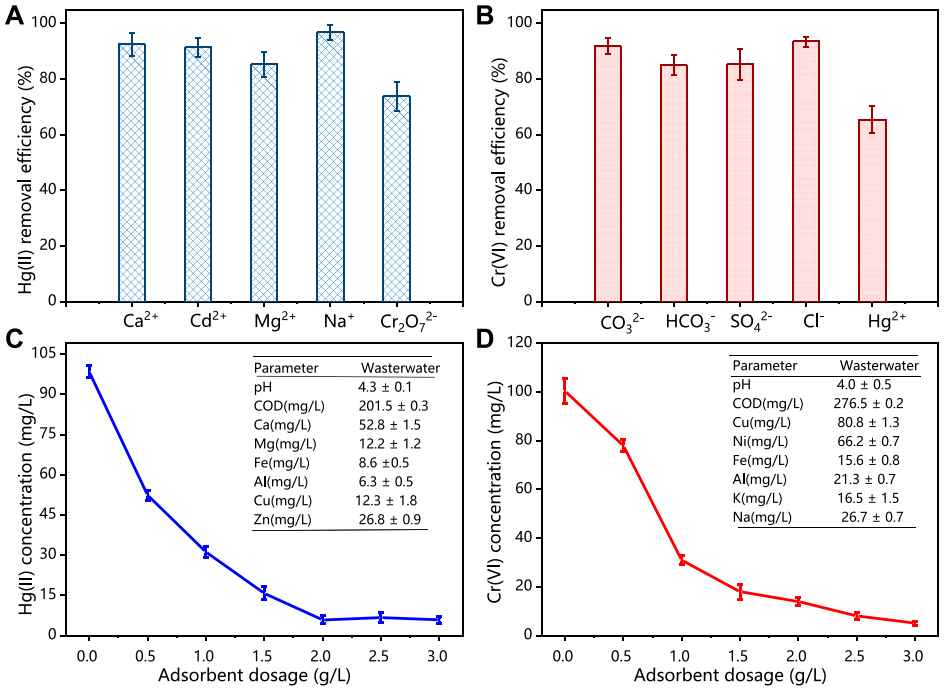

FIGURE 6
(A) Adsorption of Hg (II) by HCSS toward the mixture of metal ions. **(B)** Adsorption of Cr (VI) by HCSS toward the mixture of negatively charged ions. Conditions: concentration of competitive ions: 200 ppm; sample volume: 10 ml; dosage: 0.5 g/L; reaction time: 24 h; pH: 6.5; and temperature: 25°C. **(C)** Practical applications of HCSS for Hg (II) removal in real water. **(D)** Cr (VI) removal in real wastewater. Conditions: sample volume: 10 ml; reaction time: 24 h; and temperature: 25°C.

derived adsorbent was the leaching of chemical active species, such as leached Fe (II) for Cr (VI) reduction, or leached Ca (II) for phosphate precipitation (Fang et al., 2018). The main drawback was the lack of recyclability which limits the applications of these sorbents. However, in our study, this facile and green co-hydrothermal process successfully assembled hydrochar component onto the surface of slag skeleton; the hydrochar component was the main contributor to the capacity, and recrystallized steel slag as support, in turn, increased the stability and reusability of the adsorbent.

3.3.2 Selectivity

Coexisted metal ions in the practical wastewater system could influence the efficiency of adsorbents. Therefore, different metal ions, including Ca (II), Cd (II), Mg (II), Na (I), and K (I) from their chlorides, nitrates, and sulphates were added into solution, in order to evaluate the selective adsorption of HCSS for Hg (II) and Cr (VI) removal. As shown in Figure 6A, in the case of Hg (II) removal, the existence of competitive ions exhibited little influence for removal performance. The removal efficiency was 92.5%, 91.4%, 85.3%, 96.8%, and 73.8% for Ca^{2+}, Cd^{2+}, Mg^{2+}, Na^{+}, and $Cr_2O_7^{2-}$, respectively, which demonstrated the good selectivity of HCSS on Hg (II) removal. It should be noticed that in the presence of $Cr_2O_7^{2-}$, the removal efficiency on Hg (II) removal was still 73.8%, indicating the difference on reaction mechanism between Hg (II) and Cr (VI) removal. The decreasing removal efficiency for all coexisted metal ions might be attributed to the formation of some insoluble precipitates with sulfates or chlorides in the aqueous media (Lv et al., 2019). In addition, similar phenomenon was observed in Cr(VI) removal (Figure 6B), the removal efficiency was maintained as 91.8%, 85.1%, 85.3%, 93.5%, and 65.4% for CO_3^{2-}, SO_4^{2-}, Cl^{-}, and Hg^{2+}, respectively, indicating the good selectivity of HCSS for Cr (VI) removal among various negatively charged groups. The removal efficiency of Cr (VI) was reduced to 65.4% with the presence of Hg (II) might be attributed to the identical removal mechanisms, including formation of complexations and coprecipitation between Hg (II) ions with HCSS. However, the remaining Cr (VI) removal efficiency was contributed by the distinct mechanisms, such as chemical reduction, which would be discussed in the following section.

3.3.3 Practical wastewater test

In order to further evaluate the practicability of HCSS in real water systems, the adsorbent was conducted to selectively capture Hg (II) or Cr (VI) from different practical wastewater. As shown in Figure 6 C, D, within the presence of excess competitive cations and anions, the concentration of Hg (II) was decreased from

TABLE 4 Comparison of adsorption capacities of Hg(II) and Cr(VI) ions with some other functional materials.

Raw material	Modification	Condition		Maximum capacity (mg/g)		Equilibrium time	Reference
		Temperature (°C)	pH	Hg(II)	Cr(VI)		
Chitosan	Ethylhexadecyldimethyl ammonium bromide-impregnated chitosan	25	3.0	43.43	NA	5 h	Shekhawat et al. (2017)
Sawdust	Hydrothermally treated magnetic bio-adsorbents	25	6.5	167.2	NA	6 h	Wang et al. (2018)
Sawdust	Monomethylated thiourea sawdust	30	6	4.26	NA	4 h	Hashem et al. (2011)
Sewage sludge	Carboxymethyl chitosan–sewage sludge biochar	30	3	594.17	NA	4 h	Ifthikar et al. (2018)
Montmorillonite	Chitosan–nanoclay composite	30	2	NA	128.43	2 h	Kahraman, (2017)
Montmorillonite	Interaction of surfactant–modified sodium montmorillonite	30	3.8	NA	22.2[a]	80 min	Kumar et al. (2012)
Biomass	Nitric acid–activated carbon	25	6	NA	48	24 h	Valentín-Reyes et al. (2019)
Biomass	Chitosan modification of magnetic biochar	30	2	NA	120	200 min	Zhang et al. (2015)
Furnace slag	Ground and sieved, and H_2SO_4 was added into the solution to form $CaSO_4{\cdot}H_2O$	25	3	NA	12.3	70 min	Han et al. (2016)
Furnace slag	NaOH-activated slag	25	3	NA	6.7	4 h	Baalamurugan et al. (2018)
Steel slag	Incorporation of sawdust with steel slag by co-hydrothermal process	25	6.5	283.24	320.12	6 h for Hg (II) 5 h for Cr (VI)	This study

NA: not applicable.
[a]Calculated maximum capacity.

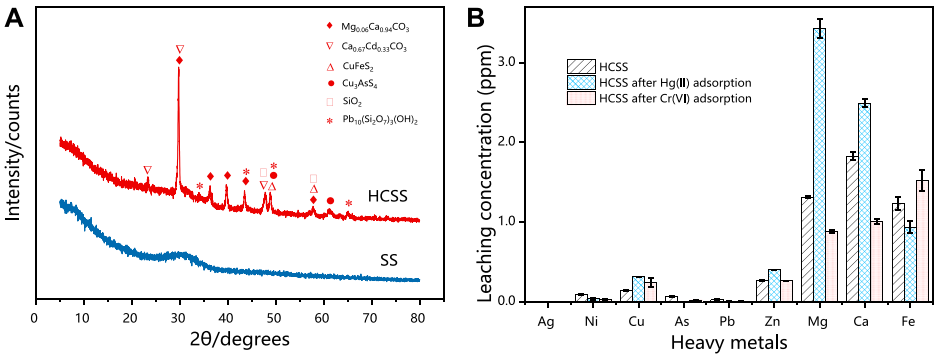

FIGURE 7
(A) XRD patterns of SS and HCSS. **(B)** Comparison of the different metal leaching concentrations of HCSS after Hg (II) and Cr (IV) removal. Conditions: C0 = 400 ppm; sample volume: 10 ml; dosage: 100.0 g/L; reaction time: 48 h; pH: 6.5; and temperature: 25°C.

98.4 to 5.9 mg/L with HCSS dosage increased from 0 to 3.0 g/L. As for Cr (VI), with the dosage of HCSS increased from 0 to 3.0 g/L, the Cr (VI) concentration decreased from 100.4 to 5.1 mg/L. These results further supported the Hg (II) or Cr (VI) removal by HCSS from real wastewater was less influenced by the variable chemistry and organic matter. Therefore, the obtained removal efficiency as 94.11% for Hg (II) and 88.65% for Cr (VI) elimination from practical wastewater, indicated the excellent feasibility and applicability of HCSS on real wastewater treatment.

3.3.4 Comparison study on the adsorption capacity

Various environmentally functional materials were compared on the adsorption capacity and reaction parameters

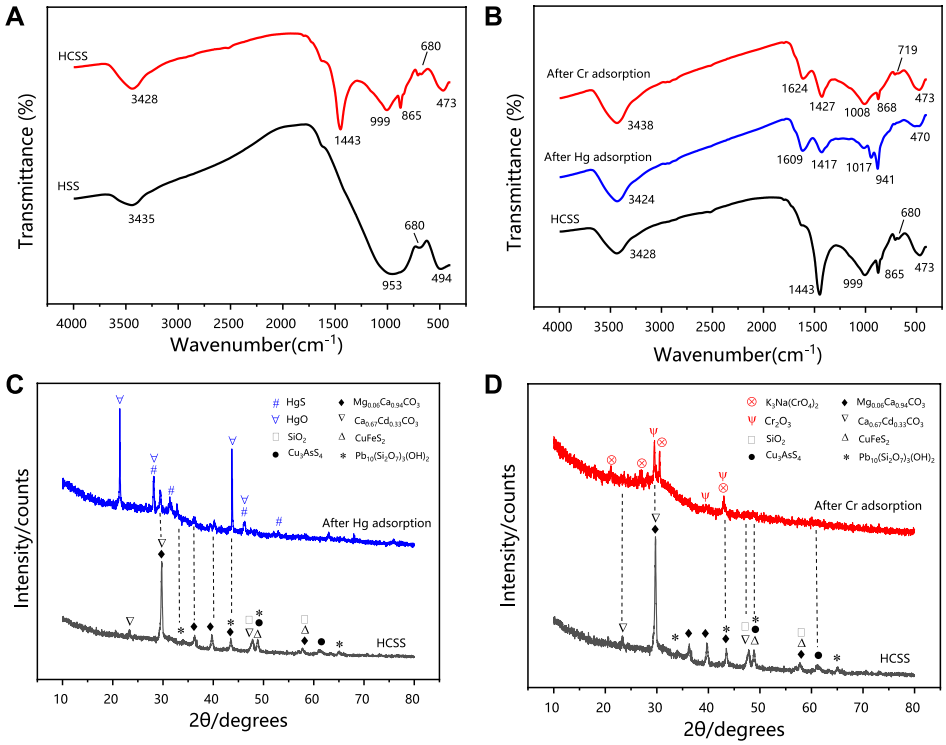

FIGURE 8
(A) FT-IR patterns of HCSS before adsorption. **(B)** FT-IR patterns of Hg-adsorbed HCSS, Cr-adsorbed HCSS, and comparison with HCSS. **(C)** XRD patterns of Hg-adsorbed HCSS. **(D)** XRD patterns of Cr-adsorbed HCSS.

for the removal of Hg (II) and Cr (VI) and summarized in Table 4. HCSS displayed superior adsorption capacity of 283.24 mg/g for Hg (II) with a dosage of 1.0 g/L, while the capacity of 320.12 mg/g for Cr (VI) with a dosage of 1.0 g/L. The high efficiency for Hg (II) and Cr (VI) removal implied this simple one-pot method was an emerging and promising method for modification of solid waste-derived materials.

3.4 Adsorption mechanisms

3.4.1 Recrystallization

The reconstruction of inorganic slag skeleton was confirmed by XRD (Figure 7A). In the case of SS, only a broad peak was observed in the range of 25.0°–35.0°, which might be attributed to the irregular structure of various indigenous metal oxides in SS. Moreover, after co-hydrothermal with biomass feedstock, the sharp and robust reflection peaks were observed for HCSS, peaks at 2Θ of 29.7°, 36.5°, 39.7°, 43.7°, and 57.6° indexed to $Mg_{0.06}Ca_{0.94}CO_3$ (JCPDS No. 01-089-1306)while peaks at 47.9° and 57.7° were ascribed to the formation of SiO_2 (JCPDS No. 00-047-1301). The alteration of characteristic reflection peaks between SS and HCSS proved the completion of the reconstruction process. The functional groups provided by biomass feedstock exhibited excellent affinity with surface metal ions, and the existence of CO_3^{2-} in the $Ca_{0.67}Cd_{0.33}CO_3$ and $Mg_{0.06}Ca_{0.94}CO_3$ oxides might be attributed to the organic functional groups involved with recrystallization process (Santamaria et al., 2018). Moreover, the reformed crystalline structure was also helpful to the adsorptive reactions for Hg (II) and Cr (VI) removal, due to the coprecipitation process between pollutants with metal oxides (Richard et al., 2016). Additionally, some crystalline structures observed in HCSS, such as $Ca_{0.67}Cd_{0.33}CO_3$ (JCPDS No. 01-072-1938), Cu_3AsS_4 (JCPDS No. 00-025-0265), and Pb_{10} (Si_2O_7) $_3$ (OH) $_2$ (JCPDS No. 00-044-0276), could reduce the potential leaching of toxic metal ions, which in turn, increased the safety and stability of HCSS (Liu et al., 2016). This result was also in good agreement with the previous indigenous metal leaching test.

Surface morphology was characterized by SEM-EDX (Supplementary Figure S3). HSS was smoother with fewer pores than SS, while SS exhibited chiseled microspore structure. This stable crystalline structure of HSS could be potential support for the assembly of surface functional groups. In addition, according to EDX results, HSS exhibited higher contents of Ca (31.63 wt%) and Fe (2.31 wt%) than SS (24.44 wt% and 0.23 wt% for Ca and Fe, respectively), this could be explained as the recrystallization benefited the exposure of

indigenous metallic elements encapsulated in the lattice (Ma et al., 2018). As mentioned before, the high ratio of metallic ions on the surface of support might be beneficial to the subsequent assembly or reaction process.

The distribution of the surface metallic elements was further detected *via* X-ray fluorescence (Supplementary Figure S4). It is mainly composed of CaO, SiO_2, and Al_2O_3 on the surface of HCSS, with the content of 36.85, 39.28, and 14.58 wt%, correspondingly. The existence of calcium ions on the surface of HCSS could be involved in ion-exchange with Hg (II) ions during the adsorption process. The formation of inner-sphere complexation between silica and heavy metals was also beneficial to the adsorption process. More importantly, the iron ions on the surface of HCSS existed as Fe (II) species, and the content of FeO was 2.92 wt%, these species might exhibit reductive property for Cr (VI) immobilization (Hu et al., 2019a).

3.4.2 Surface functional groups

To further investigate the variations of surface functional groups, FT-IR spectra were illustrated in Figure 8A. The signal at 3,435 cm^{-1} of HSS and 3,428 cm^{-1} of HCSS was attributed to the vibration of O-H (Rao et al., 2017), which evidenced the existence of -OH groups. The band at 1,443 cm^{-1} of HCSS can be endorsed to stretching of N-H, and 865 cm^{-1} was associated with the vibration of C = O (Li et al., 2015), which were both ascribed to the functional groups from the incorporation of bioresource, and were only observed on the surface of HCSS. In the case of HSS, the signal at 953 cm^{-1} was attributed to the vibration of Si-O groups, and this signal was shifted into 999 cm^{-1} in the case of HCSS, indicating the Si-O structure was transformed, and new silica-based crystals might be generated (Pala et al., 2014). This reforming of Si-O contained structure during adsorbents preparation was further confirmed by XRD spectra in the following section. The peak at 680 cm^{-1} was ascribed to the bending vibration of Fe-O, implying the existence of iron on the surface both for HCSS and HSS (Tan et al., 2015). These outcomes of FT-IR spectra confirmed the successful loading of organic components onto the surface of the supporting slag skeleton, and in turn, as-prepared HCSS comprised carbon skeleton with a high ratio of hydroxyl, carboxyl, amino, and lactone functional groups, which was consistent with S_{BET} and Boehm analysis.

The FT-IR spectra of HCSS after adsorption of Hg (II) and Cr (VI) were presented in Figure 8B. After the adsorption, significant shifts of characteristics bands from 3,428 (stretching vibrations of O-H/N-H) to 3,424 and 3,438 cm^{-1}, from 1,443 (bending vibration of N-H) to 1,417 and 1,427 cm^{-1}, from 999 (bending vibration of Si-O) to 1,017 and 1,008 cm^{-1}, from 865 (bending vibration of C = O) to 941 and 868 cm^{-1} was observed after the adsorption of Hg (II) and Cr (VI), respectively. These results illustrated the formation of surface complexations between pollutants and functional groups, and high functional groups density on the surface of HCSS improved the removal capacity, which further evidenced the functional groups on the surface was the main contributor to the removal capacity. However, the abundant functional groups only could be achieved by the co-hydrothermal process between biomass feedstock and inorganic skeleton, owing to the obtained regular backbone benefited to the adherence of functional groups. It should be noticed that the peak at 680 cm^{-1} in HCSS was ascribed to the bending vibration of Fe-O. After Cr (VI) adsorption, this peak shifted to 719 cm^{-1}, and this transformation was not observed in the case of Hg (II) removal (Wang et al., 2018). This phenomenon further proved the chemical reduction between iron and chromium ions, as the dominant iron oxides might be converted from FeO into Fe_2O_3 after Cr (VI) adsorption, which was also consistent with XRF results (Supplementary Figure S5).

3.4.3 Electron transfer

XRD spectra further provided the evidence for the chemical interaction during the adsorption process. As revealed in Figures 8C,D, characteristic XRD patterns of HgS and HgO were observed for Hg (II) removal with the typical 2Θ of 21.2°, 28.2°, 43.7°, 46.1°, and 28.2°, 28.2°, 43.7°, 46.1°, respectively (JCPDS No. 01-073-1247). The reflection peaks at 2Θ of 29.6°, 39.6°, and 43.0° indicated the existence of Cr_2O_3 in the case of Cr(VI) removal (JCPDS No. 01-081-1136). The formation of HgS, HgO, and Cr_2O_3 could be ascribed to the reactions between Hg (II), Cr (VI) with the metal oxides, while more regular crystalline oxide matrix could enhance the coprecipitation process (Deng et al., 2017). This reconstructed structure was obtained under the co-hydrothermal circumstance and considerably improved the crystallinity of the support. Moreover, the chromium species existed as Cr (III) in the resultant Cr_2O_3 demonstrated Cr (VI) could be reduced into Cr (III) by active chemical species (such as iron ions) during the adsorption (Hu et al., 2019). As illustrated in Supplementary Figure S5 XRF analysis of HCSS after the adsorption confirmed the existence of HgO (7.27 wt%), which was consistent with XRD results. More importantly, before adsorption, iron species existed as FeO in HCSS, however, after the adsorption of Cr (VI), the existence of Cr_2O_3 (7.32 wt%) and Fe_2O_3 (0.67 wt%) were confirmed, which further evidenced the reduction from Cr (VI) to Cr (III) by Fe (II) species during the adsorptive reactions.

Furthermore, redox potential, E^0, a crucial measure of the tendency of a chemical species to acquire from or lose electrons further reveal the mechanism of Cr (VI) reduction process. Herein, E^0 of $Cr_2O_7^{2-}/Cr^{3+}$, O_2/OH^-, and Fe_3O_4/Fe_2O_3, was 1.33, 0.41 and 0.215 V, respectively (Ciblak et al., 2012), indicating $Cr_2O_7^{2-}/Cr^{3+}$ could easier react with FeO (Fe_3O_4) compared with oxidized by oxygen. Therefore, the reduction process could be explained by the following equations:

$$6FeO + Cr_2O_7^{2-} + 8H^+ \rightarrow 2Cr^{3+} + 3Fe_2O_3 + 4H_2O, \quad (6)$$

$$2(2Ca \cdot SiO_2) + 4H_2O \rightarrow 3Ca \cdot 2SiO_2 \cdot 3H_2O + Ca(OH)_2, \quad (7)$$

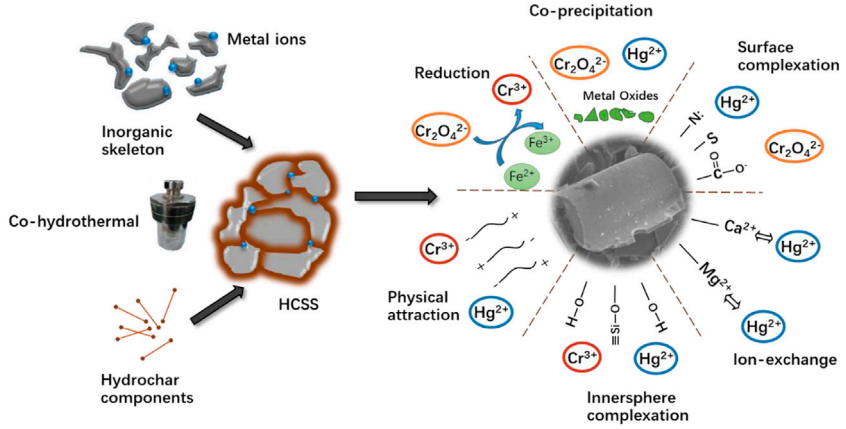

FIGURE 9
Conceptual sketch of Hg (II) or Cr (VI) removal by HCSS.

$$3\left(3Ca\cdot SiO_2\right)+6H_2O\rightarrow 3Ca\cdot 2SiO_2\cdot 3H_2O+3Ca\left(OH\right)_2, \quad (8)$$

$$2Cr^{3+}+3Ca\left(OH\right)_2\rightarrow 2Cr\left(OH\right)_3+3Ca^{2+}, \quad (9)$$

$$2Cr\left(OH\right)_3\rightarrow Cr_2O_3+3H_2O. \quad (10)$$

3.4.4 Multiple interactions

Based on the former analysis, both chemical and physical adsorption could contribute to the adsorption of Hg (II) and Cr (VI) onto HCSS. Based on the kinetics study, the initial fast stage was ascribed to the ion-exchange, electrostatic attraction, and chemical reduction, while the chemical process is the dominant step for rate determination (Sumaraj and Padhye, 2017). The chemisorption on the homogeneous surface along with monolayer reactions was also demonstrated by isothermal analysis, and more solid experimental evidence for the detailed chemical process might help to understand the superior adsorption capacity.

As evidenced by S_{BET} and SEM, the high surface areas and regular crystalline structure of HCSS enable this sorbent to be easily accessible to heavy metal ions and contribute to the further reaction (Takaya et al., 2016). The pH experiment and the measurement of pHZPC illustrated that the Hg (II) and Cr (VI) [reduced as Cr (III)] could be electrostatic attracted onto HCSS, due to the negatively charged surface of HCSS at pH 6.5 (Burton et al., 2019). Moreover, the more negatively charged property also confirmed the assembly of functional groups on the surface of the slag skeleton. The quantitative study on the concentration of metallic elements after Hg (II) and Cr (VI) adsorption was also conducted (Figure 7B). In the case of Hg (II) removal, the concentration of Mg (II) and Ca (II) after adsorption increased to 3.45 and 2.51 ppm, respectively. However, there was no noticeable increase of metal ions concentration after Cr (VI) adsorption [only 0.19 and 0.31 ppm for Mg (II) and Ca (II), respectively], which was attributed to the different charge density between chromium ions and other surface metal ions (Jobby et al., 2018). These verdicts illustrated that Hg (II) ions were adsorbed on HCSS by the process of ion-exchange through reaction Eqs. 11, 12 (Lu et al., 2012).

$$-Mg^{2+}+Hg^{2+}\rightarrow -Hg^{2+}+Mg^{2+}, \quad (11)$$

$$-Ca^{2+}+Hg^{2+}\rightarrow -Hg^{2+}+Ca^{2+}. \quad (12)$$

To sum up, the removal mechanisms for Hg (II) and Cr (VI) were proposed and demonstrated in Figure 9. After being simultaneously recrystallized and bioconverted *via* co-hydrothermal treatment, the biomass and slag exhibited a synergetic effect in Hg (II) and Cr (VI) removal. The adsorption process was a combination of physical attractions, the formation of inner-sphere complexations with hydroxyl, exchanges with internal cations, the formation of surface complexations with functional groups, coprecipitations, and formation of Si-O complexations. All these mechanisms contributed to the efficient performance of Hg (II) and Cr (VI) removal.

4 Conclusion

1) Among all sorbents (SS, HSS, HSD, HCSS, and physical mixture of HSS/HSD and SS/HSD) investigated, HCSS exhibited the superior capacity for Hg^{2+} and $Cr_2O_7^{2-}$ removal. This environmentally functional material illustrated an exceptional capacity (283.24 and 323.16 mg/g for Hg (II) and Cr (VI) removal, respectively) compared with other adsorptive materials.

2) The high capacity mainly originates from converted hydrochar components, but the excellent stability and reusability of HCSS were attributed to the physiochemically stable inorganic skeleton derived from steel slag, which was also recrystallized under the hydrothermal circumstance.
3) Cr (VI) could be chemically reduced by the indigenous reactive species in slags, such as Fe (II). The adsorption was pH-dependent, owing to the multiple mechanisms, such as rate-determining steps of chemisorption including chemical reduction, coprecipitation, inner-sphere complexation, and involved with other processes, such as ion-exchange and electrostatic attraction.
4) HCSS exhibited good selectivity on heavy metals removal, and this material was also proved satisfied with removal efficiency for real wastewater treatment, with the percentage of 94.11% and 88.65% for Hg (II) and Cr (VI), respectively, indicating the potential practical feasibility of this environmentally functional materials.
5) This simultaneous recrystallization and bioconversion process shed the new light for the support design for carbonaceous materials and reutilization of steel slag, and this co-hydrothermal treatment could be considered an emerging and promising approach for the synthesis of other solid waste-derived environmentally functional materials.

Data availability statement

The original contributions presented in the study are included in the article/Supplementary Materials; further inquiries can be directed to the corresponding authors.

Author contributions

HW: writing the original draft; RD: methodology; XZ and JW: visualization; YL: resources; RX and ZL: corresponding author and responsible for ensuring that the description is accurate and agreed by all authors.

Funding

The authors appreciate the support from the National Natural Science Foundation of China [Grant Number 21775053], the Yunnan Province Education Department Scientific Research Foundation Project [Grant Number 2022J0136], and the Applied Basic Research Foundation of Yunnan Province [Grant Numbers 202201AS070020 and 202201AU070061].

Conflict of interest

The authors declare that the research was conducted in the absence of any commercial or financial relationships that could be construed as a potential conflict of interest.

Publisher's note

All claims expressed in this article are solely those of the authors and do not necessarily represent those of their affiliated organizations, or those of the publisher, the editors, and the reviewers. Any product that may be evaluated in this article, or claim that may be made by its manufacturer, is not guaranteed or endorsed by the publisher.

Supplementary material

The Supplementary Material for this article can be found online at: https://www.frontiersin.org/articles/10.3389/fbioe.2022.961907/full#supplementary-material

References

Ahmad, S., Zhu, X., Luo, J., Shen, M., Zhou, S., Zhang, S., et al. (2019). Conversion of phosphorus and nitrogen in lincomycin residue during microwave-assisted hydrothermal liquefaction and its application for Pb2+ removal. *Sci. total Environ.* 687, 1381–1388.

Ahmed, M. J. K., and Ahmaruzzaman, M. (2016). A review on potential usage of industrial waste materials for binding heavy metal ions from aqueous solutions. *J. Water Process Engin.* 10, 39–47.

Baalamurugan, J., Ganesh Kumar, V., Govindaraju, K., Naveen Prasad, B. S., Bupesh Raja, V. K., Padmapriya, R., et al. (2018). Slag-based nanomaterial in the removal of hexavalent chromium. *Int. J. Nanosci.* 17, 1760013. doi:10.1142/s0219581x17600134

Burton, E. D., Choppala, G., Vithana, C. L., Karimian, N., Hockmann, K., and Johnston, S. G. (2019). Chromium(VI) formation via heating of Cr(III)-Fe(III)-(oxy) hydroxides: A pathway for fire-induced soil pollution. *Chemosphere* 222, 440–444.

Ciblak, A., Mao, X., Padilla, I., Vesper, D., Alshawabkeh, I., Alshawabkeh, A. N., et al. (2012). Electrode effects on temporal changes in electrolyte pH and redox potential for water treatment. *J. of Environ. Sci. and Health, Part A* 47, 718–726. doi:10.1080/10934529.2012.660088

Czech, B., Hojamberdiev, M., and Bogusz, A. (2018). Impact of thermal treatment of calcium silicate-rich slag on the removal of cadmium from aqueous solution. *J. Of Clean. Prod.* 200, 369–379. doi:10.1016/j.jclepro.2018.07.309

Dai, Y., Zhang, N., Xing, C., Cui, Q., and Sun, Q. (2019). The adsorption, regeneration and engineering applications of biochar for removal organic pollutants: A review. *Chemosphere* 223, 12–27.

Deng, J., Liu, Y., Liu, S., Zeng, G., Tan, X., Huang, B., et al. (2017). Competitive adsorption of Pb(II), Cd(II) and Cu(II) onto chitosan-pyromellitic dianhydride modified biochar. *J. colloid interface sci.* 506, 355–364.

Duan, J., and Su, B. (2014). Removal characteristics of Cd(ii) from acidic aqueous solution by modified steel-making slag. *Chem. Eng. J.* 246, 160–167. doi:10.1016/j.cej.2014.02.056

Dubey, S. P., Dwivedi, A. D., Sillanpää, A., Lee, H., Kwon, Y.-N., and Lee, C. (2014). Adsorption of As(V) by boehmite and alumina of different morphologies prepared under hydrothermal conditions. *Chemosphere* 169, 99–106.

Fang, D., Huang, L., Fang, Z., Zhang, Q., Shen, Q., Li, Y., et al. (2018). Evaluation of porous calcium silicate hydrate derived from carbide slag for removing phosphate from wastewater. *Chem. Eng. J.* 354, 1–11. doi:10.1016/j.cej.2018.08.001

Gao, H., Song, Z., Zhang, W., Yang, X., Wang, X., Wang, D., et al. (2017). Synthesis of highly effective absorbents with waste quenching blast furnace slag to remove methyl orange from aqueous solution. *J. Environ. Sci.* 53, 68–77. doi:10.1016/j.jes.2016.05.014

Ghadikolaei, N. F., Kowsari, E., Balou, S., Moradi, A., and Taromi, F. A. (2019). Preparation of porous biomass-derived hydrothermal carbon modified with terminal amino hyperbranched polymer for prominent Cr(vi) removal from water. *Bioresour. Technol.* 288, 121545. doi:10.1016/j.biortech.2019.121545

Gómez-Nubla, L., Aramendia, J., Fdez-Ortiz De Vallejuelo, S., and Madariaga, J. M. (2018). Metallurgical residues reused as filler after 35years and their natural weathering implications in A mountain area. *Sci. Of Total Environ.* 618, 39–47. doi:10.1016/j.scitotenv.2017.11.026

Gong, Y., Liu, Y., Xiong, Z., and Zhao, D. (2014). Immobilization of mercury by carboxymethyl cellulose stabilized iron sulfide nanoparticles: reaction mechanisms and effects of stabilizer and water chemistry. *Environ Sci Technol* 48, 3986–3994.

Han, C., Jiao, Y., Wu, Q., Yang, W., Yang, H., Xue, X., et al. (2016). Kinetics and mechanism of hexavalent chromium removal by basic oxygen furnace slag. *J. Environ. Sci.* 46, 63–71. doi:10.1016/j.jes.2015.09.024

He, H., Tam, N. F. Y., Yao, A., Qiu, R., Li, W. C., and Ye, Z. (2017). Growth and Cd uptake by rice (Oryza sativa) in acidic and Cd-contaminated paddy soils amended with steel slag. *Chemosphere* 189, 247–254.

Hashem, A., Hussein, H. A., Sanousy, M. A., Adam, E., and Saad, E. E. (2011). Monomethylolated thiourea – sawdust as A new adsorbent for removal of Hg (ii) from contaminated water: Equilibrium kinetic and thermodynamic studies. *Polymer-Plastics Technol. and Eng.* 50, 1220–1230. doi:10.1080/03602559.2011.566301

Hu, Y., Xue, Q., Tang, J., Fan, X., and Chen, H. (2019a). New insights on Cr(vi) retention by ferrihydrite in the presence of Fe(ii). *Chemosphere* 222, 511–516. doi:10.1016/j.chemosphere.2019.01.160

Hu, Y., Zhu, Y., Zhang, Y., Lin, T., Zeng, G., Zhang, S., et al. (2019b). An efficient adsorbent: Simultaneous activated and magnetic zno doped biochar derived from camphor leaves for ciprofloxacin adsorption. *Bioresour. Technol.* 288, 121511. doi:10.1016/j.biortech.2019.121511

Huang, R., Fang, C., Lu, X., Jiang, R., and Tang, Y. (2017). Transformation of phosphorus during (Hydro)Thermal treatments of solid biowastes: Reaction mechanisms and implications for P reclamation and recycling. *Environ. Sci. Technol.* 51, 10284–10298. doi:10.1021/acs.est.7b02011

Ifthikar, J., Jiao, X., Ngambia, A., Wang, T., Khan, A., Jawad, A., et al. (2018). Facile one-pot synthesis of sustainable carboxymethyl chitosan - sewage sludge biochar for effective heavy metal chelation and regeneration. *Bioresour. Technol.* 262, 22–31. doi:10.1016/j.biortech.2018.04.053

Jobby, R., Jha, P., Yadav, A. K., and Desai, N. (2018). Biosorption and biotransformation of hexavalent chromium [Cr(VI)]: A comprehensive review. *Chemosphere* 207, 255–266.

Johs, A., Eller, V. A., Mehlhorn, T. L., Brooks, S. C., Harper, D. P., Mayes, M. A., et al. (2019). Dissolved organic matter reduces the effectiveness of sorbents for mercury removal. *Sci. Of Total Environ.* 690, 410–416. doi:10.1016/j.scitotenv.2019.07.001

Jung, S. S., and Sohn, I. (2014). Crystallization control for remediation of an FetO-rich CaO-SiO2-Al2O3-MgO EAF waste slag. *Environ. Sci. Technol.* 48, 1889–1892.

Kahraman, H. T. (2017). Development of an adsorbent via chitosan nano-organoclay assembly to remove hexavalent chromium from wastewater. *Int. J. Of Biol. Macromol.* 94, 202–209. doi:10.1016/j.ijbiomac.2016.09.111

Khan, M. A., Alqadami, A. A., Otero, M., Siddiqui, M. R., Alothman, Z. A., Alsohaimi, I., et al. (2019). Heteroatom-doped magnetic hydrochar to remove post-transition and transition metals from water: Synthesis, characterization, and adsorption studies. *Chemosphere* 218, 1089–1099.

Kumar, A. S. K., Kalidhasan, S., Rajesh, V., and Rajesh, N. (2012). Application of cellulose-clay composite biosorbent toward the effective adsorption and removal of chromium from industrial wastewater. *Ind. Eng. Chem. Res.* 51, 58–69. doi:10.1021/ie201349h

Li, K., Wang, Y., Huang, M., Yan, H., Yang, H., Xiao, S., et al. (2015). Preparation of chitosan-graft-polyacrylamide magnetic composite microspheres for enhanced selective removal of mercury ions from water. *J. colloid interface sci.* 455, 261–270.

Li, Z., Sun, Y., Yang, Y., Han, Y., Wang, T., Chen, J., et al. (2019). Biochar-supported nanoscale zero-valent iron as an efficient catalyst for organic degradation in groundwater. *J. Of Hazard. Mater.* 383, 121240. doi:10.1016/j.jhazmat.2019.121240

Lin, W., Jiang, R., Wu, J., Wei, S., Yin, L., Xiao, X., et al. (2019). Sorption properties of hydrophobic organic chemicals to micro-sized polystyrene particles. *Sci. Of Total Environ.* 690, 565–572. doi:10.1016/j.scitotenv.2019.06.537

Liu, B., Li, J., Zeng, Y., and Wang, Z. (2016). Toxicity assessment and geochemical model of chromium leaching from aod slag. *Chemosphere* 144, 2052–2057. doi:10.1016/j.chemosphere.2015.10.103

Liu, W., Zheng, J., Ou, X., Liu, X., Song, Y., Tian, C., et al. (2018). Effective extraction of Cr(vi) from hazardous gypsum sludge via controlling the phase transformation and chromium species. *Environ. Sci. Technol.* 52, 13336–13342. doi:10.1021/acs.est.8b02213

Lu, H., Zhang, W., Yang, Y., Huang, X., Wang, S., Qiu, R., et al. (2012). Relative distribution of Pb2+ sorption mechanisms by sludge-derived biochar. *Water Res.* 46, 854–862.

Lv, D., Zhou, J., Cao, Z., Xu, J., Liu, Y., Li, Y., et al. (2019). Mechanism and influence factors of chromium(VI) removal by sulfide-modified nanoscale zerovalent iron. *Chemosphere* 224, 306–315.

Ma, S., Song, C.-S., Chen, Y., Wang, F., and Chen, H.-L. (2018). Hematite enhances the removal of Cr(vi) by Bacillus subtilis Bsn5 from aquatic environment. *Chemosphere* 208, 579–585. doi:10.1016/j.chemosphere.2018.06.037

Nelson, J., Joe-Wong, C., and Maher, K. (2019). Cr(Vi) reduction by Fe(ii) sorbed to silica surfaces. *Chemosphere* 234, 98–107. doi:10.1016/j.chemosphere.2019.06.039

Ngambia, A., Ifthikar, J., Shahib, I. I., Jawad, A., Shahzad, A., and Zhao, M. (2019). Adsorptive purification of heavy metal contaminated wastewater with sewage sludge derived carbon-supported Mg(II) composite. *Sci. total Environ.* 691, 306–321.

Pala, M., Kantarli, I. C., Buyukisik, H. B., and Yanik, J. (2014). Hydrothermal carbonization and torrefaction of grape pomace: A comparative evaluation. *Bioresource techn.* 161, 255–262.

Park, T., Ampunan, V., Maeng, S., and Chung, E. (2017). Application of steel slag coated with sodium hydroxide to enhance precipitation-coagulation for phosphorus removal. *Chemosphere* 167, 91–97. doi:10.1016/j.chemosphere.2016.09.150

Qasrawi, H. (2018). Fresh properties of green scc made with recycled steel slag coarse aggregate under normal and hot weather. *J. Of Clean. Prod.* 204, 980–991. doi:10.1016/j.jclepro.2018.09.075

Rao, Z., Feng, K., Tang, B., and Wu, P. (2017). Surface dcoration of amino-functionalized metal–organic framework/graphene oxide composite onto polydopamine-coated membrane substrate for highly efficient heavy metal removal. *ACS Applied Mat. Interfaces* 9, 2594–2605.

Richard, J.-H., Bischoff, C., Ahrens, C. G. M., and Biester, H. (2016). Mercury (ii) reduction and Co-precipitation of metallic mercury on hydrous ferric oxide in contaminated groundwater. *Sci. Of Total Environ.* 539, 36–44. doi:10.1016/j.scitotenv.2015.08.116

Santamaria, A., Faleschini, F., Giacomello, G., Brunelli, K., San José, J.-T., Pellegrino, C., et al. (2018). Dimensional stability of electric arc furnace slag in civil engineering applications. *J. Of Clean. Prod.* 205, 599–609. doi:10.1016/j.jclepro.2018.09.122

Sumarajand Padhye, L. P. (2017). Influence of surface chemistry of carbon materials on their interactions with inorganic nitrogen contaminants in soil and water. *Chemosphere* 184, 532–547.

Shekhawat, A., Kahu, S., Saravanan, D., and Jugade, R. (2017). Removal of Cd(ii) and Hg(ii) from effluents by ionic solid impregnated chitosan. *Int. J. Of Biol. Macromol.* 104, 1556–1568. doi:10.1016/j.ijbiomac.2017.02.039

Takaya, C. A., Fletcher, L. A., Singh, S., Anyikude, K. U., and Ross, A. B. (2016). Phosphate and ammonium sorption capacity of biochar and hydrochar from different wastes. *Chemosphere* 145, 518–527.

Tan, X., Liu, Y., Zeng, G., Wang, X., Hu, X., and Gu, Y. (2015). Application of biochar for the removal of pollutants from aqueous solutions. *Chemosphere* 125, 70–85.

Valentín-Reyes, J., García-Reyes, R. B., García-González, A., Soto-Regalado, E., and Cerino-Córdova, F. (2019). Adsorption mechanisms of hexavalent chromium from aqueous solutions on modified activated carbons. *J. Of Environ. Manag.* 236, 815–822. doi:10.1016/j.jenvman.2019.02.014

Wang, H., Liu, Y., Ifthikar, J., Shi, L., Khan, A., Chen, Z., et al. (2018). Towards A better understanding on mercury adsorption by magnetic bio-adsorbents with gamma-Fe2o3 from pinewood sawdust derived hydrochar: Influence of atmosphere in heat treatment. *Bioresour. Technol.* 256, 269–276. doi:10.1016/j.biortech.2018.02.019

Xia, Y., Liu, H., Guo, Y., Liu, Z., and Jiao, W. (2019). Immobilization of heavy metals in contaminated soils by modified hydrochar: Efficiency, risk assessment and potential mechanisms. *Sci. Of Total Environ.* 685, 1201–1208. doi:10.1016/j.scitotenv.2019.06.288

Xu, X., Huang, H., Zhang, Y., Xu, Z., and Cao, X. (2019). Biochar as both electron donor and electron shuttle for the reduction transformation of Cr(vi) during its sorption. *Environ. Pollut.* 244, 423–430. doi:10.1016/j.envpol.2018.10.068

Yang, F., Zhang, S., Sun, Y., Tsang, D. C. W., Cheng, K., Ok, Y. S., et al. (2019). Assembling biochar with various layered double hydroxides for enhancement of phosphorus recovery. *J. Hazard. Mat.* 365, 665–673. doi:10.1016/j.jhazmat.2018.11.047

Yin, Q., Zhang, B., Wang, R., and Zhao, Z. (2017). Biochar as an adsorbent for inorganic nitrogen and phosphorus removal from water: a review. *Environ. Sci. Pollut. Res. Int.* 24, 26297–26309.

Zhang, L., Tang, S., Jiang, C., Jiang, X., and Guan, Y. (2018a). Simultaneous and efficient capture of inorganic nitrogen and heavy metals by polyporous layered double hydroxide and biochar composite for agricultural nonpoint pollution control. *ACS Appl. Mat. Interfaces* 10, 43013–43030. doi:10.1021/acsami.8b15049

Zhang, M.-M., Liu, Y.-G., Li, T.-T., Xu, W.-H., Zheng, B.-H., Tan, X.-F., et al. (2015). Chitosan modification of magnetic biochar produced from Eichhornia crassipes for enhanced sorption of Cr(vi) from aqueous solution. *RSC Adv.* 5, 46955–46964. doi:10.1039/c5ra02388b

Zhang, W., Zhang, P., Liu, F., Liu, W., Zhang, J., Lin, Z., et al. (2019). Simultaneous oxidation of Cr(iii) and extraction of Cr(vi) from chromite ore processing residue by silicate-assisted hydrothermal treatment. *Chem. Eng. J.* 371, 565–574. doi:10.1016/j.cej.2019.04.082

Zhang, Y., Xu, X., Cao, L., Ok, Y. S., and Cao, X. (2018b). Characterization and quantification of electron donating capacity and its structure dependence in biochar derived from three waste biomasses. *Chemosphere* 211, 1073–1081. doi:10.1016/j.chemosphere.2018.08.033

Zhou, Q., Liao, B., Lin, L., Qiu, W., and Song, Z. (2018). Adsorption of Cu(ii) and Cd(ii) from aqueous solutions by ferromanganese binary oxide–biochar composites. *Sci. Of Total Environ.* 615, 115–122. doi:10.1016/j.scitotenv.2017.09.220

Zhu, Y., Fan, W., Zhou, T., and Li, X. (2019). Removal of chelated heavy metals from aqueous solution: A review of current methods and mechanisms. *Sci. Of Total Environ.* 678, 253–266. doi:10.1016/j.scitotenv.2019.04.416

frontiers | Frontiers in Bioengineering and Biotechnology

TYPE Original Research
PUBLISHED 12 September 2022
DOI 10.3389/fbioe.2022.969137

OPEN ACCESS

EDITED BY
Benyamin Khoshnevisan,
University of Southern Denmark, Denmark

REVIEWED BY
Mukesh Kumar Awasthi,
Northwest A&F University, China
Farinaz Ebrahimian,
Isfahan University of Technology, Iran

*CORRESPONDENCE
Zhanjiang Pei,
neaupzj@163.com

SPECIALTY SECTION
This article was submitted to Bioprocess Engineering, a section of the journal Frontiers in Bioengineering and Biotechnology

RECEIVED 14 June 2022
ACCEPTED 12 August 2022
PUBLISHED 12 September 2022

CITATION
Shi F, Xu C, Liu J, Sun F, Yu H, Wang S, Li P, Yu Q, Li D, Zuo X, Liu L and Pei Z (2022), Static composting of cow manure and corn stalk covered with a membrane in cold regions. *Front. Bioeng. Biotechnol.* 10:969137. doi: 10.3389/fbioe.2022.969137

Static composting of cow manure and corn stalk covered with a membrane in cold regions

Fengmei Shi[1,2,3], Chengjiao Xu[4], Jie Liu[1,2,3], Fang Sun[5], Hongjiu Yu[1,2,3], Su Wang[1,2,3], Pengfei Li[1,2,3], Qiuyue Yu[1,2,3], Dan Li[1,2,3], Xin Zuo[1,2,3], Li Liu[5] and Zhanjiang Pei[1,2,3]*

[1]Heilongjiang Academy of Black Soil Conservation and Utilization, Harbin, China, [2]Key Laboratory of Combining Farming and Animal Husbandry Ministry of Agriculture, Harbin, China, [3]Key Laboratory of Energy Utilization of Main Crop Stalk Resources, Harbin, China, [4]College of Resources and Environment, Northeast Agricultural University, Harbin, China, [5]Animal Husbandry Institute, Heilongjiang Academy of Agricultural Sciences, Harbin, China

The disposal of livestock wastes is an urgent task in China. Compost is highly regarded for its ability to treat livestock wastes and protect arable land. In particular, some problems of livestock manure in cold regions, such as low efficiency because of low environmental temperature in winter, urgently need to be solved. In order to provide valuable composting information in the cold area at low environmental temperatures, the composting experiments were carried out with cow manure and corn stalk as substrates. The properties and bacterial community of compost samples in different stages were investigated. The electrical conductivity (EC), total nitrogen (TN), total phosphorus (TP), and organic matter (OM) of the final compost were 551 μS/cm, 1.12, 0.77, and 63.5%, respectively. No *E. coli* or *Ascaris* eggs were detected. The temperature was the key factor to affect the physical-co-chemical and biological properties. The absolutely dominant genera were *Sporosarcina*, *Virgibacillus*, *Flavobacterium*, and *Steroidobacter* in heating, high temperature, cooling, and maturing stages, respectively. Also, these bacteria could act as biological indicators during the composting process. *Cryobacterium*, *Caldicoprobacter*, *Virgibacillus*, and *Sporosarcina* were relatively novel genera in the compost piles in a cold environment. The biodegradation of exogenous substances mainly occurs in the initial and maturing stages. It is proven that composting can be carried out successfully in early spring or later autumn after a harvest.

KEYWORDS

compost, corn stalk, cow manure, cold region, manure

1 Introduction

In recent years, the livestock breeding industry in China has developed rapidly. According to statistics data, the output of cow and poultry in China in 2020 was about 45.65 million and 15.57 billion heads, with an increase of 0.7 and 6.3% year-on-year, respectively (NBSPRC, 2021). A large number of livestock breeding attempts result in a large amount of manure waste. For example, the amount of livestock and poultry manure

in China is up to 3.8 billion tons every year, more than the total amount of solid wastes including industrial and agricultural wastes. The comprehensive utilization rate of livestock manure in China was around 76% by the end of 2020 (MARAPRC, 2020). According to the plan of the Ministry of Agriculture and Rural Areas, by 2025, the comprehensive utilization rate of livestock and poultry manure will reach more than 80% (NDRCPRC, 2021). More than 20% of the waste still kept untreated and led to the pollution of water, soil, air, and human health hazards because pathogenic bacteria, parasite eggs, phosphorus, heavy metals, and harmful gases such as hydrogen sulfide, ammonia, and methyl mercaptan could be released from the manure wastes (Míriam et al., 2021; Shen et al., 2021; Duan et al., 2021). The problems of livestock manure pollution have raised extensive concern, and a number of policies have been issued to promote the utilization of stock manure in China (MARAPRC, 2019; MARAPRC, 2021; SCPRC, 2021). Fertilizer use of livestock manure wastes such as composting is the main comprehensive utilization mode (Chang et al., 2019; Onwosi et al., 2017).

Composting is supposed to be a complex biochemical process and is affected by many factors such as composting methods, temperature, C/N, pH, and substrates. Yang et al. (2019) found the nitrogen loss of mixed compost was much higher than that of anaerobic compost, aerobic compost, and farmer's method. Zhong et al. (2020) studied the bacterial community during the aerobic composting process of dairy manure without any bulking agents and found that *Corynebacterium*, *Bacillus*, *Luteimonas*, and *Nonomuraea* were main functional microbes in different composting phases. *Psychrobacterium* sp., *Pseudomonas* sp., and *Clostridium* sp. were abundant during cow manure composting in the composting facility (Zhao et al., 2013). When rice husk and cow manure were mixed and composted, the unique *Sphaerobacter* and *Myceliophthora* were dominant at high temperatures (Duan and Feng., 2021). It is suggested that the anaerobic compost method might be appropriate for nitrogen retention and less energy input. However, anaerobic composting requires much time because of low efficiency, and the quality of the final product is difficult to be guaranteed (Yang et al., 2019). Methods such as adding microbial agents could facilitate the formation of the humic matter and accelerate the composting process (Abdellah. et al., 2022). Liu et al. (2011) found that the indoor compost piles with microbiological inocula had a more quick temperature elevation, a longer time span of high temperature, and shorter maturation time than natural compost (without microbiological inocula). Duan et al. (2020) studied the effect of *Bacillus subtilis* on carbon components and microbial functional metabolism during cow manure-straw composting, and the results hinted that the addition of *Bacillus subtilis* into the piles could accelerate the compost maturation and improve the final product quality. However, the systematic research on this kind of composting mode at present is few, and aerobic composting has attracted researchers' attention.

TABLE 1 Basic physicochemical properties of cow manure and corn stalks.

Substrate	WC (%)	TOC (%)	TN (%)	C/N
Cow manure	84.33	39.00	2.06	18.93
Corn stalk	15.87	41.18	0.92	44.76

Simple anaerobic compost *in situ* became the main development trend in China. The simple composting methods are commonly used in rural areas. The compost piles are built in the field near the cow farm without ventilation and frequent turnover. Part of the country is in cold regions, and composting time adapted to agriculture planting is at a low-temperature stage. For example, the anaerobic compost is often carried out in the early spring or later autumn in Heilongjiang province. How to promote the composting process and guarantee the end compost quality in cold regions such as Heilongjiang province rich in crop straw and livestock wastes urgently needs to be solved (Shi et al., 2021a; Shi et al., 2021b; Sun, 2019). Hence the feasibility of composting livestock manure in autumn, winter, and early spring in Heilongjiang province was explored. Also, the change and metabolic function of the microbial community during the composting process were studied. So the investigation has more practical significance. It can provide the research basis and data reference for the control of the composting process.

2 Material and methods

2.1 Composting material and methods

The cow manure was taken from a cow farm in Heilongjiang province. The corn straw was purchased from the farmers near the research base and crushed to 0.5–3.0 cm. The basic physical and chemical properties of the raw materials are shown in Table 1. The substrate was dried to a constant weight in a hot air circulation oven at 105°C, and the water content (WC) was calculated according to the weight before and after drying. Total nitrogen (TN) and organic matter (OM) were evaluated according to the methods specified in NY/T 1121.24-2012 and NY/T1121.6-2006. The OM divided by 1.724 is the total organic carbon (TOC) value.

The C/N and the water content of the composting mixture were about 30:1 and 60%, according to the research studies and our laboratory compost results (Sánchez et al., 2017; Macias-Corral et al., 2019). Here, 1.592 tons of cow dung, 2.556 tons of grounded straw, and 1.852 tons of water were mixed. Then, the

mixture was divided into three equal portions, which were piled up into three semi-cylindrical compost strips with a forklift on the waterproof concrete floor and covered with a 2.0-mm thick HDPE (high-density polyethylene) membrane. Three thermocouples were inserted into the front, middle, and rear of the compost pile, respectively. The experiments were carried out in an organic waste treatment plant in Heilongjiang province from March to May, lasting 70 days. The piles were turned over on the 30th day using a front loader.

2.2 Sampling and index measurement

The temperature of compost piles and the environment were measured and recorded daily, which could be viewed on a mobile phone after the construction of the piles. According to the composting pile temperature, N1, N2, N3, and N4 were sampled on the 10th day (heating stage), 20th day (high-temperature stage), 50th day (cooling stage), and 70th day (maturing stage). The method of multi-level and multi-point sampling was adopted, sampled compost was then fully mixed, and 500 g of fresh compost was collected in the same pile. Then, the collected samples from the three different piles were mixed again. Some fresh samples were stored at 4°C to measure the WC, pH, and electrical conductivity (EC). The pH and EC levels were measured in the extraction liquid of fresh compost (1:10 of compost to deionized water, v/m) using a pH meter and a conductivity meter, respectively. The methods were described by previous studies (Shi et al., 2021a; Ding et al., 2020). At the same time, the color and smell of each group were investigated. About 50 g of fresh samples were stored at −80°C ready for 16S rRNA analysis. The remaining parts were dried at room temperature and used to test TN, TP, and OM, according to the methods specified in NY/T 1121.24-2012, NY/T 88-1988, and NY/T1121.6-2006, respectively.

2.3 16S rRNA analysis

DNA (deoxyribonucleic acid) was extracted using the FastPrep DNA kit (QBIOGENE, United States), according to the kit instructions, and the extracted DNA was detected by 1% agarose gel electrophoresis. Then, 30 ng DNA samples were extracted from the qualified compost samples as PCR (polymerase chain reaction) templates. The universal primers (338F/806R) were used to PCR-amplify the V3-V4 area of 16S rDNA. The general primer sequences of 16S rRNA were as follows: F: 338F (5′-ACTCCTACGGGAGGCAGCAG-3′) and R: 806R (5′-GGACTACHVGGGTWTCTAAT-3′). PCR reaction conditions were as follows: 95°C for 3 min; 95°C for 30 s, 55°C for 30 s, 72°C for 45 s, 27 cycles; 72°C for 10 min. PCR amplification products were purified using Agencourt AMPure XP magnetic beads, dissolved in elution buffer, and labeled to complete the database building. The fragment range and concentration in the database were checked using the Agilent 2100 Bioanalyzer. The qualified database was sequenced and analyzed on the HiSeq platform. Then, the microbial function was predicted with the PICRUSt program, described in our previous study (Shi et al., 2021b).

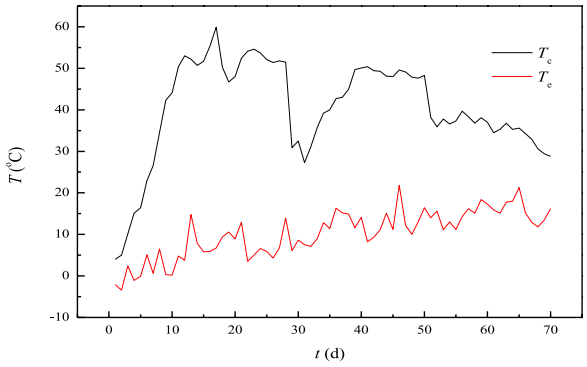

FIGURE 1
Temperature of the compost pile and environment.

2.4 Data analysis

Origin software was used to process data, plot, and calculate Pearson correlation coefficients and probability.

The Pearson correlation coefficient (r_p) describes the degree of linear correlation between two variables. A larger absolute value of r_p indicates a better correlation. The r_p between variable x and variable y can be calculated as follows:

$$r_p = \frac{\sum (x - \bar{x})(y - \bar{y})}{\sqrt{\sum (x - \bar{x})^2 \sum (y - \bar{y})^2}},$$

where x and y are the variables, and $\bar{x}$ and $\bar{y}$ are the average of the variables x and y, respectively. Then, the function t is used to evaluate the significant p.

$$t = \frac{r_p}{\sqrt{\left(1 - r_p\right) \Big/ \sqrt{n-2}}},$$

where n is the number of variables x or y. The p-value can be obtained easily *via* the t-distribution table.

3 Results

3.1 Changes of parameters of compost

3.1.1 Temperature

The temperature profiles of the compost piles were much different with different compost modes or manual management.

For example, frequent turning would lead to frequent temperature rise and fall of the compost piles, and more peaks would be found on the temperature curves [shen et al., 2019]. However, all the temperature profiles consisted of heating, high temperature, and cooling parts [Duan et al., 2020; Duan et al., 2021] The temperature during the composting process is shown in Figure 1. The temperature profiles were also multi-peaked, and composting consisted of heating, high temperature, and cooling stages. It can be seen that the temperature rose rapidly at the rate of 4.74 °C/d and reached 44.1°C in 10 days, 50.4°C in 11 days, and 59°C in 17 days, the first temperature peak. After 20 days, the temperature decreased to 48°C because of the fall in environmental temperature and then quickly recovered to above 50°C. The temperature of the composting pile decreased to about 30°C due to the heat loss because of the pile turning on the 30th day. After turning, the oxygen concentration in the compost pile increased, and the microorganisms became active gradually after adapting to the new environment. Then, the temperature of the compost pile increased at a rate of 1.9°C/d and reached 50°C on the 39th day, forming the second peak. The temperature decreased slightly at the rate of −0.19°C/dfrom the 39th to 50th day. The temperature drop was very small and negligible. The temperature dropped rapidly from 48.3°C on the 50th day to 38.2°C on the 51th day. The temperature was closely related to the metabolism of organic compounds by microorganisms and the heat loss to the environment (Schueler et al., 2021; Khalil et al., 2001). In the early stage of composting, there were abundant easily degradable organic materials such as starch, and protein, used by microorganisms for reproduction and metabolism activities. The number of microorganisms increased rapidly. A great deal of biological heat was produced, and the temperature of the pile quickly rose when the accumulated biological heat was far more than the heat lost to the environment. When the number and taxonomy of microorganisms became stable, the temperature also became stable, and compost was in the thermophilic stage. The temperature gap between the local ambient and the compost pile temperatures was much greater in the two thermophilic stages, with most of the degradable materials being degraded and utilized during the first and second high-temperature stages. The available materials in the compost pile were not enough to meet the needs of the microbial community. The growth and reproduction of microorganisms were then inhibited, the produced bio-heat decreased correspondingly, and the temperature of the compost pile decreased continuously at the rate of 0.52°C/d with the heat radiation from the reactor to the ambient.

There are a lot of pathogenic bacteria and parasite eggs in the feces of livestock and poultry, which affect the safety of land use. The pathogenic bacteria and parasite eggs were proved to be temperature-sensitive (Wichuk and McCartney, 2007; Heck et al., 2013). Most *E. coli*, *Salmonella* and *Shigella* bacteria will be killed for an hour at 55 C. If the temperature is kept for 15–20 min at 60°C, all of them will be eliminated. In composting environments, it will take a long time to obtain the same results. It took about 4 days to inactivate *Salmonella* when the composting temperature was higher than 55°C [Marilyn et al., 2009; Macias-corral et al., 2019]. *E. coli* could be eliminated in 25 days when the composting temperature was between 45 and 55°C (Wichuk and McCartney, 2007; Macias-corral et al., 2019). As a result, certain requirements for composting temperature and duration were proposed in order to meet the hygienic standards. According to the requirements of the "Technical Code for Composting of Livestock and Poultry Manure" (NY/T3442-2019) and "Technical Code for Harmless Treatment of Livestock and Poultry Manure" (GB/T36195-2018), the time span should be kept more than 14 days above 45°C for strip composting. It was 18 days from 50.4°C on the 11th day to 51.5°C on the 28th day in this experiment, which ensured the health and safety of the land use of the final compost product.

3.1.2 Indexes of composting

With the undergoing of composting, the WC of the compost decreased from 60.30% of N1 to 43.40% of N2 and then increased to 45.49% of N3 because of addition of water. When the composting was completed, the WC of the end product became 42.1%. The changes in pH were closely related to the metabolic activity of microorganisms in the compost piles. At the initial stage of composting, the composting material was basically neutral, and the pH value was 7.27. Then, the pH value increased to 9.29 due to the emission of NH_3 from protein and the accumulation of NH_4^+ in the composting matrix (Zhong et al., 2020). Then, microbial organisms used carbohydrates from biodegradable organic substances such as hemicellulose and cellulose to produce organic acids by metabolic activities. When the content of these acids was much higher than that of NH_3, the pH value kept decreasing and was 8.23 at the end of composting (Duan et al., 2021). The changes in pH values during the composting process were consistent with previous research studies (Liu et al., 2011; zhong et al., 2020). The EC of N1 was at a maximum of 5.390 ms/cm because the mineral salts were released or ammonium salts were formed (Duan et al., 2021). At the end of composting, the EC of the compost became 551 μS/cm. It was much lower than the suggested value of 4 dS/m and meant the final compost was safe for use (Sánchez et al., 2017). TN, TP, and OM of the final compost were 1.12%, 0.77%, and 63.5%, respectively. *E. coli* and *Ascaris* eggs were not detected in the final product. The compost could be used as an acid soil improvement and conditioning agent, as well as the cultivation of camptothecin crops. It should not be used in saline-alkali soil, saline soil, and crops and vegetables that were sensitive to low pH. The indexes are summarized in Table 2.

3.2 Succession of the bacterial community during composting

The composting process is carried out with the cooperation of many kinds of microorganisms. The composition and succession of microorganisms are affected by T, pH, and WC.

TABLE 2 Some properties of the compost.

Index	N0	N1	N2	N3	N4
WC(%)	60.30	48.65	43.40	45.49	42.1
pH	7.27	9.29	8.95	8.72	8.23
EC (uS/cm)	1,690	5,390	3,560	356	551
TN (%)	1.45	0.64	1.3	1.26	1.12
TP (%)	1.69	0.54	0.88	0.92	0.77
OM (%)	68.5	67.3	65.1	64.6	63.5

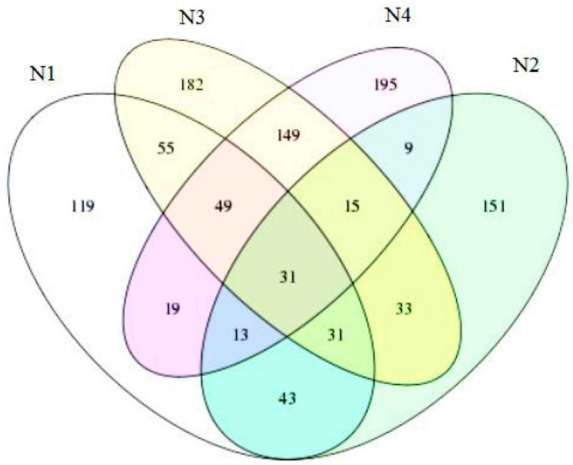

FIGURE 2
Venn diagram.

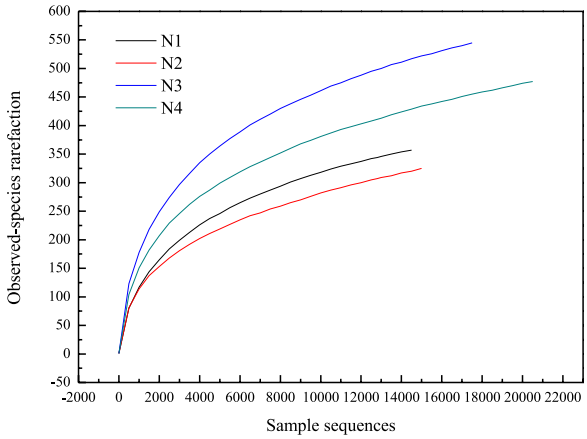

FIGURE 3
Observed-species rarefaction.

In order to study the change in the microbial community of static composting in a cold region and provide support for screening high-efficient composting bacteria or developing special composting bacteria agents, the bacterial community was studied *via* 16S rRNA.

3.2.1 Venn diagram

From the Venn diagram (Figure 2), it could be seen that the number of OTUs was N3 > N4 > N1 > N2. The common OTUs of N1, N2, N3, and N4 were 31, accounting for 8.61%, 9.51%, 5.69%, and 6.46% of their own total OTUs, respectively. Most of the OTUs in the samples were unique. Zhong et al. (2020) and Wang et al. (2018) gave similar reports. The overlapping OTUs of N2 and N4 were the least, accounting for 20.86% and 14.16% of the total OTU numbers of N2 and N4. The overlapping OTUs of N1 and N3 were the most, accounting for 31.11% and 23.33% of the total OTU numbers of N1 and N3. N1 and N2 shared 32.8% and 36.2% of the total OTU numbers of N1 and N2, respectively. N2 and N3 shared 33.7% and 20.2% of the total numbers of N2 and N3 OTUs, respectively. N3 and N4 shared 110 OTUs, which accounted for 44.8% and 50.8% of the total OTU numbers of N3 and N4, respectively. It indicated that the composting system had its own survival mechanism, and only a small number of bacteria in the whole composting process could be detected because of their good adaptability to the composting environment and great resistance to unfavorable conditions. Although these bacteria cannot be used as indicator organisms of the heating, high temperature, cooling, and maturing stages of composting, high-performance bacteria could be screened out to improve the composting efficiency or accelerate the composting process by adding them at the beginning of composting in tough composting conditions. On the other hand, the degradation of different organic compounds corresponds to different microbial communities. Therefore, the succession of microbial communities happened in different composting stages.

3.2.2 Rarefaction curve

The rarefaction curve can reflect the authenticity of the test results (Ding et al., 2020; Li and Xu., 2015). The observed-species index increased rapidly before 4,000 sample sequences and then increased slowly (Figure 3). The coverage of the four samples was higher than 0.99. The observed-species and coverage indexes indicated that the bacteria in each sample had been detected, the detection results were true. The indexes of Chao and Ace can indicate the community richness and evenness of samples, while the information on community diversity can be obtained from Shannon and Simpson rarefaction indexes (Zhong et al., 2020; Lei et al., 2021). The indexes of different rarefaction curves are summarized in Table 3. It could be seen that the indexes of Chao and Ace decreased in the order of N3, N4, N2 and N1. N1 and N3 had the lowest and highest bacterial abundance, respectively. The value of Shannon and Simpson indexes hinted that N3 had the

TABLE 3 Indexes of different rarefaction curves.

Sample	Chao	Shannon	Simpson	Ace	Coverage
N1	479.936	3.407	0.0758	461.854	0.9926
N2	496.500	3.405	0.0861	574.348	0.9923
N3	696.000	3.978	0.0746	689.282	0.9914
N4	647.787	3.812	0.0596	639.175	0.9930

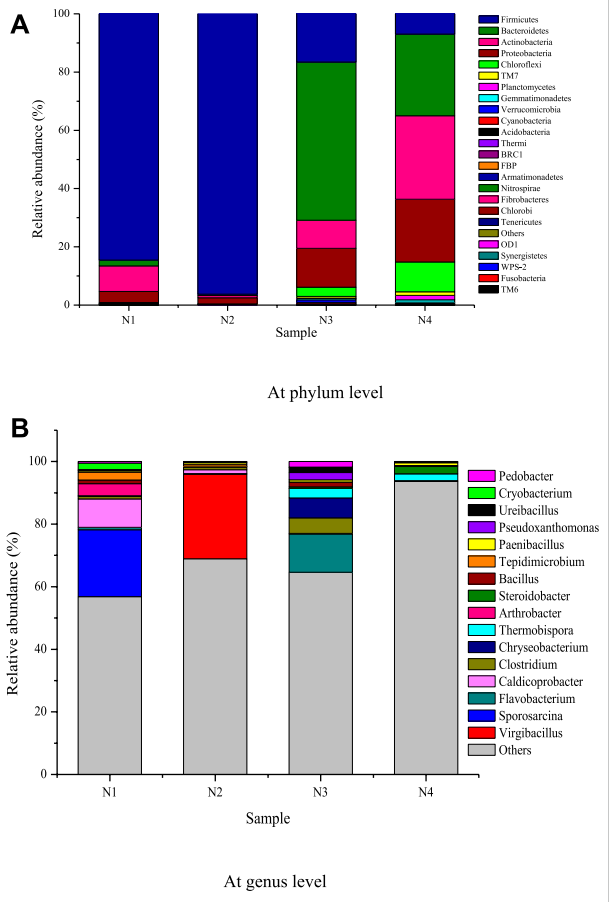

FIGURE 4
Barplot of bacterial relative abundance. **(A)** At phylum level. **(B)** At genus level.

maximum bacterial community diversity, then followed by N4, N1 and N2. The Chao index of N1 and the Shannon index of N2 were the smallest. The composting started below 10°C, and the bacteria in compost substrates were psychrophilic. Most of them were inactivated when the temperature increased rapidly and led to the least biological abundance of N1. When the temperature up to 50°C was kept for nearly 10 days, some microorganisms adapted to the compost environment and produced, leading to more biological richness in sample N2 than N1. However, there were fewer thermophilic bacteria above 50°C, and the diversity of bacteria was the least in N2. The alpha diversity of bacteria had some differences compared to those reported by Zhong et al. (2020). They reported much larger Chao and Shannon indexes. The Chao index of the samples in the thermophilic stage and the Shannon index of the sample in the cooling stage were the smallest. It can be explained by the temperature changes during the composting process. The reported composting by Zhong et al. (2020) was carried out at 28.03°C, much higher than ours. The bacteria in compost substrates were mesophilic, and the effect of high temperature on such bacteria was less than that of psychrotrophic bacteria. Hence, the initial temperature of composting would affect the bacterial performance.

3.2.3 Diversity of the microbial community

A total of 33 phyla and 16 genera were detected in the four samples, shown in Figures 4A,B. The dominant phyla (relative abundance >1%) were four in N1, two in N2, five in N3, and 7 in N4. It can be seen from Figure 4A that Proteobacteria, Actinobacteria, Bacteroidetes, and Firmicutes were the dominant phyla in N1, with relative abundance of 3.82%, 8.79%, 1.96% and 84.6%, respectively. Proteobacteria (2.08%) and Firmicutes (96.2%) still remained dominant in N2. In N3, the dominant phyla included Chloroflexi (3.16%), Proteobacteria (13.36%), Actinobacteria (9.63%), Bacteroidetes (54.32%) and Firmicutes (16.56%). In N4, the relative abundance of Planctomycetes, TM7, and Chloroflexi increased dramatically to 1.51%, 1.23% and 10.22%, respectively. The relative abundance of Proteobacteria, Actinobacteria, and Bacteroidetes was about 21.52%, 28.65% and 28.06%, respectively. The number of dominant phyla decreased with the elevating temperature (N1 to N2), then recovered after a turnover (N3) and increased in the maturing stage (N4) at a lower temperature than the other composting processes. It hinted that composting could be completed successfully with the cooperation of different microorganisms. The microbial community structure and abundance were much different in the initial, thermophilic, cooling, and maturing stages of composting. But only a few microorganisms were desired. For example, Proteobacteria, Actinobacteria, Bacteroidetes, and Firmicutes were often detected to be important in composting environments (Shen et al., 2019; Sánchez et al., 2017; Zhong et al., 2020; Duan et al., 2021). In our study, the absolutely dominant phyla were Firmicutes in N1 and N2, Bacteroidetes in N3, and Actinobacteria in N4, which played a key role in the degradation of the complex organic matrix. However, Chloroflexi and Planctomycetes emerged in N3 and N4 could be explained by their slow growth and act as indicator bacteria (Zhong et al., 2020).

The bacteria at the genus level in the four samples are shown in Figure 4B. The relative abundance of *Cryobacterium*, *Tepidimicrobium*, *Bacillus*, *Arthrobacter*, and *Sporosarcina* in

N1 was 2.05%, 2.53%, 1.17%, 3.81%, and 21.33%, respectively. *Caldicoprobacter* (1.24%) and *Virgibacillus* (27.05%) were dominant in N2. *Pedobacter*, *Ureibacillus*, *Thermobispora*, *Bacillus*, *Chryseobacterium* and *Flavobacterium* in N3 became dominant genera with the relative abundance of 1.81%, 1.57%, 3.05%, 1.56%, 6.35%, and 12.2%, respectively. In N4, *Thermobispora* (2.21%) was still kept dominant, and Steroidobacter (2.29%) appeared to be dominant for the first time. The absolutely dominant genera were *Sporosarcina* in N1, *Virgibacillus* in N2, *Flavobacterium* in N3, and *Steroidobacter* in N4. Compared with the existing studies, the dominant bacteria in our compost samples such as *Cryobacterium*, *Caldicoprobacter*, *Virgibacillus*, and *Sporosarcina* were relatively novel (Lei et al., 2021; Duan et al., 2020; Zhong et al., 2020). The differences could be explained by the initial temperature of the compost substrates and the compost piles. In sample N1, psychrophilic bacteria of *Cryobacterium*, *Sporosarcina*, and *Arthrobacter* and mesophilic bacteria of *Tepidimicrobium* coexisted because of the lower temperature of the initial composting substrates. *Caldicoprobacter* and *Virgibacillus* could endure higher temperatures and had high relative abundances. *Flavobacterium* was often reported during composting of organic wastes containing high lignocellulose (Li et al., 2019). *Steroidobacter* could be an indicator of the completion of composting.

3.3 Relationship between bacterial and compost indexes

According to the Pearson correlation coefficients with probability, about 30% of the phyla were sensitive to the temperature of compost piles. Chloroflexi, Planctomycetes, FBP, Chlorobi, OD1, Synergistetes, and TM6 were significantly negatively correlated with the temperature at the 95% confidence level. The correlation coefficients (p) of Chloroflexi, Planctomycetes, and FBP were −0.95999 (0.04001), −0.98486 (0.01514), and −0.9629 (0.03703), except that Chlorobi, OD1, Synergistetes, and TM6 were all −0.98334 (0.01666). The relative abundant phyla of Proteobacteria, Actinobacteria, Bacteroidetes, and Firmicutes in the compost piles could tolerate a certain high temperature, and their correlation coefficients (p) were −0.85301 (0.14699), −0.89596 (0.10404), −0.25194 (0.74806), and 0.67556 (0.32444), respectively. Nitrospirae was negatively associated with TN during composting, which was significant at the 95% confidence level with correlation coefficients and probability of −0.9283 and 0.03291, respectively. Therefore, the succession of bacteria was mainly affected by temperature. The species and abundance of bacteria were related to their tolerance to temperature. At the genus level, Paenibacillus had a significant negative correlation with pH and OM content

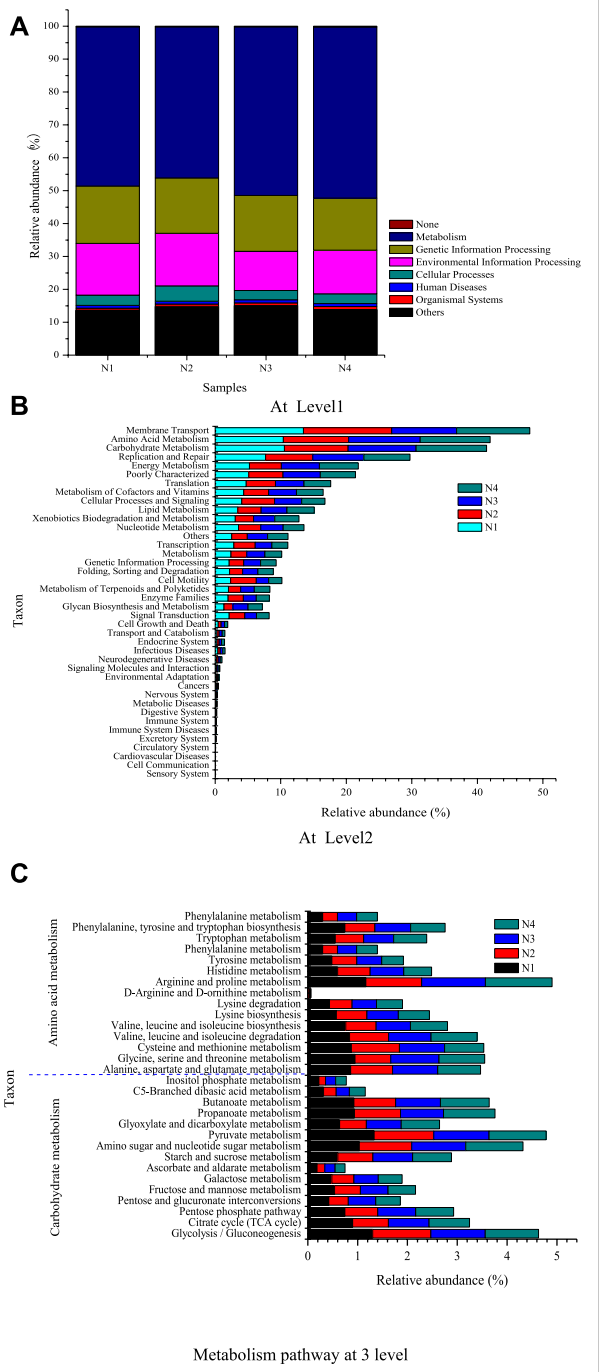

FIGURE 5
Functional prediction. **(A)** At level 1. **(B)** At level 2. **(C)** Metabolism pathway at level 3.

($p < 0.05$). *Arthrobacter* and *Sporosarcina* had significant negative correlations with TN content in the compost ($p < 0.05$), and *Steroidobacter* had a significant negative correlation with T at the 95% level ($p = 0.026$). The results, in turn,

explained the succession of the microorganism during the composting process.

3.4 Functional prediction

The metagenomic function was predicted by the PICRUSt program at three levels, and the results are shown in Figures 5A–C. It can be seen from Figure 5A that 48.42%, 45.95%, 51.25%, and 52.03% of genes related to microbial metabolism were found in N1, N2, N3, and N4, respectively, which were the most relative abundance among the eight metabolic pathways. The microbial functional pathways at level 1 including cellular processes, environmental information processing, and genetic information processing metabolism had been further classified into 40 metabolic pathways shown in Figure 5B. Membrane transport was the most abundant metabolic type in N1, N2, and N4 with a relative abundance of more than 10%. If membrane transport was not considered, the first abundant metabolic pathway was amino acid metabolism, in which arginine and proline metabolism relating to the nitrogen metabolism, CO_2, and organic acid products had an absolute advantage (Kiupakis and Scneider., 1998; Wang et al., 2018). The relative abundance of carbohydrate metabolism closely followed that of amino acid metabolism. The relative abundance of genes involved in pyruvate metabolism and glycolysis/gluconeogenesis was almost similar. Pyruvate metabolism played a pivotal role in the metabolic connection of carbohydrates, amino acids, and lipids. The pyruvate metabolism and glycolysis/gluconeogenesis pathway were responsible for the organic acids such as propanoate and butanoate, which led to the variable pH value (Duan et al., 2020). The relative abundances of genes related to xenobiotic biodegradation and metabolism were 3.06% in N1, 2.80% in N2, 3.23% in N3, and 3.67% in N4. It hinted that biodegradation of exogenous substances mainly occurred in the initial and maturing stages. In the early stage of composting, organic matter was degraded, while humus and other macromolecules were formed in the maturing stage.

According to the Pearson correlation coefficients with probability, *Thermobispora* was significantly positively correlated with glycan biosynthesis and metabolism and metabolism at the 95% confidence level with the correlation coefficients (p) of 0.98572 (0.01428) and 0.97035 (0.02965), respectively. There was a significant positive correlation between the bacterial species of *Steroidobacter* and the metabolism of terpenoids and polyketides with a p-value of 0.045, only a little less than 0.05. Except for these two genera, p-values of *Paenibacillus* between lipid metabolism and nucleotide metabolism were 0.06805 and 0.05205 with the correlation coefficients of 0.93195 and −0.94795, respectively. *p*-values of *Steroidobacter* between xenobiotic biodegradation and metabolism was 0.06396. The Pearson correlation coefficient of *Virgibacillus* and carbohydrate metabolism was −0.94973 with a *p*-value of 0.05027.

4 Discussion

Steroidobacter is a genus of the Clostridium phylum. It can degrade cellulose with endoglucanase, exoglucanase, and xylanase (Zhang et al., 2014). However, *Thermobispora bispora* can produced glucaric acid from the hemicellulose substrate by secreting uronate dehydrogenase which can exhibit more than 58% of the activity after 1 h at the temperature of 60°C and pH 7.0–7.5 (Li et al., 2018). It had good cellulose degradation activity by binding secreting endoglucanase to Ser131, Met263, Gln298, and His310 of cellulose (Paul et al., 2020). Some researchers thought it could play a dominant role in chemical metabolism and mutual nutrition (Perez et al., 2021). *Sporosarcina* can produce urease, closely related to the nitrogen cycle (Alves et al., 2022; Mahdi et al., 2021), while *Virgibacillus* can secrete amylase and protease, which are related to the degradation of protein and starch (Satabdi et al., 2020). It is also related to sulfur metabolism. *Flavobacterium* is a strictly aerobic bacterium and has high degradation activity to cellulose (Vikas et al., 2018: Di Maiuta et al., 2013). It can produce acids by fermenting glucose, fructose, and maltose.

At the initial stage of composting, easily hydrolyzable organic matter, such as protein, urea, and starch was first biodegraded and utilized. Hence Sporosarcina was the dominant strain associated with the utilization of the metabolites from protein. *Cryobacterium* associated with starch hydrolysis and *Tepidimicrobium* associated with the metabolism of hemicellulose, *Caldicoprobacter* utilizing sugars generated from starch and hemicellulose metabolism, and *Arthrobacter* related to the sulfur element from protein metabolism were more abundant Therefore, protein hudrolysis and metabolism mainly occured in this stage. In the high-temperature stage (N2), most of the genera of Actinobacteria, Bacteroidetes, and Proteobacteria were inhibited. But *Virgibacillus* in Firmicutes could adapt to the high temperatures in this stage and then hydrolyze organic compounds such as starch and hemicellulose, as well as utilize the metabolites of the bacterial community. In the N3 stage, the temperature of the compost pile dropped to about 40°C, and most bacteria were thermophilic. Chloroflexi (3.16%), Proteobacteria (13.36%), Actinobacteria (9.63%), and Bacteroidetes (54.32%) returned to the dominant phyla, except that the relative abundance of Firmicutes was still high. *Flavobacterium* in Bacteroidetes became the overwhelming dominant genera, so cellulose degradation and metabolite utilization occurred in this stage. In the maturing stage, *Steroidobacter* of Proteobacteria, a denitrifying bacterium, became a new dominant genus. It

hinted that metabolism associated with denitrification mainly happened in this stage. It was believed that lignin degradation could be ignored below 28°C or above 75°C (Tuomela et al., 2000). So the degradation of lignin may be in high temperature and cooling stages.

Research studies showed that adding bacteria or bacterial flora screened from the composting environment could prolong the high-temperature stage of composting and improve the composting efficiency (Sánchez et al., 2017; Li et al., 2019; Duan et al., 2020). In our study, *Virgibacillus* and *Caldicoprobacter* could be inoculated to improve the composting efficiency at low environmental temperatures. It was practical to identify the composting stages by biological indicators such as *Sporosarcina*, *Virgibacillus*, *Flavobacterium*, and *Steroidobacter* in the initial, thermophilic, cooling, and maturing stages of composting with cow manure and corn stalk at cold ambient temperature, respectively.

5 Conclusion

The properties and bacterial community of the static composting in the cold area at low environmental temperatures with cow manure and corn stalk as substrates were investigated. It was proved that the composting could be carried out successfully in early spring or later autumn after the harvest. The end products can meet the requirements of the relevant national safety and health standards. The succession of microbial communities could be observed in the composting process. The absolutely dominant phylum was Firmicutes in N1 and N2, Bacteroidetes in N3, and Actinobacteria in N4, respectively. And they were playing key roles in the degradation of the complex organic matrix. The absolutely dominant genus was *Sporosarcina* in N1, *Virgibacillus* in N2, *Flavobacterium* in N3, and *Steroidobacter* in N4. The bacterial flora including *Sporosarcina*, *Virgibacillus*, *Flavobacterium*, and *Steroidobacter* could be used to improve the composting efficiency. The biodegradation of exogenous substances mainly occurred in the initial and maturing stages. The functional genes of amino acid metabolism and carbohydrate metabolism were abundant and could reflect the changes of N and organic acids during the composting process.

Data availability statement

The raw data supporting the conclusion of this article will be made available by the authors, without undue reservation.

Author contributions

JL, ZP, FSHI, and FSUN conceived the experiment; SW, QY, DL, LL, and XZ conducted the experiments; PL, CX, and HY analyzed and interpreted the results; FSHI wrote and edited the manuscript. All authors reviewed the manuscript.

Funding

This work was supported by the (Heilongjiang Academy of Agricultural Sciences) under Grant nos. (2020ZSXM008, HNK2019CX15, HNK2019CX16, HNK2019CX17, HNK2019CX18, 2021YYYF001, and 2021YYYF046) and the Heilongjiang provincial popularization and innovation system project of swine and modern agricultural technology.

Conflict of interest

The authors declare that the research was conducted in the absence of any commercial or financial relationships that could be construed as a potential conflict of interest.

Publisher's note

All claims expressed in this article are solely those of the authors and do not necessarily represent those of their affiliated organizations, or those of the publisher, the editors, and the reviewers. Any product that may be evaluated in this article, or claim that may be made by its manufacturer, is not guaranteed or endorsed by the publisher.

References

Abdellah, Y. A. Y., Shi, Z., Sun, S., Luo, Y., Yang, X., Hou, W., et al. (2022). An assessment of composting conditions, humic matters formation and product maturity in response to different additives: A meta-analysis. *J. Clean. Prod.* 366, 132953. doi:10.1016/j.jclepro.2022.132953

Alves, C. M., Oliveira, M. A. C., Roberta, F., Wurdig, R. L. F., and Adão, d. S. F. (2022). Ammonia volatilization and Sporosarcina genus abundance in an Oxisol enriched with urea, compost and biochar. *Appl. Soil Ecol.* 176, 104494. doi:10.1016/J.APSOIL.2022.104494

Chang, R., Yao, Y., Cao, W., Wang, J., Wang, X., and Chen, Q. (2019). Effects of composting and carbon based materials on carbon and nitrogen loss in the arable land utilization of cow manure and corn stalks. *J. Environ. Manag.* 233, 283–290. doi:10.1016/j.jenvman.2018.12.021

Di Maiuta, N., Schwarzentruber, P., Schenker, M., and Schoelkopf, J. (2013). Microbial population dynamics in the faeces of wood-eating loricariid catfishes. *Lett. Appl. Microbiol.* 56 (6), 401–407. doi:10.1111/lam.12061

Ding, J., Wei, D., An, Zh., Zhang, C., Jin, L., Wang, L., et al. (2020). Succession of the bacterial community structure and functional prediction in two composting systems viewed through metatranscriptomics. *Bioresour. Technol.* 313, 123688. doi:10.1016/j.biortech.2020.123688

Duan, B., and Feng, Q. (2021). Comparison of the potential ecological and human health risks of heavy metals from sewage sludge and livestock manure for agricultural use. *Toxics* 9 (7), 145. doi:10.3390/TOXICS9070145

Duan, H., Ji, M., Chen, A., Zhang, B., Shi, J., et al. (2021). Evaluating the impact of rice husk on successions of bacterial and fungal communities during cow manure composting. *Environ. Technol. Innovation* 24, 102084. doi:10.1016/j.eti.2021.102084

Duan, M., Zhang, Y., Zhou, B., Qin, Z., Wu, J., Wang, Q., et al. (2020). Effects of *Bacillus subtilis* on carbon components and microbial functional metabolism during cow manure–straw composting. *Bioresour. Technol.* 303, 122868. doi:10.1016/j.biortech.2020.122868

Erickson, M. C., Liao, J., Ma, L., Jiang, X., and Doyle, M. P. (2009). Inactivation of Salmonella spp. in cow manure composts formulated to different initial C:N ratios. *Bioresour. Technol.* 100 (23), 5898–5903. doi:10.1016/j.biortech.2009.06.083

Heck, K., De Marco, G. É., Hahn, A. B. B., Kluge, M., Spiki, F. R., and Van Der, S. (2013). Temperatura de degradação de resíduos em processo de compostagem e qualidade microbiológica do composto final. *Rev. Bras. Eng. Agric. Ambient.* 17, 54–59. doi:10.1590/S1415-43662013000100008

Khalil, A., Beheary, M., and Salem, E. (2001). Monitoring of microbial populations and their cellulolytic activities during the composting of municipal solid wastes. *World J. Microbiol. Biotechnol.* 17, 155–161. doi:10.1023/a:1016682329925

Kiupakis, A. K., Schneider, B. L., and Reitzer, L. J. (1998). Arginine catabolism and the arginine succinyltransferase pathway in escherichia coli. *J. Bacteriol.* 180 (16), 4278–4286. doi:10.1128/JB.180.16.4278-4286.1998

Lei, L., Gu, J., Wang, X., Song, Z., Wang, J., Yu, J., et al. (2021). Microbial succession and molecular ecological networks response to the addition of superphosphate and phosphogypsum during swine manure composting. *J. Environ. Manag.* 279, 111560. doi:10.1016/j.jenvman.2020.111560

Li, C., Li, H., Yao, T., Su, M., Ran, F., Han, B., et al. (2019). Microbial inoculation influences bacterial community succession and physicochemical characteristics during pig manure composting with corn straw. *Bioresour. Technol.* 289, 121653. doi:10.1016/j.biortech.2019.121653

Li, S., and Xu, X.(2015). Effects of exogenous microbial inoculum on actinobacterial community structure during composting process. *J. Agric. Biotechnol.*, 23 (5) , 652–660.

Li, Y., Xue, Y., Cao, Z., Zhou, T., and Alnadari, F. (2018). Characterization of a uronate dehydrogenase from Thermobispora bispora for production of glucaric acid from hemicellulose substrate. *World J. Microbiol. Biotechnol.* 34 (7), 102–109. doi:10.1007/s11274-018-2486-8

Liu, J., Xu, X., Li, H., and Xu, Y. (2011). Effect of microbiological inocula on chemical and physical properties and microbial community of cow manure compost. *Biomass Bioenergy* 35, 3433–3439. doi:10.1016/j.biombioe.2011.03.042

MARAPRC (2003) MARAPRC. Available at: http://www.moa.gov.cn/xw/bmdt/202003/t20200311_6338635.htm.

Macias-Corral, M. A., Cueto-Wong, J. A., Morán-Martínez, J., and Reynoso-Cuevas, L. (2019). Effect of different initial C/N ratio of cow manure and straw on microbial quality of compost. *Int. J. Recycl. Org. Waste Agric.* 8 (1), S357–S365. doi:10.1007/s40093-019-00308-5

Mahdi, M., Javad, A. M., Sina, G. S., and Abbas, A. M.(2021). Urease production using corn steep liquor as a low-cost nutrient source by Sporosarcina pasteurii: Biocementation and process optimization via artificial intelligence approaches, *Environ. Sci. Pollut. Res.*, 29(10), 13767–13781. doi:10.1007/S11356-021-16568-6

MARAPRC. (2019)MARAPRC. Available at: http://www.moa.gov.cn/gk/tzgg_1/tz/201902/t20190221_6172266.htm.

MARAPRC (2021)MARAPRC(Ministry of agriculture and rural affairs of the people's Republic of China). Available at: http://www.moa.gov.cn/govpublic/SCYJJXXS/202109/t20210917_6376737.htm.

Míriam, C., Laura, B., Joan, Noguerol., Victor, R., and August, B. (2021). Ammonium and phosphate recovery in a three chambered microbial electrolysis cell: Towards Obtaining Struvite from Livestock Manure. *Processes* 9 (11), 1916. doi:10.3390/PR9111916

NBSPRC (National bureau of statistics of the People's Republic of China) (2021). *China statistical yearbook*. Beijing: China Statistics Press.

Onwosi, C. O., Igbokwe, Victor. C., Odimba, J. N., Eke, I. E., Nwankwoala, M. O., Iroh, I. N., et al. (2017). Composting technology in waste stabilization: On the methods, challenges and future prospects. *J. Environ. Manag.* 190, 140–157. doi:10.1016/j.jenvman.2016.12.051

Paul, M., Panda, G., Mohapatra, P. K. D., and Thatoi, H. (2020). Study of structural and molecular interaction for the catalytic activity of cellulases: An insight in cellulose hydrolysis for higher bioethanol yield. *J. Mol. Struct.*,1204, 127547–127547. doi:10.1016/j.molstruc.2019.127547

Perez, B. L. P., Verciano, P. R., Farage, M. L., Silva, M. L. M., Beltrame, S. F., Leister, P. J. S., et al. (2021). Genome-resolved metagenome and metatranscriptome analyses of thermophilic composting reveal key bacterial players and their metabolic interactions.*BMC Genomics*, 22(1), 652–652. doi:10.1186/S12864-021-07957-9

Sánchez, Ó. J., Ospina, D. A., and Montoya, S. (2017). Compost supplementation with nutrients and microorganisms in composting process. *Waste Manag.* 69, 136–153. doi:10.1016/j.wasman.2017.08.012

Satabdi, M., Nadarajan, J. N., and Gurunathan, J. (2020). *Virgibacillus dokdonensis* VITP14 produces α-amylase and protease with a broader operational range but with differential thermodynamic stability. *Biotechnol. Appl. Biochem.*, 69(1), 92–100. doi:10.1002/BAB.2084

Schueler, J., Naas, K., Hurst, J., Aga, Diana., and Lansing, S. (2021). Effects of on-farm dairy manure composting on tetracycline content and nutrient composition. *Antibiotics* 10, 443. doi:10.3390/antibiotics10040443

SCPCR (2021). SCPCR (state council the people's Republic of China). Available at: http://www.gov.cn/xinwen/2021-02/21/content_5588098.htm.

Shen, Q., Sun, H., Yao, X., Wu, Y., Wang, X., and Chen, Y. (2019). A comparative study of pig manure with different waste straws in an ectopic fermentation system with thermophilic bacteria during the aerobic process: Performance and microbial community dynamics. *Bioresour. Technol.* 281, 202–208. doi:10.1016/j.biortech.2019.01.029

Shen, W., Yu, Y., Zhou, R., Song, N., Liu, R., and Bu, Y. (2021). Occurrence, distribution, and potential role of bacteria and human pathogens in livestock manure and digestate: Insights from guangxi, China. *Environ. Eng. Sci.*, 38(10), 990–1000. doi:10.1089/EES.2020.0432

Shi, F., Liu, D., Pei, Z., Yu, H., Zhang, N., Wang, Su., et al. (2021a). Changes of fast test indexes during field composting of maize straw in cold region. *Heilongjiang Agric. Sci.* (01), 26–30.

Shi, F., Yu, H., Zhang, N., Wang, Su., Li, P., Yu, Q., et al. (2021b). Microbial succession of lignocellulose degrading bacteria during composting of corn stalk. *Bioengineered* 12 (2), 12372–12382. doi:10.1080/21655979.2021.2002622

Sun, Z. (2019). *Study on straw maturity returning to field and its effect on black soil fertility*. Harbin: Northeast Agricultural University.

Tuomela, M., Vikmanb, M., Hatakka, A., and Itävaara, M. (2000). Biodegradation of lignin in a compost environment: A review. *Bioresour. Technol.*, 72(2), 169–183. doi:10.1016/s0960-8524(99)00104-2

Vikas, T., Vijay, Kumar., Sanjay, K., and Dharam, S. (2018). Diverse culturable bacterial communities with cellulolytic potential revealed from pristine habitat in Indian trans-Himalaya. *Can. J. Microbiol.*, 64(11): 798–808. doi:10.1139/cjm-2017-0754

Wang, K., Mao, H., Wang, Z., and Tian, Y. (2018). Succession of organics metabolic function of bacterial community in swine manure composting. *J. Hazard. Mater.*, 360: 471–480. doi:10.1016/j.jhazmat.2018.08.032

Wichuk, K. M., and McCartney, D. (2007). A review of the effectiveness of current time–temperature regulations on pathogen inactivation during composting. *J. Environ. Eng. Sci.* 6, 573–586. doi:10.1139/S07-011

Yang, X., Liu, E., Zhu, X., Wang, H., Liu, H., Liu, X., et al. (2019). Impact of composting methods on nitrogen retention and losses during dairy manure composting. *Int. J. Environ. Res. Public Health* 16 (18), 3324. doi:10.3390/ijerph16183324

Zhang, K., Chen, X., Schwarz, W. H., and Li, F. (2014). Synergism of glycoside hydrolase secretomes from two thermophilic bacteria co-cultivated on lignocellulose. *Appl. Environ. Microbiol.*, 80(8), 2592–2601. doi:10.1128/AEM.00295-14

Zhao, H., Li, Jie., Liu, J., Lü, Y., Wang, X., and Cui, Z. (2013). Microbial community dynamics during biogas slurry and cow manure compost. *J. Integr. Agric.* 12 (6), 1087–1097. doi:10.1016/s2095-3119(13)60488-8

Zhong, X., Li, X., Zeng, Y., Wang, S., Sun, Z., and Tang, Y. Q. (2020). Dynamic change of bacterial community during dairy manure composting process revealed by high-throughput sequencing and advanced bioinformatics tools. *Bioresour. Technol.* 306, 123091. doi:10.1016/j.biortech.2020.123091

frontiers | Frontiers in Bioengineering and Biotechnology

TYPE Original Research
PUBLISHED 20 October 2022
DOI 10.3389/fbioe.2022.1023693

OPEN ACCESS

EDITED BY
Junting Pan,
Institute of Agricultural Resources and Regional Planning (CAAS), China

REVIEWED BY
Ake Liu,
Changzhi University, China, China
Xuebo Zheng,
Tobacco Research Institute (CAAS), China

*CORRESPONDENCE
Xiaoe Yang,
xeyang@zju.edu.cn
Kuai Dai,
daikuai520@163.com

SPECIALTY SECTION
This article was submitted to Bioprocess Engineering, a section of the journal Frontiers in Bioengineering and Biotechnology

RECEIVED 20 August 2022
ACCEPTED 27 September 2022
PUBLISHED 20 October 2022

CITATION
Chen D, Wang M, Wang G, Zhou Y, Yang X, Li J, Zhang C and Dai K (2022), Functional organic fertilizers can alleviate tobacco (Nicotiana tabacum L.) continuous cropping obstacle via ameliorating soil physicochemical properties and bacterial community structure.
Front. Bioeng. Biotechnol. 10:1023693.
doi: 10.3389/fbioe.2022.1023693

Functional organic fertilizers can alleviate tobacco (*Nicotiana tabacum* L.) continuous cropping obstacle *via* ameliorating soil physicochemical properties and bacterial community structure

Dan Chen[1], Mei Wang[1], Gang Wang[1], Yujie Zhou[1], Xiaoe Yang[1]*, Jiangzhou Li[2], Cuiping Zhang[2] and Kuai Dai[2]*

[1]Ministry of Education (MOE) Key Laboratory of Environment Remediation and Ecological Health, College of Environmental and Resource Sciences, Zhejiang University, Hangzhou, China, [2]Yuxi Tobacco Company, Ltd. of Yunnan Province, Yuxi, China

Continuous cropping obstacle (CCO) in tobacco is a prevalent and intractable issue and has not yet been effectively solved. Many researchers have favored exploring environmentally friendly and sustainable solutions to CCO (e.g, the application of (bio-) organic fertilizers). Therefore, to study the effects of functional organic fertilizers (FOFs) on tobacco CCO, we applied five types of fertilizers in a tobacco continuous cropping field with red soil (i.e., CF: tobacco-special chemical fertilizers; VOF: vermicompost-based FOF; HOF: humic acid-based FOF; WOF: wood biochar-based FOF; COF: compound FOF). The tobacco plant agronomic traits, leaf yield, economic value, and chemical quality (nicotine, total sugar, K_2O, Cl contents, etc.) were evaluated *via* the continuous flow method. Meanwhile, we determined rhizosphere soil physicochemical properties, phenolic acids content, and bacterial community diversity by high-throughput sequencing. The results show that FOFs improved the tobacco plant agronomic traits, leaf yield (by 2.9–42.8%), value (by 1.2–47.4%), and chemical quality when compared with CF. More content of NH_4^+-N, available P, and available K were discovered in the rhizosphere soil in VOF, HOF, and WOF. The rhizosphere sinapic acid and total phenolic acids content declined in the FOF treatments (1.23–1.56 and 7.95–8.43 mg kg^{-1} dry soil, respectively) *versus* those in the CF treatment (2.01 and 10.10 mg kg^{-1} dry soil, respectively). Moreover, the rhizosphere bacterial community structure changed under FOF functions: the beneficial microbes *Actinobacteria, Firmicutes*, *Streptomyces,* and *Bacillus* increased, and the harmful microbes *Acidobacteria* and *Gemmatimonadota* decreased in abundance. There was a positive correlation between the tobacco leaf yield and soil NH_4^+-N, TC content, and the relative abundance of *Proteobacteria* and *Actinobacteriota*. In summary, the application of VOF and WOF is a modest, practical, and

environmentally friendly strategy to alleviate tobacco CCO from the standpoint of recycling solid waste.

KEYWORDS

functional organic fertilizers, tobacco continuous cropping obstacle, soil physicochemical property, soil bacterial community, sustainable agriculture

1 Introduction

Due to the limitation of arable land, the drive for high benefits, and the lack of rational planting, crop continuous cropping (CC) in the same field is a serious and widespread phenomenon in China, and even throughout the world (Zhang et al., 2013; Yuan et al., 2014). Crop CC is often accompanied by an increase in seedling lesions, death, soil-borne diseases, and a decrease in crop yield and quality. This phenomenon is also called continuous cropping obstacles (CCOs) (Zhang et al., 2013). It is reported that over 20% of agricultural land has been threatened by the negative consequences of CC, which has caused enormous economic losses and hindered sustainable agricultural development (Bonner and Galston, 1944; Bai et al., 2019). The crops prone to CCO include pepper (*Capsicum annuum* L.) (Mao and Jiang, 2021), tomato (*Lycopersicon esculentum* Miller) (Zhao et al., 2020), tobacco (*Nicotiana tabacum* L.) (Chen et al., 2018a; Bai et al., 2019), American ginseng (*Panax quinquefolius* L.) (Liu et al., 2020), peanut (*Arachis hypogaea* L.) (Li et al., 2019), cucumber (*Cucumis sativus* L.) (Zhou and Wu, 2012), apple (*Malus pumila* Mill.) (Yin et al., 2016), and so on. Tobacco is one of the most well-characterized economic crops sensitive to CC. Approximately one-third of the world's tobacco is planted in China, and China is the biggest country producing and consuming tobacco (Zou et al., 2018). Planting tobacco has been the primary income for millions of farmers in China, particularly in poor areas such as Yunnan and Guizhou provinces. However, CCO in tobacco production is also prevalent, which has caused huge economic losses, constrained the implementation of intensive production, and has been listed as one of the important issues and challenges to be addressed in the tobacco industry (Niu et al., 2017; Chen et al., 2018b).

There are three main well-known causes for crop CCO: deterioration of the soil's physicochemical properties, an accumulation of crop allelopathic substances (primarily phenolic acids-PA), and a change of soil microbial community structure, which can be collectively referred to as an imbalance of soil micro-ecology environment (Zhou and Wu, 2012; Yin et al., 2016; Chen W et al., 2018; Bai et al., 2019). Based on this, adjusting the soil's unbalanced micro-ecology environment to its former healthy condition is a basic and crucial concept to alleviate crop CCO. Tobacco needs to absorb large quantities of nutrient elements during the growth period, especially for N, P, and K. Tobacco farmers usually apply tobacco-special compound chemical fertilizers. There is no doubt that chemical fertilizers have the advantage of being relatively cheap and quick acting, and the application of chemical fertilizers in agriculture greatly increases crop productivity and alleviates the international food crisis. However, several environmental problems have occurred alongside the over-application of chemical fertilizers, such as soil acidification, soil hardness, nutrient imbalance, excessive greenhouse gas emissions, and eutrophication of lakes and rivers after N and P losses by runoff, which threatened the sustainable utilization of soil and mineral resources (Diaz and Rosenberg, 2008; Guo et al., 2010; Jiao et al., 2016; Zhang et al., 2016). Therefore, a series of more sustainable and environmentally friendly fertilizers are urgently required to replace chemical fertilizers in a rational way. Organic fertilizers can replace chemical fertilizers, improve soil fertility, increase enzyme activity, adjust soil microbial community structure, and reduce the occurrence of soil-borne diseases, thus alleviating crop CCO and increasing crop yield and quality (Lv et al., 2011; Lazcano et al., 2013; Liu et al., 2018; Li et al., 2019). Based upon these excellent features, organic fertilizers offer a broad prospect for application.

Rapeseed cakes and mushroom residues are two by-products of agricultural activities that are available in large quantities and need to be properly utilized. Due to their high N/P/K contents and other micro-elements, they can be the main raw resources of organic fertilizers. Vermicompost is an organic compost product that is derived from organic matter decomposition and degradation processes by the action of earthworm digestion systems and the action of related microbes (Ndegwa et al., 2000). It has an excellent ability to improve soil structure, crop productivity, and quality, and thus alleviate crop CCO (Liu et al., 2019; Wang et al., 2021). Humic acid belongs to organic matter originating from the complicated decomposition and transformation processes of plant and animal residues by microorganisms (Li et al., 2019). In addition, the addition of humic acid with inorganic fertilizers can improve soil nutrient content, enhance the fertilizers' efficiency, accelerate the metabolism of substances in the soil, change the microbial community structure with the increase of beneficial microorganisms, and the reduction of harmful microbiota, and promote crop yield and quality (Chen et al., 2017; Suman et al., 2017; Ahmad et al., 2018; Li et al., 2019). Biochar is a refractory and highly aromatized carbonaceous solid that is produced from the slow thermal degradation of biological biomass under no oxygen or oxygen-deficient conditions (Lehmann and Joseph, 2009), and has the properties of high pH, carbon content, surface area, and large cation adsorption

ability (Cantrell et al., 2012; Gul et al., 2015; Yao et al., 2017). It has been widely used in environmental remediation and soil amelioration. For example, Yao et al. (2017) reported that 3 years of biochar amendment changed the soil's physicochemical properties and might be beneficial in suppressing the growth of crop diseases. Jaiswal et al. (2018) showed that biochar could enhance cucumber growth and reduce damping-off diseases through enriching soil beneficial microbiomes and increasing bacterial and fungal diversity and activity.

The use of a combination of rapeseed cakes and mushroom residues as the primary resources of N/P/K with soil functional amendments (biochar, humic acid, and/or vermicompost) has not recently been reported or applied in tobacco production. Indeed, how FOFs perform in soil and alleviate crop CCO needs to be further deciphered and validated. Returning quantities of biomass residues to the soil is expected to not only achieve the cycle utilization of biomass but also improve soil condition, crop yield, and quality. The objectives of this study are: 1) to study the effects of FOFs on tobacco CCO (primarily on tobacco yield, economic value, and chemical quality); 2) to explore the possibility of using FOFs to replace tobacco-special chemical fertilizers as base fertilizers; and 3) to elucidate the mechanisms of FOFs' function by paying attention to the changes of rhizosphere soil physicochemical properties, phenolic acids content, and bacterial community structure under field conditions. We assume that FOFs can alleviate tobacco CCO, including the improvement of tobacco yield and chemical quality, by ameliorating the soil's physicochemical properties and bacterial community structure when compared to CF. Knowledge of FOFs' efficacy and action mechanisms will provide great potential for the sustainable plantation of tobacco and other crops, and will help to improve soil quality in an environmentally friendly way.

2 Materials and methods

2.1 Experimental design

The field experiment was conducted from April to September 2020 and was located on Longjie Street, Chengjiang County, Yuxi City, Yunnan Province in China (24°38′39″N, 102°52′33″E). The climate of the study location is as follows: temperature 16–24°C, annual sunshine duration 2, 100–2,300 h; average annual precipitation 837 mm; annual frost-free period 244–365 days; and altitude 1745 m. Tobacco had been continuously cultivated for 2 years in the experimental field before 2020. The tillage regime is the rotation of tobacco and broad bean (*Vicia faba* L.) in the same year. The tobacco variety and soil type are K326 and red soil, respectively. The basic properties of the soil are as follows: pH 7.3, NH_4^+-N 7.3 mg kg^{-1}, NO_3^--N 8.3 mg kg^{-1}, available phosphorous (AP) 37.4 mg kg^{-1}, cation exchange capacity (CEC) 20.2 $cmol^+$ kg^{-1}, organic matter (OM) 26.1 g kg^{-1}, total carbon (TC) 26.6 g kg^{-1}, total nitrogen (TN) 2.1 g kg^{-1}, total phosphorous (TP) 0.9 g kg^{-1}, and total potassium (TK) 7.5 g kg^{-1}. Tobacco growers usually apply tobacco-special compound chemical fertilizers (total nutrient ≥42%, N: P_2O_5: K_2O = 12: 6: 24) as base fertilizers. We used four types of functional organic fertilizers (FOFs) to displace chemical fertilizers. Rapeseed cakes and mushroom residues are the primary components in the four FOFs, which are added with respective functional substances (i.e., vermicompost, humic acid, and/or wood biochar). Therefore, five fertilizer application programs were included in the study, as follows: CF (tobacco-special chemical fertilizers), VOF (vermicompost-based FOF), HOF (humic acid-based FOF), WOF (wood biochar-based FOF), and COF (compound FOF, vermicompost: humic acid: wood biochar-based FOF = 1: 1: 1). KNO_3, K_2SO_4, $(NH_4)_2HPO_4$, and CH_4N_2O were used to balance the N/P/K content in the FOFs compared to CF. There were four repetitions in each treatment as a randomized block design. Each block owned about 66 m^2 and was surrounded by guard rows. The CF and FOFs were applied in the planting hole as base fertilizer in April 2020, before transplanting tobacco seedlings at a rate of 225 and 1,000 kg ha^{-1}, respectively. Tobacco seedlings were planted with 1.20 × 0.55 m and cultivated according to the local optimal production technology. There were a total of five fertilizer applications during the tobacco planting period—one application of base fertilizer and four applications of topdressing.

2.2 Rhizosphere soil and tobacco leaf sampling

In July 2020, we chose four representative tobacco plants of uniform size and dug them up with roots carefully in each block. The non-rhizosphere soil (attached to the root surface loosely) was removed by shaking heavily and the rhizosphere soil (0–5 mm away from the root) of these four tobacco plants was gently collected to form one sample. Immediately, about 50 g of rhizosphere soil per sample was put into an incubator with ice bags, taken back to the laboratory, and put into a −80°C refrigerator for the determination of PA content and bacterial community diversity. The remaining rhizosphere soil was subjected to analysis of the physicochemical properties. Meanwhile, 10 representative tobacco plants in each block were chosen and labeled to determine the agronomic characteristics, including the number of productive leaves, plant height, stem thickness, largest leaf width, and length. The labeled tobacco leaves in each block were separately harvested and flue-cured. After a total of five harvests, we classified the flue-cured tobacco leaves in each block according to the local protocol, weighed each classification, and then calculated economic parameters. The cured leave samples belonging to the C3F classification (i.e., 9th to 14th leaf position, which represents middle leaves) were used to

measure chemical components (i.e., nicotine, total sugar, reducing sugar, total nitrogen, potassium, and chlorine) based on the continuous flow method (SEAL AA3, Germany) (Xiao, 1997).

2.3 Determination of rhizosphere soil physicochemical properties

The rhizosphere soil was air-dried, ground, and sieved to pass through a 2 mm mesh for analyses of soil pH, NO_3^--N, NH_4^+-N, AP, and AK contents and through a 0.15 mm sieve to determine the CEC, OM, total organic matter (TOC), TC, and TN contents. Soil pH was analyzed by a pH parameter (soil: water = 1: 2.5, Multiparameter SevenExcellence, Shanghai, China) (Bao, 2000). Soil NO_3^--N and NH_4^+-N were extracted in potassium chloride solution and determined by an ultraviolet spectrophotometer (UV-1890, Daojin Instrument Co., Ltd., Jiangsu, China; Ministry of Agriculture of the People's Republic of China, GB/T 32737-2016, 2016; Ministry of Environmental Protection of the People's Republic of China, HJ 634-2012, 2012). AP in acid and alkaline soil was extracted in HCl-H_2SO_4 and $NaHCO_3$ solution, respectively, and then determined by an ultraviolet spectrophotometer (UV-1890, Daojin Instrument Co., Ltd., Jiangsu, China) (Bao, 2000). Soil AK was extracted in ammonium acetate solution and evaluated by an atomic absorption spectrometer (AAS, Analytik Jena novAA 300, Germany; Bao, 2000). Soil extraction in hexammine cobalt trichloride solution was used to analyze CEC by a microplate reader (BioTek Epoch2, United States; Ministry of Environmental Protection of the People's Republic of China, HJ 889-2017, 2017). The TOC and OM contents were determined through the potassium dichromate-sulfuric acid method, and the TC and TN contents in the soil were measured by an elemental analyzer (Elemental Vario EL Cube, Germany) (Bao, 2000).

2.4 Determination of phenolic acid content in rhizosphere soil

The method to determine the PA content was drawn from Tan et al. (2008) with little change. Moist rhizosphere soil (15 g) was set overnight with 15 ml of 1 M NaOH and was then shaken at 210 rpm at 25°C for 30 min the next day. The suspension was centrifuged at 8,000 × *g* for 10 min 10 ml of supernate was acidified with 12 M HCl to pH 2.5 and was then put for 2 h for humic acid precipitation. After that, the suspension was centrifuged at 8,000 × *g* for 10 min and the supernate was passed through a 0.22 μm organic filter subjected to UPLC (Agilent 1,290, Agilent Technologies Inc., United States). The UPLC analytical conditions for PA were as follows: chromatographic column, C_{18} (CAPCELL PAK MGII, 4.6 × 250 mm); column temperature, 40°C; detector wavelength, 280 nm; flow velocity, 1 ml min^{-1}; and injection volume, 10 μL. The mobile phase consisted of 0.1% phosphoric acid solution (A-phase) and acetonitrile (B-phase). In total, 17 types of standard PA samples (i.e., gallic acid, phthalic acid, *p*-hydroxybenzoic acid, caffeic acid, vanillic acid, vanillin, benzoic acid, coumalic, salicylic acid, ferulic acid, sinapic acid, benzothiazole, trans-cinnamic acid, diethy phthalate, benzyl benzoate, 4-methylphenyl benzoate, and syringic acid) were measured for the retention time and peak size under a certain concentration. The PA kinds and concentrations in rhizosphere soil were identified by comparing retention time and peak size with respective standards.

2.5 Bacterial community diversity analysis in rhizosphere soil

2.5.1 DNA extraction and PCR amplification

According to the manufacturer's protocol, the microbial community genomic DNA of rhizosphere soil was extracted with the instructions of Fast DNA® Spin Kit for Soil (MP Biomedicals, LLC 29525 Fountain Parkway, Solon, OH, 44139 United States). The purity and concentration of DNA were determined based on the 260/280 and 260/230 nm ratios through a micro-spectrophotometer (Nano-300, Allsheng, Hangzhou, China). DNA integrity was determined by 1.0% agarose gel electrophoresis and visualized. The hypervariable region V3-V4 of the bacterial 16S rRNA gene was amplified using a barcode sequences primer pair 338F (5′-ACTCCTACG GGAGGCAGCAG-3′) and 806R (5′-GGACTACHVGGGTWTCTAAT-3′). The PCR reactions were performed in 20 uL reaction mixtures: 5 × *TransStart* FastPfu buffer 4 μL, 2.5 mM dNTPs 2 μL, 5 uM forward primer 0.8 μL, 5 uM reverse primer 0.8 μL, *TransStart* FastPfu DNA Polymerase 0.4 μL, BSA 0.2 μL, template DNA 10 ng, and finally ddH_2O up to 20 uL. The PCR thermal cycling conditions were performed as the regime: initial denaturation (95°C for 3 min), followed by 27 cycles of denaturation (95°C for 30 s), annealing (55°C for 30 s), extension (72°C for 45 s), and a final extension (72°C for 10 min). Each sample was amplified in triplicate. PCR product was extracted from 2% agarose gels, purified using the AxyPrep DNA Gel Extraction Kit (Axygen Biosciences, Union City, CA, United States) according to manufacturer's instructions, and quantified using Quantus™ Fluorometer (Promega, United States).

2.5.2 Illumina MiSeq sequencing

The purified amplicons were pooled in equimolar and paired-end sequenced on an Illumina MiSeq PE300 platform (Illumina, San Diego, United States) by Majorbio Bio-Pharm Technology Co. Ltd. (Shanghai, China).

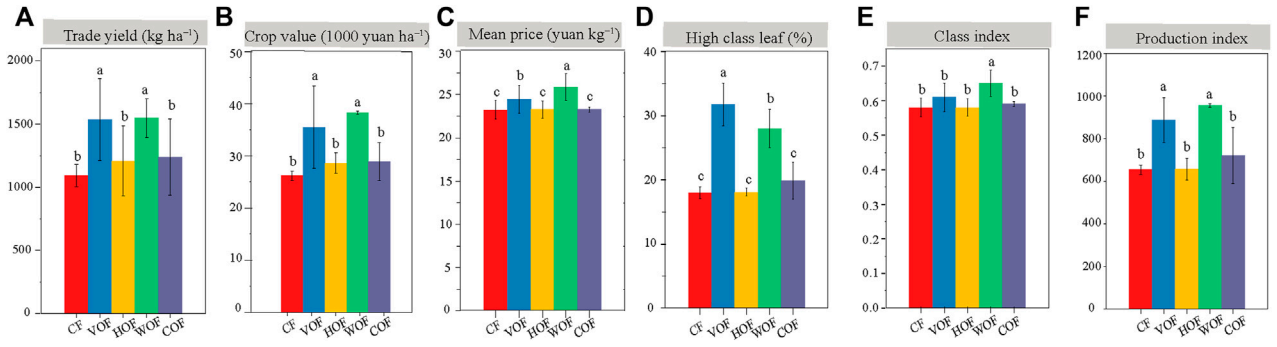

FIGURE 1
Yield **(A)** and economic value **(B–F)** of tobacco leaf. CF, VOF, HOF, WOF, and COF represent the treatments of tobacco-special chemical fertilizer, vermicompost-based, humic acid-based, wood biochar-based, and compound functional organic fertilizers, respectively. Different letters within each index show a significant difference based on the Duncan's method ($p < 0.05$).

2.5.3 Processing of sequencing data

The raw 16S rRNA gene sequencing reads were demultiplexed and quality-filtered by fastp v0.19.6 (Chen et al., 2018a). Pair-end sequences were assembled by FLASH v1.2.11 (Magoč and Salzberg, 2011). Bacterial community operational taxonomic units (OTUs) with a 97% similarity cutoff were clustered by UPARSE v7.0.1090 (Stackebrandt and Goebel, 1994; Edgar, 2013), and chimeric sequences were identified and removed. The taxonomy affiliation of each OTU representative sequence was carried out through RDP Classifier v2.11 (Wang et al., 2007) against the silva138/16S rRNA database (https://www.arb-silva.de/) with a classification confidence of 0.7.

2.5.4 Statistical analysis

Except for the microbial data, the data were analyzed by SPSS 26.0. One-way ANOVA analysis of variance followed by Duncan's test was carried out at the level of significance ($p < 0.05$). OTUs counts were normalized based on the minimum in all samples before bioinformatic analysis. All of the sequences were processed using QIIME v1.9.1 (Caporaso et al., 2010). The alpha-diversity (α-diversity) of the bacterial community was determined, including the ACE, Chao, Shannon, and Simpson indicators using Mothur v1.30.2 (Schloss et al., 2009). Petaline diagrams were constructed to show the number of OTUs exclusive and shared among treatments. For the beta-diversity (β-diversity) of microbial communities, we used permutational multivariate analysis of variance (PERMANOVA) to determine the significance of Bray-Curtis principal coordinate analysis (PCoA). The significance of Bray-Curtis non-metric multidimensional scaling (nMDS) was measured by the Analysis of similarities (ANOSIM) test. We discovered the biomarkers among five treatments using the linear discriminant analysis effect size (LEfSe) tool (Segata et al., 2011). The correlation between the relative abundance of microbial communities and soil environmental factors was analyzed by correlation heatmap and redundancy analysis (RDA). PCoA, nMDS, LEfSe, correlation heatmap, and RDA were performed by R v3.1.1 (Li et al., 2019; Liu et al., 2020). PERMANOVA and ANOSIM tests were achieved by QIIME v1.9.1 (Caporaso et al., 2010).

3 Results

3.1 The tobacco agronomic characteristics, economic, and quality parameters were improved under FOF treatments

The tobacco agronomic characteristics in the four FOFs treatment groups were all better than CF, including plant height, stem girth, maximum leaf area, and the number of productive leaves (Supplementary Figure S1). There was no evident difference in tobacco agronomic traits among four FOFs. The trade yield and value of tobacco leaf in VOF (1,537 kg ha^{-1} and 35,000 yuan ha^{-1}) and WOF (1,547 kg ha^{-1} and 38,000 yuan ha^{-1}) increased apparently ($p < 0.05$) than CF (1,093 kg ha^{-1} and 26,000 yuan ha^{-1}) (Figures 1A,B). However, they did not present a significant difference ($p \geq 0.05$) among HOF (1,083 kg ha^{-1} and 26,000 yuan ha^{-1}), COF (1,114 kg ha^{-1} and 26,000 yuan ha^{-1}), and CF. The tobacco yield and value increased by 40.6% and 35.6% in VOF, and by 41.5% and 46.1% in WOF than those in CF, respectively. Simultaneously, the tobacco leaf mean price, high class leaf rate, class index, and production index in FOFs were all higher than those in CF, with VOF and WOF presenting extraordinary enhancements (Figures 1C–F). The tobacco's chemical quality indicators are shown in Table 1 and almost all met the high-quality tobacco standard according to local protocols. The nicotine, TN, and Cl content

TABLE 1 Tobacco leaf quality parameters (mean ± SD). CF, VOF, HOF, WOF, and COF represent the treatments of tobacco-special chemical fertilizer, vermicompost-based, humic acid-based, wood biochar-based, and compound functional organic fertilizers, respectively. Different letters show a significant difference within each column based on Duncan's method ($p < 0.05$).

	Nicotine (%)	Total sugar (%)	Reducing sugar (%)	Total nitrogen (%)	K_2O (%)	Cl (%)	Total sugar/ nicotine	Reducing sugar/ nicotine	Total nitrogen/ nicotine	K_2O/Cl
CF	2.48 ± 0.16 a	25.8 ± 2.5 b	20.1 ± 1.5 c	1.88 ± 0.08 a	2.07 ± 0.00 b	0.70 ± 0.14 a	10.5 ± 1.6 b	7.6 ± 0.2 b	0.76 ± 0.05 a	2.93 ± 0.05 c
VOF	2.31 ± 0.19 b	31.8 ± 3.1 a	25.0 ± 2.6 a	1.70 ± 0.09 b	2.14 ± 0.11 ab	0.47 ± 0.08 b	13.8 ± 2.1 a	10.9 ± 1.7 a	0.74 ± 0.09 a	4.51 ± 0.17 a
HOF	2.42 ± 0.10 ab	29.5 ± 2.9 ab	23.5 ± 2.9 ab	1.82 ± 0.32 ab	2.17 ± 0.29 ab	0.67 ± 0.04 a	12.3 ± 0.7 ab	9.8 ± 0.8 ab	0.69 ± 0.10 a	3.23 ± 0.71 b
WOF	2.41 ± 0.04 ab	28.9 ± 3.3ab	23.4 ± 3.2 ab	1.76 ± 0.14 ab	2.27 ± 0.05 a	0.69 ± 0.12 a	12.0 ± 1.4 ab	9.7 ± 1.4 ab	0.73 ± 0.05 a	3.29 ± 0.63 b
COF	2.33 ± 0.13 b	28.9 ± 2.0 ab	21.7 ± 2.0 bc	1.71 ± 0.14 b	2.17 ± 0.18 ab	0.64 ± 0.18 a	12.7 ± 1.0 ab	9.8 ± 0.9 ab	0.71 ± 0.03 a	3.39 ± 0.39 b

TABLE 2 Soil physicochemical properties when sampling tobacco (mean ± SD). CF, VOF, HOF, WOF, and COF represent the treatments of tobacco-special chemical fertilizer, vermicompost-based, humic acid-based, wood biochar-based, and compound functional organic fertilizers, respectively. Different letters within each column show a significant difference in soil physicochemical properties based on Duncan's method ($p < 0.05$).

	pH	NO_3^--N (mg kg^{-1})	NH_4^+-N (mg kg^{-1})	Available P (mg kg^{-1})	Available K (mg kg^{-1})	CEC ($cmol^+$ kg^{-1})	OM (g kg^{-1})	TOC (g kg^{-1})	TC (%)	TN (%)
CF	6.73 ± 0.09 b	4.37 ± 1.71 a	3.04 ± 0.02 b	53.2 ± 13.0 c	342.7 ± 18.3 b	19.6 ± 1.5 ab	32.9 ± 4.1 a	19.1 ± 2.4 a	3.18 ± 0.47 ab	0.22 ± 0.02 a
VOF	6.80 ± 0.19 b	4.46 ± 0.10 a	4.82 ± 1.02 ab	94.4 ± 17.0 a	410.9 ± 42.5 a	20.2 ± 0.8 ab	34.9 ± 4.7 a	20.2 ± 2.7 a	3.23 ± 0.40 ab	0.23 ± 0.01 a
HOF	6.74 ± 0.15 b	4.19 ± 1.28 a	5.32 ± 1.04 a	96.3 ± 12.3 a	373.9 ± 2.0 ab	20.1 ± 0.9 ab	36.3 ± 4.6 a	21.0 ± 2.7 a	3.34 ± 0.39 a	0.23 ± 0.02 a
WOF	6.94 ± 0.18 a	4.10 ± 1.01 a	3.32 ± 1.06 b	84.1 ± 28.3 ab	369.3 ± 27.2 ab	20.8 ± 0.8 b	34.9 ± 6.6 a	20.3 ± 3.8 a	3.07 ± 0.13 ab	0.22 ± 0.01 a
COF	6.75 ± 0.04 b	3.37 ± 0.89 a	2.97 ± 0.23 b	70.0 ± 6.6 bc	332.6 ± 35.7 b	17.8 ± 2.6 a	30.5 ± 4.0 a	17.7 ± 2.3 a	2.95 ± 0.37 b	0.22 ± 0.02 a

decreased, and the total sugar, reducing sugar, and K_2O content increased in FOFs when compared with CF. Overall, the tobacco quality was improved under FOFs, with higher values of total sugar/nicotine, K_2O/Cl, reducing sugar/nicotine, and a lower value of Cl/nicotine than CF.

3.2 Rhizosphere soil physicochemical properties were ameliorated and phenolic acid content decreased in FOF treatments

Rhizosphere Soil pH showed an acidification trend after planting tobacco, which changed from 7.34 to 6.73–6.94 (Table 2). This acidification trend was mitigated under the functions of VOF and WOF. The soil's NO_3^--N and TN content did not show any obvious variance under the five treatments ($p \geq 0.05$). Although the OM, TOC, and TC contents increased in VOF and HOF, they did not present a significant difference ($p \geq 0.05$). Meanwhile, the FOFs had a greater effect on the NH_4^+-N, AP, AK contents, and CEC, particularly on the AP content. The NH_4^+-N, AK contents, and CEC showed an increasing trend under FOFs, except for COF, when compared with CF. The AP content increased by 31.6–81.0% in the four FOFs treatments when compared to CF.

Although we prepared 17 varieties of the PA's standard reference samples, only seven types (*p*-hydroxybenzoic acid, phthalic acid, vanillic acid, syringic acid, vanillin, ferulic acid, and sinapic acid) could be detected in the rhizosphere soil (Figure 2). The *p*-hydroxybenzoic acid average content was the highest (1.52–1.64 mg kg^{-1} dry soil), followed by the sinapic acid (1.23–2.01 mg kg^{-1} dry soil), vanillin (1.28–1.38 mg kg^{-1} dry soil), ferulic acid (1.11–1.42 mg kg^{-1}

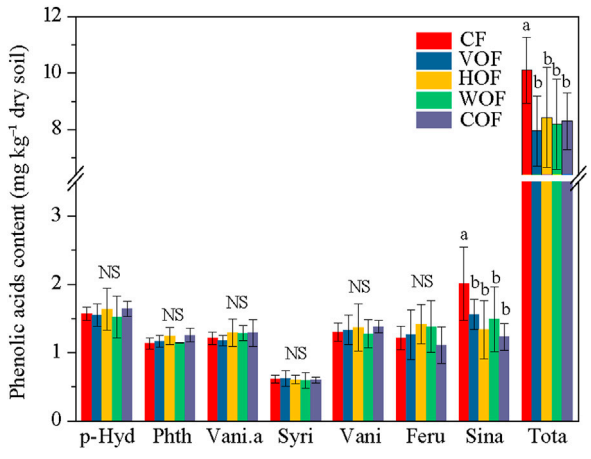

FIGURE 2
Phenolic acid content in the rhizosphere soil. CF, VOF, HOF, WOF, and COF represent treatments of tobacco-special chemical fertilizer, vermicompost-based, humic acid-based, wood biochar-based, and compound functional organic fertilizers, respectively. P-Hyd, Phth, Vani.a, Syri, Vani, Feru, Sina, and Tota represent *p*-hydroxybenzoic acid, phthalic acid, vanillic acid, syringic acid, vanillin, ferulic acid, sinapic acid, and total phenolic acids, respectively. Different letters show a significant difference among the five treatments based on the Duncan's method ($p < 0.05$), and NS indicates no significant difference ($p \geq 0.05$).

dry soil), vanillic acid (1.18–1.29 mg kg^{-1} dry soil), and phthalic acid contents (1.14–1.26 mg kg^{-1} dry soil). The syringic acid content was the lowest (0.60–0.62 mg kg^{-1} dry soil). The total PA content ranged from 7.95 to 10.10 mg kg^{-1} dry soil in all treatments. Although the sinapic acid and total PA contents decreased apparently under FOFs when compared to CF ($p < 0.05$), they did not show an obvious variance among the four FOF treatments. There was no significant difference ($p \geq 0.05$) for the other PAs among the five treatments.

3.3 Bacterial community diversities in rhizosphere soil were changed under the different treatments

A total of 2,092,458 sequences with an average length of 414 bp were produced after quality-controlled matching. The Coverage index of all samples was >97.2% and the rarefaction curve tended to reach the saturation point, which indicates that the sequencing depth was able to reflect the microbial community in our study (Supplementary Figure S2). We gained 6,876 OTUs in all samples. There were 3,474 bacterial OTUs shared among the five treatments, and 128, 170, 143, 141, and 140 OTUs were unique in CF, VOF, HOF, WOF, and COF treatments, respectively (Figure 3A). There were more OTUs numbers in VOF, HOF, and WOF when compared to CF, with WOF having the most OTUs with 5,363 (Figure 3C). However, T4 had the least OTUs with 4,952. Meanwhile, there were 780 genera shared by five treatments, and 9, 34, 16, 23, and 16 genera were unique for CF, VOF, HOF, WOF, and COF, respectively (Figure 3B). The genus types increased to 958–996 in four FOFs compared to 925 in CF (Figure 3D). The first five highest relative abundance of bacteria at the phylum level were *Actinobacteria* (40.2–43.8% in all samples), *Chloroflexi* (20.6–25.0%), *Proteobacteria* (13.5–16.4%), *Acidobacteria* (1.8–7.7%), and *Firmicutes* (3.0–9.1%), with an average total relative abundance of 90.0% (Figure 4A). The relative abundance of *Actinobacteria* and *Firmicutes* increased, and *Acidobacteria* and *Gemmatimonadota* declined in the four FOF treatments when compared to CF. The first five highest relative abundance of bacteria at the genus level were *Intrasporangium* (4.3–5.9% in all samples), *Arthrobacter* (4.1–5.7%), *norank_f__Roseiflexaceae* (3.7–5.5%), *norank_f__JG30-KF-CM45* (3.6–5.6%), and *Gaiella* (3.4–4.5%), with the average total relative abundance of 22.5% (Figure 4B). The distribution pattern of the bacterial community at the genus

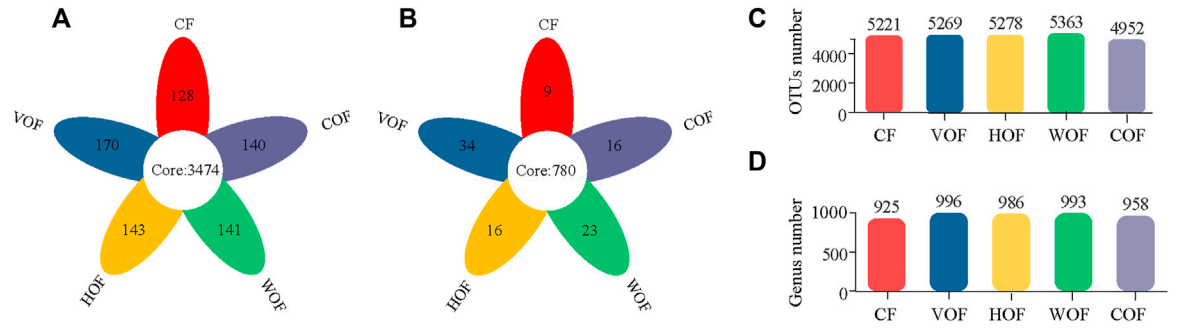

FIGURE 3
Shared, unique, and total numbers of bacterial OTUs **(A,C)** and genera **(B,D)** in the rhizosphere soil among the five treatments. CF, VOF, HOF, WOF, and COF represent the treatments of tobacco-special chemical fertilizer, vermicompost-based, humic acid-based, wood biochar-based, and compound functional organic fertilizers, respectively.

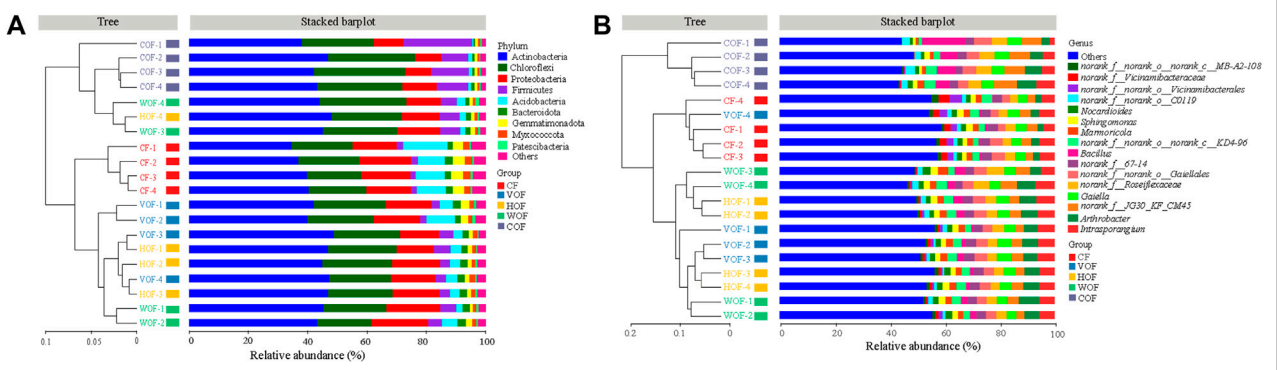

FIGURE 4
Hierarchical clustering tree of samples in bacterial community at the phylum **(A)** and genus **(B)** level in the rhizosphere soil. The horizontal histogram shows the species composition in top nine phylum **(A)** and top 16 genus **(B)** in different treatments. CF, VOF, HOF, WOF, and COF represent the treatments of tobacco-special chemical fertilizer, vermicompost-based, humic acid-based, wood biochar-based, and compound functional organic fertilizers, respectively.

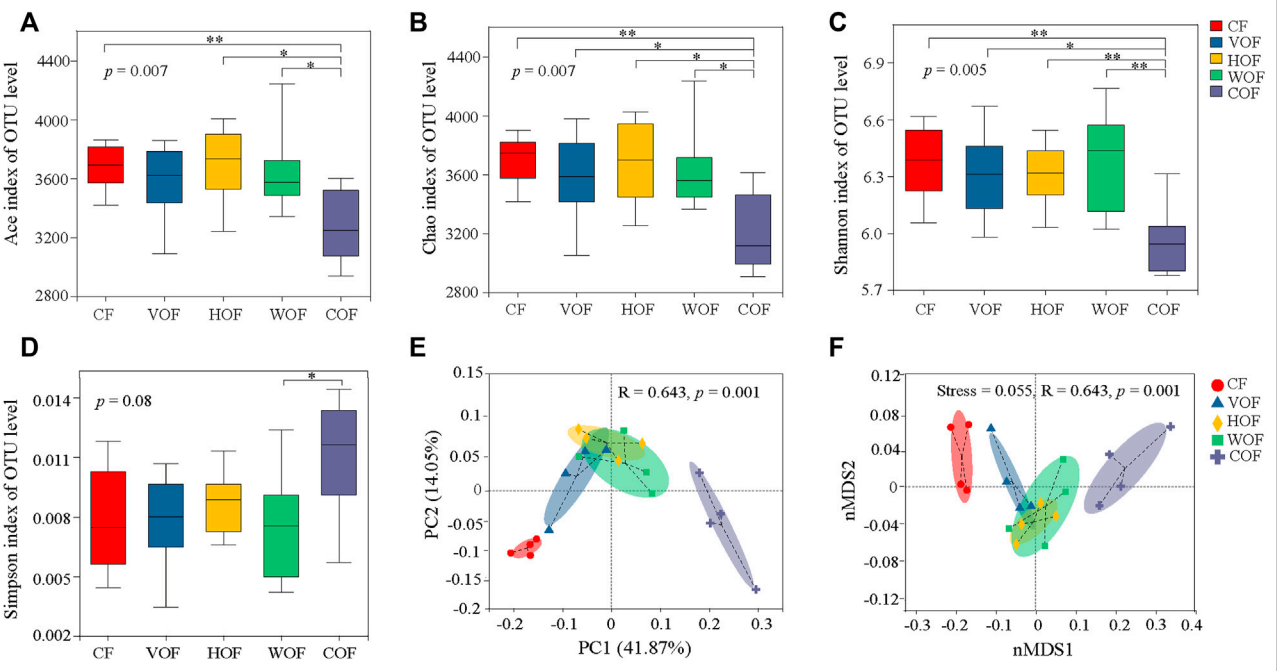

FIGURE 5
Effect of different fertilizers on bacterial community structure in the rhizosphere soil. Ace index **(A)**, Chao index **(B)**, Shannon index **(C)**, and Simpson index **(D)** of bacteria. * and ** indicate statistical significance at $p < 0.05$ and $p < 0.01$ based on the Wilcoxon rank-sum test, respectively. Principal coordinate analysis (PCoA) **(E)** and non-metric multidimensional scaling (nMDS) **(F)** of bacterial community on OTUs level based on Bray-Curtis distance. CF, VOF, HOF, WOF, and COF represent the treatments of tobacco-special chemical fertilizer, vermicompost-based, humic acid-based, wood biochar-based, and compound functional organic fertilizers, respectively.

level in COF differentiated from the other four treatments, with an apparent increase of *bacillus* in COF.

For the α-diversity of the bacterial community on the OTUs level, COF had the minimum of the Ace, Chao, and Shannon indexes, and the maximum of the Simpson index. This indicates that the α-diversity in COF was the lowest in all treatments (Figures 5A–D). Moreover, the α-diversity indexes in COF were significantly ($p < 0.05$) different from the other four treatments,

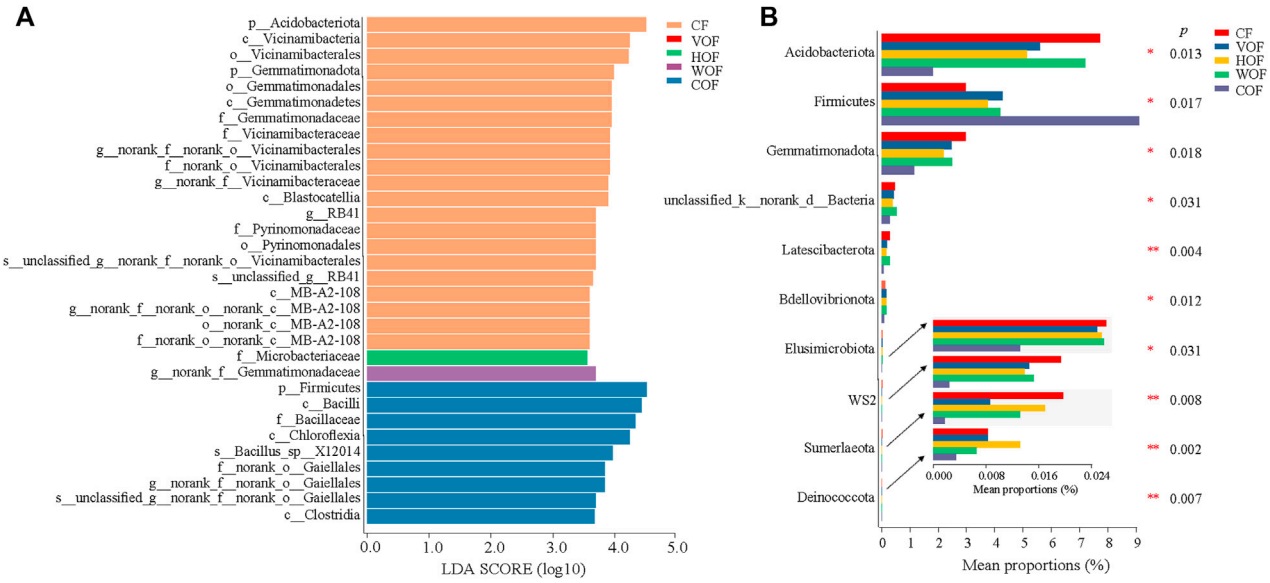

FIGURE 6
LEfSe **(A)** and comparative analyses **(B)** of bacterial community at the phylum level in the rhizosphere soil based on the Kruskal–Wallis H test. CF, VOF, HOF, WOF, and COF represent the treatments of tobacco-special chemical fertilizer, vermicompost-based, humic acid-based, wood biochar-based, and compound functional organic fertilizers, respectively. Only the top 10 bacteria that showed a significant difference ($p < 0.05$) among the five treatments are shown.

and there was no significant difference ($p \geq 0.05$) among CF, VOF, HOF, and WOF. Based on PCoA and PerMANOVA analyses on the OTUs level, the five treatments were divided from each other, particularly at the first primary component, with the first two primary components explaining 41.87% and 14.05% variance, respectively (R = 0.643, $p = 0.001$) (Figure 5E). This phenomenon was also revealed from Bray-Curtis nMDS and ANOSIM analyses (Figure 5F), which showed remarkable variations in the β-diversity of bacterial community among the five treatments (stress = 0.055, R = 0.643, $p = 0.001$). CF was prominently distinct from COF, and VOF, HOF, and WOF clustered relatively closer, presenting a more pronounced difference in the bacterial community's β-diversity between CF and COF than that among VOF, HOF, and WOF.

Based on the LEfSe analysis, every group except VOF extinguished some biomarkers contributing to group differences, and CF and COF had more varieties of biomarkers (Figure 6A; Supplementary Figure S3). This shows that the most important biomarkers per group were phylum-*Acidobacteriota* in CF, family-*Microbacteriaceae* in HOF, genus-*norank_f__Gemmatimonadaceae* in WOF, and phylum-*Firmicutes* in COF. From the significance analysis for the bacterial community at the phylum level among groups based on the Kruskal–Wallis H test, there was a significant increase in the relative abundance of *Firmicutes*, and a significant decrease of *Acidobacteriota*, *Gemmatimonadota, Elusimicrobiota, WS2* and *Sumerlaeota* in the four FOF treatments compared to CF, particularly in COF (Figure 6B). The relative abundance of *unclassified_k__norank_d__Bacteria, Latescibacterota, Bdellovibrionota*, and *Deinococcota* declined remarkably in COF when compared to the other four treatments. Meanwhile, the relative abundance of some bacterial genus-*Streptomyces, Bacillus*, *Arthrobacter,* and *Paenibacillus* increased in the four FOF treatments, without a significant difference among the five treatments (Supplementary Figure S4).

From the correlation heatmap between the bacterial community at the genus level and rhizosphere soil environmental factors, soil TC and TN were the most important factors that influence the bacterial composition, which showed an intimately similar relationship ($p < 0.05$) with more genera (Figure 7A). The relationship pattern between soil bacteria composition and TC, TN, C/N, and CEC clustered together, which is the opposite of that between soil bacteria and AP, AK. The first two predominant components explained 58.17% and 22.46% (80.63% in total) of the total variance based on the RDA analysis, respectively (Figure 7B). The four samples in the same group clustered together, and different groups separated primarily at the first primary component. Soil TC, TN, CEC, pH, NH_4^+-N, AP, and AK were the most crucial environmental factors to influence the bacterial composition. Soil TC and TN had a positive effect, while AK and AP had a negative influence on the bacterial community in CF, which was the opposite in COF. Simultaneously, there was a positive relationship between soil NH_4^+-N content and the

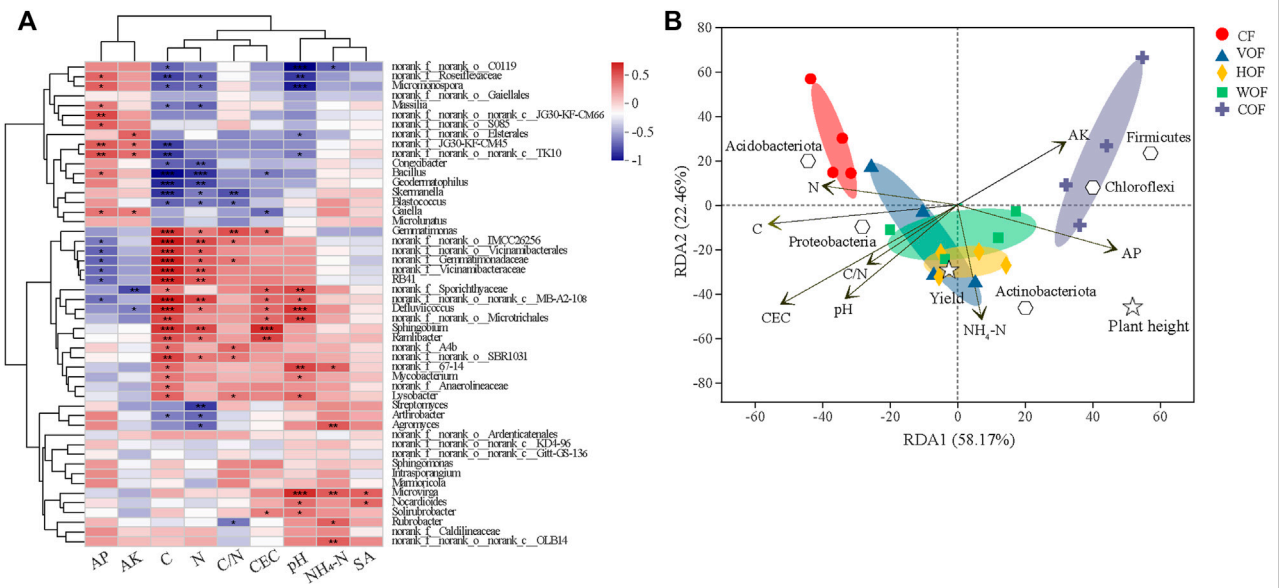

FIGURE 7
Spearman correlation heatmap between bacterial genera and soil environmental factors **(A)** and RDA of the relationship among bacterial phylum, samples, environmental variables, tobacco height, and leaf yield **(B)**. *, **, and *** indicate statistical significance at $p < 0.05$, $p < 0.01$, and $p < 0.001$, respectively. AP, AK, and SA represent the soil available P, available K, and sinapic acid contents. CF, VOF, HOF, WOF, and COF represent the treatments of tobacco-special chemical fertilizer, vermicompost-based, humic acid-based, wood biochar-based, and compound functional organic fertilizers, respectively.

bacterial community in HOF and WOF. Tobacco plant height was positively correlated with soil NH_4^+-N, AK, AP content, and the relative abundance of *Actinobacreriota*, *Chloroflexi*, and *Firmicutes*. The tobacco leaf yield, soil NH_4^+-N, TC content, and the relative abundance of *Proteobacteria* and *Actinobacteriota* were all promoted.

4 Discussion

4.1 Effects of different fertilizers on tobacco agronomic traits, leaf yield, value, and chemical quality

The tobacco agronomic traits, tobacco leaf trade yield, value, and chemical quality were improved in FOF treatments when compared to CF. The tobacco plant agronomic traits showed no apparent difference in the four FOF treatments. This indicates that FOFs could promote tobacco plant growth and that this promotion level was similar under different types of FOFs in our study. There was an evident increase in tobacco leaf trade yield and value in VOF and WOF, while no significant difference was observed among CF, HOF, and COF. Vermicompost-based and wood biochar-based FOFs promoted the enrichment of tobacco leaf biomass and the formation of high-quality tobacco leaf. However, humic acid-based and compound FOFs did not present such a phenomenon. Vermicompost performs well with high porosity, aeration, and water-holding capacities, and has abundant nutrient elements, plant growth-promoting substances, and beneficial antagonistic microbiomes, which is typical of organic fertilizers and soil conditioners (Edwards and Neuhauser, 1988; Wang et al., 2021). It can alleviate crop CCO, and improve crop yield and quality by enhancing soil physicochemical properties and microbial community structure under field conditions (Liu et al., 2019; Wang et al., 2021). Biochar is well-known to be an excellent soil ameliorant that can alleviate soil acidification; increase soil TC and nutrient contents; improve soil structure, nutrient-holding, water-holding capacities, and enzyme activities; and change the structure of the soil's microbial community (Lehmann et al., 2011). Biochar can promote the abundance and activities of beneficial microbes by providing a good habitat for them (Palansooriya et al., 2019). It has also been verified that vermicompost and biochar can improve soil properties, and can improve the yield and quality of continuous cropping cucumber for different years (Wang et al., 2021). These two FOFs can provide tobacco plants with effective nutrients and a more suitable soil micro-ecology condition, which then contribute to the growth of tobacco. Although the positive effect of humic acid fertilizer on peanut yield has been verified based on a 3-year experiment (Li et al., 2019), it was not suitable to apply to continuous cropping tobacco in the recent study. The reason for this is that humic

acid accelerates soil acidification, which is an important factor causing K326 CCO (Bai et al., 2019). Meanwhile, soil acidification in red soil is prevalent and relentless owing to the soil erosion processes, the acid atmospheric deposition, and the abuse application of chemical fertilizers. Therefore, strong acid HOF is not advisable to apply in red soil planting K326 on the basis of our results. Intriguingly, the compound FOF did not present a promotion influence on tobacco leaf yield, which could be due to an antagonistic effect among the components or to the strong influence of humic acid. Which components show an antagonistic effect and how they cooperate were not clear in the compound FOF in this study, and this needs to be further researched.

The chemical quality of tobacco leaf (total sugar/nicotine, reducing sugar/nicotine, Cl/nicotine, K_2O/Cl) was improved in the four FOF treatments. Similarly, no apparent difference in tobacco leaf quality was discovered among the four FOF treatments. The enhancement of organic fertilizers on plant yield and quality has been demonstrated in many studies (Liu et al., 2018; Yan and Liu, 2020; Chen D et al., 2022; Imran et al., 2022). Organic additives can suppress tomato disease and improve the yield compared to chemical fertilizers (Liu et al., 2018). Furthermore, Yan and Liu (2020) verified that high-carbon fertilizers could increase tobacco quality mainly by improving the soil carbon pool. The soil TOC, OM, NH_4^+-N, AP, and AK contents increased in VOF, HOF, and WOF, which could provide tobacco with more nutrients, enhance soil ventilation and aggregation environment, and thus stimulate tobacco growth. Particularly, the soil AP content showed a marked increase in all four FOF treatments. The scarcity of P element in red soil is a prevalent issue in Southern China, and it has been reported that peanut yield could be promoted as soil P status increased (Chen et al., 2018b). The application of FOFs provides an underlying effective strategy in alleviating P scarcity in broad red soil. Organic fertilizers can improve the soil OM, NH_4^+-N, AP, and AK contents when compared to chemical fertilizers, which has been verified in other studies (Liu et al., 2018; Li et al., 2019; Wang et al., 2021). Additionally, low pH can promote the occurrence of the pathogenic bacteria *Ralstonia solanacearum*, which attacks tobacco roots (Li et al., 2017). There was a possibility that FOFs inhibited the growth and colonization of underlying pathogens by improving soil pH.

4.2 Effects of different fertilizers on phenolic acid content in the rhizosphere soil

Different plants release their unique varieties of PA. Meanwhile, *P*-hydroxybenzoic acid, phthalic acid, vanillic acid, syringic acid, vanillin, ferulic acid, and sinapic acid were the main types of PA in the rhizosphere soil of K326, which was almost in accordance with the results of Chen L. M et al. (2022). The sinapic acid and total PA contents in rhizosphere soil decreased apparently ($p < 0.05$) in the four FOF treatments, and no significant difference ($p \geq 0.05$) was observed for the other PAs, which are a class of small organic substances and secondary metabolites that are released from plants and have strong allelopathy (Hiraddate et al., 2005). PAs can be enriched after continuous cropping of the same plants in the soil through plant evaporation, leaching, root secretion, and the degradation of litter and residues over the years (Weir et al., 2004). After accumulation to a specific concentration, PAs play a crucial negative role in seed germination, plant antioxidant system, cell structure, and the respiration and growth of plant roots, and can ultimately destroy the plant's normal growth (Wu and Ma, 2006). Meanwhile, there is an intimate correlation between PA and microbiota in soil. As a result, the allelopathy of PA is considered to be one of the main causes of tobacco CCO (Chen et al., 2018a; Bai et al., 2019). This allelopathy function was weakened under the function of FOFs, which may have contributed to the improvement of tobacco yield and quality in the recent study. Moreover, there was a positive relationship between the content of sinapic acid, and the relative abundance of *Microvirga* and *Nocardioides* ($p \leq 0.05$) in the rhizosphere soil based on the Spearman correlation analysis. Therefore, PA has changed the bacterial structure and diversity to some extent.

4.3 Effects of different fertilizers on the bacterial community structure and diversity in the rhizosphere soil

Our results show that the bacterial structure and diversity in rhizosphere soil were changed under the function of the FOFs. Different fertilizer management programs can significantly change the soil's microbial community, biomass, and diversity, and functional activities can be enhanced under balanced fertilization (Liu et al., 2018; Li et al., 2019; Liu et al., 2020). There were 3,474 OTUs and 780 genera shared among the five treatments from the petaline diagrams, which indicates that the major bacterial species co-existed in different treatments. There were more OTUs in the FOF treatments, except for COF, and more genera in all four FOFs treatments compared to CF. This shows that FOFs improved the rhizospheric bacterial richness. These results are similar to previous studies where there were more bacterial populations in organic-treated soils than in chemical fertilizers treatment (Witter et al., 1993). Wang et al. (2021) also found that biochar and vermicompost could increase soil bacterial numbers. From the α-diversity analysis of bacteria at the OTU level, no significant difference for Ace, Chao, Shannon, and Simpson indexes was observed in CF, VOF, HOF, and WOF. However, these four indexes in COF were obviously distinct from the other four treatments. COF obviously declined bacterial α-diversity. This may be related to an antagonism reaction among the components in COF. From the β-diversity analysis of bacteria

at the OTU level based on PCoA and nMDS, the samples in the same fertilization management program were grouped more closely, while those in distinct programs were well separated from each other along with the first component, especially for CF and COF. This indicates that FOFs changed the bacterial community structure compared with CF, with a more apparent change in COF. Other studies have reported that an application of organic additives apparently shifted the soil's microbial community (Bonanomi et al., 2010; Liu et al., 2018), which is in accordance with our results. The bacterial community structure did not distinctly vary from each other in VOF, HOF, and WOF. This happened because these three types of FOFs shared some of the same components. Meanwhile, the time interval between the application of FOFs and sampling maybe did not reach the point where it could cause a significant variance.

Actinobacteria, *Chloroflexi*, *Proteobacteria*, *Acidobacteria*, *Firmicutes*, and *Gemmatimonadota* were the most abundant bacterial phyla in the rhizosphere soil in our study, which is generally consistent with previous studies (Li et al., 2019; Liu et al., 2020). *Actinobacteria* and *Firmicutes* showed an increasing trend, while *Acidobacteria* and *Gemmatimonadota* showed a declining trend in the relative abundance in four of the FOF treatments. Wu et al. (2014) reported that *Actinobacteria* was negatively associated with tobacco bacterial wilt disease rate (r = −0.728) and was found in more abundance in organic fertilizer treatment. Li et al. (2019) also found that the abundance of *Firmicutes* increased in peanut-planting soil with the application of humic acid fertilizer, which has been reported as one type of plant-growth beneficial bacteria. From the LEfSe analysis, every group owned their biomarkers except VOF. CF and COF owned more biomarkers than other groups, which further verified a significant difference in bacterial community diversity among CF, COF, and the other three groups. Based on the significance analysis for the bacterial community at the phylum and genus level, some beneficial bacteria (e.g., Firmicutes, *Streptomyces*, *Bacillus*, *Arthrobacter*, and *Paenibacillus*) increased in the four FOF treatments, which was in line with the results of Wu et al. (2014). *Streptomyces* can control tomato diseases by producing antibiotics (Elabyad et al., 1993). Firmicutes, *Bacillus*, and *Paenibacillus* take part both in suppressing plant pathogens and promoting plant growth (Aliye et al., 2008; Algam et al., 2010). Therefore, FOFs supported the disease-suppressing and plant growth-promoting bacteria in the rhizosphere soil, which contributed to tobacco growth.

4.4 The relationships between soil bacterial community and environmental factors under different treatments

From the Spearman correlation analysis and RDA between the bacterial community and soil environmental factors, soil TC, TN, CEC, pH, and AP were the most important factors influencing bacterial composition. Simultaneously, the correlation pattern between soil TC and microbiomes was similar to that between soil TN and microbiomes. Soil C, N, and P provide soil microbiomes with principal nutrients and energy sources, which are the common environmental factors that are related to microbial composition (Liu et al., 2018; Liu et al., 2020; Zhao et al., 2020). The demand competition, acquisition, and utilization of C and N are synchronous in microorganisms, resulting in a similar relationship pattern between soil C, N, and microbiomes. There was an apparent improvement in soil AP content, which caused the change of microbiomes to some degree. It is well-known that soil pH is a crucial factor that influences microbial composition and diversity in soil physicochemical properties (Chen et al., 2018b; Bai et al., 2019; Shen et al., 2022). Specifically, soil pH takes a role in bacterial diversity by changing their osmotic pressure and surface potential directly, and indirectly the bioavailability of nutrients and the habitation conditions (Chen W et al., 2018; Bai et al., 2019). Some bacterial genera related to nutrient transition and uptake were enriched in FOF treatments (e.g., genera *Streptomyces* and *Bacillus*). It is reported that *Streptomyces* can stimulate plant growth by fixing atmospheric N into soil NH_4^+ and *Bacillus* can improve the soil AK content by effectively dissolving K minerals in soil (Sattar et al., 2019; Liu et al., 2020). Although positive correlations between *Streptomyces* and soil NH_4^+, and between *Bacillus* and soil AK were observed in the present study, they did not reach a significant level. From the RDA, tobacco leaf yield showed a positive relationship with soil pH, TC, NH_4^+-N, and AP content, and the relative abundances of *Actinobacteriota* and *Proteobacteria*. The increase of soil C, NH_4^+-N, and AP content contributed to the accumulation of tobacco leaf biomass, with NH_4^+-N extinguishing the most significant improvement effect, which is verified in our study. A significant relationship was found between the rice yield and soil chemical properties, except for AK content (Lv et al., 2011). Wang et al. (2021) also revealed that cucumber yield was significantly positively correlated with soil EC, pH, AP, and DOC content ($p < 0.01$), and soil NH_4^+-N content indirectly contributed to cucumber yield with a positive effect on bacterial numbers.

In summary, the mechanisms of FOFs on tobacco yield and quality improvement can be linked to the direct function of the plant growth-promoting substances in FOFs, and the indirect function through altering soil nutrient conditions and bacterial communities. First, FOFs changed the soil nutrient conditions (i.e., increased soil NH_4^+-N, AP, AK, TOC, and OM content), which could enable tobacco to absorb more nutrients, and enable the soil to be used more progressively and sustainably. Second, FOFs decreased the accumulation of rhizospheric PA, primarily sinapic acids, which weakened the PA's allelopathy function. Third, FOFs changed the rhizospheric bacterial community structures, with an increase in beneficial bacteria and a decrease in harmful

bacteria, which encouraged the normal growth of tobacco. This study has discussed the effects of different types of FOFs on continuous cropping tobacco yield and quality, focusing on the variance of soil physicochemical properties, the accumulation of PA, and the bacterial community structure. The application of FOFs can be extended to other broad crops at different experimental sites with a larger time scale in a further study. The interactions among FOF applications, the shift of soil environmental factors, soil microbial communities (bacteria, fungi, protists, nematodes), and crop yield, quality, and disease-suppressing ability need to be considered and revealed using various technologies. An antagonistic effect in compound FOF is observed in the present study, and the corresponding mechanisms may emerge from carefully designed experiments.

5 Conclusion

This study has shown that the application of different FOFs can improve the agronomic traits, yield, value, and chemical qualities of continuous cropping tobacco when compared to chemical fertilizers in a field experiment. Strikingly, the application of vermicompost-based and wood biochar-based FOFs showed a preferable efficacy. The FOFs took a positive role, primarily by adjusting the soil's physicochemical properties, decreasing the accumulation of PA (especially sinapic acid), and inducing a healthier rhizospheric bacterial community structure. Additionally, soil AP, TC, TN, CEC, and pH were the important environmental factors that influenced the bacterial community structure. Tobacco yield showed an active correlation with soil TC, NH_4^+-N, and AP content, and with the relative abundances of *Proteobacteria* and *Actinobacteriota*. This study provides insights into enhancing tobacco yield and chemical quality by applying proper FOFs as basal fertilizers to improve the soil's micro-ecology environment.

Data availability statement

The original contributions presented in the study are publicly available. The raw sequence data were deposited in the NCBI Sequence Read Archive (SRA) database: https://www.ncbi.nlm.nih.gov/srawith. Accession number PRJNA837398.

Author contributions

All authors contributed to the study's conception and design. DC, GW, YZ, MW, JL, and KD executed the experiments. DC, KD, and CZ performed the material preparation and data analysis. DC wrote the manuscript, and XY contributed to the revision of the manuscript. All authors read and approved the final manuscript.

Funding

This study was financially supported by the Science and Technology Key Project from the Yunnan branch of China Tobacco Corporation (2020530000241006). This study received funding from Yuxi Tobacco Company. The funder was involved in the data collection and analysis.

Conflict of interest

Author KD, CZ, and JL are employed by Yuxi Tobacco Company, Yunnan branch of China Tobacco Corporation. This study received funding from Yuxi Tobacco Company. The funder was involved in the data collection and analysis.

The remaining authors declare that the research was conducted in the absence of any commercial or financial relationships that could be construed as a potential conflict of interest.

Publisher's note

Supplementary material

The Supplementary Material for this article can be found online at: https://www.frontiersin.org/articles/10.3389/fbioe.2022.1023693/full#supplementary-material

References

Ahmad, T., Khan, R., and Khattak, T. N. (2018). Effect of humic acid and fulvic acid based liquid and foliar fertilizers on the yield of wheat crop. *J. Plant Nutr.* 41 (19), 2438–2445. doi:10.1080/01904167.2018.1527932

Algam, S. A. E., Xie, G., Li, B., Yu, S., Su, T., and Larsen, J. (2010). Effects of *Paenibacillus* strains and chitosan on plant growth promotion and control of Ralstonia wilt in tomato. *J. Plant Pathol.* 92 (3), 593–600.

Aliye, N., Fininsa, C., and Hiskias, Y. (2008). Evaluation of rhizosphere bacterial antagonists for their potential to bioprotect potato (*Solanum tuberosum*) against bacterial wilt (*Ralstonia solanacearum*). *Biol. Control* 47 (3), 282–288. doi:10.1016/j.biocontrol.2008.09.003

Bai, Y. X., Wang, G., Cheng, Y. D., Shi, P. Y., Yang, C. C., Yang, H. W., et al. (2019). Soil acidification in continuously cropped tobacco alters bacterial

community structure and diversity via the accumulation of phenolic acids. *Sci. Rep.* 9, 12499. doi:10.1038/s41598-019-48611-5

Bao, S. D. (2000). *Soil and agricultural chemical analysis*. 3rd version. Beijing: China Agriculture Press.

Bonanomi, G., Antignani, V., Capodilupo, M., and Scala, F. (2010). Identifying the characteristics of organic soil amendments that suppress soilborne plant diseases. *Soil Biol. Biochem.* 42, 136–144. doi:10.1016/j.soilbio.2009.10.012

Bonner, J., and Galston, A. W. (1944). Toxic substances from the culture media of guayule which may inhibit growth. *Bot. Gaz.* 106 (2), 185–198. doi:10.1086/335285

Cantrell, K. B., Hunt, P. G., Uchimiya, M., Novak, J. M., and Ro, K. S. (2012). Impact of pyrolysis temperature and manure source on physicochemical characteristics of biochar. *Bioresour. Technol.* 107, 419–428. doi:10.1016/j.biortech.2011.11.084

Caporaso, J. G., Kuczynski, J., Stombaugh, J., Bittinger, K., Bushman, F. D., Costello, E. K., et al. (2010). QIIME allows analysis of high-throughput community sequencing data. *Nat. Methods* 7, 335–336. doi:10.1038/nmeth.f.303

Chen, D., Zhou, Y. J., Wang, M., Munir, M. A. M., Lian, J. P., Yu, S., et al. (2022). Succession pattern in soil micro-ecology under tobacco (*Nicotiana tabacum* L.) continuous cropping circumstances in Yunnan province of southwest China. *Front. Microbiol.* 12, 785110. doi:10.3389/fmicb.2021.785110

Chen, L. M., Li, X. Y., Peng, Y. T., Xiang, P., Zhou, Y. Z., Yao, B., et al. (2022). Co-application of biochar and organic fertilizer promotes the yield and quality of red pitaya (*Hylocereus polyrhizus*) by improving soil properties. *Chemosphere* 294, 133619. doi:10.1016/j.chemosphere.2022.133619

Chen, S., Qi, G. F., Luo, T., Zhang, H. C., Jiang, Q. K., Wang, R., et al. (2018a). Continuous-cropping tobacco caused variance of chemical properties and structure of bacterial network in soils. *Land Degrad. Dev.* 29 (11), 4106–4120. doi:10.1002/ldr.3167

Chen, S., Zhou, Y. Q., Chen, Y. R., and Gu, J. (2018b). fastp: an ultra-fast all-in-one FASTQ preprocessor. *Bioinf* 34 (17), 884–890. doi:10.1093/bioinformatics/bty560

Chen, W., Teng, Y., Li, Z. G., Liu, W. X., Ren, W. J., Luo, Y. M., et al. (2018). Mechanisms by which organic fertilizer and effective microbes mitigate peanut continuous cropping yield constraints in a red soil of south China. *Appl. Soil Ecol.* 128, 23–34. doi:10.1016/j.apsoil.2018.03.018

Chen, X. G., Kou, M., Tang, Z. H., Zhang, A. J., Li, H. M., and Wei, M. (2017). Responses of root physiological characteristics and yield of sweet potato to humic acid urea fertilizer. *PLoS One* 12 (12), e0189715. doi:10.1371/journal.pone.0189715

Diaz, R. J., and Rosenberg, R. (2008). Spreading dead zones and consequences for marine ecosystems. *Science* 321, 926–929. doi:10.1126/science.1156401

Edgar, R. C. (2013). UPARSE: highly accurate OTU sequences from microbial amplicon reads. *Nat. Methods* 10 (10), 996–998. doi:10.1038/nmeth.2604

C. A. Edwards and E. Neuhauser (Editors) (1988). *Earthworms in waste and environmental management* (The Hague, Netherlands: SPB Academic Press), 21–32.

Elabyad, M. S., Elsayed, M. A., Elshanshoury, A. R., and Elsabbagh, S. M. (1993). Towards the biological control of fungal and bacterial diseases of tomato using antagonistic *Streptomyces* spp. *Plant Soil* 149 (2), 185–195. doi:10.1007/BF00016608

GB/T 32737-2016 (2016). *Soil determination of nitrate nitrogen in soil-ultraviolet spectrophotometry method*. China: National standards of the People's Republic of China. Ministry of Agriculture of the People's Republic of China.

Gul, S., Whalen, J. K., Thomas, B. W., Sachdeva, V., and Deng, H. Y. (2015). Physico-chemical properties and microbial responses in biochar-amended soils: mechanisms and future directions. *Agric. Ecosyst. Environ.* 206, 46–59. doi:10.1016/j.agee.2015.03.015

Guo, J. H., Liu, X. J., Zhang, Y., Shen, J. L., Han, W. X., Zhang, W. F., et al. (2010). Significant acidification in major Chinese croplands. *Science* 327, 1008–1010. doi:10.1126/science.1182570

Hiraddate, S., Morita, S., Furubayashi, A., Fujii, Y., and Harada, J. (2005). Plant growth inhibition by cis-cinnamoyl glucosides and cis-cinnamic acid. *J. Chem. Ecol.* 31 (3), 591–601. doi:10.1007/s10886-005-2047-0

HJ 634-2012 (2012). *Soil-determination of ammonium, nitrite and nitrate by extraction with potassium chloride solution-spectrophotometric methods*. China: Ministry of Environmental Protection of the People's Republic of China.

HJ 889-2017 (2017). *Soil quality-determination of cation exchange capacity (CEC)-hexaminecobalt trichloride solution-spectrophometric method*. China: Ministry of Environmental Protection of the People's Republic of China.

Imran, A., Sardar, F., Khaliq, Z., Nawaz, M. S., Shehzad, A., Ahmad, M., et al. (2022). Tailored bioactive compost from agri-waste improves the growth and yield of chili pepper and tomato. *Front. Bioeng. Biotechnol.* 9, 787764. doi:10.3389/fbioe.2021.787764

Jaiswal, A. K., Elad, Y., Cytryn, E., Graber, E. R., and Frenkel, O. (2018). Activating biochar by manipulating the bacterial and fungal microbiome through pre-conditioning. *New Phytol.* 219 (1), 363–377. doi:10.1111/nph.15042

Jiao, X. Q., Lyu, Y., Wu, X. B., Li, H., Cheng, L., Zhang, C., et al. (2016). Grain production versus resource and environmental costs: towards increasing sustainability of nutrient use in China. *J. Exp. Bot.* 67 (17), 4935–4949. doi:10.1093/jxb/erw282

Lazcano, C., Gomez-Brandon, M., Revilla, P., and Dominguez, J. (2013). Short-term effects of organic and inorganic fertilizers on soil microbial community structure and function. *Biol. Fertil. Soils* 49 (6), 723–733. doi:10.1007/s00374-012-0761-7

Lehmann, J., and Joseph, S. (2009). "Biochar for environmental management: an introduction," in *Biochar for environmental management: science and technology*. Editors J. Lehmann and S. Joseph (London: Earthscan), 1–12.

Lehmann, J., Rillig, M. C., Thies, J., Masiello, C. A., Hockaday, W. C., and Crowley, D. (2011). Biochar effects on soil biota–a review. *Soil Biol. Biochem.* 43, 1812–1836. doi:10.1016/j.soilbio.2011.04.022

Li, S., Liu, Y., Wang, J., Yang, L., Zhang, S., Xu, C., et al. (2017). Soil acidification aggravates the occurrence of bacterial wilt in south China. *Front. Microbiol.* 8, 703. doi:10.3389/fmicb.2017.00703

Li, Y., Fang, F., Wei, J. L., Wu, X. B., Cui, R. Z., Li, G. S., et al. (2019). Humic acid fertilizer improved soil properties and soil microbial diversity of continuous cropping peanut: a three-year experiment. *Sci. Rep.* 9, 12014. doi:10.1038/s41598-019-48620-4

Liu, H. J., Xiong, W., Zhang, R. F., Huang, X. N., Wang, D. S., Li, R., et al. (2018). Continuous application of different organic additives can suppress tomato disease by inducing the healthy rhizospheric microbiota through alterations to the bulk soil microflora. *Plant Soil* 423, 229–240. doi:10.1007/s11104-017-3504-6

Liu, M. L., Wang, C., Wang, F. Y., and Xie, Y. J. (2019). Maize (*Zea mays*) growth and nutrient uptake following integrated improvement of vermicompost and humic acid fertilizer on coastal saline soil. *Appl. Soil Ecol.* 142, 147–154. doi:10.1016/j.apsoil.2019.04.024

Liu, N., Shao, C., Sun, H., Liu, Z., Guan, Y., Wu, L., et al. (2020). Arbuscular mycorrhizal fungi biofertilizer improves American ginseng (*Panax quinquefolius* L.) growth under the continuous cropping regime. *Geoderma* 363, 114155. doi:10.1016/j.geoderma.2019.114155

Lv, M. R., Li, Z. P., Che, Y. P., Han, F. X., and Liu, M. (2011). Soil organic C, nutrients, microbial biomass, and grain yield of rice (*Oryza sativa* L.) after 18 years of fertilizer application to an infertile paddy soil. *Biol. Fertil. Soils* 47 (7), 777–783. doi:10.1007/s00374-011-0584-y

Magoč, T., and Salzberg, S. L. (2011). FLASH: fast length adjustment of short reads to improve genome assemblies. *Bioinformatics* 27 (21), 2957–2963. doi:10.1093/bioinformatics/btr507

Mao, T. T., and Jiang, X. L. (2021). Changes in microbial community and enzyme activity in soil under continuous pepper cropping in response to *Trichoderma hamatum* MHT1134 application. *Sci. Rep.* 11 (1), 21585. doi:10.1038/s41598-021-00951-x

Ndegwa, P. M., Thompson, S. A., and Das, K. C. (2000). Effects of stocking density and feeding rate on vermicomposting of biosolids. *Bioresour. Technol.* 71 (1), 5–12. doi:10.1016/S0960-8524(99)00055-3

Niu, J. J., Chao, J., Xiao, Y. H., Chen, W., Zhang, C., Liu, X. D., et al. (2017). Insight into the effects of different cropping systems on soil bacterial community and tobacco bacterial wilt rate. *J. Basic Microbiol.* 57 (1), 3–11. doi:10.1002/jobm.201600222

Palansooriya, K. N., Wong, J. T. F., Hashimoto, Y., Huang, L. B., Rinklebe, J., Chang, S. X., et al. (2019). Response of microbial communities to biochar-amended soils: a critical review. *Biochar* 1 (1), 3–22. doi:10.1007/s42773-019-00009-2

Sattar, A., Naveed, M., Ali, M., Zahir, Z. A., Nadeem, S. M., Yaseen, M., et al. (2019). Perspectives of potassium solubilizing microbes in sustainable food production system: a review. *Appl. Soil Ecol.* 133, 146–159. doi:10.1016/j.apsoil.2018.09.012

Schloss, P. D., Westcott, S. L., Ryabin, T., Hall, J. R., Hartmann, M., Hollister, E. B., et al. (2009). Introducing mothur: open-source, platform-independent, community-supported software for describing and comparing microbial communities. *Appl. Environ. Microbiol.* 75 (23), 7537–7541. doi:10.1128/aem.01541-09

Segata, N., Izard, J., Waldron, L., Gevers, D., Miropolsky, L., Garrett, W. S., et al. (2011). Metagenomic biomarker discovery and explanation. *Genome Biol.* 12 (6), R60. doi:10.1186/gb-2011-12-6-r60

Shen, M. C., Zhang, Y. Z., Bo, G. D., Yang, B., Wang, P., Ding, Z. Y., et al. (2022). Microbial responses to the reduction of chemical fertilizers in the rhizosphere soil of flue-cured tobacco. *Front. Bioeng. Biotechnol.* 9, 812316. doi:10.3389/fbioe.2021.812316

Stackebrandt, E., and Goebel, B. M. (1994). Taxonomic note: a place for DNA-DNA reassociation and 16S rRNA sequence analysis in the present species definition in bacteriology. *Int. J. Syst. Evol. Microbiol.* 44 (4), 846–849. doi:10.1099/00207713-44-4-846

Suman, S., Spehia, R. S., and Sharma, V. (2017). Humic acid improved efficiency of fertigation and productivity of tomato. *J. Plant Nutr.* 40 (3), 439–446. doi:10.1080/01904167.2016.1245325

Tan, X. M., Wang, H. T., Kong, L. G., and Wang, Y. P. (2008). Accumulation of phenolic acids in soil of a continuous cropping Poplar plantation and their effects on soil microbes. *J. Shandong Univ. Nat. Sci.* . 43 (1), 14–19. Chinese.

Wang, F. L., Wang, X. X., and Song, N. N. (2021). Biochar and vermicompost improve the soil properties and the yield and quality of cucumber (*Cucumis sativus* L.) grown in plastic shed soil continuously cropped for different years. *Agric. Ecosyst. Environ.* 315, 107425. doi:10.1016/j.agee.2021.107425

Wang, Q., Garrity, G. M., Tiedje, J. M., and Cole, J. R. (2007). Naive Bayesian classifier for rapid assignment of rRNA sequences into the new bacterial taxonomy. *Appl. Environ. Microbiol.* 73 (16), 5261–5267. doi:10.1128/AEM.00062-07

Weir, T. L., Park, S-W., and Vivanco, J. M. (2004). Biochemical and physiological mechanisms mediated by allelochemicals. *Curr. Opin. Plant Biol.* 7 (4), 472–479. doi:10.1016/j.pbi.2004.05.007

Witter, E., Martensson, A. M., and Garcia, F. V. (1993). Size of the soil microbial biomass in a long-term field experiment as affected by different n-fertilizers and organic manures. *Soil Biol. Biochem.* 25 (6), 659–669. doi:10.1016/0038-0717(93)90105-K

Wu, F. Z., and Ma, F. M. (2006). Effect of exogenous cinnamic acid on structure and function of plasmalemma in cucumber seedlings. *Allelopathy J.* 18 (2), 287–297.

Wu, K., Yuan, S. F., Wang, L. L., Shi, J. X., Zhao, J., Shen, B., et al. (2014). Effects of bio-organic fertilizer plus soil amendment on the control of tobacco bacterial wilt and composition of soil bacterial communities. *Biol. Fertil. Soils* 50 (6), 961–971. doi:10.1007/s00374-014-0916-9

Xiao, X. Z. (1997). *Tobacco chemistry*. 1st version. Beijing: China Agricultural Science and Technology Press.

Yan, S., and Liu, G. S. (2020). Effect of increasing soil carbon content on tobacco aroma and soil microorganisms. *Phytochem. Lett.* 36, 42–48. doi:10.1016/j.phytol.2020.01.011

Yao, Q., Liu, J. J., Yu, Z. H., Li, Y. S., Jin, J., Liu, X. B., et al. (2017). Three years of biochar amendment alters soil physiochemical properties and fungal community composition in a black soil of northeast china. *Soil Biol. Biochem.* 110, 56–67. doi:10.1016/j.soilbio.2017.03.005

Yin, C. M., Xiang, L., Wang, G. S., Wang, Y. F., Shen, X., Chen, X. S., et al. (2016). How to plant apple trees to reduce replant disease in apple orchard: a study on the phenolic acid of the replanted apple orchard. *PLoS One* 11 (12), e0167347. doi:10.1371/journal.pone.0167347

Yuan, L., Zhang, Z. C., Cao, X. C., Zhu, S. C., Zhang, X., and Wu, L. H. (2014). Responses of rice production, milled rice quality and soil properties to various nitrogen inputs and rice straw incorporation under continuous plastic film mulching cultivation. *Field Crops Res.* 155, 164–171. doi:10.1016/j.fcr.2013.09.009

Zhang, W. F., Cao, G. X., Li, X. L., Zhang, H., Wang, C., Liu, Q., et al. (2016). Closing yield gaps in China by empowering smallholder farmers. *Nature* 537 (7622), 671–674. doi:10.1038/nature19368

Zhang, X. H., Lang, D. Y., Zhang, E. H., Bai, C. C., and Wang, H. Z. (2013). Diurnal changes in photosynthesis and antioxidants of *Angelica sinensis* as influenced by cropping systems. *Photosynthetica* 51 (2), 252–258. doi:10.1007/s11099-013-0013-6

Zhao, F. Y., Zhang, Y. Y., Li, Z. J., Shi, J. W., Zhang, G. X., Zhang, H., et al. (2020). Vermicompost improves microbial functions of soil with continuous tomato cropping in a greenhouse. *J. Soils Sediments* 20 (1), 380–391. doi:10.1007/s11368-019-02362-y

Zhou, X. G., and Wu, F. Z. (2012). *P*-Coumaric acid influenced cucumber rhizosphere soil microbial communities and the growth of *Fusarium oxysporum* f.sp. *cucumerinum* Owen. *PLoS One* 7 (10), e48288. doi:10.1371/journal.pone.0048288

Zou, C. M., Li, Y., Huang, W., Zhao, G. K., Pu, G. R., Su, J. E., et al. (2018). Rotation and manure amendment increase soil macro-aggregates and associated carbon and nitrogen stocks in flue-cured tobacco production. *Geoderma* 325, 49–58. doi:10.1016/j.geoderma.2018.03.017

frontiers | Frontiers in Bioengineering and Biotechnology

TYPE Original Research
PUBLISHED 03 November 2022
DOI 10.3389/fbioe.2022.972361

OPEN ACCESS

EDITED BY
Junting Pan,
Institute of Agricultural Resources and Regional Planning (CAAS), China

REVIEWED BY
Le Zhang,
National University of Singapore, Singapore
Xiaoyu Zuo,
Beijing University of Chemical Technology, China
Jianfeng Liu,
Tianjin Institute of Industrial Biotechnology (CAS), China

*CORRESPONDENCE
Ming Wang,
mwang2016@163.com

†These authors have contributed equally to this work

SPECIALTY SECTION
This article was submitted to Bioprocess Engineering, a section of the journal Frontiers in Bioengineering and Biotechnology

RECEIVED 18 June 2022
ACCEPTED 24 October 2022
PUBLISHED 03 November 2022

CITATION
Li P, Wang J, Peng H, Li Q, Wang M, Yan W, Boboua SYB, Li W, Sun Y, Zheng G and Zhang H (2022), The effect of heat pre-treatment on the anaerobic digestion of high-solid pig manure under high organic loading level. *Front. Bioeng. Biotechnol.* 10:972361. doi: 10.3389/fbioe.2022.972361

The effect of heat pre-treatment on the anaerobic digestion of high-solid pig manure under high organic loading level

Pengfei Li[1,2†], Jianlin Wang[1†], Hao Peng[1], Qichen Li[3], Ming Wang[1,4*], Wencong Yan[1], Stopira Yannick Benz Boboua[1], Wenzhe Li[5], Yong Sun[1,4], Guoxiang Zheng[1,4] and Hongqiong Zhang[1,4]

[1]College of Engineering, Northeast Agricultural University, Harbin, China, [2]Key Laboratory of Combining Farming and Animal Husbandry, Heilongjiang Academy of Black Soil Conservation and Utilization, Ministry of Agriculture, Harbin, China, [3]Institute of Environment and Sustainable Development in Agriculture, Chinese Academy of Agricultural Sciences (CAAS), Beijing, China, [4]Key Laboratory of Pig-breeding Facilities Engineering, Ministry of Agriculture and Rural Affairs, Harbin, China, [5]Huanghe Science and Technology College, Zhengzhou, China

Since more and more large-scale farms appear in China and changes in fecal sewage source disposal, the production of high-concentration solid manure waste is also increasing, and its conversion and utilization are gaining attention. This study investigated the effect of heat pre-treatment (HPT) on the thermophilic anaerobic digestion (AD) of high-solid manure (HSM). Pig manure (PM) feed with a total solids of 13% was used for the HPT and subsequent anaerobic digestion (AD) test. The HPT was carried out at 60°C, 80°C, and 100°C, respectively, for 15 min after the heating reached the set temperature. The results show that HPT led to PM feed COD solubilization, observing a maximum increase of 24.57% after pretreated at 100°C, and the treated PM feed under this condition received the maximum methane production potential of 264.64 mL·g^{-1} VS in batch AD test, which was 28.76% higher than that of the untreated group. Another semi-continuous AD test explored the maximum volume biogas production rate (VBPR). It involves two organic loading rates (OLR) of 13.4 and 17.8 g VS_{added}·L^{-1}·d^{-1}. The continuous test exhibited that all the HPT groups could produce biogas normally when the OLR increased to the high level, while the digester fed with untreated PM showed failure. The maximum VBPR of 4.71 L L^{-1}·d^{-1} was observed from PM feed after pre-treated at 100°C and running at the high OLR. This reveals that thermal treatment can weaken the impact of a larger volume of feed on the AD system. Energy balance analysis demonstrates that it is necessary to use a heat exchanger to reuse energy in the HPT process to reduce the amount of energy input. In this case, the energy input to energy output (E_i/E_o) ranged from 0.34 to 0.55, which was much less than one, suggesting that biogas increment due to heat treatment can reasonably cover the energy consumption of the pre-treatment itself. Thus combining HPT and high-load anaerobic digestion of PM was suitable.

KEYWORDS
heat pretreatment, biogas production, energy balance, organic waste, pig manure

Introduction

In recent years, more large-scale modern pig farms have emerged in China to improve management efficiency and ensure food safety. However, the pressure of centralized manure treatment is also increasing (Qian et al., 2018; Pan et al., 2021). Both the methods of dry-wet separation (DYS) collection and mechanical extrusion dehydration are widely used in the initial treatment of manure. As a result, these farms generate two types of waste: low-solids wastewater (LSW) and high-solids manure (HSM). LSW can be discharged or reused after biochemical, filtration, and disinfection treatments. The solid content of HSM is generally above 15%. It contains a large amount of animal digestive waste and is the primary source of pollution. Thus the treatment or conversion of HSM has been the focus of attention in large-scale farms. Since HSM's water content is still higher than 80%, it is not ideal for natural composting conditions. However, it can be an excellent feedstock for anaerobic digestion (AD) (Wang et al., 2021).

AD is widely recognized and utilized as an important form of organic matter conversion because of its ability to produce biogas (CH_4 + CO_2). Biogas can be used as a sustainable energy source to reduce carbon emissions from fossil energy (Awe et al., 2017). Many studies have revealed that high-solid anaerobic digestion (HSAD) has higher biogas production than digestion under low-solid AD mode. Jha reported that the biogas production efficiency and volatile solids (VS) removal rate obtained by the dry fermentation process (total solids (TS) = 15.18%) were higher than those obtained by wet fermentation (TS = 7.68%) (Jha et al., 2013). Wu also found that the methane yield could be improved by up to 39.5% when the AD process was run in a high-solid mode (Wu et al., 2017). Our previous study has also shown that feeding with food waste at a solid ratio of 19.0% resulted in a significantly higher biogas production efficiency than feeding food waste with a solids content of 9.5% (Wang et al., 2015). In addition, at the same organic loading rate (OLR), HSAD tends to have smaller volumes of daily influent and effluent, indicating less consumption of water, heat, and microbes from the tank, which is more favorable for the production of biogas or energy. That is to say, HSAD can easily create a high OLR under small feed and discharge volume with a small impact on the reactor. At the same time, an appropriate increase in organic loading rate (OLR) could improve the volumetric biogas production rate (VBPR), which has been validated in the AD of food waste with a high OLR ranging from 7 to 14 g VS.·L^{-1}·d^{-1} (Zhang et al., 2015; Liu et al., 2017; Tassakka et al., 2019). And a higher VBPR can better balance the insulation cost per cubic meter of gas output and thus reduce operating costs (Zhou et al., 2022). In the past, Chinese farms were dominated by large amounts of water flushing operations, which produced manure waste with low solids and promoted the leaching of nutrients, resulting in low yields of HSM. This may be an important reason why HSAD had not received much attention in the AD of manure waste.

Many previous studies have reported that some pre-treatment methods can improve biogas production in the AD process. Such as heat (Ferrer et al., 2008; Kim et al., 2015), ultrasound (Castrillón et al., 2011), advanced oxidation (Almomani et al., 2019), alkaline cracking, dry milling, steam explosion (Fjørtoft et al., 2019), etc. Most of these methods have been proven to be effective. Still, they are challenging to be used in practical engineering due to equipment investment, chemical reagent consumption, and high energy consumption (Orlando and Borja, 2020), which has limited the promotion of pre-treatment technology. Thus, reducing the energy input has been a hot direction in pre-treatment research.

Heat pre-treatment (HPT) at atmospheric pressure at a temperature below 100°C is a gentle and low energy consumption method and is more suitable for the pre-treatment of materials not rich in cellulosic matters, such as sewage sludge (Liao et al., 2016; Liu et al., 2021), food waste (Ariunbaatar et al., 2015), kitchen waste (Li and Jin, 2015) and manure (Lin et al., 2021). Sutaryo revealed that the methane production of pig manure (PM) and dehydrated PM could be increased respectively by 9.5%–22.5% and 6.1%–25.3% when the raw materials were treated by HPT at the temperature from 65°C to 80°C before input (Sutaryo et al., 2014). Passos reported that pre-treatment of microalgae at 95°C for 10 hours could increase the VS solubilization by 1,188%, the initial methane production rate by 90%, and the final methane yield by 60% compared with the control (Passos et al., 2013). Liu demonstrated that the maximum methane production of low-organic content sludge could reach around 294.73 ml g^{-1} VS after 36 h of 90°C pre-treatment, which is 5.56 folds that of the untreated sludge (Liu et al., 2021). Additionally, less equipment investment and lower operation requirements confer HPT with great popularization and application potential.

Although HPT has been proven to improve the specific methane yield, few studies have focused on the HPT application to enhance biogas production both in HSAD and high OLR mode. Besides, the relationship between HPT's energy input and AD's energy output has received less attention in previous studies, which is directly related to practical applications' economics. Therefore, this work aims to evaluate the effect of HPT below 100°C on PM AD performance and energy balance. Methanation potential and kinetics are investigated in a batch test. In contrast, another continuous anaerobic AD test mainly observes the possibility of obtaining the maximum VBPR and discusses the energy balance problem.

TABLE 1 Characteristics of PM and inoculum.

Parameters	pH	TS (%)	VS (%)[a]	TOC (%)[a]	TKN (%)[a]	C/N ratio	SCOD (mg·L^{-1})
PM	7.45	24.1	82.3	42.5	2.91	14.6	20320
Inoculum	7.85	6.42	76.4	36.3	1.89	19.3	3,425
PM feed[b]	7.34	13.0	—	—	—	—	15090

[a]On a dry basis.
[b]Obtained by dilution of raw pig manure and used for HTPT and AD test.

Materials and methods

Materials

The PM used in this study was collected from a pig farm in the Harbin suburbs, China, where the DYS cleaning mode was adopted for manure collection. The produced dry PM from the farm had a TS above 15%. The inoculum was taken from a continuous stirred tank reactor (CSTR) which had only been used for PM digestion in our laboratory. The reactor operated in semi-continuous AD mode. Its total volume, working volume, operation temperature, pH, hydraulic retention time (HRT), and total solids (TS) content were 15 L, 10 L, 55 ± 1°C, 7.48 ± 0.12, 20 days, 41.5 ± 1.8 g L^{-1}, respectively. Before the inoculum was used, it should be fermented for a few days to confirm that it does not produce biogas. The collected PM and inoculum were stored in a 4°C refrigerator before use. The characteristics of the prepared PM and the inoculum are shown in Table 1.

HPT process

Before heat pre-treatment, the raw PM was mixed with tap water into a TS of 13%, which concentration was at a medium-to-high level and could be pumped and mixed on a large scale, more conducive to practical engineering. The temperature of HPT was set at three levels, including 60°C, 80°C, and 100°C. The heating process was carried out with a glass beaker (2 L) placed in an oil bath, stirring during heating, and maintained for 15 min when the temperature reached the desired value. Then, the hot PM feed was cooled down to the fermentation temperature before being put into the digester.

Biochemical methane potential test

The BMP test was carried out with an automatic methane test system (AMPTS-II, Sweden), and the volume of each reactor was 500 ml. This test involved four groups, including three pre-treatment groups and one untreated group (set as the control). All groups were tested simultaneously, and each was performed in three replicates for 12 bottles. Before start-up, 300 ml of inoculum and 100 ml of PM feed were added to each reactor, and then these reactors were purged with nitrogen gas for 1 minute to remove oxygen fully. The used PM feed TS, the substrate inoculum ratio, the working volume, and the digestion temperature were 13%, 1:3 (V/V), 400 ml, and 55 ± 1°C, respectively. The pH was not controlled, and the running time was more than 20 days. The data fitting of biogas production was conducted with the modified Gompertz model, as shown below (Syaichurrozi et al., 2020).

$$y = A\exp\left\{-\exp\left(\frac{\mu_m e}{A}(\lambda - t) + 1\right)\right\} \quad (1)$$

In the model (1), y is the cumulative biogas production on day t (mL·g^{-1}); t is the fermentation time (d); A is the maximum methane yield (mL·g^{-1}); μ_m is the maximum daily gas production rate (mL·g^{-1}·d^{-1}); λ is the delay time of gas production (d); and e is the natural constant (2.718,282).

Semi-continuous AD test

The semi-continuous AD process was executed by a CSTR digester with a total volume of 9 L and a working volume of 6 L. The CSTR was kept warm with a hydrothermal jacket, and its feed pipe extended from the side to the internal and below the liquid level to ensure the sealing of the reactor, while the discharge port was located at the bottom of the reactor and controlled by a ball valve. The biogas outlet was located at the top of the reactor and connected to a wet gas flowmeter (LMF-1, Qingdao). After coming out of the flowmeter, the gas was collected in a collecting bag (aluminum foil, 5 L). Before running, the reactor was first added with 6 L of inoculum, and then the test was conducted at a low OLR until stable biogas production to activate or rejuvenate the microorganisms in the inoculum to reduce the impact of the inoculum on the subsequent high load test (Wang et al., 2017). The semi-continuous AD test was also operated under thermophilic conditions (55 ± 1°C), and the PM feeds with different treatments were successively fed into the reactor in the order of untreated samples and pre-treated samples at 60°C, 80°C, and 100°C. Since the solid content of the feed was constant, the condition of ultra-high OLR could be constructed only by reducing the HRT (Ariunbaatar et al., 2021), and two HRT levels of 8 days and 6 days were used for creating two ultra-high OLR

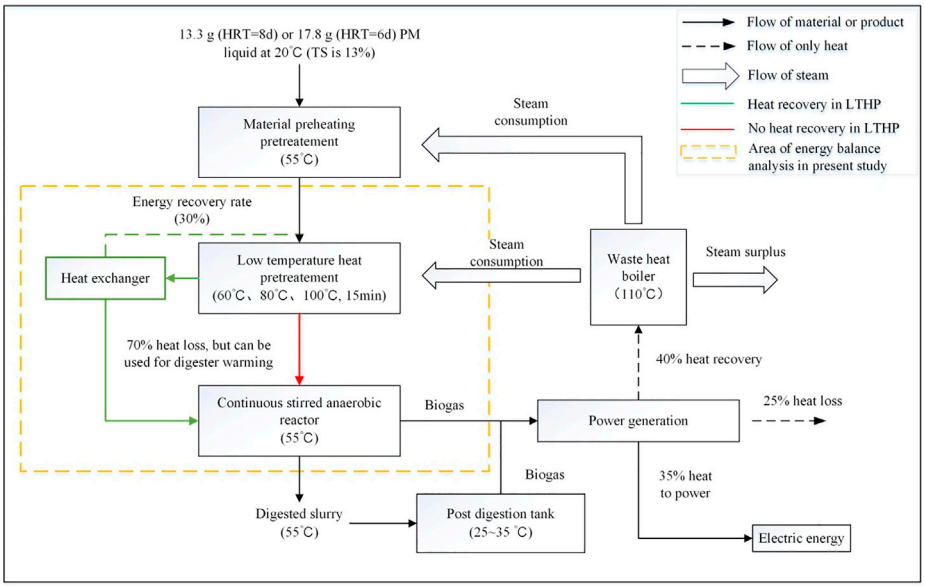

FIGURE 1
Flows of materials, products and energy of HSAD containing HPT.

conditions of 13.4 g $VS_{added}{\cdot}L^{-1}{\cdot}d^{-1}$ and 17.8 g $VS_{added}{\cdot}L^{-1}{\cdot}d^{-1}$, respectively. After adding each sample, the digester was run twice the time of HRT. The biogas volume and methane content were recorded daily, and the effluent's physical and chemical parameters were measured before the feed replacement. All the experimental values were obtained from the average values of three parallel tests.

Energy balance analysis

Since other operation parameters were consistent, the increased energy input should be mainly consumed in the HPT process. The working volume of the simulated digester was set as 1 L; daily feed and discharge volume was calculated as the working volume divided by HRT, and the operating temperature was set as 55°C. In addition, the whole heating process of fresh materials could be divided into two steps: first, the PM feed was heated from ambient temperature to 55°C and then heated to the pre-treatment temperature. The former could be regarded as necessary energy consumption; thus, it was not included in the benefits analysis for simplification. In addition, due to the short pre-treatment time, the thermal insulation energy consumption could be ignored (Zhou et al., 2021). Figure 1 illustrates the operation of a biogas plant with a heat pre-treatment process. The part in the yellow dashed line clarifies the relationship between energy and material flow in the present simulation assay, and both the heat recovery path (green line) and no heat recovery path (red line) will be discussed.

The ratio of energy input to energy output (E_i/E_o) under each pre-treatment was considered an indicator of the energy balance. Values lower and equal to 1 represent positive and neutral balance, respectively (Passos et al., 2013; Ometto et al., 2014). The heating energy input (E_i) was only related to the energy required for heating the PM feed from 20°C (T_0) to the pre-treatment temperature (T_p: 60°C, 80°C, and 100°C), which was estimated using Eq. 2. In practice, a general liquid heating process could be carried out by using a heat exchanger for energy saving, and the heat recovery efficiency (φ) was assumed to be equal to 50% for 80°C pre-treatment, 60% for 100°C pre-treatment and no heat recovery for 60°C pre-treatment. Because the heated feed liquid only needs to be cooled to 55°C, the heat exchange temperature difference is relatively small, which leads to the fact that the current set φ value is lower than the previously reported value of 85% (Lu et al., 2008). While the heat for heating the apparatus was assumed to be negligible, thus the energy output (E_o) was calculated from the biogas increment (ΔP) multiplied by its heating value (ξ). Thus, E_i and E_o can be calculated by Eq. 2 and Eq. 3, respectively.

$$E_i = V \times \rho \times \gamma \times \left(T_p - T_0\right) \times \left(1 - \varphi\right) \quad (2)$$

$$E_O = \Delta P \times \xi / 1000 \quad (3)$$

In model (2), E_i is the heating energy input (kJ); V is the daily PM feed volume (L); ρ is the specific density of PM feed and is assumed equal to 1 kg L^{-1}; γ specific heat value of PM feed and is assumed equal to 4.18 kJ·(kg·°C)$^{-1}$; T_p and T_0 are respectively the temperatures before and after preheating (°C); φ is the heat reuse

efficiency of the heating process (%). In model (3), E_o is the extra energy output (kJ); ΔP is the biogas increment after pre-treatment (L); ξ is the lower heating value of biogas (≈18 kJ L^{-1}).

Soluble chemical oxygen demand

SCOD was used to determine the amount of organic matter in the liquid phase. Its growth rate could be used to evaluate the effect of organic matter released from solid particles on the liquid phase under heat pre-treatment. The calculation of solubilization COD was carried out by Eq. 4 (Vlyssides and Karlis, 2004; Şenol et al., 2020);

$$\text{Solubilization COD}\ (\%) = (SCOD_T - SCOD_0)/(COD_0 - COD_0) \times 100 \quad (4)$$

, where $SCOD_0$ and COD_0 are the initial SCOD and COD of PM feed, respectively, and $SCOD_T$ is the SCOD after pre-treatment at each temperature in the unit of mg·L^{-1}.

Biogas recovery rate (BRR) of semicontinuous AD

In practical biogas production, the most direct way to improve the VBPR is to increase the OLR, which is often achieved by reducing the HRT. Thus, some organic matter with slow degradation may be discharged from the reactor before being completely transformed into biogas. Besides, due to the characteristic of complete mixing of the CSTR, the daily input substrate will be inevitably discharged from the digester to various degrees with the effluent of the next day, which is a continuously ongoing process. As a result, the biogas yield from the CSTR running with semi-continuous AD mode is usually lower than that under the batch mode (such as the BMP test). Therefore, a parameter of BRR was defined in the present study to evaluate the biogas yield from the daily added material in the semi-continuous AD process, which could be calculated by Eq. 5:

$$\text{BRR}\,(\%) = (continuous/y_{\text{BMP}}) \times 100 \quad (5)$$

where $_{\text{continuous}}$ is the biogas yield obtained from the semi-continuous AD process, mL·g^{-1} VS_{added}; y_{BMP} is the maximum methane yield obtained by fitting the data of the BMP test with the modified Gompertz model, mL·g^{-1} VS.

Experimental parameters and analytical methods

The biogas composition was determined with a gas chromatograph (GC-6890N, Agilent Inc. United States) equipped with a stainless steel column (1.5 m × 3 mm i.d.

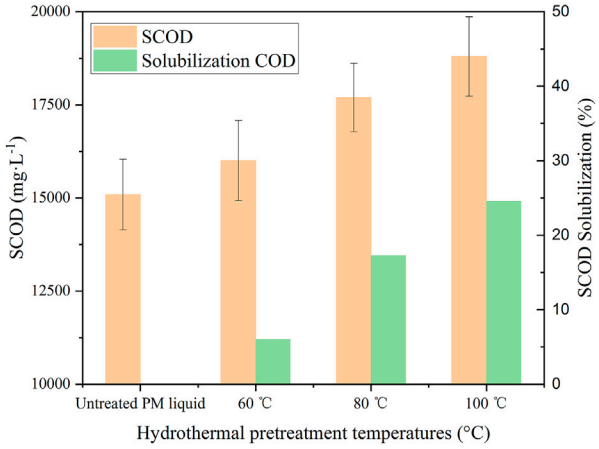

FIGURE 2
Enhancement of SCOD and COD solubilization by HPT.

Carbon molecular sieve TDX-01: 1.5–2.0 nm) and a thermal conductivity detector (TCD) using argon as the carrier gas. Volatile organic acids (VFAs) were determined by the same GC-6890N equipped with a flame ionization detector (FID) and a capillary column (30 m × 0.25 mm, Agilent 19091N-133) using nitrogen as the carrier gas. The total solids (TS), volatile solids (VS.), pH (Sartorius basic pH meter PB-10, Germany), ammonia nitrogen (AN), total organic carbon (TOC), chemical oxygen demand (COD), and total Kjeldahl nitrogen (TKN) were determined according to standard methods (APHA and AWWA, 2005). Soluble COD (SCOD) of the PM feed was analyzed after vacuum filtration through 0.45 μm membrane filter paper (Borzooei et al., 2021). All measurements were conducted in triplicate, and the averaged data were presented.

Results and discussion

Effect of HPT on solubilization

Previous studies have demonstrated that the solubility of some particulate matter in the raw material can be improved by heat pre-treatment. This improvement is mainly ascribed to the promoted dissolution or hydrolysis of the material in a hydrothermal environment, which has been proven to be related to the improvement of biogas production (Kim et al., 2015; Usman Khan and Kiaer Ahring, 2021). Menardo pre-treated dehydrated PM, digested it at 120°C and found that methane production increased by 35%–171%. Increasing soluble COD may be the main reason for improving biogas production of PM after LTPT (Menardo et al., 2011). Huang pre-treated swine manure at 110–130°C for 30 min and achieved a

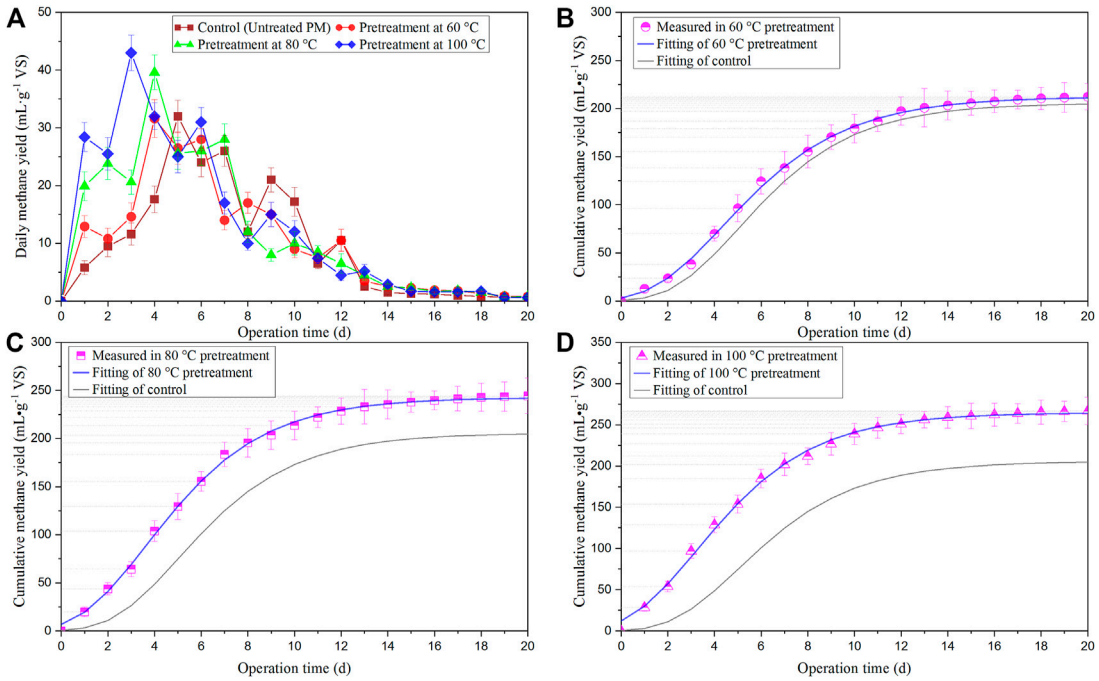

FIGURE 3
Daily methane yields **(A)** and the measured cumulative methane yields with their fitting curves **(B–D)** in the BMP test of PM feed.

CH_4 yield of 280.18–328.93 ml g^{-1} VS_{fed} increasing 14%–34%. The reason may be the increase of 13%–26% in soluble organic carbon concentration after pre-treatment (Huang et al., 2017). Bonmatífound that the concentration of soluble compounds in pig slurry rose after hydrothermal pre-treatment below 90°C, increasing methane yield (Bonmatí et al., 2001).

The increment of solubility after pre-treatment can be expressed by solubilization COD which was calculated as Eq. 4 (Vlyssides and Karlis, 2004). As shown in Figure 2, all the SCOD of PM feed increased with increasing pre-treatment temperature under HPT. Pre-treatment at 100°C resulted in the maximum solubilization COD (24.57%), followed by pre-treatment at 80°C (17.25%), while pre-treatment at 60°C only slightly increased by 6.02%. Saragih found that heat pre-treatment of food waste at 70°C increased SCOD and solubilization by 10.2% and 24.7%, respectively (Saragih et al., 2019). Passos studied the HPT in microalgae, finding that pre-treatment at 75°C and 95°C significantly improved the soluble matter content and biogas yield of microalgae. In comparison, that at 55°C only resulted in slight increases in both parameters (Passos et al., 2013). Dhar also observed that pre-treatment at 70°C increased the SCOD/TCOD ratio by 18%–19% in the sample and that at 90°C increased the ratio by 35%–37% (Dhar et al., 2012). The results of the present study and previous literature indicate that heat pre-treatment at a temperature above 70°C can promote the dissolution of the solid matter. However, the temperature has a different influence on the SCOD of different materials, which may be ascribed to the biomass's different characteristics (composition, TS and VS/TS content) (Ruffino et al., 2015).

Additionally, the growth of SCOD obtained by HPT in the present study was lower than that obtained from the pre-treatment under high temperature and pressure (Usman Khan and Kiaer Ahring, 2021), indicating that short-time HPT has little effect on the hydrolysis of recalcitrant organic compounds. Kamaraj found that hemicellulose and cellulose can only be effectively hydrolyzed at high temperatures such as 150–180°C, and cellulose is generally hydrolyzed slowly or sometimes even not hydrolyzed (Kaparaju et al., 2009).

BMP test

Figure 3 presents the daily methane yield (a) and the deviation of the measured cumulative methane production (scatter) from its fitted curves (solid line in b, c, and d), and the fitting results are summarized in Table 2. All the fit curves' determination coefficients (R2) were higher than 0.99, indicating that the model was well-fitted. As shown in Figure 3, all the BMP tests had 20 days, after which the daily biogas production dropped below 1% of the cumulative production (VDI 4630, 2006). As shown in Figure 3A, the daily biogas production of pre-

TABLE 2 Fitting results of methane production kinetics in BMP test.

Pretreatment TEMP	A/mL·g^{-1} VS		μ_m/mL·g^{-1}·d^{-1}		λ/d		R^2
	Estimated value	Std. Deviation	Estimated value	Std. Deviation	Estimated value	Std. Deviation	
Control	205.53	1.25	26.77	0.64	2.21	0.09	0.9992
60°C	212.34	1.12	25.82	0.52	1.34	0.08	0.9985
80°C	242.7	1.28	31.08	0.69	0.78	0.09	0.9991
100°C	264.64	1.75	34.02	0.98	0.36	0.12	0.9983

treated and untreated PM had a biogas production duration between 1 and 12 days. HPT promoted the initiation of the digestion process, resulting in much higher daily biogas production in the first days of the test. This can also be reflected by the shorter delay time of gas production (λ) under 80°C and 100°C pre-treatments (Table 2). Although an initial lag phase in methane production was observed in all of the tests, the methane production started immediately on the first day of all the pre-treatment digestion (Li et al., 2016). Scarcelli indicated that when thermal pre-treatment was applied to the substrates, the methane yield increased, especially in the first few days, due to a higher share of soluble COD (Scarcelli et al., 2020).

As shown in Table 2, the PM feed pre-treated at 60°C, 80°C, and 100°C had 3.31%, 18.09%, and 28.76% higher methane yields than the untreated PM feed, respectively. And the μ_m values obtained from 80°C to 100°C pre-treatments were higher than the control. This indicates that the pre-treatment at above 80°C can greatly improve anaerobic digestion and conversion efficiency ($p < 0.05$), which is consistent with some previous conclusions. For instance, Rafique found that pre-treatment at 100°C significantly increased the maximum methane production potential of dehydrated PM, while that at 50°C and 70°C had no such noticeable effect (Rafique et al., 2010). Passos reported that only pre-treatment at a higher temperature of 95°C could achieve a higher biogas production of microalgae (Passos et al., 2013). Gnaoui proved that food waste pre-treated at 100°C for 30 min showed a methane yield improvement of 23.68% compared to the control (Gnaoui et al., 2020). In addition, Appels discovered that pre-treatment at 70°C slightly decreased the efficiency of the subsequent anaerobic digestion of sludge, but pre-treatment at a higher temperature would significantly increase biogas production (Appels et al., 2010). However, some studies found that heat pre-treatment at a low temperature of 65°C or 70°C can also improve biogas yield (Sutaryo et al., 2014; Ruffino et al., 2015; Lin et al., 2021). Besides, other studies have also pointed out that pre-treatment below 100°C has a negligible effect on the final methane production, even if it promotes COD solubilization. Raju found that PM improved biogas production at pre-treatment temperatures of 125°C, while pre-treatment at 100°C did not improve. They also revealed that LTPT has little effect on the cellulose and hemicellulose fractions (Raju et al., 2013). Carrère proved that pre-treatment of 70–90°C can only increase the soluble substances and biogas production of the liquid part of PM while improving the overall biogas production need a higher temperature of >150°C (Carrère et al., 2009). The main reason for these discrepant findings may be that HPT is affected by various factors such as treatment time, substrate composition, and liquid TS.

Semi-continuous AD test

The semi-continuous AD mode is generally used in practical engineering, and the parameter of volumetric biogas production rate (VBPR, L·L^{-1}·d^{-1}) is often employed to evaluate the output efficiency of a continuous AD tank (Liu et al., 2012; Li et al., 2015), mainly because the AD tank accounts for a large proportion of the engineering investment and high operation energy consumption for heat preservation and mixing (Mahmoodi-Eshkaftaki et al., 2017). Besides, the parameter of biogas production rate (BPR, mL·g^{-1} VS_{added}) is also crucial for calculating the cost because it can represent the utilization efficiency of raw materials. Hence, both parameters were considered better to evaluate the AD performance in a semi-continuous process.

As shown in Figure 4, the whole process can be divided into two phases (phase I and phase II) according to the different operations of HRT. In each phase, VBPR and BPR showed an upward trend with replacing untreated PM with heat pre-treated PM in digester feeding. However, the obtained specific values were quite different between the two phases. The maximum VBPR of 4.71 L L^{-1}·d^{-1} (OLR = 17.8 g VS_{added}·L^{-1}·d^{-1}) and the highest BPR of 297.9 ml g^{-1} VS. (OLR = 13.4 g VS_{added}·L^{-1}·d^{-1}) were observed from the PM pre-treated by 100°C in phase II and phase I, respectively. Moreover, when operating under HRT for 8 days, all treatments resulted in a stable biogas production performance, and pre-treatment at 60°C, 80°C, and 100°C resulted in 4.3%, 30.6%, and 43.0% higher average VBPR than the control, respectively. When HRT was reduced to 6 days, the

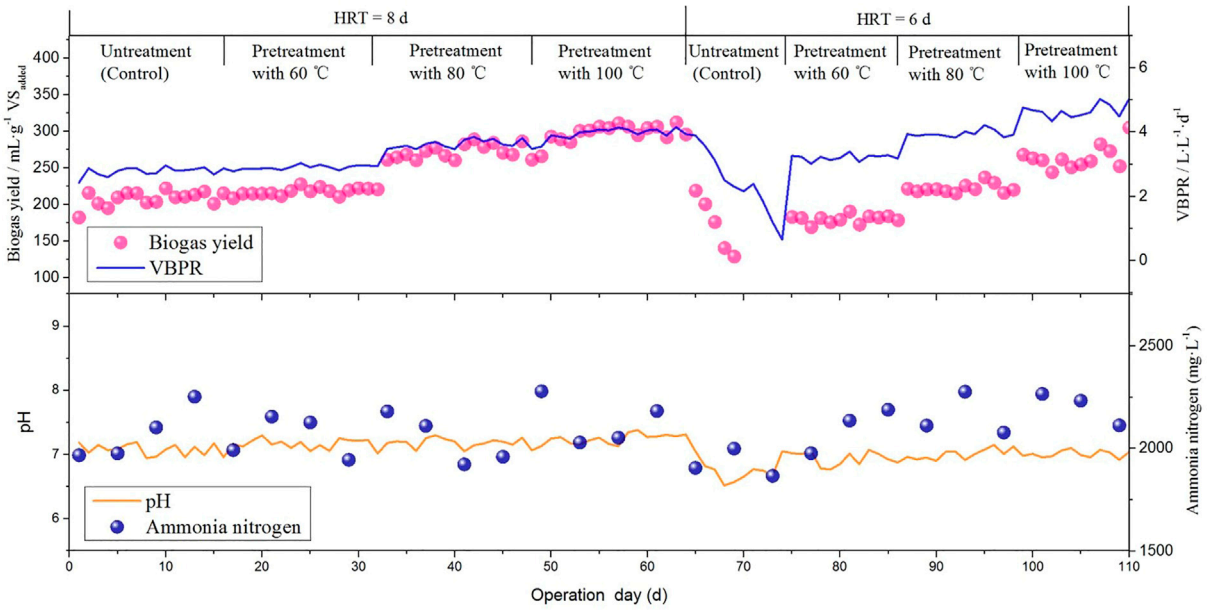

FIGURE 4
Changes of daily biogas production, pH and ammonia nitrogen in semi-continuous AD test.

feeding of untreated PM resulted in a sharp decrease in biogas production. Sánchez observed that when the OLR increased up to 7 g VS.·L^{-1}·d^{-1}, a drastic reduction in the VS removal rate was found in the mesophilic semi-continuous anaerobic digestion of swine waste (Sánchez et al., 2021). However, in the present assay, the digester was paused for some time to buffer and then run using heat pre-treated PM feed. As a result, biogas production was recovered. This indicates that the digester will have a stronger capacity to bear higher OLR upon feeding heat pre-treated PM. Guo also revealed that co-digestion of heat pre-treated dewatered activated sludge and other municipal biowastes can significantly improve the ability of the digester to withstand high OLR and VFA accumulation (Guo et al., 2014).

With decreasing HRT from 8 days to 6 days, all the VBPR showed an increasing trend, while BPR was just the opposite. The maximum VBPR of 4.71 L L^{-1}·d^{-1} (OLR = 17.8 g VS_{added}·L^{-1}·d^{-1}) and the highest BPR of 297.9 ml g^{-1} VS (OLR = 13.4 g VS_{added}·L^{-1}·d^{-1}) were observed from the PM feed pre-treated by 100°C, respectively. This result is consistent with some previous studies. Zhou proved that the volumetric methane production rate (0.25–5.69 L L^{-1}·d^{-1}) increased with increasing OLR (Zhou et al., 2022). Mazareli claimed that a higher OLR improved the volumetric methane production of swine wastewater (Mazareli et al., 2016). Increasing OLR can improve the biogas production of the semi-continuous AD tank but will also decrease its capacity to convert materials. I found that the VBPR of co-digested straw and manure increased with increasing OLR, but it was different for the BPR (Li et al., 2015). Tassakka optimized the OLR in the AD process of food waste and found that a higher OLR of 10 kg VS.·m^{-3}·d^{-1} can achieve the highest biogas production, while a further increase in OLR will lead to a decrease in VS. conversion (Tassakka et al., 2019).

Table 3 shows that the BRR values range from 49.56% to 66.32%, indicating that a part of organic matters were not effectively utilized in semi-continuous AD process, and higher OLR and shorter HRT would correspond to lower BRR, which can be mainly ascribed to the characteristics of the semi-continuous AD mode. Under HRT of 8 days, all the BRR values of heat pre-treatments were higher than those of the control, suggesting that heat pre-treatment can promote the substrate conversion rate. Luste and Luostarinen found that pasteurization (70°C, 60 min) increased both the soluble substance and bioavailability of the mixture of slaughterhouse waste and sludge and enhanced the maximum methane yield by 24% compared with the control in a continuous AD process (Luste and Luostarinen, 2010). This can also be explained by the accumulation of VFAs, as the control had higher VFA accumulation than the heat pre-treatment groups.

Additionally, it has been found that the AN exceeding 3,000 mg L^{-1} will lead to a toxic effect on the methanogens (Calli et al., 2005), while all the AN values observed in the present study were lower than this threshold (Figure 4; Table 3). It is also worth noting that pH fluctuations are present throughout the semi-continuous AD process. However, it is still stable in a small area except for the stage when HRT decreased to 6 days to start feeding untreated pig manure liquid, which may be due to the relatively large volume of

TABLE 3 Performance of biogas production in semi-continuous AD process.

Parameters	Phase I: HRT of 8 days				Phase II: HRT of 6 days		
	Control	60°C	80°C	100°C	60°C	80°C	100°C
pH of effluent	7.08	7.20	7.30	7.43	6.84	7.05	7.14
AN of effluent/mg·L^{-1}	2,248	2,319	2,513	2,700	1908	2,350	2,508
VFAs of effluent/g·L^{-1}	2.35	1.79	1.12	0.98	1.69	1.41	1.18
BPR/mL·g^{-1} VS_{added}	208.3	217.6	271.9	297.9	180.2	220.1	264.4
VBPR/L·L^{-1}·d^{-1}	2.77	2.89	3.62	3.96	3.21	3.92	4.71
CH_4/%	54.5	55.4	57.2	56.3	56.4	55.2	56.9
BRR/%	57.26	58.82	66.32	65.63	49.56	51.87	58.85

TABLE 4 Energy expenditure and income of an assumed semi-continuous AD process.

Parameters	Phase I: HRT of 8 days				Phase II: HRT of 6 days		
	Control	60°C	80°C	100°C	60°C	80°C	100°C
[a]Daily PM feed volume/L	0.125	0.125	0.125	0.125	0.167	0.167	0.167
VBPR/L·L^{-1}·d^{-1}	2.77	2.89	3.62	3.96	3.21	3.92	4.71
ΔP/L	—	0.12	0.85	1.19	0.44	1.15	1.94
E_o/kJ	—	2.23	15.23	21.46	7.88	20.66	34.85
E_i/kJ	—	2.61	13.06	23.51	3.49	17.45	31.41
E_i/E_o	—	1.17	**0.86**	1.10	**0.44**	**0.84**	**0.90**
[b]E_i/kJ	—	—	6.53	11.76	—	6.98	12.57
[b]E_i/E_o	—	—	**0.43**	**0.55**	—	**0.34**	**0.36**

[a]Calculated as working volume of 1L divided by HRT.
[b]Represents that a heat exchanger was used for energy recovery in HPT, and the heat energy recovery rates (φ) of pre-treated at 80°C and pre-treated at 100°C are calculated as 50% and 60% respectively.
Bolded values represent positive energy balance.

daily feed; bringing in more oxygen often causes reactor fluctuations.

Energy balance analysis

Although thermal pre-treatment is an available approach used in the pilot- and full-scale implementation (Millati et al., 2020), it also needs to consume energy. Thus, considering pre-treatment's energy balance is necessary to evaluate its efficiency and benefits (Marsolek et al., 2014). Under most tested conditions, the extra biogas production is insufficient to offset the energy required in pre-treatment (Cho et al., 2013; Ometto et al., 2014). The energy ratios (E_i/E_o) are summarized in Table 4, where values below 1 indicate a positive energy balance. It can be seen that all treatments can obtain a positive energy yield (E_i/E_o < 1) running at HRT of 6 days. However, running at HRT of 8 days and without considering the heating energy recovery, no positive energy gain can be obtained for both 60°C and 100°C pre-treatment. This is not quite consistent with previous studies. Carrillo-Reyes reported the longest HRT of 30 days resulted in a positive energy balance, while a short HRT of 15 days showed a negative balance (Carrillo-Reyes et al., 2021). Sun also proved that mesophilic conditions operated in the longest HRT of 30 days obtained the highest E_o/E_i (Sun et al., 2014). Moreover, the obtained E_i/E_o values are lower than those reported in previous literature (Passos et al., 2013; Ometto et al., 2014). This is the advantage of HSAD mode, which has the potential to obtain high VBPR so as to achieve a higher energy output, while high water contents in organic substrates have been identified as a main factor for the excessive energy consumption during the pre-treatment (Tang et al., 2010).

Additionally, the observed E_i/E_o values without energy recovery in HPT are higher than that in energy recovery heating mode. This is attributed to the high energy demand for heating PM feed. It confirms that it is necessary to recover part of the energy in HPT with a heat recovery device such as a heat exchanger. Figure 5 shows the data plotted on a log-log scale

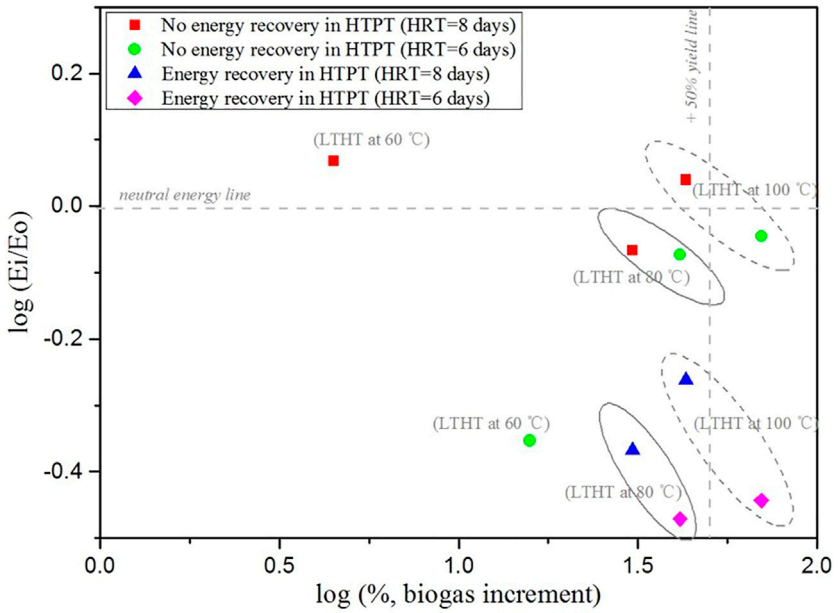

FIGURE 5
Energy balance of all the treatments and the related increment in biogas production.

chart (E_i/E_o ratio vs. biogas increment) for different treatments. The log E_i/E_o values of pre-treatment with energy recovery in HPT are located at the bottom right part of the graph, representing a better energy balance than the control group. While the log E_i/E_o values of pre-treatment without energy recovery in HPT are located near the neutral energy line, representing a weak energy balance. This indicates that adopting heat exchange to recover energy is necessary for the preheating process.

Cho and Ometto found that it is difficult to obtain a positive energy balance in microalgae AD process with heat pre-treatment, and attributed this phenomenon to the release of lower energy content compounds compared with those released after ultrasound and enzymatic hydrolysis (Cho et al., 2013; Ometto et al., 2014). Thus, whether to use heat pre-treatment in actual production, this also often depends on the biomass material characteristics. Besides, it also should consider the influence of heating temperature, exposure time (González-Fernández et al., 2012), material particle size (Menardo et al., 2012), chemical catalyst (Seyed Abbas et al., 2018), and the AD operation conditions on the results of energy balance.

Conclusion

The present study investigates HPT's effects on AD of high-solid PM feed for biogas production. HPT promotes the dissolution of particulate matter, resulting in the maximum solubilization COD of 24.57% at 100°C pre-treatment, followed by pre-treatment at 80°C (17.25%). In comparison, pre-treatment at 60°C only slightly increased by 6.02%. Similarly, the maximum methanation potential of 264.64 ml g^{-1} VS was obtained with 100°C pre-treatment, that in 80°C pre-treatment is 242.7 ml g^{-1} VS, they showed an increase of 28.76% and 18.09% compared to control, respectively. And the methanation potential of 60°C pre-treatment increased by only 3.31%. In the continuous test, HPT can reduce the impact of large-volume feed on the anaerobic system, which helps the reactor operate under shorter HRT or higher OLR to obtain a greater VBPR. The VBPR increased by 30.69% and 70.04% in the pre-treatment groups at 80°C and 100°C, respectively. This leads to E_i/E_o values as low as 0.43–0.55, which shows that heat pre-treatment can get a positive energy balance in the HSAD of PM with high OLR.

Data availability statement

The original contributions presented in the study are included in the article/Supplementary Material, further inquiries can be directed to the corresponding author.

Author contributions

PL, JW, and MW conceived the research ideas and designed the experimental scheme. PL and JW wrote the first draft of the

manuscript. QL and SB modified the article's grammar and polished the full text. All authors reviewed and commented on the entire manuscript.

Funding

This work was supported by the Dongnong scholar program of NEAU (20YJXG02), the National Natural Science Foundation of China (52076034), National Key R&D Program of China (2019YFD1100603), National Natural Scientific Foundation of China (U21A20162), Key Research and Development Program of Heilongjiang Province (GY2021ZB0253/GA21D009), Senior Foreign Expert Intoduction Program (State-funded, G2022022017L).

Conflict of interest

The authors declare that the research was conducted in the absence of any commercial or financial relationships that could be construed as a potential conflict of interest.

Publisher's note

References

Almomani, F., Bhosale, R. R., Khraisheh, M. A. M., and Shawaqfah, M. (2019). Enhancement of biogas production from agricultural wastes via pre-treatment with advanced oxidation processes. *Fuel* 253, 964–974. doi:10.1016/j.fuel.2019.05.057

APHA; AWWA (2005). "Standard methods for examination of water and wastewater," in *Water environment federation*. 21st ed. (Washington, DC: WEF publication)).

Appels, L., Degrève, J., Van der Bruggen, B., Van Impe, J., and Dewil, R. (2010). Influence of low temperature thermal pre-treatment on sludge solubilisation, heavy metal release and anaerobic digestion. *Bioresour. Technol.* 101, 5743–5748. doi:10.1016/j.biortech.2010.02.068

Ariunbaatar, J., Bair, R., Ozcan, O., Ravishankar, H., Esposito, G., Lens, P. N. L., et al. (2021). Performance of AnMBR in treatment of post-consumer food waste: Effect of hydraulic retention time and organic loading rate on biogas production and membrane fouling. *Front. Bioeng. Biotechnol.* 8, 4. doi:10.3389/fbioe.2020.00004

Ariunbaatar, J., Panico, A., Yeh, D. H., Pirozzi, F., Lens, P. N. L., and Esposito, G. (2015). Enhanced mesophilic anaerobic digestion of food waste by thermal pretreatment: Substrate versus digestate heating. *Waste Manag.* 46, 176–181. doi:10.1016/j.wasman.2015.07.045

Awe, O. W., Zhao, Y., Nzihou, A., Minh, D. P., and Lyczko, N. (2017). A review of biogas utilisation, purification and upgrading technologies. *Waste Biomass Valorization* 8, 267–283. doi:10.1007/s12649-016-9826-4

Bonmatí, A., Flotats, X., Mateu, L., and Campos, E. (2001). Study of thermal hydrolysis as a pretreatment to mesophilic anaerobic digestion of pig slurry. *Water Sci. Technol.* 44, 109–116. doi:10.2166/wst.2001.0193

Borzooei, S., Simonetti, M., Scibilia, G., and Zanetti, M. C. (2021). Critical evaluation of respirometric and physicochemical methods for characterization of municipal wastewater during wet-weather events. *J. Environ. Chem. Eng.* 9, 105238. doi:10.1016/j.jece.2021.105238

Calli, B., Mertoglu, B., Inanc, B., and Yenigun, O. (2005). Effects of high free ammonia concentrations on the performances of anaerobic bioreactors. *Process Biochem.* 40, 1285–1292. doi:10.1016/j.procbio.2004.05.008

Carrère, H., Sialve, B., and Bernet, N. (2009). Improving pig manure conversion into biogas by thermal and thermo-chemical pretreatments. *Bioresour. Technol.* 100, 3690–3694. doi:10.1016/j.biortech.2009.01.015

Carrillo-Reyes, J., Buitrón, G., Arcila, J. S., and López-Gómez, M. O. (2021). Thermophilic biogas production from microalgae-bacteria aggregates: Biogas yield, community variation and energy balance. *Chemosphere* 275, 129898. doi:10.1016/j.chemosphere.2021.129898

Castrillón, L., Fernández-Nava, Y., Ormaechea, P., and Marañón, E. (2011). Optimization of biogas production from cattle manure by pre-treatment with ultrasound and co-digestion with crude glycerin. *Bioresour. Technol.* 102, 7845–7849. doi:10.1016/j.biortech.2011.05.047

Cho, S., Park, S., Seon, J., Yu, J., and Lee, T. (2013). Evaluation of thermal, ultrasonic and alkali pretreatments on mixed-microalgal biomass to enhance anaerobic methane production. *Bioresour. Technol.* 143, 330–336. doi:10.1016/j.biortech.2013.06.017

Dhar, B. R., Nakhla, G., and Ray, M. B. (2012). Techno-economic evaluation of ultrasound and thermal pretreatments for enhanced anaerobic digestion of municipal waste activated sludge. *Waste Manag.* 32, 542–549. doi:10.1016/j.wasman.2011.10.007

Ferrer, I., Ponsá, S., Vázquez, F., and Font, X. (2008). Increasing biogas production by thermal (70°C) sludge pre-treatment prior to thermophilic anaerobic digestion. *Biochem. Eng. J.* 42, 186–192. doi:10.1016/j.bej.2008.06.020

Fjørtoft, K., Morken, J., Hanssen, J. F., and Briseid, T. (2019). Pre-treatment methods for straw for farm-scale biogas plants. *Biomass Bioenergy* 124, 88–94. doi:10.1016/j.biombioe.2019.03.018

Gnaoui, Y. E., Karouach, F., Bakraoui, M., Barz, M., and Bari, H. E. (2020). Mesophilic anaerobic digestion of food waste: Effect of thermal pretreatment on improvement of anaerobic digestion process. *Energy Rep.* 6, 417–422. doi:10.1016/j.egyr.2019.11.096

González-Fernández, C., Sialve, B., Bernet, N., and Steyer, J. P. (2012). Thermal pretreatment to improve methane production of Scenedesmus biomass. *Biomass Bioenergy* 40, 105–111. doi:10.1016/j.biombioe.2012.02.008

Guo, J., Wang, W., Liu, X., Lian, S., and Zheng, L. (2014). Effects of thermal pretreatment on anaerobic co-digestion of municipal biowastes at high organic loading rate. *Chemosphere* 101, 66–70. doi:10.1016/j.chemosphere.2013.12.007

Huang, W., Zhao, Z., Yuan, T., Huang, W., Lei, Z., and Zhang, Z. (2017). Low-temperature hydrothermal pretreatment followed by dry anaerobic digestion: A sustainable strategy for manure waste management regarding energy recovery and nutrients availability. *Waste Manag.* 70, 255–262. doi:10.1016/j.wasman.2017.09.011

Jha, A. K., Li, J., Zhang, L., Ban, Q., and Jin, Y. (2013). Comparison between wet and dry anaerobic digestions of cow dung under mesophilic and thermophilic conditions. *Adv. Water Resour. Prot.* 1, 28–38. doi:10.1126/science.134.3484.971

Kaparaju, P., Serrano, M., Thomsen, A. B., Kongjan, P., and Angelidaki, I. (2009). Bioethanol, biohydrogen and biogas production from wheat straw in a biorefinery concept. *Bioresour. Technol.* 100, 2562–2568. doi:10.1016/j.biortech.2008.11.011

Kim, D., Lee, K., and Park, K. Y. (2015). Enhancement of biogas production from anaerobic digestion of waste activated sludge by hydrothermal pre-treatment. *Int. Biodeterior. Biodegrad.* 101, 42–46. doi:10.1016/j.ibiod.2015.03.025

Li, D., Liu, S., Mi, L., Li, Z., Yuan, Y., Yan, Z., et al. (2015). Effects of feedstock ratio and organic loading rate on the anaerobic mesophilic co-digestion of rice straw and cow manure. *Bioresour. Technol.* 189, 319–326. doi:10.1016/j.biortech.2015.04.033

Li, Y., and Jin, Y. (2015). Effects of thermal pretreatment on acidification phase during two-phase batch anaerobic digestion of kitchen waste. *Renew. Energy* 77, 550–557. doi:10.1016/j.renene.2014.12.056

Li, Y., Jin, Y., Li, J., Li, H., and Yu, Z. (2016). Effects of thermal pretreatment on the biomethane yield and hydrolysis rate of kitchen waste. *Appl. Energy* 172, 47–58. doi:10.1016/j.apenergy.2016.03.080

Liao, X., Li, H., Zhang, Y., Liu, C., and Chen, Q. (2016). Accelerated high-solids anaerobic digestion of sewage sludge using low-temperature thermal pretreatment. *Int. Biodeterior. Biodegrad.* 106, 141–149. doi:10.1016/j.ibiod.2015.10.023

Lin, Y., Liu, Z., Hu, Y., He, F., and Yang, S. (2021). Thermal treatment's enhancement on high solid anaerobic digestion: Effects of temperature and reaction time. *Environ. Sci. Pollut. Res.* 28, 59696–59704. doi:10.1007/s11356-021-14926-y

Liu, C., Wang, W., Anwar, N., Ma, Z., Liu, G., and Zhang, R. (2017). Effect of organic loading rate on anaerobic digestion of food waste under mesophilic and thermophilic conditions. *Energy* 31, 2976–2984. doi:10.1021/acs.energyfuels.7b00018

Liu, T., Wu, C., Wang, Y., Xue, G., Zhang, M., Liu, C., et al. (2021). Enhanced deep utilization of low-organic content sludge by processing time-extended low-temperature thermal pretreatment. *ACS Omega* 6, 28946–28954. doi:10.1021/acsomega.1c04006

Liu, X., Gao, X., Wang, W., Zheng, L., Zhou, Y., and Sun, Y. (2012). Pilot-scale anaerobic co-digestion of municipal biomass waste: Focusing on biogas production and GHG reduction. *Renew. Energy* 44, 463–468. doi:10.1016/j.renene.2012.01.092

Lu, J., Gavala, H. N., Skiadas, I. V., Mladenovska, Z., and Ahring, B. K. (2008). Improving anaerobic sewage sludge digestion by implementation of a hyper-thermophilic prehydrolysis step. *J. Environ. Manag.* 88, 881–889. doi:10.1016/j.jenvman.2007.04.020

Luste, S., and Luostarinen, S. (2010). Anaerobic co-digestion of meat-processing by-products and sewage sludge – effect of hygienization and organic loading rate. *Bioresour. Technol.* 101, 2657–2664. doi:10.1016/j.biortech.2009.10.071

Mahmoodi-Eshkaftaki, M., Ebrahimi, R., and Ghasemi-Pirbaloti, A. (2017). Design of stirred digester with optimization of energy and power consumption. *Environ. Prog. Sustain. Energy* 36, 104–110. doi:10.1002/ep.12451

Marsolek, M. D., Kendall, E., Thompson, P. L., and Shuman, T. R. (2014). Thermal pretreatment of algae for anaerobic digestion. *Bioresour. Technol.* 151, 373–377. doi:10.1016/j.biortech.2013.09.121

Mazareli, R. C. da S., Duda, R. M., Leite, V. D., and Oliveira, R. A. de (2016). Anaerobic co-digestion of vegetable waste and swine wastewater in high-rate horizontal reactors with fixed bed. *Waste Manag.* 52, 112–121. doi:10.1016/j.wasman.2016.03.021

Menardo, S., Airoldi, G., and Balsari, P. (2012). The effect of particle size and thermal pre-treatment on the methane yield of four agricultural by-products. *Bioresour. Technol.* 104, 708–714. doi:10.1016/j.biortech.2011.10.061

Menardo, S., Balsari, P., Dinuccio, E., and Gioelli, F. (2011). Thermal pre-treatment of solid fraction from mechanically-separated raw and digested slurry to increase methane yield. *Bioresour. Technol.* 102, 2026–2032. doi:10.1016/j.biortech.2010.09.067

Millati, R., Wikandari, R., Ariyanto, T., Putri, R. U., and Taherzadeh, M. J. (2020). Pretreatment technologies for anaerobic digestion of lignocelluloses and toxic feedstocks. *Bioresour. Technol.* 304, 122998. doi:10.1016/j.biortech.2020.122998

Ometto, F., Quiroga, G., Pšenička, P., Whitton, R., Jefferson, B., and Villa, R. (2014). Impacts of microalgae pre-treatments for improved anaerobic digestion: Thermal treatment, thermal hydrolysis, ultrasound and enzymatic hydrolysis. *Water Res.* 65, 350–361. doi:10.1016/j.watres.2014.07.040

Orlando, M.-Q., and Borja, V.-M. (2020). Pretreatment of animal manure biomass to improve biogas production: A review. *Energies* 13, 3573. doi:10.3390/en13143573

Pan, D., Tang, J., Zhang, L., He, M., and Kung, C.-C. (2021). The impact of farm scale and technology characteristics on the adoption of sustainable manure management technologies: Evidence from hog production in China. *J. Clean. Prod.* 280, 124340. doi:10.1016/j.jclepro.2020.124340

Passos, F., García, J., and Ferrer, I. (2013). Impact of low temperature pretreatment on the anaerobic digestion of microalgal biomass. *Bioresour. Technol.* 138, 79–86. doi:10.1016/j.biortech.2013.03.114

Qian, Y., Song, K., Hu, T., and Ying, T. (2018). Environmental status of livestock and poultry sectors in China under current transformation stage. *Sci. Total Environ.* 622-623, 702–709. doi:10.1016/j.scitotenv.2017.12.045

Rafique, R., Poulsen, T. G., Nizami, A.-S., Murphy, J. D., Asam, Z. U. Z., and Kiely, G. (2010). Effect of thermal, chemical and thermo-chemical pre-treatments to enhance methane production. *Energy* 35, 4556–4561. doi:10.1016/j.energy.2010.07.011

Raju, C. S., Sutaryo, S., Ward, A. J., and Møller, H. B. (2013). Effects of high-temperature isochoric pre-treatment on the methane yields of cattle, pig and chicken manure. *Environ. Technol.* 34, 239–244. doi:10.1080/09593330.2012.689482

Ruffino, B., Campo, G., Genon, G., Lorenzi, E., Novarino, D., Scibilia, G., et al. (2015). Improvement of anaerobic digestion of sewage sludge in a wastewater treatment plant by means of mechanical and thermal pre-treatments: Performance, energy and economical assessment. *Bioresour. Technol.* 175, 298–308. doi:10.1016/j.biortech.2014.10.071

Sánchez, E., Herrmann, C., Maja, W., and Borja, R. (2021). Effect of organic loading rate on the anaerobic digestion of swine waste with biochar addition. *Environ. Sci. Pollut. Res.* 28, 38455–38465. doi:10.1007/s11356-021-13428-1

Saragih, F. N. A., Priadi, C. R., Adityosulindro, S., Abdillah, A., and Islami, B. B. (2019). The effectiveness of anaerobic digestion process by thermal pre-treatment on food waste as a substrate. *IOP Conf. Ser. Earth Environ. Sci.* 251, 012014. doi:10.1088/1755-1315/251/1/012014

Scarcelli, P. G., Serejo, M. L., Paulo, P. L., and Boncz, M. Á. (2020). Evaluation of biomethanization during co-digestion of thermally pretreated microalgae and waste activated sludge, and estimation of its kinetic parameters. *Sci. Total Environ.* 706, 135745. doi:10.1016/j.scitotenv.2019.135745

Şenol, H., Açıkel, Ü., Demir, S., and Oda, V. (2020). Anaerobic digestion of cattle manure, corn silage and sugar beet pulp mixtures after thermal pretreatment and kinetic modeling study. *Fuel* 263, 116651. doi:10.1016/j.fuel.2019.116651

Seyed Abbas, R., Hossein Haji Agha, A., and Rahman, S. (2018). Enhancement anaerobic digestion and methane production from kitchen waste by thermal and thermo-chemical pretreatments in batch leach bed reactor with down flow. *Res. Agr. Eng.* 64, 128–135. doi:10.17221/16/2017-RAE

Sun, Y., Wang, D., Yan, J., Qiao, W., Wang, W., and Zhu, T. (2014). Effects of lipid concentration on anaerobic co-digestion of municipal biomass wastes. *Waste Manag.* 34, 1025–1034. doi:10.1016/j.wasman.2013.07.018

Sutaryo, S., Ward, A. J., and Møller, H. B. (2014). The effect of low-temperature thermal pre-treatment on methane yield of pig manure fractions. *Anim. Prod.* 16, 55–62.

Syaichurrozi, I., Basyir, M. F., Farraz, R. M., and Rusdi, R. (2020). A preliminary study: Effect of initial pH and *Saccharomyces cerevisiae* addition on biogas production from acid-pretreated Salvinia molesta and kinetics. *Energy* 207, 118226. doi:10.1016/j.energy.2020.118226

Tang, B., Yu, L., Huang, S., Luo, J., and Zhuo, Y. (2010). Energy efficiency of pre-treating excess sewage sludge with microwave irradiation. *Bioresour. Technol.* 101, 5092–5097. doi:10.1016/j.biortech.2010.01.132

Tassakka, M. I. S., Islami, B. B., Saragih, F. N. A., and Priadi, C. R. (2019). Optimum organic loading rates (OLR) for food waste anaerobic digestion: Study case universitas Indonesia. *IJTech.* 10, 1105. doi:10.14716/ijtech.v10i6.3613

Usman Khan, M., and Kiaer Ahring, B. (2021). Improving the biogas yield of manure: Effect of pretreatment on anaerobic digestion of the recalcitrant fraction of manure. *Bioresour. Technol.* 321, 124427. doi:10.1016/j.biortech.2020.124427

VDI 4630 (2006). "Fermentation of organic materials–characterisation of the substrate, sampling, collection of material data, fermentation tests," in *Verein deutscher ingenieure (VDI)*. (Düsseldorf, Germany: Verein Deutscher Ingenieure).

Vlyssides, A. G., and Karlis, P. K. (2004). Thermal-alkaline solubilization of waste activated sludge as a pre-treatment stage for anaerobic digestion. *Bioresour. Technol.* 91, 201–206. doi:10.1016/S0960-8524(03)00176-7

Wang, M., Li, W., Li, P., Yan, S., and Zhang, Y. (2017). An alternative parameter to characterize biogas materials: Available carbon-nitrogen ratio. *Waste Manag.* 62, 76–83. doi:10.1016/j.wasman.2017.02.025

Wang, M., Li, W., Yin, L., Li, P., Zhu, Q., and Li, H. (2015). High solid concentration feedstock improving performance of continuous anaerobic digestion of food waste. *Trans. Chin. Soc. Agric. Eng.* 31, 283–287. doi:10.3969/j.issn.1002-6819.2015.03.038

Wang, Y., Zhang, Y., Li, J., Lin, J.-G., Zhang, N., and Cao, W. (2021). Biogas energy generated from livestock manure in China: Current situation and future trends. *J. Environ. Manag.* 297, 113324. doi:10.1016/j.jenvman.2021.113324

Wu, J., Hu, Y., Wang, S., Cao, Z., Li, H., Fu, X.-M., et al. (2017). Effects of thermal treatment on high solid anaerobic digestion of swine manure: Enhancement assessment and kinetic analysis. *Waste Manag.* 62, 69–75. doi:10.1016/j.wasman.2017.02.022

Zhang, C., Su, H., Wang, Z., Tan, T., and Qin, P. (2015). Biogas by semi-continuous anaerobic digestion of food waste. *Appl. Biochem. Biotechnol.* 175, 3901–3914. doi:10.1007/s12010-015-1559-5

Zhou, H., Jiang, J., Zhao, Q., Li, L., Wang, K., and Wei, L. (2022). Effects of organic loading rates on high-solids anaerobic digestion of food waste in horizontal flow reactor: Methane production, stability and mechanism. *Chemosphere* 293, 133650. doi:10.1016/j.chemosphere.2022.133650

Zhou, W., Tuersun, N., Zhang, Y., Wang, Y., Cheng, C., and Chen, X. (2021). Optimization and system energy balance analysis of anaerobic co-digestion process of pretreated textile dyeing sludge and food waste. *J. Environ. Chem. Eng.* 9, 106855. doi:10.1016/j.jece.2021.106855

frontiers | Frontiers in Bioengineering and Biotechnology

TYPE Original Research
PUBLISHED 14 November 2022
DOI 10.3389/fbioe.2022.1054801

OPEN ACCESS

EDITED BY
Li Yeqing,
China University of Petroleum, China

REVIEWED BY
Yong Sun,
Northeast Agricultural University, China
Ahmed I. Osman,
Queen's University Belfast,
United Kingdom

*CORRESPONDENCE
Rui Xu,
ecowatch_xr@163.com

†These authors have contributed equally to this work and share first authorship

SPECIALTY SECTION
This article was submitted to Bioprocess Engineering,
a section of the journal
Frontiers in Bioengineering and Biotechnology

RECEIVED 27 September 2022
ACCEPTED 25 October 2022
PUBLISHED 14 November 2022

CITATION
Luo Q, Chen D, Cui T, Duan R, Wen Y, Deng F, Li L, Wang H, Zhang Y and Xu R (2022), Selenite elimination *via* zero-valent iron modified biochar synthesized from tobacco straw and copper slag: Mechanisms and agro-industrial practicality.
Front. Bioeng. Biotechnol. 10:1054801.
doi: 10.3389/fbioe.2022.1054801

Selenite elimination *via* zero-valent iron modified biochar synthesized from tobacco straw and copper slag: Mechanisms and agro-industrial practicality

Qiong Luo†, Dingxiang Chen†, Ting Cui, Ran Duan, Yi Wen, Fang Deng, Lifang Li, Huabin Wang, Yong Zhang and Rui Xu*

[1]School of Energy and Environment Science, Yunnan Normal University, Kunming, China, [2]Yunnan Key Laboratory of Rural Energy Engineering, Kunming, China

Cost-effectively improving the performance of biochar is essential for its large-scale practical application. In this work, the agro-industrial by-products copper slag and tobacco straw were employed for the preparation of modified biochar (CSBC). The obtained CSBC exhibited satisfactory capacity on Se(IV) immobilization of 190.53 mg/g, with surface interactions determined by the monolayer and mainly chemisorption. The removal mechanisms included chemical reduction, electrostatic attraction, co-precipitation, and formation of complexations. Interestingly, the existence of Cu_2Se structure after adsorption indicated the involvement of Cu species within Se(IV) elimination. Moreover, the industrial agricultural practicality of CSBC was evaluated by regeneration tests, economic assessment, and pot experiments. The results demonstrate that iron species-modified biochar prepared from two agro-industrial by-products is a promising and feasible candidate for selenite removal from wastewater.

KEYWORDS

selenite removal, modified biochar, copper slag, tobacco straw, practical feasibility

Introduction

Selenium (Se) is an indispensable element for human beings, but excessive Se intake could be detrimental, resulting in liver damage, reproductive failure, and hair and nail loss (Kushwaha et al., 2022). The main chemical states of Se that exist in wastewater are selenide, elemental selenium, selenate, and selenite, which are referred as Se^{2-}, Se^0, SeO_3^{2-}, and SeO_4^{2-}, respectively (Li J et al., 2021). Among these species, Se(IV), which normally exists as SeO_3^{2-}, is the most toxic for human beings because of its lower mobility and negligible bio-degradability (Xiong et al., 2022).

The main sources of selenium pollution in the environment include both natural and anthropogenic sources. The natural sources of Se mainly include volcanic eruptions and biogeochemical processes of selenium-containing rocks. Volcanoes can shoot large amounts of toxic metal elements (including Se) into the environment (Li, et al., 2022). The main anthropogenic activities leading to Se pollution are mining, fossil fuel burning, fertilization, and precious metal processing. The concentration of Se(IV) in wastewater ranges from 0.2 to 74 mg/L (Zhang X et al., 2022).

Biochar derived from biomass is widely employed as an environmental functional material due to its high functionality, cost-effectiveness, and environmentally benign nature (Zhu et al., 2021; Yang et al., 2022). However, the major bottleneck of biochar-based adsorbents is their limited removal capacity. Consequently, many researchers have attempted to develop an economically feasible method to modify biochar to enhance its adsorption performance and introduce a pilot-scale application for Se(IV) pollution control (Liang et al., 2021).

Iron (Fe) is considered one of the most available and abundant elements on the Earth and many different iron-based materials have been employed for biochar fabrication (Xu et al., 2022). On one hand, the existence of Fe in biochar could enhance its removal capacity due to surface interactions between pollutants and these chemically reactive species. On the other hand, Fe-contained materials could offer more functionalities, such as magnetism and chemically reductive property (Yang X et al., 2021). Magnetic nanomaterials are superior adsorbents in water remediation application (Abdel Maksoud et al., 2020). Our group applied $FeCl_3$ to prepare magnetic biochar for Hg(II) removal, and the capacity reached 167.22 mg/g (Wang L et al., 2018). Other metal slats are also commonly employed for biochar modification, such as $Fe(NO_3)_3$, $MgFe_2O_4$, K_2FeO_4, and $FeSO_4$ (Wang Q et al., 2021; Yang F et al., 2021; Wen et al., 2022). However, their high price violates the principle of cost-effectiveness and hinders the practical application of these biochar materials. To solve this problem, there is now a novel trend toward applying iron-containing solid wastes as an iron source for biochar fabrication, such as municipal sewage sludge (Ifthikar et al., 2017), red mud (Wang J et al., 2020 (Wang, et al., 2022a)), aluminum residues (Zhao R et al., 2021), steel pickling waste (Yi et al., 2021), and steel slag (Wang, et al., 2022b). However, the influence of major impurities in these Fe-contained by-products on biochar properties has mostly been ignored (e.g., aluminum in red mud and phosphate in sludge), which urgently needs to be analyzed (Godlewska et al., 2021).

The copper metallurgy industry generates a large amount of copper slag (CS); usually 2.2–3.0 tons of CS is produced for 1 ton of Cu production (Zhao Z et al., 2021). The iron content in CS is generally close to 40 wt%, while the remaining part is Si, Cu, Al, Ca, and so on (Mikula et al., 2021). Currently, CS is normally applied for building construction, such as road paving, or as a substitute for cement. Meanwhile, efficient reutilization of Fe species in CS has attracted little attention (Li Y et al., 2021). Recently, researchers have attempted to reutilize CS as replacement for conventional iron salts to modify biochar. Gao et al. (2021) applied CS to prepare porous silicate supported Fe^0 to activate persulfate and remove orange G. They employed 20% anthracite as a reductant during co-pyrolysis at a temperature of 1100°C, which provided a novel approach for the synthesis of Fe activators *via* this carbothermal reduction process. Hence, CS could be employed for biochar fabrication, which could reduce the preparation cost for the synthesis of efficient and effective bio-adsorbents and further benefit their large-scale application. Tobacco straw is a bio-resource that is generated during cigarette production, whose reutilization and recycling has been less reported (Wang et al., 2019). This straw could be applied as a precursor for biochar preparation. Its high cellulose content and the lignin in its structure gives it a large surface area and a significant increase of microporous and mesoporous structures, which can be used as an effective place to capture target pollutants (Osman, et al., 2022b). This might be of benefit to Se(IV) removal. Therefore, a promising solution could be to use CS as an iron source and carbothermal reduced by tobacco straw to prepare functional biochar for Se(IV) pollution control.

In this work, copper slag and tobacco straw were employed as raw materials for preparation of Fe^0-modified biochar (CSBC) and then applied for Se(IV) removal from wastewater. The physicochemical properties of the obtained CSBC were comprehensively investigated to evaluate the loading of chemically reactive species. The Se(IV) removal capacity was then tested, and thermodynamics analyses were employed to illustrate the surface interactions. Several techniques have been adopted to elucidate the reaction mechanisms. Finally, recycling test, economic assessment, and pot experiments were conducted to evaluate the field feasibility of this environmentally functional material.

Materials and methods

Materials and regents

The copper slag (CS) that was applied in this study was collected from Xuanwei Smelting Plant, Yunnan Province (104.10°E, 26.22°N). The CS powders were washed with DI water three times and then dried in an oven overnight at 60°C. They were then crushed manually and passed through 200 meshes for further analysis. The chemical elements of CS are listed in Table 1. We found that there were 5.84% Cu, 18.32% Si, 40.52% Fe, and 0.89% Ca in the CS. The tobacco straw that was applied in this study was collected from rural areas near the Yunnan Normal University. They were washed with DI water

TABLE 1 Chemical constitution of CS (X-ray fluorescence data).

Element	Fe	Cu	Si	Al	Ca	Mg	Na	K	O	As	Zn
Constitutes (wt%)	40.52	5.84	18.32	4.35	0.89	0.74	1.35	1.58	30.14	0.24	2.58

SCHEME 1
Scheme of the preparation process of CSBC.

and stored for 12 h at 60°C. After it was dried, the biomass was smashed and sieved *via* 200 meshes. The chemical reagents—including ethanol, NaOH, HNO_3, HCl, and Na_2SeO_3—were all obtained from Sinopharm Co. Ltd. and used without further purification.

Preparation of CSBC

The fabrication process that was used for CSBC is given in Scheme 1. Carbothermal reduction was employed for preparation of CSBC, which was modified from our former work (Wang H et al., 2020). Briefly, 4.0 g CS and 2.0, 4.0, and 8.0 g tobacco straw were added to the 40 ml NaOH solution (0.5 M). The mixture was ultra-sonicated for 0.5 h and then stirred magnetically for another 2 h. The slurry was then transferred into an autoclave for hydrothermal treatment for 10 h at 140°C. The high temperature and autogenous high pressure under hydrothermal action ensures a good consistency between additives and bases. After cooling, the slurry was poured out, filtered, and the solid parts were dried. The solid part was then placed in a furnace for pyrolysis, the temperature was set at 400–800°C and kept for 1.0 h, the increasing rate was 5°C/min, and the whole process was protected with nitrogen (99.999%). The obtained biochar was washed with ethanol and DI water and dried in a vacuum oven for further tests. The CSBC prepared in this study is labeled as CSBCX-Y, where X refers to the pyrolysis temperature and Y represents the weight ratios between CS and biomass, such as CSBC800-0.5. The weight ratio between CS and tobacco straw was 0.5: 1, while pyrolysis was under 800°C.

Characterization methods

The surface morphology of CSBC was observed by scanning electron microscopy equipped with energy-dispersive spectroscopy (SEM-EDS, Hitachi Regulus8100, Japan). The micro-structure and surface area of the adsorbents were investigated by nitrogen adsorption–desorption isotherms (ASAP2460, Micrometrics, United States) and calculated by the Brunauer–Emmett–Teller (BET) method. Fourier transform infrared spectroscopy (FT-IR, Thermo scientific Nicolet iS 10, United States) was employed to analyze the surface functional group on CSBC with the conventional KBr method. The crystalline structure was investigated by X-ray diffraction (XRD, Nalytical X'Pert PRO MPD, Holland), with the radiation of Cu–Kα and a scanning rate of 5°/min. X-ray photoelectron spectroscopy (XPS, Thermo Scientific ESCALAB 250XI, United States) was used to analyze the chemical states of the surface elements of the CSBC. The chemical composition and elemental concentration of the CSBC were tested with an atomic adsorption spectrophotometer (AAS, Shimadzu AA7700, Japan) and X-ray fluorescence spectrometer (XRF, PANalytical Axios, Holland), respectively. The concentration of heavy metals was digested with 1 M HNO_3, diluted, and tested by using an Inductively Coupled Plasma Optical Emission Spectrometer (ICP-OES, PerkinElmer 8300, United States). Each sample was analyzed in triplicate to ensure the integrity of the data.

Batch experiments

CSBC samples were placed into serum bottles with a dosage of 2.0 g/L, and 10 ml Se(IV) solution was applied for capacity evaluation at an initial concentration of 10 ppm. The mixture was sealed and stirred for 24 h at a speed of 200 rpm and at room temperature (25°C). The effects of initial solution pH (2.0-9.0) and adsorbent dosage (10–40 g/L) were also investigated with similar procedures. The concentration of residual Se(IV) species was tested by ICP-OES, and a 0.22-μm filter was used to collect the supernatant before testing. Se(IV) removal capacity (Qe, mg/g) and efficiency (η) by CSBC were calculated by the following equations:

$$\eta = \frac{(C_0 - C_t)}{C_0} * 100\%, \tag{1}$$

$$Q_e = \frac{(C_0 - C_t)V}{m}, \tag{2}$$

where C_t (mg/L) and C_0 (mg/L) represent the Se(IV) concentration at time t and 0, respectively; V (ml) and m (mg) represent solution volume and mass of adsorbents, respectively.

Kinetics analysis was adopted with an initial solution concentration of 50 ppm, a dosage of 2.0 g/L, and the reaction was conducted at 25°C and tested with different time intervals (from 0.1 h to 14 h). The pseudo-first-order (Eq. 3) and pseudo-second-order (Eq. 4) models were employed for data fitting:

$$Q_t = Q_e\left(1 - e^{tk_1}\right), \tag{3}$$

$$Q_t = \frac{k_2 Q_e^2 t}{1 + k_2 Q_e t}, \tag{4}$$

where t (min) represents reaction time, Q_t (mg/g) represents the selenite uptake at time t, and k_1 and k_2 represent the rate constant for the pseudo-first-order and pseudo-second-order model, respectively.

The adsorption isotherms were conducted as the Se(IV) initial concentration varied from 10 to 400 mg/L, the initial pH was 2, adsorbent dosage was 2.0 g/L, and was reacted for 24 h at room temperature (25°C). The Langmuir (Eq. 5) and Freundlich (Eq. 6) models were applied to analyze the experimental data,

$$Q_e = \frac{K_L Q_{max} C_e}{1 + K_L C_e}, \tag{5}$$

$$Q_e = K_F C_e^{1/n_F}, \tag{6}$$

where K_L and K_F represent the isotherm constant for Langmuir and Freundlich models, respectively; n_F represents the parameter for adsorption intensity evaluation; and Q_{max} (mg/g) represents the maximum capacity calculated by models.

Thermodynamic parameters of enthalpy change (ΔH), entropy change (ΔS), and Gibbs free energy (ΔG) can be calculated by the following formulas:

$$\ln\left(\frac{q_e}{c_e}\right) = \frac{\Delta S}{R} - \frac{\Delta H}{RT}, \tag{7}$$

$$\Delta G = \Delta H - \Delta ST. \tag{8}$$

Recycling test and pot experiments

The regenerative capability of CSBC was confirmed by bath solution experiments. The common pyrolysis recycling method was applied for CSBC regeneration. The Se(IV)-loaded biochar was washed and then dried in a vacuum oven. The sample was then heated at 600°C for 1 h with the protection of nitrogen, and the obtained CSBC was directly applied to another cycle in the solution. The pyrolysis-based recycling method could regenerate chemically reactive species and also provide more adhering sites (Wang et al., 2022).

A series of soil experiments was employed to evaluate the practicality of the prepared CSBC on Se(IV) polluted soil remediation. The design of these experiments was based on the work of Man et al. (2021). In detail, 4 kg garden soil was added into each pot, and Se(IV) concentration was set as 100 mg/kg. Selenium slats were dissolved, and 50 ml solution was mixed into the uncontaminated soil to form different samples. These polluted soil samples were incubated for 30 days under room conditions to ensure the uniform distribution of the pollutants. Subsequently, different adsorbent materials—that is, CS, BC, CS + BC, and CSBC (1 g/kg)—were added into each pot to react with the contaminated species. After another 30 days of incubation, bok choy seeds (provided by Weifang city, Shandong Province) were planted in the experimental pots in duplicate. The growth status was recorded after 30 days of cultivation and the heavy metal content in the plants was tested by harvesting 1.0 g stems, leaves, and roots digested with concentrated HNO_3, which were diluted and analyzed by ICP-OES.

Results and discussion

Physicochemical characterizations

The elementary distribution and morphology of prepared CSBC was observed by SEM-EDS (see Supplementary Data). The porous structure of BC was obtained indicating the feasibility of this biochar as a backbone for loading of CS functional species. After adding CS, obvious aggregated Fe ions loaded on to the biochar surface and the rough structure was maintained, and the porous surface and existence of Fe species provided sufficient reactive sites for contaminant adherence (Yan et al., 2021). The distribution of metals on the adsorbents was shown in EDS mapping images. The almost uniform distribution of Fe, Cu, Si, and Al indicates the successful preparation of CSBC. Moreover,

the content of Fe (38.53%) was much higher than that of other metals, which is in agreement with the composition analysis results of CS.

The N_2 adsorption–desorption isotherm was applied to evaluate the surface parameters of the obtained CSBC (see Supplementary Data). The hysteresis loop associated with the type III curve is based on the classification, while the desorption and adsorption data did not fully coincide. This demonstrates the abundant mesoporous structure of CSBC (Bao et al., 2021). Meanwhile, according to the BET calculation, the specific surface area of the obtained CSBC was 124.26 m^2/g. The mesoporous dominated interior and rough surface structure of CSBC are beneficial to pollutant capture. It may also be beneficial to the reduction of pollutants (Fawzy, et al., 2022).

XRD was performed to analyze the crystal structure of CSBC (see Supplementary Data). The pattern reveals that the mineral composition of CSBC was complicated, which was in accordance with the chemical composition analysis. Fe_2O_3 with peaks at 31.28°, 33.01°, and 39.07° (PDF#01-073–0603) and Fe_3O_4 with peaks at 36.16, 52.34°, and 58.37° (PDF#01-089–0951) were the major Fe phases. Meanwhile, the peaks of Fe^0 were detected at the 2θ of 44.69°and 64.23° (PDF#00-006–0696). This indicates that ZVI was successfully generated. The XRD pattern shows that the intensity of Fe^0 peak increased with increasing temperature, which was related to more reducing gas being produced at high temperature and was conducive to the reduction of iron oxide to ZVI. In addition, the XRD image of the CS content (see Supplementary Data) shows that the Fe^0 peak intensity of more CS had no obvious change. This may happen because the reducing gas generated in the biochar pyrolysis process can only reduce parts of iron oxide to ZVI.

The information of surface functional groups on the surface of adsorbents was analyzed by FT-IR (see Supplementary Data). The abundant peaks with various wavenumbers in CSBC indicate the rich components from the tobacco straw, such as 3345 cm^{-1} for the vibration of -OH groups, while the wavenumbers of 1632, 1396, 1080, and 872 cm^{-1} correspond to the existence of C=O, C=C, C-C, and C-H, respectively (Wang F et al., 2021). The vibration of Fe-O was observed in the case of 550 cm^{-1}, demonstrating the loading of Fe species in the biochar substrate. All these results proved the abundant functional groups on the surface of adsorbents, which could react with the contaminants.

XPS can interpret the elemental chemical compositions on the adsorbent's surface (see Supplementary Data). The characteristic peaks of C1s with the binding energy of 284.1, 285.4, 287.8, and 288.5 eV were associated with the structure of C=C, C-O, C=O, and O-C=O, respectively (Huang et al., 2021). These carbon structures were assigned with the FT-IR results. Furthermore, the peaks of Fe^0 were observed with the binding energy of 719.3 eV. This indicates that a carbothermal reduction occurred and that CS successfully acted as an iron source. Moreover, the peaks of Cu^0 in Cu 2p at 932.2 and 952.9 eV provided evidence of copper reduction from Cu(II) to Cu^0, which might interact with selenite contaminants (Zhou et al., 2021).

Influence of preparation parameters

The effects of synthesis conditions of CSBC were analyzed, including pyrolysis temperature and weight ratios between components. As shown in Figure 1, the CSBC prepared with different temperatures exhibited obvious changes. As the pyrolysis temperature increased, the removal capacity increased from 23.53 mg/g of CSBC400-1 to 46.07 mg/g of CSBC800-1. This could be caused by the varying surface area and crystalline structure with CSBC synthesized at different temperatures. Moreover, the Se(IV) removal efficiency reached 92.20% for CSBC800-1, which indicates that this CSBC functional material is a potential and promising adsorbent for selenite pollution control.

The influence of weight ratios between CS and biomass was also investigated, as shown in Figure 1. According to the results, CSBC800-0.5 exhibited lower capacity (42.63 mg/g) than CSBC800-1 and CSBC800-2 (46.07 and 43.75 mg/g, respectively), but was higher than that of the pristine CS or BC. This proves the vital role played by the functional species provided by CS and also the synergistic effects between CS and BC after successful preparation. Interestingly, the capacity for CSBC800-1 and CSBC800-2 was 46.07 and 43.79 mg/g, respectively. This negligible decrease (4.88%) indicates the limitation for CS loading of the BC substrate—too much iron species could block the pore-structure of BC. This provides evidence for the multiple mechanisms of Se(IV) removal by CSBC.

Se(IV) adsorption performance

Dosage is an essential factor for the adsorption processes. Based on the results (Figure 1), the removal efficiency increased from 87.01% to 98.35% as the adsorbent dosage increased from 10 to 40 g/L, respectively. This may have happened because there was more CSBC in the solution that provided the sufficient reactive sites for Se(IV) adherence, which contributes to the high removal efficiency of the system. However, when the CSBC dosage kept increasing from 10 to 40 g/L, the capacity dropped obviously from 119.04 to 33.67 mg/g, respectively. This is in accordance with our former reports, which showed that more CSBC leads to the capacity for per unit functional materials. Hence, based on this analysis, the CSBC800-1 was applied for further experiments. The adsorbent dosage was set as 2.0 g/L to get a balance between capacity and Se(IV) removal efficiency.

The influence of initial solution pH was considered an important parameter for surface interactions, as depicted in

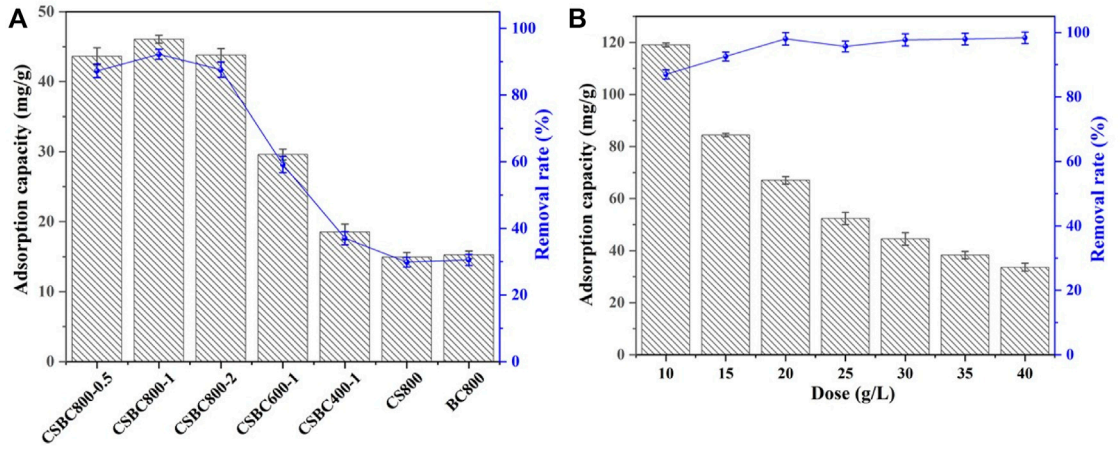

FIGURE 1
Adsorption capacity and removal rate of CSBC at different pyrolysis temperatures, weight ratios between CS and biomass **(A),** and different dosage **(B)**.

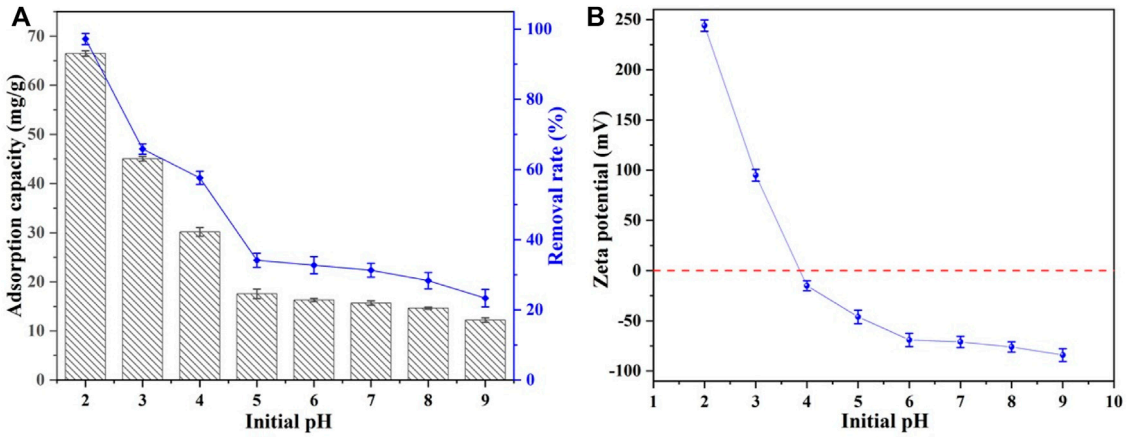

FIGURE 2
Adsorption capacity and removal rate of CSBC with different initial pH solution **(A)** and zeta potential **(B)**.

Figure 2. The removal capacity of Se(IV) by CSBC was decreased from 66.47 mg/g at pH 2 to 12.23 mg/g at pH of 9. This could be attributed to the better electron shuttling effects of Fe^0 species under acid conditions (Liu et al., 2022). Moreover, the surface zeta potential of CSBC was tested (see Supplementary Data), and the pH_{ZPC} of CSBC was 3.91. When the solution's pH moved beyond pH_{zpc}, the surface was charged, and the anionic Se(IV) and sorbent surface repelled one another. This reduces the efficiency of Se(IV) elimination. When it decreased below pH_{zpc}, the positive charge became a negative charge, which admirably adsorbs the cationic Se(IV) molecules (Osman, et al., 2022a). This indicates the positively charged adsorbent surface under acid conditions, which further benefits the attraction of SeO_3^{2-} oxyanions. The maximum capacity of Se(IV) contaminants was 66.47 mg/g with pH 2. However, this severe acid situation barely exists in conventional water surroundings—Se-containing wastewater is generally acidic to weakly alkaline (3.0–8.0) (Zhang L et al., 2022). Hence, the initial solution pH in the following sections was set as 4. Therefore, electrostatic attraction could be one of the removal mechanisms, while more inter-surface reactions could be elucidated by thermodynamics analysis.

TABLE 2 Kinetic and isotherm model fitting parameters.

		Parameter 1	Parameter 2	R^2
Adsorption kinetics				
Pseudo-first-order		Q_m = 23.16 mg·g^{-1}	K_1 = 8.68 min^{-1}	0.942
Pseudo-second-order		Q_m = 24.54 mg·g^{-1}	K_2 = 0.52 mg/g·min^{-1}	0.995
Adsorption isotherm				
Langmuir	298K	Q_m = 353.62 mg·g^{-1}	K_L = 0.0014 L·mg^{-1}	0.991
	308K	Q_m = 399.42 mg·g^{-1}	K_L = 0.0014 L·mg^{-1}	0.989
	318K	Q_m = 423.37 mg·g^{-1}	K_L = 0.0015 L·mg^{-1}	0.997
Freundlich	298K	K_F = 1.131 mg·g^{-1}	n = 0.789	0.988
	308K	K_F = 1.423 mg·g^{-1}	n = 0.773	0.984
	318K	K_F = 1.637 mg·g^{-1}	n = 0.768	0.998

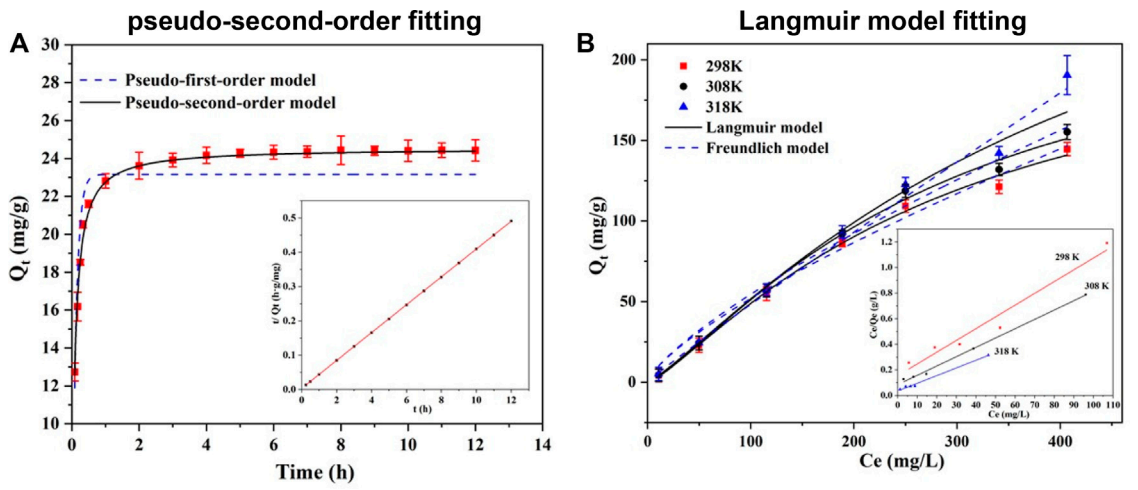

FIGURE 3
Fitting picture of kinetic **(A)** and isothermal models **(B)** for the adsorption of Se(IV) by CSBC.

According to the kinetics study, Se(IV) removal by CSBC800-1 reached equilibrium within 240 min, with a capacity of 24.16 mg/g. The conventional models of pseudo-first-order and pseudo-second-order were applied to mimic the removal processes, and the results are listed in Table 2. The fitting parameters of the pseudo-second-order models exhibited better results, with a capacity of 24.54 mg/g and coefficient values of 0.996, when compared with the pseudo-first-order model (23.16 mg/g and 0.942, respectively), This is consistent with the previous research results that the adsorption of Se(IV) and Se(VI) by various adsorbents followed the quasi-second-order kinetic model (Tong, et al., 2022), indicating the interactions were dominated by chemisorption.

The Langmuir and Freundlich models were applied to fit the adsorption isotherm data, as shown in Figure 3. The coefficient

TABLE 3 Thermodynamic analysis and fitting results.

ΔH (KJ·mol^{-1})	ΔS (KJ·mol^{-1})	ΔG (KJ·mol^{-1})		
		298 K	308 K	318 K
43.53	0.17	−7.13	−8.83	−10.53

obtained by the Langmuir model (0.993) was higher than that of the Freundlich model (0.982). This demonstrates that this adsorption mainly occurred on the monolayer, with an estimated capacity of 190.53 mg/g. Furthermore, the value of R_L represented the affinity between Se(IV) and CSBC, while R_L>1,R = 1, 1 > R > 0, and R = 0 were associated with the poor adsorption, linear adsorption, better adsorption performance,

and irreversible adsorption, respectively (Ifthikar et al., 2021). Because these values are within the range of 0.768–0.789, the inter-surface reaction between CSBC and contaminants was favorable for adherence.

Thermodynamic analysis was employed to investigate whether the reaction was spontaneous and endothermic, as depicted in Figure 3 and calculated in Table 3. Based on the calculated results, the decreasing of Gibbs free energy (ΔG) within the increasing of reaction temperature from −7.13 to −10.53 kJ/mol suggests that the Se(IV) adsorption was spontaneous and the higher reaction is conductive for removal. The enthalpy change (ΔH) revealed the endothermic nature of adsorption, while the capacity could be accelerated with higher system temperature. The entropy change (ΔS) is positive. Hence, the Se(IV) elimination by CSBC was an endothermic and spontaneous process that involved many mechanisms, which needs further investigation.

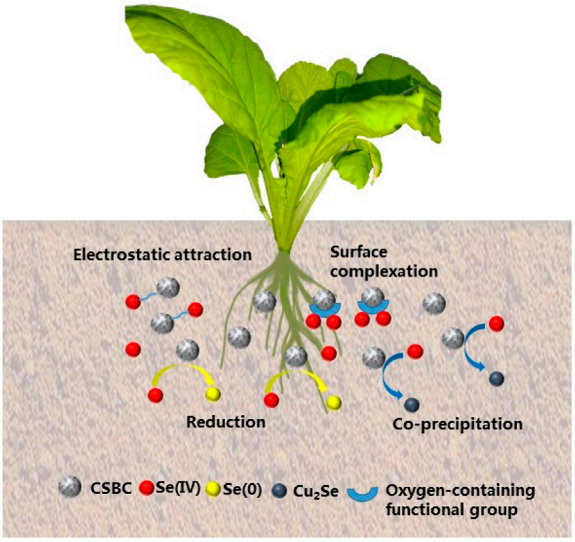

FIGURE 4
Mechanism of Se(IV) adsorption by CSBC.

Removal mechanisms

The removal mechanisms of Se(IV) were elucidated by various techniques. First, the variations of the crystalline structure of adsorbents were investigated (see Supplementary Data). The generated 31.26°, 36.34°, and 52.18°peaks indicate the presence of Se^0 according to the databases. These results indicate that chemical reduction occurred between Se(IV) and Fe^0, which was also reported by other groups (Wei et al., 2021). The generation of Fe_2O_3 and Fe_3O_4 minerals could also support this speculation on the existence of Fe oxidation. More importantly, the obvious peaks with 2θ of 43.32° and 64.32° correspond to the Cu_2Se crystalline structure. This phenomenon could be explained by the familiar chemical properties of sulfur and selenium (i.e., they belong to the elemental sixth-row main group), and the Se(IV) species were reduced with the oxidation of iron materials.

The variations of chemical states of surface elements were further investigated by XPS spectra. In the case of CSBC, the peaks with binding energies of 711.08, 713.48, 719.88, 724.28, and 727.68 eV were associated with the iron states of Fe^{2+}, Fe^{3+}, Fe^0, Fe^{2+}, and Fe^{3+}, respectively. After adsorption, the molar ratios of Fe^0 decreased from 9.81% to 6.91%, while the value of Fe2+ decreased from 60.85% to 55.24.31%, and that of Fe^{3+} increased from 29.31% to 37.85%. These results provide direct evidence for the chemical reactions between Se(IV) and CSBC. Moreover, the detailed XPS spectra of selenium after adsorption was also investigated (see Supplementary Data). In total, 48.04% Se(IV) pollutants were reduced into Se(0) and Se(-II) after adsorption, which was in accordance with the oxidation of Fe^0 species. Furthermore, the C1s spectra were also depicted (see Supplementary Data). The peaks with the binding energies of 283.78, 285.26, 287.08, 288.98, and 292.88 eV, referred to as C=C, C-O, C=O, O-C=O, and π–π, respectively, while the variations of molar ratios of different carbon structure indicate the function of surface groups on Se(IV) species. Meanwhile, from the spectra of Cu 2p, the Cu(I) was observed and further proved the formation of Cu_2Se co-precipitants, which is in accordance with XRD results.

The FT-IR results offer evidence for the reactions between Se(IV) and functional groups and also apply for the mechanism analysis (see Supplementary Data). As shown, the wavenumbers of 3314 and 1642 cm^{-1} were related to the stretching vibration of hydroxyl (-OH) and carbonyl (C=O) groups. Meanwhile, the C-H vibration in different groups as C=C, C-O, and C-H correspond with the wavenumbers of 1394, 1084, and 876 cm^{-1}, respectively. These results suggest the abundant functional groups on the surface of CSBC. The peaks of Fe-O with wavenumber of 550 cm^{-1} also proved the successful loading of these functional species. After adsorption, obvious shifting and weakening were observed with the wavenumber of 3291, 1626, 1398, and 1115 cm^{-1}, based on former analysis. These results prove the involvement of various oxygen-contained functional groups during Se(IV) elimination.

Based on various characterizations after adsorption, the Se(IV) elimination process by CSBC can be attributed to the co-precipitation, chemical reduction, formation of complexations, electrostatic attraction, and so on. These mechanisms contribute to the acceptable capacity for Se(IV) immobilization. The mechanisms of adsorption on Se(IV) are shown in Figure 4. A comparison of removal capacity with other bio-adsorbents is given in Table 4. These results prove that these industrial product-derived functional materials could be promising adsorbents for selenite pollution control. Therefore, further evaluation should be conducted for its future application.

TABLE 4 Comparison of adsorbents for Se(IV) removal.

Adsorbents	Carbon substrate	Fabricants	Preparation method (main step)	Experimental conditions			Capacity (mg/g)	Ref.
				Initial pH	Initial concentration (mg/L)	Adsorbent dosage (g/L)		
Fe-BC	Purchased AC	Magnetite	Wet chemistry	5.3	0.2	0.2	1.26	Kwon et al. (2015)
Fe_2O_3-CNT	Carbon nanotubes	Iron (III) nitrate	Wet chemistry	6.0	0–40	0.2	111.00	Bakather et al. (2017)
Ca/P-BC	Date palm	Hydroxy apatite	Wet chemistry	5.0	50–200	2.0	57.27	Li et al. (2022)
UiO-66-BC	Purchased AC	MOFs	Dispersion and formation	7.0	0.1–200	1.0	168.00	Solis et al. (2020)
CS-PEI-GO	Graphene oxide	Chitosan and polymer	Surface modification	4.0	5–250	30.0	1.62	Bandara et al. (2019)
PAA-MGO	Graphene oxide	Fe salts and polymer	Co-precipitation	5.8	0–140	0.1	120.10	Lu et al. (2017)
LDHs-GO	Graphene oxide	MgAl-LDH	Wet chemistry	6.0	7.9–39.5	0.2	65.90	Koilraj et al. (2018)
PAMAM-GO	Graphene oxide	Polymer	Dispersion and formation	6.0	0–100	0.5	60.90	Xiao et al. (2016)
Fe-GO	Graphene oxide	Iron (III) nitrate	Wet chemistry	2.0	0.003–0.015	0.3	18.69	Koudelkova et al. (2019)
ZVI/BC	Brew waste	$FeSO_4$ & $NaBH_4$	Fe loading and reduction	4.0	10–100	2.8	34.77	Suganya and Senthil Kumar, (2019)
CSBC	Rice straw	Copper slag	Carbothermal reduction	2.0	100	2	190.53	This study
				4.0	100	2	30.17	

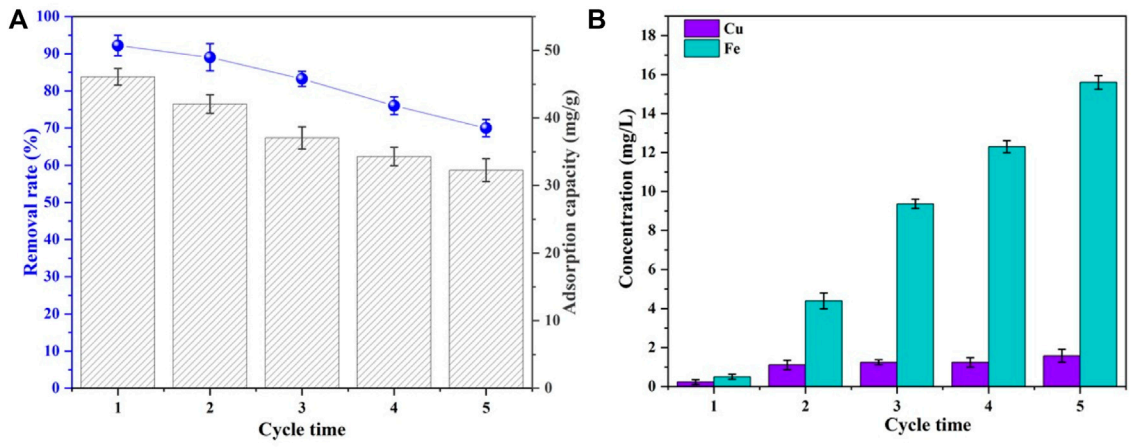

FIGURE 5
Removal rates and adsorption capacity **(A)** and leaching of Cu and Fe at each cycle of CSBC **(B)**.

Agro-industrial feasibility assessment

The recyclability and leaching performance of the adsorbents are given in Figure 5. The Se(IV) removal rate and adsorbing capacity by CSBC were decreased from 92.2% to 70.01% and 46.07 to 32.27 mg/g after adsorption–desorption recycled for 5 times, respectively. This indicates the acceptable reusability of CSBC. Meanwhile, the leaching inherent metal ions were also

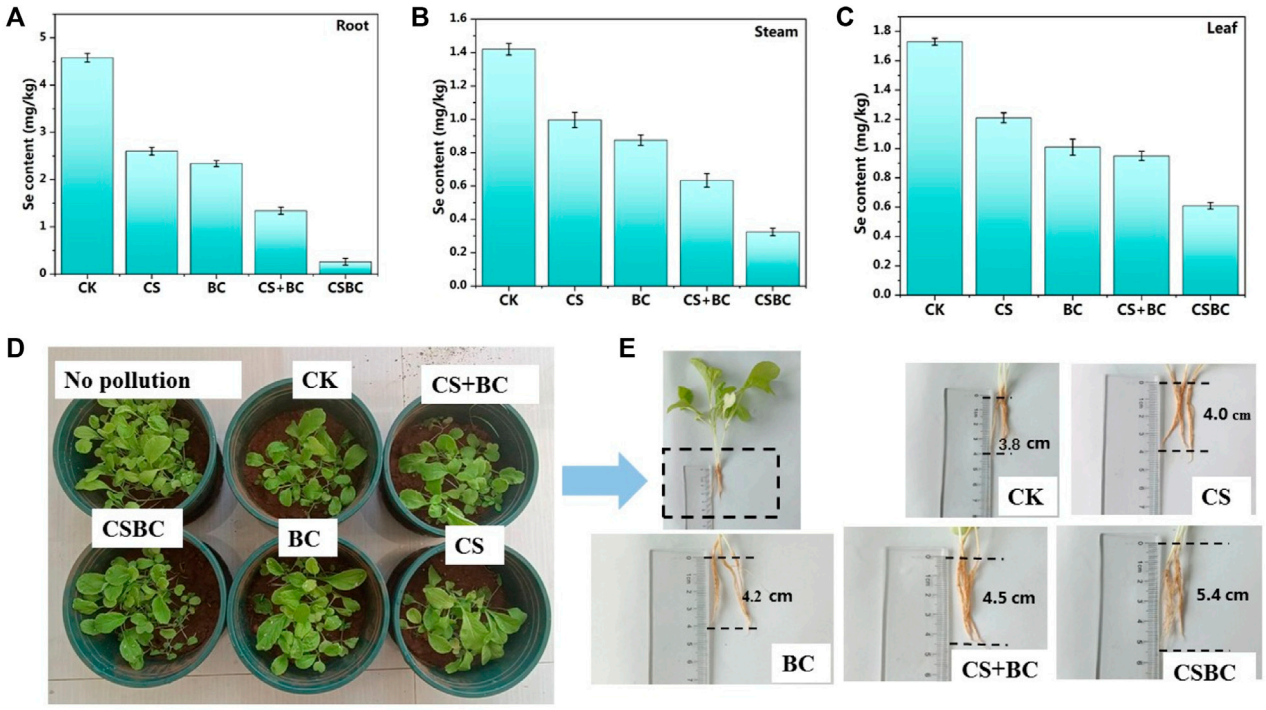

FIGURE 6
Se(IV) content in roots **(A)**, stems **(B)**, and leaves **(C)** and growth picture **(D) (E)** of bok choy under various adsorbent treatments.

detected as 0.23, 0.98, 1.11, 1.24, and 1.58 mg/L for Cu and 0.5, 4.39, 9.37, 12.31, and 15.62 mg/L for Fe. These values all met the national standard in China (GB 8978–1996) on wastewater effluent. One of the major concerns is the leaching of As from copper slag to the environment. However, in our study, the leaching of As was almost neglectable. This indicates the capsuling effect of biochar on the heavy metals, which is similar to other research (Li G et al., 2021). Simultaneously, the leaching concentrations of other heavy metals (Pb, Zn, Cd, and Cr) were measured, and the results are shown in Supplementary Table S1. The leaching concentrations of major heavy metals were within the range of the municipal wastewater quality discharge A standard (CJ343-2010). This indicates the reliability of CSBC as a functional adsorbent in practical applications.

The economic cost of CSBC is important for its further large-scale application. Due to the solid waste nature of CS and tobacco straw, the major CSBC preparation cost would be incurred by the pyrolysis processes. Hence, considering the labor costs and energy consumption, these values could vary from region to region. For example, the Taupo Carbon Producers prepared biochar at a cost of 144 USD per ton (Das et al., 2016), but this unmodified material exhibited limited performance when used for pollution control (Suliman et al., 2016). According to a field study, biochar prepared from 358 to 728 USD per ton could obviously enhance rice production and the ratio of bio-adsorbent to soil played a critical role (Wang H et al., 2018). Furthermore, Fe^0-modified biochar exhibited better performance but normally higher preparation cost is involved, including chemicals such as iron salts and reductants ($NaBH_4$ or hydrogen) (Kamali et al., 2019). Based on this analysis, the synthesis of CSBC was: 80 (Raw materials) +105 (Chemicals) +12 (Electricity) = 197 USD. This relatively acceptable cost was related to the facile steps and little labor force needed for CSBC, while chemical reductants were avoided and industrial by-products CS were reused as an iron source, which dramatically reduced the preparation cost (Kamali et al., 2022).

The soil remediation experiments of CSBC800-1 were conducted, and the results are given in Figure 6. Most of the bok choy plants were hypogenetic, and some were almost dead and sparse, which could be caused by the selenite contamination. However, for samples repaired by CSBC, the bok choy growth was more luxuriant. This could be explained by the mediation effects of CSBC functional materials. The heavy metal contents in the roots, stems, and leaves were also tested, and the results are given in Figure 6. The Se content in roots, stems, and leaves of bok choy treated by CSBC was the lowest and the root growth was the longest when compared with other restorative agents. This indicates that CSBC could reduce the bioavailability of Se (Łabaj et al., 2021). Based on these pot experiments, the CSBC

exhibited potential soil remediation capability and inhibited bioaccumulation on bok choy to suppress heavy metal transfer between the biosphere and soil.

In summary, based on agro-industrial practicality evaluation, the CSBC exhibited promising and potential applicability with advantages of recyclability, cost-effectiveness, and plant-growth enhancement. Therefore, the direct and indirect benefits of CSBC for agricultural and wastewater purification highlight its potential future application.

Conclusion

In this work, tobacco straw and copper slag were employed for preparation of iron-fabricated biochar to eliminate Se(IV) from wastewater. The physicochemical characterizations indicate the successful loading of iron species. The Se(IV) removal process was fitted by the kinetics and isotherm adsorption model. The removal was endothermic and spontaneously occurred on the monolayer dominated by chemisorption, with the mechanisms of electrostatic attraction, precipitation, chemical reduction, and formation of complexations. The existence of Cu_2Se indicates the function of copper ions in co-precipitation with reduced Se ions. These results prove the feasibility of this copper slag and tobacco straw-derived bio-adsorbent in selenium-contained wastewater purification.

Data availability statement

The original contributions presented in the study are included in the article/Supplementary Material; further inquiries can be directed to the corresponding author.

Author contributions

QL: writing—original draft, data curation. DC: writing—original draft and data curation. TC: software and formal analysis. RD: data curation and visualization. YW: formal analysis. FD: data curation and formal analysis. LL: data curation. HW: writing—original draft and writing—review and editing. YZ: conceptualization and methodology. RX: funding acquisition and writing—review and editing.

Acknowledgments

The authors appreciate the support from the National Natural Science Foundation of China (21775053), the Yunnan Province Education Department Scientific Research Foundation Project (2022J0136), and the Applied Basic Research Foundation of Yunnan Province (202201AS070020 and 202201AU070061).

Conflict of interest

The authors declare that the research was conducted in the absence of any commercial or financial relationships that could be construed as a potential conflict of interest.

Publisher's note

All claims expressed in this article are solely those of the authors and do not necessarily represent those of their affiliated organizations, or those of the publisher, the editors, and the reviewers. Any product that may be evaluated in this article, or claim that may be made by its manufacturer, is not guaranteed or endorsed by the publisher.

Supplementary material

The Supplementary Material for this article can be found online at: https://www.frontiersin.org/articles/10.3389/fbioe.2022.1054801/full#supplementary-material

References

Abdel Maksoud, M. I. A., Elgarahy, Ahmed M., Farrell, Charlie, Al-Muhtaseb, A. H., Rooney, D. W., and Osman, A. I. (2020). Insight on water remediation application using magnetic nanomaterials and biosorbents. *Coord. Chem. Rev.* 403, 213096. doi:10.1016/j.ccr.2019.213096

Bakather, O. Y., Kayvani Fard, A., Khraisheh, M., Nasser, M. S., and Atieh, M. A. (2017). Enhanced adsorption of selenium ions from aqueous solution using iron oxide Impregnated carbon Nanotubes. *Bioinorganic Chem. Appl.* 2017, 4323619. doi:10.1155/2017/4323619

Bandara, P. C., Perez, J. V. D., Nadres, E. T., Nannapaneni, R. G., Krakowiak, K. J., and Rodrigues, D. F. (2019). Graphene oxide nanocomposite Hydrogel Beads for removal of selenium in contaminated water. *ACS Appl. Polym. Mater.* 1 (10), 2668–2679. doi:10.1021/acsapm.9b00612

Bao, J., Ning, P., Wang, F., Sun, X., Wang, C., Song, X., et al. (2021). Thermal modification of copper slag via phase transformation for simultaneous removal of SO2 and NOx from acid-making tail gas. *Chem. Eng. J.* 425, 131646. doi:10.1016/j.cej.2021.131646

Das, O., Bhattacharyya, D., and Sarmah, A. K. (2016). Sustainable eco–composites obtained from waste derived biochar: A consideration in performance properties, production costs, and environmental impact. *J. Clean. Prod.* 129, 159–168. doi:10.1016/j.jclepro.2016.04.088

Fawzy, S., Osman, A. I., Mehta, N., Moran, D., Al-Muhtaseb, A. H., and Rooney, D. W. (2022). Atmospheric carbon removal via industrial biochar systems: A techno-economic-environmental study. *J. Clean. Prod.* 371, 133660. doi:10.1016/j.jclepro.2022.133660

Gao, C., Yu, W., Zhu, Y., Wang, M., Tang, Z., Du, L., et al. (2021). Preparation of porous silicate supported micro-nano zero-valent iron from copper slag and used as persulfate activator for removing organic contaminants. *Sci. Total Environ.* 754, 142131. doi:10.1016/j.scitotenv.2020.142131

Godlewska, P., Ok, Y. S., and Oleszczuk, P. (2021). The Dark Side of Black Gold: Ecotoxicological aspects of biochar and biochar-amended soils. *J. Hazard. Mater.* 403, 123833. doi:10.1016/j.jhazmat.2020.123833

Huang, W.-H., Lee, D.-J., and Huang, C. (2021). Modification on biochars for applications: A research update. *Bioresour. Technol.* 319, 124100. doi:10.1016/j.biortech.2020.124100

Ifthikar, J., Wang, J., Wang, T., Wang, H., Khan, A., Jawad, A., et al. (2017). Highly efficient lead distribution by magnetic sewage sludge biochar: Sorption mechanisms and Bench applications. *Bioresour. Technol.* 238, 399–406. doi:10.1016/j.biortech.2017.03.133

Ifthikar, J., Zhao, M., Shahib, I. I., Wang, J., Wang, H., et al. (2021). Recyclable process modeling study of hexavalent chromium elimination by thiol-based electron donor: Implications for practical applicability. *J. Environ. Chem. Eng.* 9 (4), 105645. doi:10.1016/j.jece.2021.105645

Kamali, M., Costa, M. E., Aminabhavi, T. M., and Capela, I. (2019). Sustainability of treatment technologies for industrial biowastes effluents. *Chem. Eng. J.* 370, 1511–1521. doi:10.1016/j.cej.2019.04.010

Kamali, M., Sweygers, N., Al-SalemAppels, L., Aminabhavi, T. M., and Dewil, R. (2022). Biochar for soil applications-sustainability aspects, challenges and future prospects. *Chem. Eng. J.* 428, 131189. doi:10.1016/j.cej.2021.131189

Koilraj, P., Kamura, Y., and Sasaki, K. (2018). Cosorption characteristics of SeO42– and Sr2+ Radioactive Surrogates using 2D/2D graphene oxide-Layered Double hydroxide Nanocomposites. *ACS Sustain. Chem. Eng.* 6 (11), 13854–13866. doi:10.1021/acssuschemeng.8b02056

Koudelkova, Z., Bytesnikova, Z., Xhaxhiu, K., Kremplova, M., Hynek, D., Adam, V., et al. (2019). Electrochemical evaluation of selenium (IV) removal from its aqueous solutions by unmodified and modified graphene oxide. *Molecules* 24 (6), 1063. doi:10.3390/molecules24061063

Kushwaha, A., Goswami, L., Lee, J., Sonne, C., Brown, R. J. C., and Kim, K. H. (2022). Selenium in soil-microbe-plant systems: Sources, distribution, toxicity, tolerance, and detoxification. *Crit. Rev. Environ. Sci. Technol.* 52 (13), 2383–2420. doi:10.1080/10643389.2021.1883187

Kwon, J. H., Wilson, L. D., and Sammynaiken, R. (2015). Sorptive uptake of selenium with magnetite and its supported materials onto activated carbon. *J. Colloid Interface Sci.* 457, 388–397. doi:10.1016/j.jcis.2015.07.013

Łabaj, J., Blacha, L., Jodkowski, M., Smalcerz, A., Frohlichova, M., and Findorak, R. (2021). The use of waste, fine-grained carbonaceous material in the process of copper slag reduction. *J. Clean. Prod.* 288, 125640. doi:10.1016/j.jclepro.2020.125640

Li, G., Li, X., Qi, X., and Zhang, A. (2021). Copper slag gel encapsulates sludge through encapsulation and precipitation in weakly acidic to strongly basic environments. *J. Clean. Prod.* 294, 126227. doi:10.1016/j.jclepro.2021.126227

Li, J., Otero-Gonzalez, L., Michiels, J., Lens, P. N., Du Laing, G., and Ferrer, I. (2021). Production of selenium-enriched microalgae as potential feed supplement in high-rate algae ponds treating domestic wastewater. *Bioresour. Technol.* 333, 125239. doi:10.1016/j.biortech.2021.125239

Li, T., Xu, H., Zhang, Y., Hu, X., Sun, Y., et al. (2022). Treatment technologies for selenium contaminated water: A critical review. *Environ. Pollut.* 299, 118858. doi:10.1016/j.envpol.2022.118858

Li, Y., Qi, X., Li, G., and Wang, H. (2021). Efficient removal of arsenic from copper smelting wastewater via a synergy of steel-making slag and KMnO4. *J. Clean. Prod.* 287, 125578. doi:10.1016/j.jclepro.2020.125578

Liang, J., Luo, L., Li, D., Varjani, S., Xu, Y., and Wong, J. W. (2021). Promoting anaerobic co-digestion of sewage sludge and food waste with different types of conductive materials: Performance, stability, and underlying mechanism. *Bioresour. Technol.* 337, 125384. doi:10.1016/j.biortech.2021.125384

Liu, X., Wei, J., Wu, Y., Zhang, J., Xing, L., Zhang, Y., et al. (2022). Performances and mechanisms of microbial nitrate removal coupling sediment-based biochar and nanoscale zero-valent iron. *Bioresour. Technol.* 345, 126523. doi:10.1016/j.biortech.2021.126523

Lu, Z., Yu, J., Zeng, H., and Liu, Q. (2017). Polyamine-modified magnetic graphene oxide nanocomposite for enhanced selenium removal. *Sep. Purif. Technol.* 183, 249–257. doi:10.1016/j.seppur.2017.04.010

Man, Y., Wang, B., Wang, J., Slany, M., Yan, H., Li, P., et al. (2021). Use of biochar to reduce mercury accumulation in Oryza sativa L: A trial for sustainable management of historically polluted farmlands. *Environ. Int.* 153, 106527. doi:10.1016/j.envint.2021.106527

Mikula, K., Izydorczyk, G., Skrzypczak, D., Moustakas, K., Witek-Krowiak, A., and Chojnacka, K. (2021). Value-added strategies for the sustainable handling, disposal, or value-added use of copper smelter and refinery wastes. *J. Hazard. Mater.* 403, 123602. doi:10.1016/j.jhazmat.2020.123602

Osman, A. I., Elgarahy, A. M., Mehta, N., Al-Muhtaseb, A. H., Al-Fatesh, A. S., and Rooney, D. W. (2022a). Facile synthesis and Life cycle assessment of highly active magnetic sorbent composite derived from mixed Plastic and biomass waste for water remediation. *ACS Sustain. Chem. Eng.* 10 (37), 12433–12447. doi:10.1021/acssuschemeng.2c04095

Osman, A. I., Fawzy, S., Farghali, M., El-Azazy, M., Elgarahy, A. M., Fahim, R. A., et al. (2022b). Biochar for agronomy, animal farming, anaerobic digestion, composting, water treatment, soil remediation, construction, energy storage, and carbon sequestration: A review. *Environ. Chem. Lett.* 20 (4), 2385–2485. doi:10.1007/s10311-022-01424-x

Solis, K. L. B., Kwon, Y.-H., Kim, M.-H., An, H. R., Jeon, C., and Hong, Y. (2020). Metal organic framework UiO-66 and activated carbon composite sorbent for the concurrent adsorption of cationic and anionic metals. *Chemosphere* 238, 124656. doi:10.1016/j.chemosphere.2019.124656

Suganya, S., and Senthil Kumar, P. (2019). An investigation of adsorption parameters on ZVI-AC nanocomposite in the displacement of Se(IV) ions through CCD analysis. *J. Industrial Eng. Chem.* 75, 211–223. doi:10.1016/j.jiec.2019.03.026

Suliman, W., Harsh, J. B., Abu-Lail, N. I., Fortuna, A. M., Dallmeyer, I., and Garcia-Perez, M. (2016). Modification of biochar surface by air oxidation: Role of pyrolysis temperature. *Biomass Bioenergy* 85, 1–11. doi:10.1016/j.biombioe.2015.11.030

Tong, J., Yang, J., Zhang, L., Liu, T., Peng, C., Ni, X., et al. (2022). Efficient removal of Se-79 from highly acidic solution using SiO2 particles functionalised with iron hydroxide. *Chem. Eng. J.* 446, 137387. doi:10.1016/j.cej.2022.137387

Wang, F., Wang, H., Sun, C., and Yan, Z. (2021). Conventional bioretention column with Fe-hydrochar for stormwater treatment: Nitrogen removal, nitrogen behaviour and microbial community analysis. *Bioresour. Technol.* 334, 125252. doi:10.1016/j.biortech.2021.125252

Wang, H., Cai, J., Liao, Z., Jawad, A., Ifthikar, J., Chen, Z., et al. (2020). Black liquor as biomass feedstock to prepare zero-valent iron embedded biochar with red mud for Cr(VI) removal: Mechanisms insights and engineering practicality. *Bioresour. Technol.* 311, 123553. doi:10.1016/j.biortech.2020.123553

Wang, H., Cui, T., Chen, D., Luo, Q., Xu, J., Sun, R., et al. (2022a). Hexavalent chromium elimination from wastewater by integrated micro-electrolysis composites synthesized from red mud and rice straw via a facile one-pot method. *Sci. Rep.* 12 (1), 14242. doi:10.1038/s41598-022-18598-7

Wang, H., Duan, R., Zhou, X., Wang, J., Liu, Y., Xu, R., et al. (2022b). Efficient removal of mercury and chromium from wastewater via biochar fabricated with steel slag: Performance and mechanisms. *Front. Bioeng. Biotechnol.* 10, 961907. doi:10.3389/fbioe.2022.961907

Wang, H., Liu, Y., Ifthikar, J., Shi, L., Khan, A., Chen, Z., et al. (2018). Towards a better understanding on mercury adsorption by magnetic bio-adsorbents with gamma-Fe2O3 from pinewood sawdust derived hydrochar: Influence of atmosphere in heat treatment. *Bioresour. Technol.* 256, 269–276. doi:10.1016/j.biortech.2018.02.019

Wang, J., Shen, M., Wang, H., Du, Y., Zhou, X., Liao, Z., et al. (2020). Red mud modified sludge biochar for the activation of peroxymonosulfate: Singlet oxygen dominated mechanism and toxicity prediction. *Sci. Total Environ.* 740, 140388. doi:10.1016/j.scitotenv.2020.140388

Wang, L., Li, L., Cheng, K., Ji, C., Yue, Q., Bian, R., et al. (2018). An assessment of emergy, energy, and cost-benefits of grain production over 6 years following a biochar amendment in a rice paddy from China. *Environ. Sci. Pollut. Res.* 25 (10), 9683–9696. doi:10.1007/s11356-018-1245-6

Wang, Q., Luo, C., Lai, Z., Chen, S., He, D., and Mu, J. (2022). Honeycomb-like cork activated carbon with ultra-high adsorption capacity for anionic, cationic and mixed dye: Preparation, performance and mechanism. *Bioresour. Technol.* 357, 127363. doi:10.1016/j.biortech.2022.127363

Wang, Q., Zhang, Z., Xu, G., and Li, G. (2021). Pyrolysis of penicillin fermentation residue and sludge to produce biochar: Antibiotic resistance genes destruction and biochar application in the adsorption of penicillin in water. *J. Hazard. Mater.* 413, 125385. doi:10.1016/j.jhazmat.2021.125385

Wang, T., Yang, Q., Wang, Y., Wang, J., Zhang, Y., and Pan, W. P. (2019). Arsenic release and transformation in co-combustion of biomass and coal: Effect of mineral elements and volatile matter in biomass. *Bioresour. Technol.* 297, 122388. doi:10.1016/j.biortech.2019.122388

Wei, X., Li, X. D., Tang, L., Yu, J. F., Deng, J. Q., Luo, T., et al. (2021). Exploring the role of Fe species from biochar-iron composites in the removal and long-term immobilization of SeO42- against competing oxyanions. *J. Hazard. Mater.* 418, 126311. doi:10.1016/j.jhazmat.2021.126311

Wen, Q., Chen, Y., Rao, X., Yang, R., Zhao, Y., Li, J., et al. (2022). Preparation of magnesium Ferrite-Doped magnetic biochar using potassium ferrate and seawater mineral at low temperature for removal of cationic pollutants. *Bioresour. Technol.* 350, 126860. doi:10.1016/j.biortech.2022.126860

Xiao, W., Yan, B., Zeng, H., and Liu, Q. (2016). Dendrimer functionalized graphene oxide for selenium removal. *Carbon* 105, 655–664. doi:10.1016/j.carbon.2016.04.057

Xiong, J., Wang, H., Yao, J., He, Q., Ma, J., Yang, J., et al. (2022). A critical review on sulfur reduction of aqueous selenite: Mechanisms and applications. *J. Hazard. Mater.* 422, 126852. doi:10.1016/j.jhazmat.2021.126852

Xu, W., Yang, T., Liu, S., Du, L., Chen, Q., Li, X., et al. (2022). Insights into the Synthesis, types and application of iron Nanoparticles: The overlooked significance of environmental effects. *Environ. Int.* 158, 106980. doi:10.1016/j.envint.2021.106980

Yang, F., Du, Q., Sui, L., and Cheng, K. (2021). One-step fabrication of artificial humic acid-functionalized colloid-like magnetic biochar for rapid heavy metal removal. *Bioresour. Technol.* 328, 124825. doi:10.1016/j.biortech.2021.124825

Yan, Y., Meng, Y., Zhao, H., Lester, E., Wu, T., and Pang, C. H. (2021). Miscanthus as a carbon precursor for graphene oxide: A possibility influenced by pyrolysis temperature. *Bioresour. Technol.* 331, 124934. doi:10.1016/j.biortech.2021.124934

Yang, K., Wang, X., Cheng, H., and Tao, S. (2022). Enhanced immobilization of cadmium and lead adsorbed on crop straw biochars by simulated aging processes. *Environ. Pollut.* 302, 119064. doi:10.1016/j.envpol.2022.119064

Yang, X., Pan, H., Shaheen, S. M., Wang, H., and Rinklebe, J. (2021). Immobilization of cadmium and lead using phosphorus-rich animal-derived and iron-modified plant-derived biochars under dynamic redox conditions in a paddy soil. *Environ. Int.* 156, 106628. doi:10.1016/j.envint.2021.106628

Yi, Y., Tu, G., Ying, G., Fang, Z., and Tsang, E. P. (2021). Magnetic biochar derived from rice straw and stainless steel pickling waste liquor for highly efficient adsorption of crystal violet. *Bioresour. Technol.* 341, 125743. doi:10.1016/j.biortech.2021.125743

Zhang, L., Zheng, H., Wu, B., Gan, Y., Zhang, G., and Zhang, S. (2022). Diketone-mediated photochemical reduction of selenite to elemental selenium: Role of carbon-centered radicals and complexation. *Chem. Eng. J.* 445, 136831. doi:10.1016/j.cej.2022.136831

Zhang, X., Wang, L., Zeng, T., Liu, Y., Liu, J., et al. (2022). The removal of selenite and cadmium by immobilized biospheres: Efficiency, mechanisms and bacterial community. *Environ. Res.* 211, 113025. doi:10.1016/j.envres.2022.113025

Zhao, R., Wang, B., Theng, B. K. G., Wu, P., Liu, F., Lee, X., et al. (2021). Fabrication and environmental applications of metal-containing solid waste/biochar composites: A review. *Sci. Total Environ.* 799, 149295. doi:10.1016/j.scitotenv.2021.149295

Zhao, Z., Wang, Z., Xu, W., Qin, W., Lei, J., Dong, Z., et al. (2021). Arsenic removal from copper slag matrix by high temperature sulfide-reduction-volatilization. *J. Hazard. Mater.* 415, 125642. doi:10.1016/j.jhazmat.2021.125642

Zhou, X., Jawad, A., Luo, M., Luo, C., Zhang, T., Wang, H., et al. (2021). Regulating activation pathway of Cu/persulfate through the incorporation of unreducible metal oxides: Pivotal role of surface oxygen vacancies. *Appl. Catal. B Environ.* 286, 119914. doi:10.1016/j.apcatb.2021.119914

Zhu, S., Yang, X., Zhang, Z., Zhang, H., Li, Y., Zhang, Y., et al. (2021). Tolerance of photo-fermentative biohydrogen production system amended with biochar and nanoscale zero-valent iron to acidic environment. *Bioresour. Technol.* 338, 125512. doi:10.1016/j.biortech.2021.125512

frontiers | Frontiers in Environmental Science

TYPE Original Research
PUBLISHED 17 November 2022
DOI 10.3389/fenvs.2022.1058071

OPEN ACCESS

EDITED BY
Guanghui Yu,
Tianjin University, China

REVIEWED BY
Ning Ling,
Nanjing Agricultural University, China
Dan Wan,
Tiangong University, China

*CORRESPONDENCE
Jianning Zhao,
zhaojianning@caas.cn
Dianlin Yang,
yangdianlin@caas.cn

SPECIALTY SECTION
This article was submitted to Soil Processes,
a section of the journal
Frontiers in Environmental Science

RECEIVED 04 October 2022
ACCEPTED 01 November 2022
PUBLISHED 17 November 2022

CITATION
Zhou Z, Zhang S, Jiang N, Xiu W, Zhao J and Yang D (2022), Effects of organic fertilizer incorporation practices on crops yield, soil quality, and soil fauna feeding activity in the wheat-maize rotation system.
Front. Environ. Sci. 10:1058071.
doi: 10.3389/fenvs.2022.1058071

Effects of organic fertilizer incorporation practices on crops yield, soil quality, and soil fauna feeding activity in the wheat-maize rotation system

Zhongkai Zhou[1,2], Siyu Zhang[1], Na Jiang[1], Weiming Xiu[1], Jianning Zhao[1]* and Dianlin Yang[1]*

[1]Agro-Environmental Protection Institute (CAAS), Ministry of Agriculture and Rural Affairs, Tianjin, China, [2]Key Laboratory for Protected Agricultural Engineering in the Middle and Lower Reaches of Yangtze River, Ministry of Agriculture and Rural Affairs, Institute of Facilities and Equipment in Agriculture, Jiangsu Academy of Agricultural Sciences, Nanjing, China

The decline in soil quality is becoming a significant process of soil degradation. Optimizing organic fertilizer incorporation practices in cropland is essential to enhancing crop productivity and soil health. However, that requires a comprehensive understanding of crop yield and soil quality reaction across an application gradient of organic fertilizer. We investigated the effect of organic fertilizer incorporation practices on crop yield, soil quality, and fauna feeding activity from fluvo-aquic soils on wheat (*Triticum aestivum*)-maize (*Zea mays*) rotation field. The six treatments included were unfertilized N control (UC), traditional chemical fertilizer application (TF, 600 N kg ha^{-1} year^{-1}), and recommended chemical fertilization (RF, 400 N kg ha^{-1} year^{-1}) with no organic fertilizer application rate, low-level 15.0 (RFLO), medium-level 30.0 (RFMO), and high-level 45.0 t ha^{-1} year^{-1} (RFHO) application, respectively. The research findings show that the yield with organic fertilizer incorporation treatments increased 26.4%–44.6% for wheat and 12.5%–40.8% for maize compared to RF plots. The long-term organic fertilizer incorporation rate increased organic carbon from 54.7% to 110.6% versus UC plots and 27.9%–74.0% versus chemical fertilizer (TF and RF) treatments, and the total nitrogen content of soil increased from 41.8% to 59.2%, and 24.6%–39.2%. The long-term inorganic fertilizer combined with organic fertilizer incorporation practices significantly enhanced soil sucrose (30.1%–51.9%), urease (28.4%–38.3%), and β-1,4-glucosidase (34.6%–122.4%) activity. Still, nitrite reductase, polyphenol oxidase, and catalase significantly lower 27.3%–49.9%, 8.5%–26.3% and 23.3%–34.3% than single applications of inorganic N fertilizer groups. Meanwhile, the results showed that organic fertilizer incorporation practices improved soil fauna feeding activity by 35.2%–42.5%, and the excessive application of inorganic N fertilizer reduced the activity level of soil fauna.

KEYWORDS

soil organic carbon, soil nutrients, organic fertilizer incorporation, soil enzymes, soil fauna feeding activity, feeding activity

Introduction

Organic fertilizers are materials with defined chemical composition and high nutritional value that can provide adequate nutrients for plant growth (Moller and Schultheiss, 2015; Rajan and Anandhan, 2015). Organic fertilizers were mainly made by composting animal manure, human excrement, or plant matter (such as straw and garden waste) under microorganisms fermenting at high temperatures (Chew et al., 2019). Organic fertilizers improve the soil structure, provide a wide range of plant nutrients, and add beneficial microorganisms to the soil. Because of the benefits of organic fertilizers on soil structure and crop yield were widely used in the agricultural system (Brar et al., 2015; Maltas et al., 2018).

Organic fertilization practices can improve crop yields and soil quality, and combining organic and inorganic fertilizers was considered an effective solution to maintain the sustainability of crop ecosystems (Gentile et al., 2008). The application of organic fertilizers can not only improve soil structure and fertility, and increase soil organic carbon and other nutrients (Diacono and Montemurro, 2010; Liu et al., 2010). Many studies have shown that applying organic fertilizers to the soil surface can provide a rich food source for microorganisms and significantly increase microbial community composition and diversity compared to no application (Chang et al., 2007; Diacono and Montemurro, 2010). In addition, applying organic fertilizers significantly changes cation exchange capacity (CEC) and increases soil moisture content, causing changes in soil fauna community structure and composition in acidic soils (Zelles et al., 1992; Abbott and Murphy, 2007). Adding organic fertilizers benefits the formation and stability of earthworm communities due to the more stable nutrients in organic manure after aerobic fermentation (Bertrand et al., 2015). In contrast, others have found that long-term use of chemical fertilizers may reduce soil OM content and change the activity of soil biota, resulting in changes in soil microbial composition, and resulting in decreased soil invertebrates abundance and diversity due to environmental constraints and reductions in soil pH (Fauci and Dick, 1994; Davies et al., 2022). Wahyuningsih et al. (2019) show that the short-term applications of inorganic fertilizers (urea) significantly increased the soil fauna feeding activity after 2 days, compared to before the application. Tao et al. (2016) also show that soil organic matter (empty fruit bunch) plays an important role in soil ecosystem functioning by enhancing soil fauna feeding activity. Therefore, many studies have announced the effects of fertilization practice on soil nutritions, but the effects of inorganic combined with organic fertilizers on soil biota remain unclear.

In the wheat-maize rotation system, long-term fertilization is an essential factor affecting soil physicochemical properties and biota functions (Welbaum et al., 2004; Kaiser et al., 2007; Thomas et al., 2007; Miao et al., 2011; Chen et al., 2015b; Miller et al., 2020; Miner et al., 2020), and its response mechanism is mainly related to local climatic conditions, soil types, and fertilizer types (Lupwayi et al., 2011; Yu et al., 2015). Qaswar et al. (2020) and Gao et al. (2015) studies show that combining organic and inorganic fertilizers is one of the essential techniques to replace part of the inorganic chemical fertilizers and stabilize wheat and maize yield. Many studies have shown that replacing 20%–30% of chemical fertilizers with organic fertilizers can increase wheat-maize yields and improve soil availability and organic matter (Zhang et al., 2016b). Then, the applications of organic fertilizers were a relatively large range of variation, and the fresh weight of compost was generally from 10.0 to 35.0 t ha^{-1} (Hannet et al., 2021), and the application rate of dry matter of compost between 8.8 and 14.0 t ha^{-1}, but liquid manure up to 68.3 t ha^{-1} (Feng et al., 2013). This suggests the need for a better balance of the impact of fertilization with different organic fertilizer incorporation rates on the wheat-maize rotation system. Moreover, few have conducted long-term investigations of inorganic chemical fertilizers combined application of organic fertilizers with different incorporation rates for soil quality and health, including total soil carbon, organic carbon, nutrients, enzyme activities, and soil fauna activities.

The study aimed to determine the influence of inorganic combined with organic fertilizer incorporation practices (high, medium, and low levels) on crop yields, soil quality, and the fauna feeding activity on fluvo-aquic soil in north China.

Methods and materials

Site description

The research treatments were set up starting in 2015 at Tianjin Experimental Farm (TEF), which is located in the suburbs of Tianjin, North China (39°28′N, 117°42′E, Supplementary Figure S1). The region belongs to a temperate monsoon climate, with an annual mean air temperature of 12.9°C and rainfall 586 mm, respectively (2015–2020) (Zhou et al., 2021). Rainfall is concentrated between July and September, with a tremendous annual variation. This soil was classified as fluvo-aquic soil, and the values of TN, OM, TP, and pH in soil (0–20 cm) were 0.82, 12.6, 0.80 and 8.1 g kg^{-1}, respectively.

Experimental design

The research treatments were conducted on a wheat-maize rotation system with the same cultivation and management practice from October 2019 to October 2020. In previous

TABLE 1 Application rates of fertilizers under different fertilization treatments.

Treatment	2019				2020				
	October				April	June			August
	Organic	N	P	K	N	N	P	K	N
	($t \cdot ha^{-1}$)	($kg \cdot ha^{-1}$)							
UC	0	0	50	50	0	0	50	50	0
RF	0	120	50	50	80	120	50	50	80
RFLO	15	120	50	50	80	120	50	50	80
RFMO	30	120	50	50	80	120	50	50	80
RFHO	45	120	50	50	80	120	50	50	80
TF	0	180	50	50	120	180	50	50	120

years, all wheat-maize straw was returned to the field following management practices. The six trial treatments of each area being 288 m^2 with three replicates, were established in 2015. The treatments included were unfertilized N control (UC), traditional chemical fertilizer application (TF, 600 N $kg \cdot ha^{-1}$ $year^{-1}$), and recommended chemical fertilization (RF, 400 N $kg \cdot ha^{-1}$ $year^{-1}$) with zero organic fertilizer (O) application rate, low-level 15.0 (RFLO), medium-level 30.0 (RFMO), and high-level 45.0 t ha^{-1} $year^{-1}$ (RFHO) application, respectively. The recommended fertilization was based on the local soil characteristics and the crop target yield, combined with precision irrigation conditions (Cai and Qin., 2006; Yang et al., 2015). The recommended inorganic NPK fertilizers were urea (46.4% N), diammonium phosphate (18% N and 20.09% P), and potassium chloride (49.6% K), respectively (Zhou et al., 2021). In this study, inorganic nitrogen fertilizer was the limiting factor; when applying inorganic N fertilizer, simultaneously apply 200 kg ha^{-1} $year^{-1}$ P and K fertilizer as base fertilizer. The organic fertilizer was produced through high-temperature fermentation of garden wastes and agricultural straw, by Xixing Fertilizer Technology Co., Ltd. (Shijiazhuang, China). The values of OM, TN, and TP in organic fertilizer were 86.6 ± 4.9, 6.18 ± 0.10, and 3.39 ± 0.07 g kg^{-1}, respectively (Zhou et al., 2021). The inorganic NPK rate in each wheat and maize season was half the annual application amount in six trial treatments, respectively. The application rates of fertilizers under different fertilization treatments was shown in Table 1. Two-thirds of the inorganic nitrogen fertilizer and the entire quantity diammonium phosphate and muriate potash fertilizer was applied when sowing as basal fertilizer, and one-third of nitrogen fertilizer is mainly used for top-dressing applications of wheat and maize, respectively. The organic fertilizer was applied to the soil surface by scattering before wheat sowing and incorporated into the topsoil by rotary tillage.

Field sampling and processing

The quadrat method determined the winter wheat yield by harvesting three 1 m^2 sampling areas per treatment (Lu et al., 2018). At the summer maize maturity stage, 20 plants were randomly selected from the middle row of each plot and harvested manually to determine the yield (Lu et al., 2018). The remaining crop was harvested mechanically.

Less than 1 week after harvest, three soil samples (each was a composite of five cores that formed one sample, 5.0 cm in diameter) were collected from each treatment at 20 cm depth on 24 October 2019 and 22 October 2020 to determine the chemical properties (Zhou et al., 2021). The chemical properties of soil were determined, including TC, TOC, TN, AN, TP, AP, TK, exchangeable Ca, Mg, K, Na concentrations, and CEC, EC, and soil pH values. The pH value and electric conductivity (EC) of the soil were measured with a glass electrode and extracted in a 1:2.5 soil/water (H_2O) suspension after being allowed to stand for 30 min (Zhang et al., 2016b). The Dumas dry-combustion method analyzed all dry soil samples collected for total soil nitrogen (TC) and soil nitrogen (TN) contents using a PerkinElmer 2400 Series II CHNS/O Analyzer (PerkinElmer Inc., Shelton, CT, United States). Soil total organic carbon (TOC) was determined using $K_2Cr_2O_7$–H_2SO_4 digestion. The alkaline hydrolysis diffusion method determined the available soil nitrogen (AN). The molybdenum blue colorimetrically determined the soil's total phosphorus (TP) content after extraction with a mixed acid solution of H_2SO_4 and $HClO_4$. Available phosphorus (AP) was determined colorimetrically after sodium bicarbonate extraction at pH 8.5. The content of total potassium (TK) in soil was determined by flame photometer

detection using H_2SO_4–H_2O_2 digestion (Bao, 2008; Sunnemann et al., 2021). The concentrations of exchangeable Na, Mg, K, and Ca in soil were measured by ICP-OES (Agilent, 710 Series) after extraction with 1.0 mol L^{-1} ammonium acetate (Setia et al., 2013). The cation exchange capacity (CEC) was calculated with colorimetrically after using a hexamminecobalt (III) chloride extraction (ISO, 2018). Air-dried soil samples were sifted through a 2 mm sieve for soil enzyme activity determination. The six soil enzymes activity involved in C and N cycling were studied, including soil catalase, soil nitrite reductase, soil sucrase, soil urease, soil polyphenol oxidase, and soil β-1,4-glucosidase, and was determined spectrophotometrically with the soil enzyme kits provided by Suzhou Comin Biotechnology Company Limited (Suzhou, China) (Liu et al., 2018; Gao et al., 2019).

Soil fauna feeding activity

Törne (1990) set up the bait lamina test for soil fauna feeding activity for soil environmental quality assessment. The bait lamina is made of polyvinyl chloride board (PVC board, gray), and the size by 120 mm × 6.0 mm × 1.0 mm (length × width × thickness) with a set of 16 double tapered holes (inner diameter 1.5 mm, outer diameter 2.0 mm) at the lower 85 mm, with the aperture spacing of 5 mm (Römbke et al., 2006). The standard feed for bait lamina filling usually consists of 70% cellulose (microparticles), 27% bran flakes (<500 mm), and 3% activated carbon (Eisenhauer et al., 2014). After filling double tapered holes with standard feed, insert the bait strip vertically into the soil, and the top hole was just below the soil surface (Supplementary Figure S2). In this study, soil fauna activities were measured from September 15 to 30 in 2019 and September 9 to 24 in 2020, respectively. Five test areas were set up for each treatment, and 5 strips per area were placed about 15–20 cm apart to monitor the feeding activities of soil fauna with 150 bait lamina in total. After 2 weeks of monitoring, the bait strips were taken from the soil and evaluated with filled (0), partly empty (0.5), and empty (1) (Vorobeichik and Bergman, 2021), to calculate the number of perforated bait strips at each study site and evaluate the percentage of perforated bait strips to the number of test holes in the field. In this study, soil temperature was measured using a HOBO U23-003 sensor (Onset Computer Corporation, Pocasset, MA, United States).

Statistical analysis

Statistical analysis used the Statistical Analysis System (SAS 9.2) software package and Origin Pro 2022 software. Analysis of variance and comparisons of means between treatments was determined using Duncan's multiple range test, and correlations between soil chemical properties were determined using Spearman's correlation coefficient analysis. Treatment impacts were reported to be significant at the 5% probability level.

Results

Crop production

The grain yields of wheat and maize according to fertilization management practices are shown in Figure 1. Different fertilization management practices significantly affect wheat and maize yields, and there was no significant difference in the yield of wheat and maize between different years (Table 2). The grain yields ranged from 0.68 to 6.35 t ha^{-1} for wheat and 5.40 to 9.77 t ha^{-1} for maize in 2018–2020. There was no difference in the wheat yields between different organic fertilizer (RFLO, RFMO, RFHO) incorporation and traditional fertilization (TF) treatments in 2018–2019, while the RFHO and TF significantly ($p < 0.05$) increased the maize yield by 34.7%, 36.6% as compared with RF, respectively. In 2019–2020, the medium and high organic fertilizer (RFMO, RFHO) incorporation and TF treatments increased the wheat yield by 36.4%, 50.6%, and 41.5% compared to RF, respectively ($p < 0.05$). There was no difference in wheat yields between RFMO, RFHO, and TF treatments. Similar to the 2018–2019 year, the RFHO and TF plots increased the maize yield by 47.2%, and 42.8% compared to RF, respectively ($p < 0.05$).

Soil physicochemical properties

Table 3 shows the soil chemical variables under each soil fertilizer management practice at 0–20 cm soil depth. Eleven variables were significantly affected by long-term inorganic combined with organic fertilizer incorporation practices compared with inorganic fertilizer plots (Table 3). The soil chemical parameters were significant correlations (Table 4). Organic fertilizer incorporation led to significant changes in total organic carbon (TOC) and total carbon (TC), levels of soil nutrients (Total N and P, Available N and P), and soil chemical properties of RFHO, RFMO, and RFLO plots, as compared to the RF and TF. The long-term organic fertilizer incorporation rate increased total organic carbon (TOC) from 54.7% to 110.6% versus unfertilized soil and 27.9%–74.0% versus chemical fertilizer treatments. TC content showed the same trend as TOC, increasing 19.5%–49.1% compared with UC and 17.2%–46.3% compared with RF. Soil total organic carbon (TC) and total organic carbon (TOC) increased positively under organic fertilizer plots with higher 2.2–6.0 g kg^{-1} for TC, and 2.4–6.4 g kg^{-1} for TOC than RF.

The contents of total soil nitrogen (TN) and available nitrogen (AN) in the organic fertilizer incorporation plots increased significantly by 41.8%–59.2%, 56.1%–82.7% versus

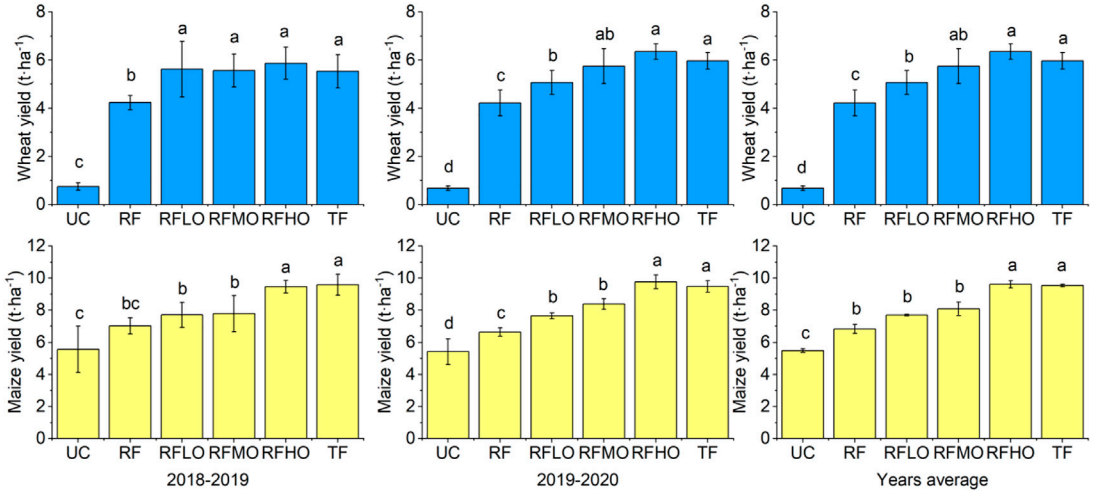

FIGURE 1
Wheat and maize yield (2018–2019, 2019–2020) is according to fertilization management practices. UC, unfertilized control; RF, recommended mineral fertilizer application of 400 kg ha^{-1} N; RFLO, RF plus 15 t ha^{-1} of organic fertilizer; RFMO, RF plus 30 t ha^{-1} of organic fertilizer; RFHO, RF plus 45 t ha^{-1} of organic fertilizer; TF, traditional mineral fertilizer application of 600 kg ha^{-1} N, whole wheat-maize growing season. The same letters are not significantly different at 5% level by Duncan's Multiple Range Test.

TABLE 2 Effects of fertilizer management practices and years on crop yield.

	Wheat			Maize		
	DF	F Value	*p* Value	DF	F Value	*p* Value
Treatment (T)	5	143.0	$p < 0.0001$	5	61.22	$p < 0.0001$
Yearly (Y)	1	0.3167	0.5757	1	0.04022	0.8417
Treatment * yearly	5	1.266	0.2901	5	0.7645	0.5790

unfertilized soil (UC), and 24.6%–39.2%, 25.6%–46.9% compared with the application of recommended mineral fertilizer (RF), with the increase of the amount of organic fertilizer. Still, RFLO, RFMO, and RFHO treatments did not reach a significant level ($p > 0.05$). Compared with the RF treatment, the contents of total phosphorus (TP) and available phosphorus (AP) in the RFHO plots increased by 33.3% and 95.4%, respectively, and RFMO plots increased by 37.0% and 115.8%, and RFLO plots increased by 18.2% and 43.2%, respectively. However, there was no significant difference between RFHO and RFMO treatments ($p > 0.05$). Soil TK concentration remained at the same levels across all plots.

Compared with the UC, the fertilization treatment plots pH decreased by 0.49%–5.68%, while the organic fertilizer (RFLO, RFMO, RFHO) incorporation significantly reduced the pH by 3.40%, 5.44%, and 5.68% ($p < 0.05$), respectively. The content of exchangeable Ca in the organic fertilizer incorporation was significantly lower 10.05%, 7.64%, and 9.82%, than in the TF plots ($p < 0.05$). While no difference in the exchangeable Mg and CEC between different organic fertilizer (RFLO, RFMO, RFHO) incorporation and chemical fertilizer plots. The contents of exchangeable K and Na in the organic fertilizer incorporation plots significantly increased 49.4%–122.2%, and 21.4%–107.4%, compared with inorganic fertilizer. Figure 2 shows PCA for soil characteristics according to fertilization management practices. The PCA results show that the cumulative contribution of the first three principal components reached 84.7% (PC1: 62.9%; PC2: 13.8%; PC3: 8.0%; Supplementary Table S1).

Soil enzyme activity

Organic fertilizer incorporation led to significant changes in the nitrite reductase, catalase, sucrase, urease, β-1,4-

TABLE 3 Soil chemical variables under each soil fertilizer management practice at 0–20 cm soil depth.

Soil chemical index	UC	RF	RFLO	RFMO	RFHO	TF
Total N ($g{\cdot}kg^{-1}$)	0.98 ± 0.05b	1.12 ± 0.04b	1.39 ± 0.06a	1.48 ± 0.15a	1.56 ± 0.14a	1.11 ± 0.11b
Available N ($mg{\cdot}kg^{-1}$)	46.3 ± 4.13c	57.6 ± 9.06bc	72.3 ± 5.76ab	81.4 ± 13.21a	84.6 ± 12.63a	52.1 ± 5.26c
Total carbon ($g{\cdot}kg^{-1}$)	12.7 ± 0.5c	12.9 ± 0.5c	15.1 ± 1.2bc	17.2 ± 1.9ab	18.9 ± 2.5a	13.1 ± 1.2c
Total organic carbon ($g{\cdot}kg^{-1}$)	7.19 ± 0.57c	8.7 ± 0.57c	11.12 ± 0.66b	14.28 ± 0.94a	15.14 ± 2.54a	7.88 ± 0.61c
Total P ($g{\cdot}kg^{-1}$)	0.83 ± 0.05bc	0.86 ± 0.12bc	1.02 ± 0.08ab	1.18 ± 0.19a	1.15 ± 0.09a	0.81 ± 0.0c
Available P ($mg{\cdot}kg^{-1}$)	50.6 ± 10.2cd	55.1 ± 29.9cd	79.0 ± 17.3bc	119 ± 33.3a	107.7 ± 15.4ab	30.2 ± 5.2d
Total K ($g{\cdot}kg^{-1}$)	18.4 ± 0.69a	18.9 ± 0.89a	19.2 ± 0.35a	19.0 ± 0.57a	19.3 ± 0.86a	18.9 ± 0.52a
Exchangeable Ca ($mg{\cdot}kg^{-1}$)	5142 ± 236ab	5139 ± 241ab	4833 ± 245b	4963 ± 236b	4846 ± 205b	5374 ± 125a
Exchangeable K ($mg{\cdot}kg^{-1}$)	337 ± 37c	394 ± 43c	588 ± 51.7b	766 ± 98.8a	843 ± 136.3a	380 ± 28.9c
Exchangeable Mg ($mg{\cdot}kg^{-1}$)	1015 ± 43.2b	1133 ± 53.6a	1165 ± 43a	1186 ± 36.9a	1155 ± 41.2a	1192 ± 10.9a
Exchangeable Na ($mg{\cdot}kg^{-1}$)	267 ± 28.5c	253 ± 27.8c	348 ± 96.7bc	465 ± 105.1ab	524 ± 129.7a	287 ± 54.5c
pH	8.25 ± 0.18a	8.12 ± 0.28ab	7.97 ± 0.12ab	7.8 ± 0.29b	7.78 ± 0.19b	8.21 ± 0.25a
Electric conductivity (μs/cm)	309 ± 80c	367 ± 91bc	427 ± 82bc	493 ± 91ab	593 ± 91a	376 ± 64bc
CEC ($cmol{\cdot}kg^{-1}$)	16.1 ± 0.62b	18.8 ± 0.74a	19.9 ± 0.38a	19.7 ± 0.83a	19.9 ± 0.83a	18.9 ± 0.54a

Values are means ± SD. Means followed by the different lower case letters are significantly different at 5% level by Duncan's multiple range test.

TABLE 4 Spearman's correlation coefficients between soil chemical variables.

Variable	TN	AN	TC	TOC	TP	AP	TK	Ca	K	Mg	Na	pH	EC
TN	1												
AN	0.92***	1											
TC	0.92***	0.84***	1										
TOC	0.91***	0.91***	0.83***	1									
TP	0.82***	0.83***	0.79***	0.84***	1								
AP	0.75***	0.74***	0.74***	0.81***	0.83***	1							
TK	0.24ns	0.37*	0.19ns	0.34*	0.25ns	0.0ns	1						
Ca	−0.46**	−0.30ns	−0.38*	−0.47**	−0.39*	−0.53***	−0.04ns	1					
K	0.93***	0.93***	0.91***	0.93***	0.85***	0.75***	0.35*	−0.32ns	1				
Mg	0.37*	0.46**	0.37*	0.29ns	0.20ns	0.03ns	0.18ns	0.38*	0.44**	1			
Na	0.72***	0.64***	0.75***	0.69***	0.63***	0.69***	0.20ns	−0.43**	0.72***	0.11ns	1		
pH	−0.71***	−0.80***	−0.70***	−0.71***	−0.85***	−0.65***	−0.37*	0.05ns	−0.78***	−0.40*	−0.44**	1	
EC	0.59***	0.42**	0.59***	0.58***	0.50**	0.58***	0.09ns	−0.71***	0.52**	0.04ns	0.65***	−0.27ns	1
CEC	0.75***	0.83***	0.69***	0.69***	0.67***	0.49**	0.32ns	−0.09ns	0.79***	0.66***	0.44**	−0.74***	0.30ns

Significance levels are * 0.05, ** 0.01, *** 0.001, respectively, *ns*, not significant. TN, total N concentration ($g{\cdot}kg^{-1}$); AN, available nitrogen ($mg{\cdot}kg^{-1}$); TC, total C concentration ($g{\cdot}kg^{-1}$); TOC, organic C concentration ($g{\cdot}kg^{-1}$); TP, total P concentration ($g{\cdot}kg^{-1}$); AP, available P concentration ($mg{\cdot}kg^{-1}$); TK, total K concentration ($g{\cdot}kg^{-1}$); Ca, exchangeable Ca concentration ($mg{\cdot}kg^{-1}$); K, exchangeable K concentration ($mg{\cdot}kg^{-1}$); Mg, exchangeable Mg concentration ($mg{\cdot}kg^{-1}$); Na, exchangeable Na concentration ($mg{\cdot}kg^{-1}$); EC, electrical conductivity ($\mu s{\cdot}cm^{-1}$); CEC, cation exchange capacity ($cmol{\cdot}kg^{-1}$).

glucosidase, and polyphenol oxidase at different plots (Table 5). Compared to RF plots, organic fertilizer incorporation plots significantly increased by 28.4%–38.3%, 34.6%–122.4%, and 30.1%–51.9% of soil urease, β-1,4-glucosidase, and sucrase activity ($p < 0.05$). The nitrite reductase and catalase activity in the organic fertilizer plots was 3.17–4.59 $\mu mol\ d^{-1}\ g^{-1}$ and 14.9–17.2 $\mu mol\ d^{-1}\ g^{-1}$, significantly lower 27.3%–49.9%, and 23.3%–34.3% than in the RF plots, respectively ($p < 0.05$). In the TF plots, the activity of nitrite reductase increased 98.7% and 27.6% more than in all organic fertilizer treatments and RF plots ($p < 0.05$). Compared with organic fertilizer treatments and RF plots, the polyphenol oxidase activity of TF plots increased by 65.5% and 35.3%, respectively. However, the activity of polyphenol oxidase was not significantly different between TF and UC plots ($p < 0.05$).

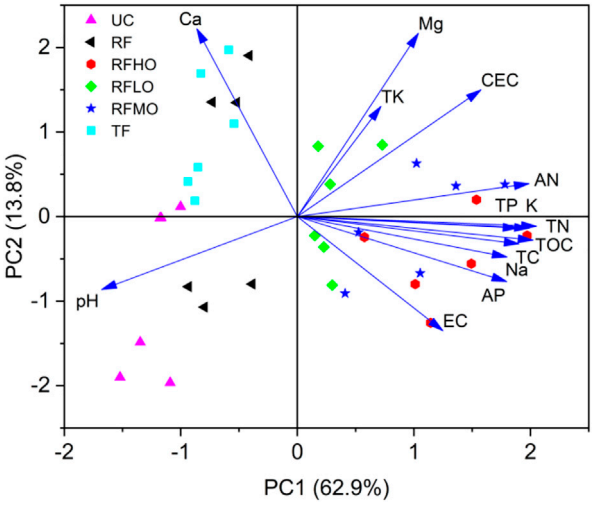

FIGURE 2
Principal component analysis (PCA) for soil chemical characteristics (2019, 2020) is formed by the first principal component (PC1) and the second principal component (PC2) according to fertilization management practices. * Ca, exchangeable Ca concentration (mg·kg^{-1}); Mg, exchangeable Mg concentration (mg·kg^{-1}); TK, total K concentration (g·kg^{-1}); CEC, cation exchange capacity (cmol·kg^{-1}); AN, available nitrogen (mg·kg^{-1}); TP, total P concentration (g·kg^{-1}); K, exchangeable K concentration (mg·kg^{-1}); TN, total N concentration (g·kg^{-1}); TOC, organic C concentration (g·kg^{-1}); TC, total C concentration (g·kg^{-1}); Na, exchangeable Na concentration (mg·kg^{-1}); AP, available P concentration (mg·kg^{-1}); EC, electrical conductivity (μs·cm^{-1}).

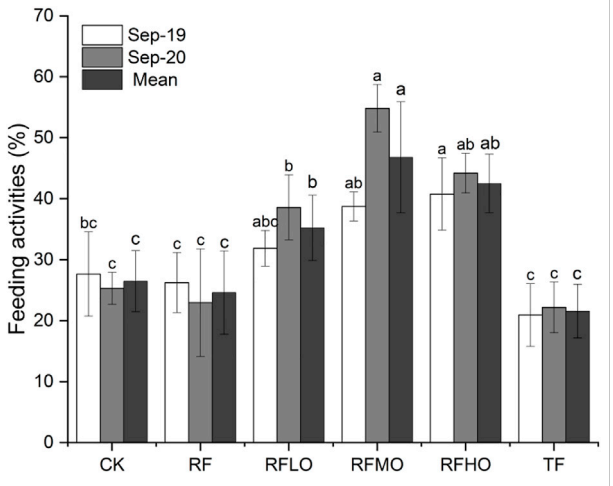

FIGURE 3
Feeding activities (%) in the six fertilization management practices were determined by the bait-lamina test (n = 150 bait laminae) after 15 days of exposure in September 2019, and 2020. The data are median values, and the vertical bars represent SDs. Columns marked by different letters indicate significant differences at $p < 0.05$.

Soil fauna feeding activity

This study significantly reduced soil fauna feeding activity in inorganic fertilizer plots. The feeding activities of soil fauna in the traditional fertilization (TF) and recommended fertilization (RF) site were lower than in all the other plots, about 24.6% in the RF site and 21.6% in the TF site (Figure 3). We measured the highest average feeding activities in RFLO (35.2%), RFMO (46.8%), and RFHO (42.5%) compared with the other three investigation sites between 2019 and 2020. In RFLO, RFMO, and RFHO, adjoint with increased organic fertilizer incorporation, soil fauna feeding activities were significantly increased compared with RF and TF plots; however, the differences were not statistically significant in RFMO and RFHO plots. Furthermore, RFLO (31.9%) and RFMO (38.8%) in 2019, which had been treated additionally with organic fertilizer, showed higher feeding activities than UC (26.3%), but not significant. Throughout the 0–8 cm soil depth, the UC, RF, and TF treatments showed identical distributions, while RFLO, RFMO, and RFHO had consistent distribution trends (Figure 4). Compared with the organic fertilizer sites, feeding activities in RF and TF treatments showed that they rapidly decreased with increasing soil depth, compared with RFLO, RFMO, and RFHO, and reached a plateau after 4 cm. In the 0–6 cm layer soil depth, the soil fauna feeding activity in organic fertilizer plots was significantly higher compared with the UC and inorganic fertilizer plots (Figure 4).

Discussion

Effect of organic fertilizer incorporation on crop yields

The results showed that compared with the recommended fertilization, the application of organic fertilizer significantly increased the yield of wheat ($p < 0.05$). Compared with the recommended fertilization (RF), the treatment of medium (RFMO) and low organic fertilizer (RFLO) had no significant influence on maize yield ($p > 0.05$), and the RFMO and RFLO plots were significantly lower than the high amount of organic fertilizer (RFHO) and the traditional fertilization treatment (TF). Similarly, Yang et al. (2014) reported that combinations of organic and inorganic nitrogen are likely to increase achievable yields and improve soil fertility with the wheat-maize system. This might be due to all organic fertilizers being used as base fertilizers in the wheat season, all chemical fertilizers being used in maize planting, and organic fertilizer incorporation into the soil, which increased soil OM contents, soil water availability, and aeration (Choudhary et al., 2018; Li et al., 2020). Welbaum et al.

TABLE 5 Soil enzyme variables under each soil fertilizer management practice at 0–20 cm soil depth.

Soil enzyme index	UC	RF	RFLO	RFMO	RFHO	TF
S-NiR (μmol·d^{-1}·g^{-1})	3.52 ± 0.32de	6.32 ± 0.37b	4.59 ± 0.49cd	4.85 ± 0.70c	3.17 ± 0.19e	8.06 ± 0.58a
S-CAT (μmol·d^{-1}·g^{-1})	23.4 ± 0.99a	22.8 ± 0.74a	17.4 ± 0.69b	17.2 ± 0.71b	14.9 ± 0.70c	18.4 ± 0.27b
S-SC (mg·d^{-1}·g^{-1})	1.90 ± 0.40d	2.53 ± 0.16c	3.84 ± 0.31a	3.28 ± 0.13ab	3.39 ± 0.01ab	3.11 ± 0.05bc
S-UE (μg·d^{-1}·g^{-1})	624 ± 55c	736 ± 28bc	1017 ± 43a	945 ± 44a	990 ± 21a	827 ± 47b
S-B-GC (μmol·d^{-1}·g^{-1})	14.3 ± 0.66bcd	11.2 ± 0.56d	15.0 ± 0.32bc	24.8 ± 2.86a	17.1 ± 0.56b	13.4 ± 0.92cd
S-PPO (mg·d^{-1}·g^{-1})	32.9 ± 1.70ab	27.1 ± 1.44bc	20.0 ± 2.0d	24.8 ± 2.5cd	22.2 ± 4.72cd	36.6 ± 0.98a

S-NiR, nitrite reductase; S-CAT, catalase; S-SC, sucrase; S-UE, urease; S-B-GC, β-1,4-glucosidase; S-PPO, polyphenol oxidase. Values are means ± SD. Means followed by the different lower case letters are significantly different at 5% level by Duncan's multiple range test.

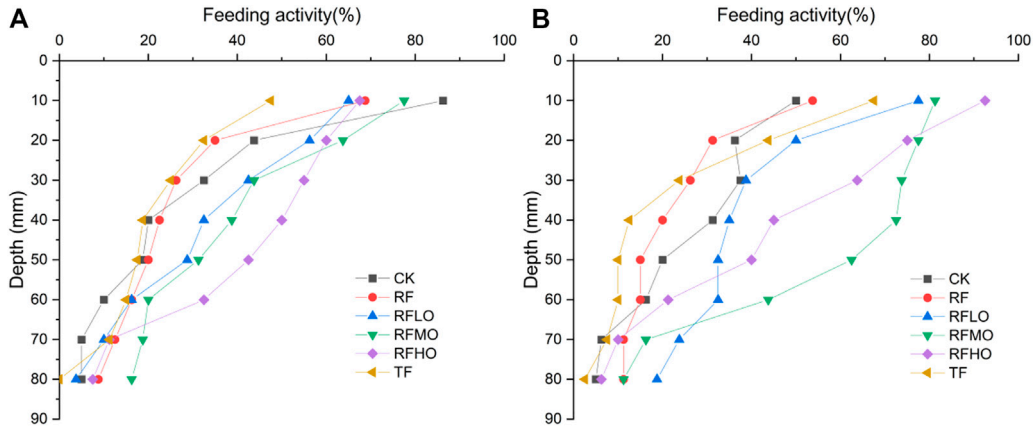

FIGURE 4
Depth profiles of the feeding activities (%) in the six fertilization management practices were determined by the bait-lamina test (*n* = 150 bait laminae) after 15 days of exposure in September 2019 **(A)**, and 2020 **(B)**.

(2004) and Li et al. (2012) reported that when organic fertilizers incorporation can delay the senescence rate of crop roots and leaves, prolong the photosynthetic time of crops, increase the grain quality of ears by prolonging the grain filling time, and finally increase the yield. Studies have shown that the recommended fertilization amount requires good water and fertilizer management to maximize crop yield (Zhang et al., 2021). The lower wheat yield in the recommended fertilization amount in this study may be caused by flood irrigation resulting in reduced plant availability of nitrogen (Li and Rao, 2003; Shang et al., 2015). The traditional fertilization (TF) could increase crop yields, indicating that inorganic N fertilizer input significantly affects crop yields; the soil organic fertilizers incorporation significantly affects TOC content and yields (Table 2). This result suggests that long-term studies were required to identify the effect of the inorganic combined with organic fertilizers on wheat-maize yield constraints and soil fertility.

Effect of organic fertilizer incorporation on soil chemical properties

The combined application of organic-inorganic fertilizers can provide quick-acting nutrients for crop growth, and effectively increase fertilizer efficiency and ensure the continuous supply of soil nutrients (Diacono and Montemurro, 2010). This study found that organic fertilizer incorporation benefited TC and TOC content, and medium and high levels (>30 t ha^{-1} year^{-1}) significantly increased TC, and TOC contents compared to RF and TF treatment. The content of nitrogen (TN, AN) and phosphorus (TP, AP) in the organic-inorganic fertilizers treatment was higher than in the no fertilizer treatment and chemical fertilizer treatment, the same trend as TC and TOC. Liu et al. (2015) and Cai and Qin (2006) research shows that organic fertilizer incorporation can increase TOC capacity by improving agricultural root biomass and exudates. Chen et al. (2015a) studies indicate that soil nutrient content increases after organic fertilizer

incorporation and the increase rate is mainly affected by the type and amount of organic fertilizer. Organic fertilizer incorporation increased crop yields, and soil organic matter and nutrient content were improved, consistent with the research of Gao et al. (2015) and Choudhary et al. (2018). The traditional mineral fertilizer (TF) significantly increased wheat and maize yields. Still, it did not have a significant influence on TC and TOC ($p > 0.05$), similar to the findings of Chen et al. (2015a) considered that the balanced application of inorganic fertilizers could keep farmers high, but it has a limited impact on soil carbon sequestration. Moreover, additional C, N, and P releases in the high-rate organic fertilizers could partly explain our findings. In addition, combined application of organic-inorganic fertilizers treatments increased exchangeable K, while the same treatments did not significantly increase the content of soil TK, relative to the UC and RF, consistent with the research of Hannet et al. (2021), indicating that potassium in the soil is not a limiting factor in alkaline soils. In this study, organic fertilizer incorporation significantly decreased soil pH and exchangeable Ca concentration, while exchangeable Na concentration and electrical conductivity increased in these plots compared with inorganic fertilizer. The pH of alkaline soil tends to decrease with the increase of commercial organic fertilizer application years, and the soil pH tends to be neutral, which is beneficial to the better growth of crops (Oyetunji et al., 2022). Demelash et al. (2014) reported increased Ca and Mg content with applying organic-inorganic fertilizers treatments, but it was not observed to increase the levels of other alkaline elements (K, Na). In this study, although the exchangeable Ca decreased, the exchangeable Na and K concentrations increased significantly. Organic fertilizer and soil type may be the main reasons for these differences (Abu Bakar et al., 2011; Manolikaki and Diamadopoulos, 2019; Jain and Kalamdhad, 2020). In this study, the cation exchange capacity (CEC) of soil increased by 4.9%–5.6% due to organic fertilizer incorporation; the same finding by Ouédraogo et al. (2001) and Cooper et al. (2020) studies that the increase in CEC with organic fertilizer application could be attributed to an increase in TOC. Still, it did not significantly affect (CEC) relative to the inorganic fertilizer plots in this study. It shows that based on stabilizing the wheat-maize yield, the soil quality of the wheat-maize planting area can be improved by combining organic and inorganic methods.

Effect of organic fertilizer incorporation on soil enzyme activity

Studies have shown that fertilization management and incorporation of organic matter can affect soil enzyme activity (Zhao et al., 2016; Li et al., 2017). Urease is closely related to soil nitrogen supply, and improving urease activity in the soil can convert organic nitrogen with high stability to available nitrogen (Zhang et al., 2016a). Therefore, the improvement of urease activity indicated that adding organic fertilizer incorporation improved soil nitrogen conversion. Li et al. (2010) and Wang et al. (2021) study found that soil catalase activity increased with more organic nitrogen, while Yang et al. (2018) showed no significant effect with the incorporation of cattle manure and biochar. The fertilization management practices decreased soil catalase, and nitrite reductase activity in this study may be caused by different soil types, organic fertilizer types and sampling time (Li et al., 2017). Soil sucrose and β-1,4-glucosidase reflects soil organic carbon accumulation and are an essential indicator of soil fertility (Zhang et al., 2016b; Ullah et al., 2019). The response of invertase and β-1,4-glucosidase to different fertilization practices was consistent with that of urease. The long-term addition of organic fertilizers significantly increased the activity of soil sucrose and β-1,4-glucosidase, mainly due to the soil organic carbon increase (Table 3). Polyphenol oxidase may suppress the synthesis of humic substances from phenolic intermediates produced during the mineralization of organic C, resulting in the accumulation of phenolic compounds (Wang et al., 2022). Applying organic fertilizers significant reduces the accumulation of phenolic substances and possible poisoning. In the long-term organic fertilizer incorporation plots, the decomposed organic matter provides sufficient energy and carbon source for soil microbial activities, accelerates the reproduction and growth of microorganisms, and improves soil physicochemical properties (Tiemann and Billings, 2011; Ai et al., 2012; Bowles et al., 2014). At the same time, organic fertilizer also contains many enzymes, which are beneficial to improve soil enzyme activity (Li et al., 2017). Therefore, the inorganic fertilizer combined with organic fertilizer incorporation practices can significantly increase the activities of urease (S-UE), sucrose (S-SC), and β-1,4-glucosidase (S-B-GC) in the soil compared with the chemical fertilizer.

Effect of organic fertilizer incorporation on soil fauna feeding activity

This study found that soil fertilizer management influenced the feeding activities of soil fauna, and these responses were closely related to soil nutrition. Organic fertilizer application greatly enhanced soil fauna feeding activity, and then inorganic nitrogen fertilizer reduced the soil fauna feeding activity. The highest feeding activity rates were found in plots RFMO and RFHO with a larger amount of organic fertilizer incorporation practices, and traditional fertilization treatment (TF) had the lowest feeding activities

(Figure 3). However, the feeding activity of soil fauna showed no significant differences between the control UC and inorganic fertilizer (RF and TF) plots. Studies have shown that the experimental time of using the Bait Lamina test is short, usually 3–15 days, and microorganisms cannot decompose and perforate organic matter in a short time, and nematodes, microarthropods such as earthworms, mites, enchytraeids, and collembolans was the main soil fauna causing bait perforation (Gongalsky et al., 2008; Birkhofer et al., 2011). Although some microorganisms are involved in feeding activities, the feeding activities is negligibly small compared to soil fauna (Gestel et al., 2003; Ashford et al., 2013). Applying organic fertilizers increased soil fauna feeding activities, which may be related to the changed soil fauna community's abundance and composition, leading to higher soil fauna feeding activity (Tao et al., 2016). This may explain why the highest feeding activity rates were found in plots RFMO and RFHO with a larger amount of organic fertilizer incorporation practices. The feeding activity of soil fauna in the inorganic fertilizer combined with organic fertilizer polts was high in the 0–6 cm depth range. Many studies show that feeding activities of soil fauna were strongly reduced from 4 to 8 cm soil layer in grassland and forest sites (Larade et al., 2012; Filzek et al., 2004; Gongalsky et al., 2008; Rożen et al., 2010). Other studies showed that soil fauna feeding activities were higher in the bottom of 5–8 cm soil layer than in topsoil layers at ryegrass and soybean fields (Marx et al., 2016; Mousavi et al., 2022). The long-term inorganic fertilizer combined with organic fertilizer incorporation practices significantly increased the soil fauna feeding activity, while the application of RFHO and RFMO did not significantly increase. Soil fertilizer management may affect soil fauna feeding activities by the soil chemical properties; meanwhile, the feeding activities of soil fauna affect the soil physicochemical properties by regulating the decomposition process of soil organic matter (Römbke et al., 2006; Briones and Schmidt, 2017). Geissen and Brummer (1999) research show a strong correlation between soil fauna feeding activities and chemical parameters, and fauna feeding activity increased with higher pH values in acid soil.

In contrast, we found that the soils under organic fertilizer had the higher exchangeable K, Na, EC, nutrients (AN, AP), and TOC of all the management practices; however, the lowest pH and exchangeable Ca in alkaline soil (Table 3). The feeding activity of soil fauna was in organic fertilizer plots significantly higher than inorganic fertilized (RF and TF) plots and unfertilized (UC) plots. Soil water content and soil temperature are the main environmental factors affecting fauna feeding activities. The feeding activity of fauna measured with the bait-laminae showed that the feeding activities increased with temperature (Gongalsky et al., 2008). Drought seriously affects the activities of invertebrates, especially earthworms that like moist soil (Eggleton et al., 2009). Törne (1990) research showed that in cracked clay with low moisture content in Germany, the percentage of bait bar perforation was between 4% and 16%. Precipitation explained the variation in feeding rates observed between 2019 and 2020 (Supplementary Figure S3).

Conclusion

We examined the effects of inorganic fertilizer combined with organic fertilizer incorporation practices on crop yields, soil quality, and fauna feeding activity. We showed that long-term inorganic fertilizer combined with organic fertilizer incorporation practices enhanced soil organic carbon, nutrition, and fauna feeding activity and significantly enhanced soil sucrose, urease, and β-1,4-glucosidase activity. Soil organic carbon, total nitrogen, and fauna activity showed a linear increase of 27.9%–74.0%, 24.6%–39.2%, and 35.2% %-42.5%, respectively, but the enzyme activity did not increase with the increase of organic fertilizer incorporation. In our studied area, the treatment of medium levels (30 t ha^{-1} $year^{-1}$) may be recommended from crop yields and soil carbon sequestration. Our study findings have important significance for the application of organic fertilizer to the wheat-maize rotation systems.

Data availability statement

The original contributions presented in the study are included in the article/Supplementary Material, further inquiries can be directed to the corresponding authors.

Author contributions

ZZ: data curation, formal analysis, writing—original draft, and writing—review and editing. SZ: data curation, formal analysis, and writing—review and editing. NJ: formal analysis, investigation. WX: investigation, validation, and writing—review and editing. JZ: conceptualization, funding acquisition, and writing—review and editing. DY: funding acquisition, methodology, writing review and editing, supervision.

Funding

This work was supported by the Central Public-Interest Scientific Institution Basal Research Fund (Agro-Environmental Protection Institute, Ministry of Agriculture and Rural Affairs) and the Cooperative Innovation Project of

Agricultural Science and Technology Innovation Program of CAAS (CAAS-XTCX2016015).

Acknowledgments

We sincerely appreciate the cooperation and assistance of the Tianjin Experimental Farm in the implementation of this field study.

Conflict of interest

The authors declare that the research was conducted in the absence of any commercial or financial relationships that could be construed as a potential conflict of interest.

Publisher's note

Supplementary material

The Supplementary Material for this article can be found online at: https://www.frontiersin.org/articles/10.3389/fenvs.2022.1058071/full#supplementary-material

References

Abbott, L. K., and Murphy, D. V. (2007). "What is soil biological fertility?" in *Soil biological fertility: A key to sustainable land use in agriculture*. Editors L. K. Abbott and D. V. Murphy (Dordrecht, Netherlands: Springer), 1–15.

Abu Bakar, R., Darus, S. Z., Kulaseharan, S., and Jamaluddin, N. (2011). Effects of ten year application of empty fruit bunches in an oil palm plantation on soil chemical properties. *Nutr. Cycl. Agroecosyst.* 89 (3), 341–349. doi:10.1007/s10705-010-9398-9

Ai, C., Liang, G., Sun, J., Wang, X., and Zhou, W. (2012). Responses of extracellular enzyme activities and microbial community in both the rhizosphere and bulk soil to long-term fertilization practices in a fluvo-aquic soil. *Geoderma* 173-174, 330–338. doi:10.1016/j.geoderma.2011.07.020

Ashford, O. S., Foster, W. A., Turner, B. L., Sayer, E. J., Sutcliffe, L., and Tanner, E. V. J. (2013). Litter manipulation and the soil arthropod community in a lowland tropical rainforest. *Soil Biol. Biochem.* 62, 5–12. doi:10.1016/j.soilbio.2013.03.001

Bao, S. D. (2008). *Soil agrochemistry analysis*. Beijing: Chinese Agric Press.

Bertrand, M., Barot, S., Blouin, M., Whalen, J., Oliveira, T., and Roger-Estrade, J. (2015). d.Earthworm services for cropping systems. A review. *Agron. Sustain. Dev.Agronomy Sustain. Dev.* 35 (2), 553–567. doi:10.1007/S13593-014-0269-7

Birkhofer, K., Diekötter, T., Boch, S., Fischer, M., Müller, J., Socher, S., et al. (2011). Soil fauna feeding activity in temperate grassland soils increases with legume and grass species richness. *Soil Biol. Biochem.* 43 (10), 2200–2207. doi:10.1016/j.soilbio.2011.07.008

Bowles, T. M., Acosta-Martínez, V., Calderón, F., and Jackson, L. E. (2014). Soil enzyme activities, microbial communities, and carbon and nitrogen availability in organic agroecosystems across an intensively-managed agricultural landscape. *Soil Biol. Biochem.* 68, 252–262. doi:10.1016/j.soilbio.2013.10.004

Brar, B. S., Singh, J., Singh, G., and Kaur, G. (2015). Effects of long term application of inorganic and organic fertilizers on soil organic carbon and physical properties in maize-wheat rotation. *Agron. (Basel).* 5 (2), 220–238. doi:10.3390/agronomy5020220

Briones, M. J. I., and Schmidt, O. (2017). Conventional tillage decreases the abundance and biomass of earthworms and alters their community structure in a global meta-analysis. *Glob. Chang. Biol.* 23 (10), 4396–4419. doi:10.1111/GCB.13744

Cai, Z. C., and Qin, S. W. (2006). Dynamics of crop yields and soil organic carbon in a long-term fertilization experiment in the Huang-Huai-Hai Plain of China. *Geoderma* 136 (3-4), 708–715. doi:10.1016/j.geoderma.2006.05.008

Chang, E. H., Chung, R. S., and Tsai, Y. H. (2007). Effect of different application rates of organic fertilizer on soil enzyme activity and microbial population. *Soil Sci. Plant Nutr.* 53 (2), 132–140. doi:10.1111/J.1747-0765.2007.00122.X

Chen, H., Zhao, Y., Feng, H., Li, H., and Sun, B. (2015a). Assessment of climate change impacts on soil organic carbon and crop yield based on long-term fertilization applications in Loess Plateau, China. *Plant Soil* 390 (1), 401–417. doi:10.1007/s11104-014-2332-1

Chen, X., Li, Z., Liu, M., Jiang, C., and Che, Y. (2015b). Microbial community and functional diversity associated with different aggregate fractions of a paddy soil fertilized with organic manure and/or NPK fertilizer for 20 years. *J. Soils Sediments* 15 (2), 292–301. doi:10.1007/s11368-014-0981-6

Chew, K. W., Chia, S. R., Yen, H. W., Nomanbhay, S., Ho, Y. C., and Show, P. L. (2019). Transformation of biomass waste into sustainable organic fertilizers. *Sustainability* 11 (8), 2266. doi:10.3390/su11082266

Choudhary, M., Panday, S. C., Meena, V. S., Singh, S., Yadav, R. P., Mahanta, D., et al. (2018). Long-term effects of organic manure and inorganic fertilization on sustainability and chemical soil quality indicators of soybean-wheat cropping system in the Indian mid-Himalayas. *Agric. Ecosyst. Environ.* 257, 38–46. doi:10.1016/j.agee.2018.01.029

Cooper, J., Greenberg, I., Ludwig, B., Hippich, L., Fischer, D., Glaser, B., et al. (2020). Effect of biochar and compost on soil properties and organic matter in aggregate size fractions under field conditions. *Agric. Ecosyst. Environ.* 295, 106882. doi:10.1016/j.agee.2020.106882

Davies, B., Coulter, J. A., and Pagliari, P. H. (2022). Soil enzyme activity behavior after urea nitrogen application. *Plants (Basel).* 11, 2247. doi:10.3390/plants11172247

Demelash, N., Bayu, W., Tesfaye, S., Ziadat, F., and Sommer, R. (2014). Current and residual effects of compost and inorganic fertilizer on wheat and soil chemical properties. *Nutr. Cycl. Agroecosyst.* 100 (3), 357–367. doi:10.1007/s10705-014-9654-5

Diacono, M., and Montemurro, F. (2010). Long-term effects of organic amendments on soil fertility. A review. *Agron. Sustain. Dev.* 30 (2), 401–422. doi:10.1051/AGRO/2009040

Eggleton, P., Inward, K., Smith, J., Jones, D. T., and Sherlock, E. (2009). A six year study of earthworm (Lumbricidae) populations in pasture woodland in southern England shows their responses to soil temperature and soil moisture. *Soil Biol. Biochem.* 41 (9), 1857–1865. doi:10.1016/j.soilbio.2009.06.007

Eisenhauer, N., Wirsch, D., Cesarz, S., Craven, D., Dietrich, P., Friese, J., et al. (2014). Organic textile dye improves the visual assessment of the bait-lamina test. *Appl. Soil Ecol.* 82, 78–81. doi:10.1016/j.apsoil.2014.05.008

Fauci, M. F., and Dick, R. P. (1994). Soil microbial dynamics: Short- and long-term effects of inorganic and organic nitrogen. *soil Sci. Soc. Am. J.* 58 (3), 801–806. doi:10.2136/SSSAJ1994.03615995005800030023X

Feng, W., Xu, M., Fan, M., Malhi, S. S., Schoenau, J. J., Six, M., Xu, J., et al. (2013). Testing for soil carbon saturation behavior in agricultural soils receiving long-term manure amendments. *Canadian J. of Soil Sci.* 94 (3), 281–294. doi:10.4141/cjss2013-012

Filzek, P. D. B., Spurgeon, D. J., Broll, G., Svendsen, C., Hankard, P. K., Parekh, N., et al. (2004). Metal effects on soil invertebrate feeding: Measurements using the bait lamina method. *Ecotoxicology* 13 (8), 807–816. doi:10.1007/s10646-003-4478-0

Gao, G.-F., Li, P.-F., Zhong, J.-X., Shen, Z.-J., Chen, J., Li, Y. T., et al. (2019). Spartina alterniflora invasion alters soil bacterial communities and enhances soil N2O emissions by stimulating soil denitrification in mangrove wetland. *Sci. Total Environ.* 653, 231–240. doi:10.1016/j.scitotenv.2018.10.277

Gao, W., Yang, J., Ren, S.-r., and Hailong, L. (2015). The trend of soil organic carbon, total nitrogen, and wheat and maize productivity under different long-term fertilizations in the upland fluvo-aquic soil of North China. *Nutr. Cycl. Agroecosyst.* 103 (1), 61–73. doi:10.1007/s10705-015-9720-7

Geissen, V., and Brummer, G. W. (1999). Decomposition rates and feeding activities of soil fauna in deciduous forest soils in relation to soil chemical parameters following liming and fertilization. *Biol. Fertil. Soils* 29 (4), 335–342. doi:10.1007/s003740050562

Gentile, R., Vanlauwe, B., Chivenge, P., and Six, J. (2008). Interactive effects from combining fertilizer and organic residue inputs on nitrogen transformations. *Soil Biol. Biochem.* 40 (9), 2375–2384. doi:10.1016/j.soilbio.2008.05.018

Gestel, C. A. M., Kruidenier, M., and Berg, M. P. (2003). v., Kruidenier, M., & Berg, M. PSuitability of wheat straw decomposition, cotton strip degradation and bait-lamina feeding tests to determine soil invertebrate activity. *Biol. Fertil. Soils* 37 (2), 115–123. doi:10.1007/s00374-002-0575-0

Gongalsky, K. B., Persson, T., and Pokarzhevskii, A. D. (2008). Effects of soil temperature and moisture on the feeding activity of soil animals as determined by the bait-lamina test. *Appl. Soil Ecol.* 39 (1), 84–90. doi:10.1016/j.apsoil.2007.11.007

Hannet, G., Singh, K., Fidelis, C., Farrar, M. B., Muqaddas, B., and Bai, S. H. (2021). Effects of biochar, compost, and biochar-compost on soil total nitrogen and available phosphorus concentrations in a corn field in Papua New Guinea. *Environ. Sci. Pollut. Res.* 28 (21), 27411–27419. doi:10.1007/s11356-021-12477-w

ISO (2018). "ISO 23470:2018," in *Soil quality — determination of effective cation exchange capacity (CEC) and exchangeable cations using a hexamminecobalt(III)chloride solution* (Geneva, Switzerland: International Organization for standardization (ISO)), 22.

Jain, M. S., and Kalamdhad, A. S. (2020). Soil revitalization via waste utilization: Compost effects on soil organic properties, nutritional, sorption and physical properties. *Environ. Technol. Innovation* 18, 100668. doi:10.1016/j.eti.2020.100668

Kaiser, M., Ellerbrock, R. H., and Gerke, H. H. (2007). Long-term effects of crop rotation and fertilization on soil organic matter composition. *Eur. J. Soil Sci.* 58 (6), 1460–1470. doi:10.1111/J.1365-2389.2007.00950.X

LaRade, S. E., Bork, E. W., and Willms, W. D. (2012). Assessment of soil biological activity in Northern Aspen Parkland native and seeded pasture using bait lamina. *J. Agric. Sci.* 4 (5), 83–90. doi:10.5539/jas.v4n5p83

Li, F., Yu, J., Nong, M., Kang, S., and Zhang, J. (2010). Partial root-zone irrigation enhanced soil enzyme activities and water use of maize under different ratios of inorganic to organic nitrogen fertilizers. *Agric. Water Manag.* 97 (2), 231–239. doi:10.1016/j.agwat.2009.09.014

Li, G., Zhang, Z. S., Gao, H. Y., Liu, P., Dong, S. T., Zhang, J. W., et al. (2012). Effects of nitrogen on photosynthetic characteristics of leaves from two different stay-green corn (Zea mays L.) varieties at the grain-filling stage. *Can. J. Plant Sci.* 92 (4), 671–680. doi:10.4141/Cjps2012-039

Li, J., and Rao, M. (2003). Field evaluation of crop yield as affected by nonuniformity of sprinkler-applied water and fertilizers. *Agric. Water Manag.* 59 (1), 1–13. doi:10.1016/S0378-3774(02)00123-3

Li, S., Chen, J., Shi, J. L., Tian, X. H., Li, X. S., Li, Y. B., et al. (2017). Impact of straw return on soil carbon indices, enzyme activity, and grain production. *Soil Sci. Soc. Am. J.* 81 (6), 1475–1485. doi:10.2136/sssaj2016.11.0368

Li, X. G., Liu, X. P., and Liu, X. J. (2020). Long-term fertilization effects on crop yield and desalinized soil properties. *Agron. J.* 112 (5), 4321–4331. doi:10.1002/agj2.20338

Liu, E. K., Yan, C. R., Mei, X. R., He, W. Q., Bing, S. H., Ding, L. P., et al. (2010). Long-term effect of chemical fertilizer, straw, and manure on soil chemical and biological properties in northwest China. *Geoderma* 158 (3-4), 173–180. doi:10.1016/j.geoderma.2010.04.029

Liu, W. X., Wang, Q. L., Wang, B. Z., Wang, X. B., Franks, A. E., Teng, Y., et al. (2015). Changes in the abundance and structure of bacterial communities under long-term fertilization treatments in a peanut monocropping system. *Plant Soil* 395 (1-2), 415–427. doi:10.1007/s11104-015-2569-3

Liu, Y., Zhao, L., Wang, Z., Liu, L., Zhang, P., Sun, J., et al. (2018). Changes in functional gene structure and metabolic potential of the microbial community in biological soil crusts along a revegetation chronosequence in the Tengger Desert. *Soil Biol. Biochem.* 126, 40–48. doi:10.1016/j.soilbio.2018.08.012

Lu, X. L., Lu, X. N., and Liao, Y. C. (2018). Conservation tillage increases carbon sequestration of winter wheat-summer maize farmland on Loess Plateau in China. *PLoS ONE* 13 (9), e0199846. doi:10.1371/journal.pone.0199846()

Lupwayi, N. Z., Clayton, G. W., O'Donovan, J. T., and Grant, C. A. (2011). Soil microbial response to nitrogen rate and placement and barley seeding rate under No till. *Agron. J.* 103 (4), 1064–1071. doi:10.2134/AGRONJ2010.0334

Maltas, A., Kebli, H., Oberholzer, H. R., Weisskopf, P., and Sinaj, S. (2018). The effects of organic and mineral fertilizers on carbon sequestration, soil properties, and crop yields from a long-term field experiment under a Swiss conventional farming system. *Land Degrad. Dev.* 29 (4), 926–938. doi:10.1002/ldr.2913

Manolikaki, I., and Diamadopoulos, E. (2019). Positive effects of biochar and biochar-compost on maize growth and nutrient availability in two agricultural soils. *Commun. Soil Sci. Plant Analysis* 50 (5), 512–526. doi:10.1080/00103624.2019.1566468

Marx, M. T., Yan, X. M., Wang, X. F., Song, L. H., Wang, K. H., Zhang, B., et al. (2016). Soil fauna abundance, feeding and decomposition in different reclaimed and natural sites in the sanjiang plain wetland, northeast China. *Wetlands* 36 (3), 445–455. doi:10.1007/s13157-016-0753-8

Miao, Y. X., Stewart, B. A., and Zhang, F. S. (2011). Long-term experiments for sustainable nutrient management in China. A review. *Agron. Sustain. Dev.* 31 (2), 397–414. doi:10.1051/agro/2010034

Miller, J. J., Owen, M. L., Yang, X. M., Drury, C. F., Reynolds, W. D., and Chanasyk, D. S. (2020). Long-term cropping and fertilization influences soil organic carbon, soil water repellency, and soil hydrophobicity. *Can. J. Can. J. Soil Sci.* 100 (3), 234–244. doi:10.1139/cjss-2019-0129

Miner, G. L., Delgado, J. A., Ippolito, J. A., and Stewart, C. E. (2020). Soil health management practices and crop productivity. *Agric. Environ. Lett.* 5 (1), 23. doi:10.1002/AEL2.20023

Moller, K., and Schultheiss, U. (2015). Chemical characterization of commercial organic fertilizers. *Archives Agron. Soil Sci.* 61 (7), 989–1012. doi:10.1080/03650340.2014.978763

Mousavi, H., Cottis, T., Hoff, G., and Solberg, S. O. (2022). Nitrogen enriched organic fertilizer (NEO) and its effect on ryegrass yield and soil fauna feeding activity under controlled conditions. *Sustainability* 14 (4), 2005. doi:10.3390/su14042005

Ouédraogo, E., Mando, A., and Zombré, N. P. (2001). Use of compost to improve soil properties and crop productivity under low input agricultural system in West Africa. *Agric. Ecosyst. Environ.* 84 (3), 259–266. doi:10.1016/S0167-8809(00)00246-2

Oyetunji, O., Bolan, N., and Hancock, G. (2022). A comprehensive review on enhancing nutrient use efficiency and productivity of broadacre (arable) crops with the combined utilization of compost and fertilizers. *J. Environ. Manag.* 317, 115395. doi:10.1016/j.jenvman.2022.115395

Qaswar, M., Jing, H., Ahmed, W., Li, D. C., Liu, S. J., Lu, Z., et al. (2020). Yield sustainability, soil organic carbon sequestration and nutrients balance under long-term combined application of manure and inorganic fertilizers in acidic paddy soil. *Soil Tillage Res.* 198, 104569–104611. doi:10.1016/j.still.2019.104569

Rajan, J., and Anandhan, S. V. (2015). Survey on nutrient content of different organic fertilisers. *Environ. Monit. Assess.* 187 (6), 385. doi:10.1007/s10661-015-4632-1

Rożen, J., Sobczyk, Ł., Liszka, K., and Weiner, J. (2010). Soil faunal activity as measured by the bait-lamina test in monocultures of 14 tree species in the Siemianice common-garden experiment, Poland. *Applied Soil Ecology* 45 (3), 160–167. doi:10.1016/j.apsoil.2010.03.008

Römbke, J., Hofer, H., Garcia, M. V. B., and Martius, C. (2006). Feeding activities of soil organisms at four different forest sites in Central Amazonia using the bait lamina method. *J. Trop. Ecol.* 22, 313–320. doi:10.1017/S0266467406003166

Setia, R., Rengasamy, P., and Marschner, P. (2013). Effect of exchangeable cation concentration on sorption and desorption of dissolved organic carbon in saline soils. *Sci. Total Environ.* 465, 226–232. doi:10.1016/j.scitotenv.2013.01.010

Shang, F., Ren, S., Yang, P., Li, C., and Ma, N. (2015). Effects of different fertilizer and irrigation water types, and dissolved organic matter on soil C and N mineralization in crop rotation farmland. *Water, Air, Soil Pollut.* 226 (12), 396. doi:10.1007/s11270-015-2667-0

Sunnemann, M., Alt, C., Kostin, J. E., Lochner, A., Reitz, T., Siebert, J., et al. (2021). Low-intensity land-use enhances soil microbial activity, biomass and fungal-to-bacterial ratio in current and future climates. *J. Appl. Ecol.* 58 (11), 2614–2625. doi:10.1111/1365-2664.14004

Tao, H.-H., Slade, E. M., Willis, K. J., Caliman, J.-P., and Snaddon, J. L. (2016). Effects of soil management practices on soil fauna feeding activity in an Indonesian oil palm plantation. *Agric. Ecosyst. Environ.* 218, 133–140. doi:10.1016/j.agee.2015.11.012

Thomas, G. A., Dalal, R. C., and Standley, J. (2007). No-till effects on organic matter, pH, cation exchange capacity and nutrient distribution in a Luvisol in the semi-arid subtropics. *Soil Tillage Res.* 94 (2), 295–304. doi:10.1016/j.still.2006.08.005

Tiemann, L. K., and Billings, S. A. (2011). Indirect effects of nitrogen amendments on organic substrate quality increase enzymatic activity driving decomposition in a mesic grassland. *Ecosystems* 14 (2), 234–247. doi:10.1007/s10021-010-9406-6

Törne, E. (1990). Assessing feeding activities of soil-living animals 1. Bait-Lamina-Tests. *Pedobiologia* 34 (2), 89–101.

Ullah, S., Ai, C., Huang, S., Zhang, J., Jia, L., Ma, J., et al. (2019). The responses of extracellular enzyme activities and microbial community composition under nitrogen addition in an upland soil. *PLoS ONE* 14 (9), e0223026. doi:10.1371/journal.pone.0223026()

Vorobeichik, E. L., and Bergman, I. E. (2021). Bait-lamina test for assessment of polluted soils: Rough vs. Precise scales. *Ecol. Indic.* 122, 107277. doi:10.1016/j.ecolind.2020.107277

Wahyuningsih, R., Marchand, L., Pujianto, S., and Caliman, J. P. (2019). Impact of inorganic fertilizer to soil biological activity in an oil palm plantation. *IOP Conf. Ser. Earth Environ. Sci.* 336 (1), 012017. doi:10.1088/1755-1315/336/1/012017

Wang, C., Ning, P., Li, J. Y., Wei, X. M., Ge, T. D., Cui, Y. X., et al. (2022). Responses of soil microbial community composition and enzyme activities to long-term organic amendments in a continuous tobacco cropping system. *Appl. Soil Ecol.* 169, 104210. doi:10.1016/j.apsoil.2021.104210

Wang, Y., Huang, C., Liu, M., and Yuan, L. (2021). Long-term application of manure reduced nutrient leaching under heavy N deposition. *Nutr. Cycl. Agroecosyst.* 119 (2), 153–162. doi:10.1007/s10705-020-10107-4

Welbaum, G. E., Sturz, A. V., Dong, Z. M., and Nowak, J. (2004). Managing soil microorganisms to improve productivity of agro-ecosystems. *Crit. Rev. Plant Sci.* 23 (2), 175–193. doi:10.1080/07352680490433295

Yang, L., Bian, X. G., Yang, R. P., Zhou, C. L., and Tang, B. P. (2018). Assessment of organic amendments for improving coastal saline soil. *Land Degrad. Dev.* 29 (9), 3204–3211. doi:10.1002/ldr.3027

Yang, X., Sun, B., and Zhang, S. (2014). Trends of yield and soil fertility in a long-term wheat-maize system. *J. Integr. Agric.* 13 (2), 402–414. doi:10.1016/S2095-3119(13)60425-6

Yang, Z., Zhao, N., Huang, F., and Lv, Y. (2015). Long-term effects of different organic and inorganic fertilizer treatments on soil organic carbon sequestration and crop yields on the North China Plain. *Soil Tillage Res.* 146, 47–52. doi:10.1016/j.still.2014.06.011

Yu, C., Hu, X. M., Deng, W., Li, Y., Xiong, C., Ye, C. H., et al. (2015). Changes in soil microbial community structure and functional diversity in the rhizosphere surrounding mulberry subjected to long-term fertilization. *Appl. Soil Ecol.* 86, 30–40. doi:10.1016/j.apsoil.2014.09.013

Zelles, L., Bai, Q. Y., Beck, T., and Beese, F. (1992). Signature fatty acids in phospholipids and lipopolysaccharides as indicators of microbial biomass and community structure in agricultural soils. *Soil Biol. Biochem.* 24 (4), 317–323. doi:10.1016/0038-0717(92)90191-Y

Zhang, P., Chen, X., Wei, T., Yang, Z., Jia, Z., Yang, B., et al. (2016a). Effects of straw incorporation on the soil nutrient contents, enzyme activities, and crop yield in a semiarid region of China. *Soil Tillage Res.* 160, 65–72. doi:10.1016/j.still.2016.02.006

Zhang, X., Xiao, G., Bol, R., Wang, L., Zhuge, Y., Wu, W., et al. (2021). Influences of irrigation and fertilization on soil N cycle and losses from wheat–maize cropping system in northern China. *Environ. Pollut.* 278, 116852. doi:10.1016/j.envpol.2021.116852

Zhang, Y., Li, C., Wang, Y., Hu, Y., Christie, P., Zhang, J., et al. (2016b). Maize yield and soil fertility with combined use of compost and inorganic fertilizers on a calcareous soil on the North China Plain. *Soil Tillage Res.* 155, 85–94. doi:10.1016/j.still.2015.08.006

Zhao, S., Li, K., Zhou, W., Qiu, S., Huang, S., and He, P. (2016). Changes in soil microbial community, enzyme activities and organic matter fractions under long-term straw return in north-central China. *Agric. Ecosyst. Environ.* 216, 82–88. doi:10.1016/j.agee.2015.09.028

Zhou, Z., Yang, D., Zhao, J., Zhang, H., and Wang, L. (2021). Emissions of greenhouse gas and ammonia from an intensive wheat site affected by different fertilization practices. AvaliableAt: https://elibrary.asabe.org/abstract.asp?aid=52457&t=5.

frontiers | Frontiers in Bioengineering and Biotechnology

TYPE Original Research
PUBLISHED 05 December 2022
DOI 10.3389/fbioe.2022.1087933

OPEN ACCESS

EDITED BY
Junting Pan,
Institute of Agricultural Resources and Regional Planning (CAAS), China

REVIEWED BY
Huabin Wang,
Yunnan Normal University, China
Peizhen Zhang,
Chinese Academy of Agricultural Sciences (CAAS), China

*CORRESPONDENCE
Mario A. Heredia Salgado,
heredia.mario@ua.pt

SPECIALTY SECTION
This article was submitted to Bioprocess Engineering,
a section of the journal
Frontiers in Bioengineering and Biotechnology

RECEIVED 02 November 2022
ACCEPTED 21 November 2022
PUBLISHED 05 December 2022

CITATION
Heredia Salgado MA, Coba S JA, Cianferoni A, Säumel I and Tarelho LAC (2022), Conversion of quinoa and lupin agro-residues into biochar in the Andes: An experimental study in a pilot-scale auger-type reactor.
Front. Bioeng. Biotechnol. 10:1087933.
doi: 10.3389/fbioe.2022.1087933

Conversion of quinoa and lupin agro-residues into biochar in the Andes: An experimental study in a pilot-scale auger-type reactor

Mario A. Heredia Salgado[1,2]*, Jonathan A. Coba S[3], A. Cianferoni[4], Ina Säumel[1] and Luís A. C. Tarelho[2]

[1]Integrative Research Institute for Transformation of Human-Environment Systems (IRITHEsys), Humboldt Universität zu Berlin, Berlin, Germany, [2]Department of Environment and Planning, Centre for Environmental and Marine Studies (CESAM), University of Aveiro, Aveiro, Portugal, [3]Bioenergía de los Andes (BDA), José L. Tamayo y R. Teran. Quito, Ecuador, [4]European Comitee for Training and Agriculture (CEFA), Eloy Alfaro y Amazonas, Quito, Ecuador

In the last decades, the cultivation of quinoa and lupin became an important source of income for Andean farmers due to the demand for high nutrient-density foods from the Global North. The increase in the cultivation intensity caused by this exogenous demand led to the overexploitation of local ecosystems and a decrease in soil fertility. As an alternative to recover and improve soil quality, this work uses a pilot-scale auger pyrolysis reactor, implemented in the Andes, to assess the conversion of the agro residues generated in the post-harvesting processes of quinoa and lupin into biochar for soil amendment. Following the European Biochar Certificate guidelines, the pyrolyzed quinoa stems can be classified as biochar while the pyrolyzed quinoa husks can be classified as pyrogenic carbonaceous material. Both can be used for soil amendment considering their molar ratios (H/C_{org}, O/C_{org}) and carbon content. It was not possible to carbonize lupin stems and seedcases. Despite the altitude (2,632 m.a.s.l), the CO concentration during the carbonization of quinoa stems and husks were 1,024.4 and 559 mg/Nm^3, this last, near the European eco-design standard of 500 mg/Nm^3. A subsequent SWOT analysis showed the need to explore low-cost and low-complexity pyrolysis reactors that allow the decentralized conversion of agro residues at the farm-scale. The development of local standards to regulate the production and use of biochar is also essential to grant the safety of the processes, the quality of the products, and mobilize funds that allow implementation at relevant scales.

KEYWORDS

pyrolysis, agro residues, biochar, *Chenopodium* quinoa Wild, Lupinus mutabilis Sweet

1 Introduction

Quinoa (*Chenopodium quinoa Wild*) and lupin (*Lupinus mutabilis Sweet*) are Andean grains typically cultivated in the highlands of Ecuador, Bolivia, and Peru. Both contain large amounts of protein, dietary fibers, essential fatty acids, vitamins, minerals, and carbohydrates. These Andean grains have been of major importance for the food security of farmer communities living in the Andes where access to meat protein sources is limited (FAO and CIRAD, 2015). Before 2000, the consumption of quinoa and lupin was not usual outside South America (Graf et al., 2016; Kouris-Blazos and Belski, 2016). However, the outstanding quality of their protein -it contains lysine and leucine - besides being gluten-free, positioned these Andean grains as an upper-class food in wealthy countries of the Global North. In these countries the interest in foods with potential health benefits and high nutrient density often referred as "superfoods", is increasing (Bellemare et al., 2018; Bryant et al., 2022).

Besides the health and nutritional interest, the "superfoods" like quinoa and lupin are also considered alternatives to implement a plant-based diet in the Global North. It is claimed that quinoa consumption can reduce meat production along with the environmental consequences linked with animal farming, for instance, land or forest clearing and enteric methane emissions (Abbis et al., 2017; Stubbs et al., 2018). From 2010, these perceptions concerning Andean grains gave rise a sustained demand from wealthy countries triggering a historical price increase (Bedoya-Perales et al., 2018; Bonifacio et al., 2022). Accordingly, the area dedicated to its cultivation in the producer countries in the Andean highlands increased becoming a relevant source of income for farmers that saw in these crops an opportunity for poverty alleviation (Stensrud, 2019).

Recently, the increasing supply of quinoa and lupin grew in Europe, Africa, and the United States of America has displaced Andean production and the prices have lowered (Jacobsen, 2017; Maliro et al., 2021). Nonetheless, the environmental impacts in the producer regions of the Andes highlands caused by the once commercial success of quinoa and lupin remain, namely, soil over-exploitation, intensive use of fertilizers, and biodiversity loss due to the conversion of typical highland eco-systems into cropland (Jacobsen, 2011; Fuentes et al., 2012; Bellemare et al., 2018). In the Andean highlands, soil overexploitation during the quinoa and lupin boom has also caused a decline in its usually high nutritional density, putting at risk the food security of farmers' communities (Silva et al., 2020; Bonifacio et al., 2022). Accordingly, the identification of alternatives to improve soil quality and prevent erosion is relevant for the restoration of highland ecosystems and to grant access to quality protein sources for local communities.

It is stated that the agro-residues generated during the post-harvesting processes of quinoa and lupin could be a potential feedstock to produce organic soil amendments such as biochar which is a solid carbonaceous material produced through pyrolysis. There are 2.4 and 7 tons of agro-residues being generated per ton of quinoa and lupin grain threshed, respectively (Heredia et al., 2017). The use of biochar made from these types of agro residues can be an alternative to bring back to the soil part of the carbon and minerals absorbed by the biomass during growth (Scholz et al., 2014). Concerning the use of biochar in quinoa crops, it is reported an increase in biomass yield after application, improvement of soil fertility, reduction of inputs of N-fertilizer, and increase of organic carbon content in the soil (Kammann et al., 2015). The application of biochar on sandy soils, such as the ones used for quinoa and lupin cultivation, promotes the growth of leaf areas, increases drought tolerance and water use efficiency (Kammann et al., 2011; Egamberdieva et al., 2017).

It is worth to note that the studies that refer to the use of biochar as a soil amendment in quinoa and lupin crops, rather than considering locally available residual biomass, that is, the agro-residues generated in the post-harvesting processes, consider feedstocks for the production of biochar such as peanut hull residues (Kammann et al., 2011), residual forest biomass and maize (Egamberdieva et al., 2017), and wood chips made of 80–20 wt% coniferous and deciduous wood (Kammann et al., 2015). These experimental studies on the use of biochar as a soil amendment in quinoa and lupin crops do not consider locally available feedstocks to produce biochar probably because they were performed by foreign research institutions in laboratories not located in the Andes highlands.

In the Andean region, few studies refer to the use of agro-residues generated during the post-harvesting processes of quinoa and lupin as feedstock for biochar production. For instance, a study made in Ecuador through a numerical model (Heredia et al., 2017) shows that the theoretical yield of biochar

TABLE 1 Proximate and elemental composition of the agro-residues generated after the post-harvesting processes of quinoa and lupin in the highlands of Ecuador (Heredia et al., 2017).

	Quinoa		Lupin	
	Stem	Husk	Stem	Seedcase
Proximate Analysis (%$wt_{,wb}$)				
Moisture	2.6	4.8	3.6	4.8
Volatile	77.9	71.9	79.4	72
Ash	5	15.6	4.9	15.6
Fixed carbon[a]	14.5	7.7	12.1	5.9
Elemental Analysis (%$wt_{,db}$)				
Ash	5.3	18.5	5.2	18.5
C	46.3	42.6	47	45.7
H	5.7	5.2	5.9	5.8
N	10.7	15.4	11.5	9.7
S	0.5	0.5	0.5	0.4
O[a]	31.5	17.8	29.8	19.9
Lower Heating Value - LHV (MJ/kg_{db})	17.8	15.3	17.1	17.5

[a]Calculated by difference.

produced from quinoa and lupin agro-residues ranges from 22.4 wt% to 28.4 wt% when the pyrolysis temperatures are 450°C and 550 C, respectively. This study further shows that the thermal energy required to drive the pyrolysis process can be supplied through the combustion of pyrolysis gases. The referential proximal and elemental composition of the quinoa and lupin agro-residues is shown in Table 1.

Regarding laboratory tests performed in the Andes highlands, there is an experimental study that explored the use of quinoa stems not to obtain biochar, but as feedstock to produce a pelletized solid fuel to be used in rural stoves for food cooking (Alarcon et al., 2017). That study focuses on the mechanical properties of the produced pellets rather than the performance and behavior of the quinoa agro-residue during its thermochemical conversion process. For the case of lupin stems and seedcases, outside the quantification of the rate of agro-residues produced in the post-harvesting process and the characterization of their proximal and elemental composition shown in Table 1, there are no experimental data concerning their use as feedstock for biochar production neither as solid fuel.

Concerning the thermochemical conversion of quinoa stems and husks, there is a thermogravimetric analysis performed by (Paniagua Bermejo et al., 2020) that revealed two stages of weight loss under an oxidative atmosphere. Furthermore, two heat release stages were identified when the experiment was performed under an inert atmosphere. That study claims that the stages of thermochemical conversion were influenced by the content of cellulose and lignin. Following the results of the thermogravimetric analysis performed under oxidative and under an inert atmosphere, the authors state that stems should be preferred as feedstock whether for combustion or carbonization processes.

As shown, to produce biochar from quinoa and lupin agro residues, the reviewed experimental studies use lab-scale reactors, usually fixed beds, which are batch operated and fed with samples of a few grams of biomass (Alarcon et al., 2017; Heredia et al., 2017; Paniagua Bermejo et al., 2020). In these types of bench-scale laboratory research infrastructures, the potential constraints linked with process scale up to practical size and the effect of local conditions, as the altitude, over the process operating conditions can hardly be explored and has not been yet done. A step forward from these numerical and lab-scale studies requires the demonstration of the pyrolysis process at a relevant scale that could provide insights into the feasibility of implementing this technology for the benefit of farmers' communities of the Andes highlands and the local ecosystems.

In this context, the present study provides new information on using the agro residues generated during the post-harvesting processes of quinoa and lupin, namely, quinoa stems and husks together with lupin stems and husks as feedstocks in a pilot-scale auger pyrolysis reactor implemented in the Andes highlands (capacity 30 kg/h) which was designed for the combined production of biochar and thermal energy. This reactor has been previously demonstrated effective for the conversion of agro-residues produced in palm oil mills, into biochar (Heredia Salgado et al., 2020). The pyrolysis experiments were performed for each feedstock under conditions of relevance for the producer countries in the Andes, namely at 2,632 m.a.s.l. The operating conditions of the pyrolysis process along with the properties of the carbonized products are reported and discussed concerning its use for soil amendment. Flue gas emissions from the pilot-scale reactor are also monitored and assessed according to widely recognized eco-design standards. Finally, a SWOT analysis based on participant observations and expert meetings is included to discuss the extent to which the technology used to produce biochar is adaptable to the context where the quinoa and lupin agro-residues are being generated.

FIGURE 1
(A) Quinoa stems crushed in the hammer mill. **(B)** Quinoa husks collected from the thresher. **(C)** Lupin stems crushed in a hammer mill. **(D)** lupin seedcases collected from th thresher.

2 Materials and methods

2.1 Study site and collection of agro-residues

The agro-residues used in the pyrolysis experiments were collected following the participant observation method. The principal author of this work (Mario Heredia) got invited by the community San Francisco de Bishud, province of

Chimborazo in Ecuador (S2°17′8.2″ W78°45′30.8”) to participate in the harvest and post-harvesting process of quinoa and lupin. The post-harvesting processes followed the typical tasks performed by farmers in the Andes highlands as described by (Silva et al., 2020) and (FAO and CIRAD, 2015). Thus, after harvesting, the collected quinoa and lupin plants were dried by the stacking method which involves arranging the plants in stacks (cone-shaped mounds). Then, the dried plants were fed to a threshing machine to separate the grain from the panicle.

The collected samples were threshed by the mechanical method using a machine with a capacity of 500 kg/h driven by a gasoline engine. The threshing machine separated the grain from the stems and the husks/seedcases in one single process. The four types of agro-residues collected from the thresher, namely quinoa stems and husk and lupin stems and seedcases, were saved in jute sacks considering batches of 350 kg following the norm UNE-CEN/TS 14778-1:EX.

After the threshing process, the quinoa and lupin stems resemble sticks with a length between 0.8 and 1.5 m. Before the pyrolysis experiments, these quinoa and lupin stems were crushed in a hammer mill, to a particle size between 5 and 15 mm. The quinoa husks and the lupin seedcases were used in the pyrolysis experiments as collected from the thresher because their particle size was already between 1 and 5 mm. Figure 1 shows the feedstocks used in the pyrolysis experiments, namely quinoa stems (QS), quinoa husks (QH), lupin stems (LS), and lupin seedcases (LSC).

2.2 Pilot-scale auger-type pyrolysis reactor

The agro-residues described in Section 2.1 were pyrolyzed in a pilot-scale auger-type reactor previously used to convert agro residues generated in palm oil mills into biochar (Heredia Salgado et al., 2020). This research facility located at 2,632 m.a.s.l (S 0°17′30.8′′ W78°30′7.9′′) which are relevant conditions to assess potential constraints in the implementation of pyrolysis processes in the Andes highlands. Further specifications, heat exchange methods and constructive details of devices, systems and sub systems of the pilot-scale auger-type pyrolysis reactor can be consulted elsewhere (Heredia Salgado, 2020). The pilot-scale auger-type pyrolysis reactor used in the pyrolysis experiments is composed of two integrated modules of thermochemical conversion, namely, a combustion module and a pyrolysis module. The combustion module consists of a horizontal burner prototype (HBP) (numbers one to four in Figure 2) that uses a fraction of the agro-residues as a solid fuel to produce the thermal energy required to heat the pyrolysis module and start the pyrolysis process. Details about the HBP can be found in previous works, namely (Heredia Salgado et al., 2019a) and (Heredia Salgado et al., 2019b).

The pyrolysis module includes the ancillaries required to feed the agro-residues (number 12 in Figure 2), discharge the biochar (number 14 in Figure 2), and those required for the energetic conversion of pyrolysis gas by combustion, that is, a pyrolysis gas burner (PGB) (number 15 in Figure 2). Accordingly, the HBP and the PGB share the combustion chamber where the hot gases generated by the combustion processes -whether from solid agro-residues or pyrolysis gases-supply the heat required by the pyrolysis process. The flue gas generated during these combustion processes is discharged into the atmosphere through a chimney (number eight in Figure 2).

The residual biomass used for the experiments is fed to the pyrolysis module from a hopper using a rotary vane valve (number 12 in Figure 2). The biomass feed rate of this valve for all the experiments was 30 kg/h. Additional gases were not used to promote an inert atmosphere in the pyrolysis module nor to drag the pyrolytic gases. The tightness of the pyrolysis module was assured by keeping a constant level of agro-residues in the hopper and owing to the seals placed in the vanes of the rotary valve. Finally, the hopper cover forms a seal of three stages.

After the agro-residues have passed through the rotary vane valve, the auger rotation (number 13 in Figure 2) moves it along the horizontal axis until the end of the pyrolysis chamber. The residence time of the agro-residues within the pyrolysis chamber for all the experiments was 15 min. Then, the carbonized agro-residues (the biochar) are discharged by a coil conveyor (item 13 in Figure 2). A control volume of biochar is always kept over the level of the coil conveyor to avoid air entrance along with a water seal. During the discharge, the water seal is replaced by a nozzle that sprays water over the biochar to prevent dust formation and auto-ignition.

The pilot-scale pyrolysis reactor is operated through two independent controllers namely: a controller for the combustion module and a controller for the pyrolysis module. The controller of the combustion module (number 20 in Figure 2) manages exclusively the ignition process, operating conditions, and thermal output power of the HBP. The controller of the pyrolysis module (number 21 in Figure 2) manages the activation, rotation speed, and rotation direction of the rotary vane valve, the auger, the discharge valve, the air blower of the PGB, and the water nozzle. The changes in the operating parameters implemented in the pyrolysis and combustion controllers are sent through a serial protocol towards a computer interface (number 22 in Figure 2) where they are recorded for later analysis.

2.3 Sampling process of pyrolyzed agro-residues

During the pyrolysis experiments, biochar samples of 3.5 kg were collected from the discharge port (number 14 in Figure 2) following the norm UNE-CEN/TS 14778-1:EX. The moisture,

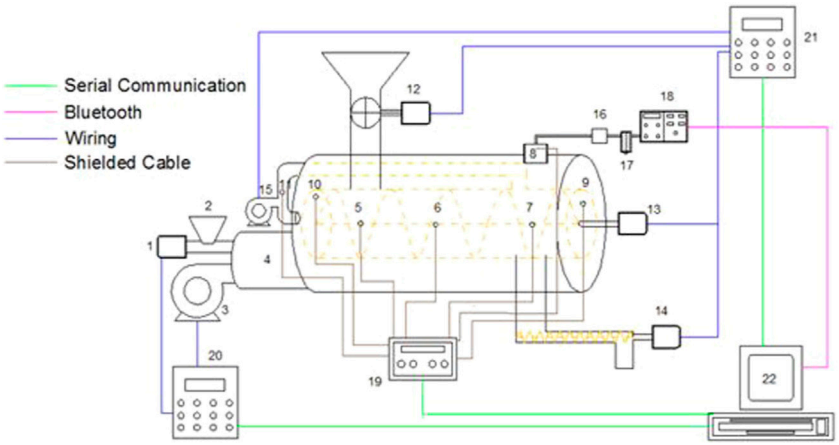

FIGURE 2
Pilot-scale auger-type pyrolysis reactor used to produce biochar from agro-residues generated during the post-harvesting processes of quinoa and lupin. Legend: 1. HBP feeder, 2. HBP hopper, 3. HBP blower, 4. HBP frame, 5. Combustion chamber thermocouple (T1), 6. Combustion chamber thermocouple (T2), 7. Combustion chamber thermocouple (T3), 8. Chimney thermocouple (T4), 9. Carbonization chamber outlet thermocouple (T5), 10. Carbonization chamber inlet thermocouple (T6), 11. Pyrolysis gas thermocouple (17), 12. Rotary vane valve, 13. Auger shaft and motor, 14. Discharge valve, 15 Pyrolysis gas burner, 16. Particle filter, 17. Condenser filter. 18. On line gas analyzer 19. Thermocouples data logger, 20. Combustion module controller, 21. Pyrolysis module controller, 22. Computer. Adapted from (Heredia Salgado et al., 2020).

ash, and volatile matter content were determined following the standards BS EN 14774-3:2009, BS EN 14775:2009, BS EN 15148: 2009, respectively. The heating value and the composition of C-H-N-S of the biochar were determined following the standards ASTM D 1989-96 and BS EN 15104:2011, respectively. The quality of the biochar produced in the experiments as a soil amendment for the quinoa and lupin crops, namely its stability in the soil (molar ratio O/C_{org}), carbon content, and its degree of carbonization (molar ratio H/C_{org}) were assessed following the European guidelines for the sustainable production of biochar (European Biochar Foundation, 2018). All the samples of biochar were collected during the periods of operation in steady state. Therefore, the biochar was collected when constant temperatures were observed in the combustion and pyrolysis modules along with a steady composition of the flue gas.

2.4 Process monitoring: Temperature profiles and flue gas composition

The composition of the flue gas was monitored using an AU Mobile Brain Bee infrared online analyzer (number 18 in Figure 2). The gas analyzer monitors: CO (0–9.99%vol), CO_2 (0–19.9%vol), HC (0–13,999 ppm, expressed as hexane), and O_2 (0–24.99%vol). The gas analyzer resolution is 0.01%vol for CO and O_2, 0.1%vol for CO_2, and 1ppm for HC. A particle matter filter followed by a gas condenser submerged in cold water for moisture and condensable material removal was placed before the gas analyzer (see numbers 16 and 17 in Figure 2). The flue gas analyzer communicates with a computer interface (number 22 in Figure 2) where the gas concentrations are plotted in real-time and recorded for later analysis. The conversion efficiency of the combustion processes was assessed by monitoring the CO concentration in the flue gas following the European emissions standards for fixed combustion sources (The European Commission, 2015). Accordingly, the CO concentration in the flue gas was corrected to an O_2 concentration of 11%vol $O_{2\ dry\ gas}$ (Heredia Salgado et al., 2019a).

Seven thermocouples were distributed between the combustion and pyrolysis modules to monitor the temperature profiles of the combustion and pyrolysis processes. K-type thermocouples were used with a measurement range between 95 and 1,260 C and an accuracy of 2.2°C. Three thermocouples were placed in the horizontal axis of the combustion chamber, namely: thermocouple 1 (number five in Figure 2) is at 0.27 m from the HBP exit, thermocouple 2 (number six in Figure 2) is at 0.55 m from thermocouple 1, and thermocouple 3 (number seven in Figure 2) is at 0.55 m from thermocouple 2. Thermocouple 4 (number eight in Figure 2) was placed in the exit flue gas duct to further calculate an estimative of thermal energy associated with the exiting combustion flue gases. The thermocouples used to monitor the temperature in the combustion module have a length of 100 mm and 5 mm in thickness.

The temperatures in the pyrolysis module were monitored at the inlet and outlet of the auger within the pyrolysis chamber and were placed through the front and rear covers of the combustion chamber (see numbers 9 and 10 in Figure 2). The thermocouple located in the front cover of the combustion chamber, that is at the HBP side, is 300 mm in length, 5 mm in thickness, and is located at 140 mm up

from the central axis of the auger shaft. The thermocouple located in the rear cover of the combustion chamber is 100 mm in length, 5 mm in thickness, and is located 140 mm up from the auger shaft. The temperature of the pyrolysis gas was monitored at the suction duct of the PGB with a thermocouple of 25 mm length and 5 mm thickness (number 11 in Figure 2). The temperature signal of the seven thermocouples is acquired with an interval of one second and sent through a temperature datalogger (number 19 in Figure 2) by serial communication to the computer interface (number 22 in Figure 2) to be plotted in real-time and recorded for later analysis.

2.5 SWOT analysis: Internal capabilities and external constraints linked with the local communities concerning biochar production

The reviewed studies about the use of biochar in quinoa and lupin crops barely consider the local knowledge and ignore the available residual biomass (see Section 1). In this sense, this SWOT analysis is intended to grasp whether biochar can be effectively implemented in the Andes highlands as an alternative for soil amendment. To do so, it relies on the participant observations made by the principal author (Mario Heredia) who participated in a complete cycle of quinoa and lupin harvesting and post-harvesting process, invited by an Andean community (see Section 2.1).

Accordingly, information on the execution of harvesting and post-harvesting processes in the community along with the procedures and machinery involved were registered with photographs and field notes. Data concerning the current uses of the agro residues generated during the threshing process and soil fertilization practices were gathered using open interviews with the farmers involved in the threshing processes. The SWOT analysis was then complemented with the criteria of practitioners and experts from international cooperation agencies with experience in the cooperative sector linked with quinoa and lupin, specifically from the European Committee for Training and Agriculture (CEFA) in Ecuador. References from the technical literature published in Spanish by local research institutions, namely the Instituto Nacional de Investigaciones Agropecuarias (INIAP) in Ecuador were also included in the SWOT analysis as contrast and verification of the information gathered through the participant observation method (Caicedo and Peralta, 2000; Caicedo et al., 2001; Peralta et al., 2012).

3 Results and discussion

3.1 Pilot-scale auger-type pyrolysis reactor: Heating process

As shown in Section 2.2, the pilot-scale auger-type pyrolysis reactor has two modules, namely a combustion module and a pyrolysis module. In the combustion module, the reactor uses a fraction of the agro residues to produce the thermal energy required to heat the pyrolysis module to the point that the carbonization process is maintained under steady conditions. Therefore, during the first stage of the experimental work, four independent experiments were considered in the combustion module using QS, QH, LS, and LSC as solid fuels. Once the pyrolysis module is hot, the feed of QS, QH, LS, and LSC towards the pyrolysis chamber was tested individually. Table 2 shows the observations made while conveying these agro-residues from the hopper of the combustion module towards the combustion bed and from the hopper of the pyrolysis module towards the pyrolysis chamber.

Regarding the combustion module, it was observed that LS and LSC are difficult to transport from the HBP hopper toward the combustion bed. Irregular flow in the hopper was observed due to stagnant regions of particles that tend to adhere to the hopper walls regardless of the surface angle implemented. These stagnate regions of LS and LSC within the hopper resulted in the reported "bridging" or "dome" formation (Dai et al., 2012) which causes an intermittent and inconsistent feed towards the combustion bed.

Unlike the lupin agro-residues, QS and QH were constantly conveyed from the hopper of the combustion module towards the HBP bed. Nonetheless, the air stream provided by the blower linked with the HBP during the low-temperature ignition process dragged most of the QS and QH particles, that already reached the combustion bed, out of the burner. The issues concerning particles dragging by the stream of combustion air are typical of biomass-derived fuels with low particle density as QS and QH (Polonini et al., 2019).

This dragging and dome effects linked with QS, QH, LS, and LSC caused problems to ignite these agro residues in the combustion module and it was not possible to fixate a steady flame front. Accordingly, QS, QH, LS, and LSC were discarded as fuel sources for the initial heating process of the pilot-scale auger-type pyrolysis reactor. The reactor hoppers do not have stirring mechanisms, and thus the flow of agro-residues particles in the hopper of the combustion module depends mainly on gravity. Accordingly, an agro-residue with higher bulk density had to be used as solid fuel in the combustion module during the initial heating process of the pilot-scale auger-type pyrolysis reactor, namely palm oil kernel shell. This decision follows the initial demonstration of the operation of this pilot-scale auger-type reactor in which the initial heating process of the pyrolysis chamber was performed by feeding palm oil kernel shells (1,120 kg/m^3) in the combustion module (Heredia Salgado et al., 2020).

Thus, the heating process increase the temperature of the combustion chamber to 550 C (thermocouple T3 in Figure 2). The corresponding temperature at the inlet of the carbonization chamber was 400 C (thermocouple T6 in Figure 2). Under these conditions, the rotary vane valve of the pyrolysis module

TABLE 2 Observations made during the conveying process of QH, QS, LS and LSC from the hopper of the combustion module towards the combustion bed and from the pyrolysis module hopper towards the carbonization chamber.

Feedstock	Feeding	Combustion Module: Observation	Feeding	Pyrolysis module: Observation
Quinoa stems (QS)	✗	Dragging: QS particles reach the combustion bed. Afterward, QS was dragged by the combustion air stream out of the combustion chamber	✓	QS was fed at a steady rate of 30 kg/h
Quinoa husks (QH)	✗	Dragging: QS particles reach the combustion bed. Then, QS was dragged by the combustion air stream out of the combustion chamber	✓	QH was fed at a steady rate of 30 kg/h
Lupin stems (LS)	✗	Bridging: irregular flow of particles in the hopper, stagnant regions, and dome formation	✗	Bridging: irregular flow of particles in the hopper, stagnantregions, and dome formation. Leakage of pyrolysis gas through the hopper cover. Vapor condensation within the hopper moist the feedstock
Lupin seedcases (LSC)	✗	Bridging: irregular flow of particles in the hopper, stagnant regions, and dome formation	✗	Bridging: irregular flow of particles in the hopper, stagnant regions, and dome formation. Leakage of pyrolysis gas through the hopper cover. Vapor condensation within the hopper moist the feedstock

(number 12 in Figure 2) was activated to start conveying QS, QH, LS, and LSC towards the pyrolysis chamber in individual experiments.

3.2 Pilot-scale auger-type pyrolysis reactor: The pyrolysis module

During the pyrolysis experiments using LS and LSC as feedstock, a constant void in the center of the biomass hopper of the pyrolysis module was observed (see Table 2). As the feed of the LS and LSC towards the pyrolysis module starts, a mass of static material develops around a void in the center of the hopper through which the lupin agro residues eventually flow, that is, the often-mentioned bridging, arching, or rathole effect (Dai et al., 2012).

As described in Section 2.2. The pilot-scale auger-type reactor does not use additional gases to secure an inert atmosphere in the pyrolysis module because the feedstock in the secondary hopper, the rotary vane valve, and a sealed cover in the hopper act as a triple seal that grants tightness. The voids observed in the hopper while conveying LS and LSC causes the pyrolysis gas to bypass the rotary vane valve and slight pyrolysis gas leakages were observed through the hopper cover in the pyrolysis module. Fifteen minutes after starting to convey the LS and LSC, the condensable species in the pyrolysis gas (i.e., water and tar), starts condensing in the hopper cover of the pyrolysis module and falling over the agro-residues (LS and LSC) within the hopper. This condensing effect moistens the agro-residues in the hopper, turning impossible to feed them through the rotary vane valve towards the pyrolysis chamber. Furthermore, the high temperature of the pyrolysis gases accumulated in the hopper caused the failure of the hopper cover seals, and significant pyrolysis gas leakages from the hopper were observed thereafter.

The unsteady supply of LS and LSC towards the pyrolysis chamber and the leakages of pyrolysis gas from the hopper cover caused an unsteady carbonization process. Furthermore, the temperatures within the combustion and pyrolysis modules did not reach the values required to achieve an auto-thermal operation mode, as reported by Heredia Salgado, 2020, during the operation of the same reactor with agro-residues of high particle density. Therefore, the carbonization experiments with LS and LSC were suspended.

It is worth mentioning that during the grinding of LS, elongated fibers were detected within the mill. These long fibbers became continuously entangled in the rotor of the mill making it difficult to reduce and adjust the granulometry to the desired particle size. Although these long fibers of the LS were manually removed during the grinding process, a remaining fraction of broken fibers of smaller size eventually passed the outlet mesh of the mill. During the pyrolysis experiments with LS, the movement of material in the hopper revealed that these remaining fractions of broken fibers interact with the larger LS particles and tend to form small agglomerates like scourers (see Figure 3). The trend to form these scourers in the hopper is the main cause of the transporting problems, that is, the dynamic bridging that prevented the use of LS as feedstock to produce biochar in the pilot-scale auger-type pyrolysis reactor. This dynamic bridging effect was also observed in experiments that used LSC as feedstock.

3.3 Pyrolysis of quinoa stems and husks

As shown in Table 2, QS and QH were fed from the pyrolysis module hopper towards the carbonization chamber under steady-state conditions and without a bridging effect. The QS and QH were fed when the temperature at the inlet of the

FIGURE 3
(A) Mass of static bulk material around a void observed in the center in the pyrolysis module hopper while conveying LS and LSC towards the carbonization chamber. **(B)** Scourers found in the hopper that result from the interaction between LS and LSC particles with small broken fibers. **(C)** Pyrolysis module hopper with cover and rotary valve. **(D)** Failure of seals and tars condensed in the rotary vane valve.

pyrolysis chamber was 400 C (thermocouple T6 in Figure 2). During the experiments, the mass flow of QS and QH was 30 kg/h and the residence time of the feedstock within the pyrolysis chamber was 15 min. As the feedstock is distributed along the pyrolysis chamber, the gases generated during the initial steps of devolatilization are dragged by the PGB (number 15 in Figure 2), from the pyrolysis chamber towards the combustion chamber. Accordingly, the thermal energy required by the pyrolysis process is supplied by the hot gases generated from the combustion of pyrolysis gases and the combustion of biomass fuel in the HBP, that is, a co-combustion condition.

During the pyrolysis of palm oil kernel shells, it is possible to shift from this co-combustion stage to an auto-thermal condition in which the thermal energy required by the pyrolysis process is supplied exclusively by the combustion of the pyrolysis gases (Heredia Salgado et al., 2020). To shift from the co-combustion stage towards the auto-thermal operation mode, the thermal power output of the HBP is decreased progressively as the temperature in the combustion chamber increases due to the increase in the yield of pyrolysis gas. Nonetheless, during the co-combustion stage corresponding to the experiments with QS and QH, although there is a steady flame front in the PGB, the progressive decrease of the PGB thermal power output caused a decrease in the temperatures of the combustion (thermocouples T1, T2 and T3 in Figure 2) and pyrolysis chambers (thermocouples T5, T6 and T7 in Figure 2). Consequently, the pyrolysis process was not maintained under steady-state conditions and the flame front of the PGB was extinguished 10 min after turning off the HBP.

During the experiments that use QS and QH, the HBP remained on to maintain steady temperatures in the combustion and pyrolysis chambers. The feeding rate of solid fuel (palm kernel shell) implemented in the HBP to support the combustion process in the PGB was 4.5 kg/h. Under these operating conditions, a steady flame front in the PGB was observed and the pilot-scale auger-type pyrolysis reactor reaches steady-state operation. The mean temperatures observed in the combustion and pyrolysis modules during the experiments with QS, QH and the corresponding standard deviation is shown in Table 3. It is important to note that thermocouples T5 and T6 shown in Table 3 are meant to represent the temperature in this zone of the reactor which is not necessarily the temperature of the feedstock particles flowing through the pyrolysis chamber. The technical limitation that implies the installation of a thermocouple in direct contact with the particles moving along the pyrolysis chamber, and whether this measurement is representative of the temperature of the particles in different positions within the reactor, is a limitation typically associated with continuous and semicontinuous pilot-scale pyrolysis reactors as the one used in this study (Brassard et al., 2017; Campuzano et al., 2019). As an alternative to overcome this limitation, the use of computational fluid dynamics may aid the exploration of the temperature distribution of the particles within the pyrolysis chamber (Aramideh et al., 2015).

In general, the temperatures observed in the combustion and pyrolysis modules during the carbonization of QS, and QH (see thermocouples T5 and T6 in Table 3) are lower than those observed during the carbonization process of palm oil kernel shells, which were up to 600 C in the same reactor type (Heredia Salgado et al., 2020). In the current study, the inability to raise the temperature of the pyrolysis chamber above 500 C and the fact of not reaching the auto-thermal operation condition can be related to the physical and chemical properties of the pyrolysis gas. It should be noted that the physical and chemical composition of the feedstock of the pyrolysis process influences the properties, composition, and LHV of the pyrolysis gas as reported by (Rosas et al., 2014) and (Dunnigan et al., 2018). It is recognized that the lower heating value (LHV) of the pyrolysis gas decreases as the pyrolysis temperature decreases. Furthermore, the content of pyrolytic water in the pyrolysis gas is higher at pyrolysis temperatures below 500 C (Neves et al., 2011). Accordingly, the gas generated during the pyrolysis of QS and QH at a temperature of 500 C is expected to have a lower LHV and a higher content of pyrolytic water than the gas generated during the pyrolysis of palm oil kernel shells at temperatures of 600 C.

TABLE 3 Temperatures (mean and standard deviation) observed during the pyrolysis process of QS, and QH in the pilot-scale auger-type reactor. Location of thermocouples in the reactor is shown in Fig.2.

Temperature (°C)	Quinoa stems (QS)		Quinoa husks (QH)	
	Mean	Standard deviation	Mean	Standard deviation
Combustion chamber, T1	418.4	22.4	419.6	26.2
Combustion chamber, T2	368.6	15	389.6	15.9
Combustion chamber, T3	554.3	41.5	563.5	47.9
Flue gas, T4	402.5	50.8	435.1	54.1
Pyrolysis chamber outlet, T5	500.4	7.7	500	37.6
Pyrolysis chamber inlet, T6	435.3	36.8	426.2	42.7
Pyrolysis gas, T7	235.9	21.7	209.3	22.9

TABLE 4 Flue gas composition (mean and standard deviation) observed during the pyrolysis experiments with QS, and QH.

	CO (mg/Nm^3,dry gas, at 11% O_2, dry gas)		HC (mg/Nm^3,dry gas, at 11% O_2, dry gas)		CO_2 (mg/Nm^3,dry gas, at 11% O_2, dry gas)	
	Mean	Standard deviation	Mean	Standard deviation	Mean	Standard deviation
QS	1,024.4	658.6	35.3	4.1	180,000	2,701.4
QH	559	387.3	20.4	7.1	172,317.1	2,516.7

*The CO, HC, and CO_2 concentration is presented according to the implementing directive of the European Parliament concerning eco-design requirements for solid fuel boilers (500 mg/Nm^3), that is, corrected to an O_2 concentration in the flue gas of 11 %vol, dry gas.

These changes in the composition of pyrolysis gas that are linked with the pyrolysis temperatures will influence the performance of the combustion module.

The mean concentration of CO, CO_2, and HC observed during the pyrolysis experiments of QS and QH (co-combustion condition) in a monitoring period of 4 hours under steady-state conditions is shown in Table 4. There was a difference in the concentration of CO in the flue gas for the carbonization experiment that used QH and QS, namely 559 and 1,024.4 mg/Nm^3 (at 11% vol. O_2, dry gases), respectively. The particle dynamics of the QS and QH in the hopper of the pyrolysis module influenced this difference between the two sets of experiments shown in Table 4. Although QS and QH were successfully conveyed from the biomass hopper towards the pyrolysis chamber, practically no voids were observed in the biomass hopper during the pyrolysis experiment of QH. The lower tendency of the QH particles to form voids became evident because, unlike QS, the pyrolysis gas that eventually bypass the seals of the pyrolysis module and leaks through the cover of the hopper was not noticeable in the pyrolysis experiment that used QH. This observation is attributed to the better dynamic flowing properties of the QH particles over the QS particles which resulted in a steadier feed toward the pyrolysis chamber. Thus, the better feeding conditions of QH particles can justify the lower CO and HC concentration in the combustion flue gases observed in the corresponding pyrolysis experiment. As observed before in this type of reactor, a steady feed of agro-residues is fundamental to achieve a good conversion efficiency of the pyrolysis gases. Considering a similar feed rate of 30 kg/h in the same type of reactor, the CO concentration in the flue gas observed during the pyrolysis process of palm oil kernel shells was 197 mg/Nm^3 (at 11% vol. O_2, dry gases) (Heredia Salgado et al., 2020).

As shown in Table 4, the CO concentration in the combustion flue gas during the experiment of pyrolysis of QS almost doubles the CO concentration in the combustion flue gas observed during the experiment of pyrolysis of QH, and the limit of 500 mg/Nm^3 referred to in the European eco-design standard was exceeded. It is not clear if the eco-design standard considered (The European Commission, 2015), that is usually applied for boilers and space heaters that use solid fuels and operate at sea level, may be applied for the operating condition implemented in this study, namely co-combustion of gaseous and solid fuels at an altitude of 2,634 m.a.s.l. In this study, the O_2 concentration in the atmospheric air supplied towards the burners (HBP and PGB) decreases from 21% to 16% due to the decrease of the atmospheric pressure corresponding to an altitude of 2,634 m.a.s.l (Heredia Salgado et al., 2019a). Furthermore, the flue gas concentration shown in Table 4 corresponds to a co-combustion operating condition, that is, the combined operation

TABLE 5 Proximate and elemental analysis the biochar produced during the pyrolysis experiments of quinoa stems (QS) and the PCM produced during the pyrolysis of quinoa husks (QH).

Proximate analysis (%wt, wet basis)	Quinoa stems (QS) biochar	Quinoa husk (QH) PCM
Moisture	10.2	11
Volatile matter	11.5	20.9
Ash	22.1	30.1
Fixed carbon[a]	56.2	38
Ultimate Analysis (%wt, dry basis)		
Ash	28.4	43.1
C	54.9	40.4
H	2.2	3.6
N	1	1.8
S[b]	nd	0.3
O[a]	13.5	10.8
Lower Heating Value (MJ/kg, dry basis)	23.7	15
Biochar molar ratios		
H/C_{org}	0.5	1.1
O/C_{org}	0.2	0.2

[a]Calculated by difference.
[b]Below the detection limit of the method 100 ppm wt. nd-not determined.

of the HBP using palm oil kernel shells as fuel and the PGB using the gas generated in the pyrolysis chamber as fuel. Although the limitations of the eco-design standard concerning the context of the study, the exploration of alternatives to increase the combustion temperatures (T1, T2 and T3 in Table 3) and thus, improve the conversion degree of the flammable species as CO and HC is of relevance. For instance, the implementation of air stagging techniques (Qiu, 2013), the alteration of combustion chamber design to increase the residence time of flammable gases and flue gas recirculation (Míguez et al., 2012).

3.4 Properties and classification of the solid carbonaceous materials produced in the pyrolysis experiments using QS and QH as feedstock

Table 5 shows the proximal and elemental analysis of the solid carbonaceous materials produced from QS and QH pyrolysis. Usually, a concern regarding the use of the carbonaceous materials produced by pyrolysis in soil applications has to do with the content of volatile organic compounds, that is, tars that condense on their surface (Zheng et al., 2019). The properties of the carbonaceous materials produced by pyrolysis, as the content of volatile organic compounds, is affected mainly by pyrolysis temperature and feedstock type (Tomczyk et al., 2020). In this regard, reach a temperature in the pyrolysis process of at least 400 C is critical to reduce toxicity of the produced carbonaceous materials making them suitable for soil application (Lyu et al., 2016). Table 3 shows that the temperatures at which the carbonaceous materials made from QH and QS were produced, that is, the temperatures at the inlet and outlet of the pyrolysis chamber, were between 426.2 and 500 C, respectively (see T5 and T6 in Table 3). Furthermore, the fluctuation of temperatures at the inlet and outlet of the pyrolysis chamber was never above 8% (see Table 3), being that the guidelines for the sustainable production of biochar allow a fluctuation up to 20%. Accordingly, the volatile matter of the produced carbonaceous materials is seven and three times lower than the volatile matter content of the raw QS and QH, respectively (see Tables 1 and 5). Despite the important reduction of the volatile matter content that result of implementing proper operating temperatures, an estimation of the content of volatile organic compounds by thermal-gravimetric-analysis could also be performed as a further indicator for the evaluation of the pyrolysis process and the quality of the carbonaceous materials obtained.

Table 5 shows that the solid carbonaceous material produced from QS have a carbon content higher than 50 wt%, an O/C_{org} ratio lower than 0.4, and an H/C_{org} ratio lower than 0.7. Accordingly, it meets the biochar properties following the

European standard (European Biochar Foundation, 2018). Concerning the solid carbonaceous material made from QH pyrolysis, the carbon content is lower than 50 wt% and the H/C_{org} molar ratio (degree of carbonization) is higher than the limit of 0.7 suggested by the European guidelines for the sustainable production of biochar (European Biochar Foundation, 2018). These particular properties can be linked with an incomplete pyrolysis process, namely inadequate residence time and low pyrolysis temperatures. However, temperatures up to 500 C (see Table 3) were registered during the pyrolysis of QH, which agree with the European standards and studies that report positive effects of adding biochar -produced at these conditions-to quinoa and lupin crops (Kammann et al., 2011, 2015; Egamberdieva et al., 2017). In these cases, the European standard used in this study state that the use of mineral-rich materials as feedstock may result in solid carbonaceous materials with high ash and low carbon content and classify them, rather than biochar, as pyrogenic carbonaceous materials (PCMs) (European Biochar Foundation, 2018). This does mean that the carbonized QH can be classified as a PCM and could be used for soil amendment. The PCMs have high nutrient content, therefore representing a valuable product for soil amendment (Paz-Ferreiro et al., 2018). It should be noted that the ash content of the raw QH is higher than that of QS (see Table 1). Consequently, the ash content of the PCM made from QH is around two times higher than that of the biochar made from QS (see Table 4). Therefore, the differences in the carbon content and the H/C_{org} molar ratio observed between the PCM made from QH and the biochar made from QS are not related to an incomplete or inadequate pyrolysis process but rather related to high ash content.

3.5 Learning from farmers and local practitioners through the lens of SWOT analysis

In the Andes highlands, before the implementation of a pyrolysis process to convert agro residues into biochar one must consider that unlike traditional commodities such as cocoa, palm oil, or sugar cane, quinoa, and lupin are not large-scale monocultures. Both are cultivated in small-scale farms geographically dispersed along the territory and there are no centralized facilities dedicated to collect and process the panicles, neither for drying nor the threshing process. Accordingly, threshing is a farm delivery service in which the threshing machines are transported from one farm to another using small trucks. After the threshing process, the agro residues accumulate forming small mounts that remain on the many farms of the region to rot, burn in the open or as a low-quality source of organic matter for the soil. Accordingly, the SWOT analysis shown in Table 6 argues that the implementation of a centralized infrastructure for the conversion of agro residues into products for soil amendment as biochar or PCMs would demand collection and transporting operations, which in the case of agro residues with low bulk-density, is costly and inefficient (Chen et al., 2015). Along with the collection and transport operations, the milling processes required to reduce the particle size before pyrolysis in auger-type pyrolysis reactors as the one used in this study (see Section 2.1) also represent a weakness as the initial investment costs and the operating costs will increase.

The alternative to deploy a decentralized operation for the conversion of agro residues into biochar and PCMs, similar to the portable threshing service currently used, may not be an option because the pilot-scale auger-type pyrolysis reactor requires an electricity supply to power its electric devices and the automation system. According to our participant observations, the threshing machines use gasoline to produce mechanical work because electricity supply is not available on every farm. Thus, the implementation of a portable auger-type pyrolysis reactor to deliver pyrolysis as a farm delivery service may not be entirely feasible. In this context, Table 6 points as an opportunity the study, adaptation, and later implementation of low-complexity technologies for the production biochar, for instance, top lift updraft gasifiers TLUD´s or flame curtain retort kilns (Obi et al., 2016; Pandit et al., 2017). These types of low-cost reactors may allow the use of the agro residues on each farm, avoiding collection, transporting, and even milling operations. Nonetheless, the quality of the biochar produced in low-cost reactors must be carefully analyzed to guarantee its safe application for soil amendment. In this regard, the results presented in Section 3.4 concerning the properties and composition of the biochar and PCMs made from QS and QH are a major quality reference.

Moreover, a set of studies made in the same reactor used in this work and using operating conditions similar to that disclosed in Section 3.3 states that the biochar made from QS can be used to prevent cadmium absorption in aqueous solutions, reducing up to 71% of the bioavailable cadmium in acidic soils used to grow cocoa (López et al., 2020, 2022). Hence, the biochar made from quinoa agro residues could be relevant not only to prevent soil erosion at the local level but for a wide range of environmental remediation applications. Accordingly, Table 6 claims that the conversion of QS into biochar may generate new sources of income in rural areas, for instance, those derived from the marketing of surplus biochar for use in other sectors such as animal husbandry, water filtration or environmental remediation (Man et al., 2020).

During the participant observations, the farmers revealed that some farms have in place infrastructures for the elaboration of bio inputs such as compost, bokashi (organic fertilizer made by fermentation), and biols (liquid fertilizer made from anaerobic digestion of manure). Hence, the implementation of low-cost and complexity technologies for biochar production in the farms can be an opportunity to complement these infrastructures and potentially improve the bio inputs used in the farms. Our SWOT analysis also shows that the implementation of

TABLE 6 Results of a SWOT analysis that explore the constraints and prospects concerning the conversion of agro-residues produced during the post-harvesting processes of Quinoa and Lupin into biochar for soil amendment in the Andes highlands.

	Strengths	Weaknesses
Internal	- Availability of reasonable quantities of already dry-agro residues - The biochar made from QS and the PCM made from QH fulfill the international requirements to be safely used for soil amendment - Biochar and PCM made from local agro residues can be used to prevent erosion of Andean soils and mitigate, in part, the environmental impacts linked with the past boom of quinoa and lupin crops - Currently, farmers of the highlands produce bio inputs as bokashi, vermicompost, and liquid fertilizers "biol" which can be improved-complemented including biochar and PCMs as an additive - Despite the altitude (2,634 m.a.s.l.), the flue gas during the pyrolysis process follows the European eco-design standards - Ecuador has knowledge concerning high-complexity pyrolysis technologies for biochar production. namely, pilot-scale auger-type reactors. Accordingly, the study, adaptation, and deployment of low-cost and complexity reactors should not be a constraint	- The threshing process is decentralized. There is not a single facility that accumulates and processes the panicles. Thus, agro residues are scattered throughout the territory - An auger-type pyrolysis reactor requires an electricity supply to power electric devices and for automation. Electricity supply in the farms where agro-residues are accumulated is scarce. Thus, there will be constraints in setting up complex reactors in a decentralized operation model in the Andes highlands - The agro residues must be milled to reduce the particle size before pyrolysis. High initial investment costs and operation costs linked with auger-type pyrolysis reactors - The properties and quality of the biochar produced in low-cost and complexity reactors (TLUD´s, flame curtain kilns) may be heterogeneous or not within the guidelines for its safe use in soils - The available agro residues (QH, QS, LS, LSC) could not be used as fuel sources for the initial heating process of the pilot-scale auger-type pyrolysis reactor, demanding the use of alternative solid fuels not necessarily at the reach of farmers in the highlands
	Opportunities	**Threats**
External	- Biochar made from QS pyrolysis and PCM made from QH pyrolysis are alternatives to recycle soil nutrients, supply organic matter and ultimately, restore eroded and overexploited soils - QS biochar can be relevant for environmental remediation applications in other agriculture sectors and regions of the country (e.g. Cd adsorption in cocoa crops) - Biochar can also be used as a feed supplement for cows and sheep's husbandry or rainwater filtration - If surplus biochar and PCMs are marketed by local communities, can be a new source of familiar income - The alternative of using low-cost and complexity reactors as top-lit-up draft gasifiers or flame curtain kilns and retorts - Low-cost and complexity technologies could be replicated by other quinoa producers in the region, namely Perú and Bolivia which also face the consequences of soil over-exploitation - Creation of jobs in the rural sector: sales and operation of pyrolysis reactors (tech as a service), maintenance and management of pyrolysis facilities. Sale of surplus biochar - Carbon removal certificates that result from the application of biochar in soils could be claimed by farmers' communities. The emergence of carbon sequestration standards tailored for small-scale farmers	- Environmental regulations: currently, there are no specific standards in Ecuador, nor in other producer countries as Peru and Bolivia to regulate the use and efficiency of pyrolysis reactors (e.g., flue gas emissions standards) - Indeed, there is no dedicated standard to regulate the biochar composition or its use in soils - The Ecuadorian constitution (Art 74) forbids the trade of carbon removal certificates generated from ecosystem services. Accordingly, monetization of carbon sequestration services using soil as carbon sinks is uncertain - High-cost international certification for farmers as providers of carbon sequestration services - Inadequate use of low-cost and low-complexity reactors to convert agro residues into biochar may result in low-quality products and dangerous gaseous emissions

valorization technologies to convert agro residues generated locally into biochar or PCMs can be an opportunity to create jobs, for instance, those required to provide, manage, operate (tech as a service), repair, and maintain these pyrolysis reactors.

It is worth to highlight that application of biochar in soils by Andean farmers can result in carbon removal certificates, that properly traced and traded, could be another source of income for farmers (Heredia Salgado et al., 2021). However, complex technical and bureaucratic processes are required to register a farmer as a provider of carbon sequestration services (Bier et al., 2020; Schmidt et al., 2020). Currently, Ecuador does not have a technical standard to regulate the use of biochar in soils. In addition, there is an ongoing discussion regarding the interdict established by the Ecuadorian constitution (art 74), which prevents privates from appropriating and trading with services derived from ecosystems, for example, the carbon removal certificates, or carbon credits linked with carbon sequestration in soils, including those considering forestation and afforestation. Perhaps, the alternatives of carbon sequestration that are not linked with ecosystem services, for instance, the use of biochar as an additive in cement (sequestration in gray infrastructures, buildings, dams, *etc.*) may be out of the constitution interdict. Nonetheless, great uncertainty remains as to whether the implementation of pyrolysis facilities for biochar production can turn farmers into providers of carbon sequestration services. In this regard, the lack of local standards and regulations constitute a threat that is currently preventing the mobilization of funds for the implementation of alternatives for the conversion of agro residues into biochar and PCM´s.

4 Conclusion

The studies that support the use of biochar in quinoa and lupin crops and that validate its effect on the restoration of

degraded ecosystems have been performed using biochars produced from agro residues not necessarily available in the Andean highlands, for example, peanut hull residues. Biochar could become an alternative to improve soil management practices and material to restore the overexploited ecosystems during the quinoa and lupin boom, to the extent that the agro residues available in the Andean highlands may be used as the feedstock of the pyrolysis process. Our study shows that the agro residues generated after the threshing processes of quinoa, namely QS and QH can be transformed into materials for soil amendment using a pilot-scale auger-type pyrolysis reactor.

Following the European guidelines for the sustainable production of biochar, the solid carbonaceous material produced from QS pyrolysis can be categorized as biochar while the carbonaceous material produced from QH pyrolysis can be categorized as pyrogenic carbonaceous material (PCM). The agro residues generated during lupin threshing, namely lupin stems and lupin seedcases were not properly pyrolyzed. Our study further shows that the concentration of CO in the flue gas observed during the pyrolysis of QS and QH was 1,024.4 and 559 mg/Nm^3, respectively. The experiments were performed in the Andes highlands at an altitude of 2,634 m.a.s.l., that is, the oxygen concentration in the air decreased from 21 to 16% due to the decrease in atmospheric pressure. Despite the low oxygen concentration in the air, we observed that the differences in the composition of the flue gas in these experiments were influenced by the individual free fall density of the agro residues particles. Accordingly, a steady flow of QH particles in the reactor hopper and along the pyrolysis chamber resulted in a CO concentration of 559 mg/Nm^3 which is near the European eco-design standard of 500 mg/Nm^3.

From the participant observations and subsequent SWOT analysis, we claim that the implementation of an auger-type pyrolysis reactor may not be feasible in practice whether the operation model considers a centralized or decentralized valorization of agro residues. A centralized operation using an auger-type pyrolysis reactor will result in high collection, transportation and operating costs. Likewise, a decentralized operation will also be problematic because the electricity required to power the automation and electric devices as controllers, motors and blowers is not usually available in remote farms. Accordingly, we suggest the study and adaptation of low-cost and complexity reactors as an alternative for the decentralized pyrolysis of quinoa and lupin agro residues, namely, the top-lit updraft gasifiers (TLUD) and flame curtain kilns. Unlike low-cost and complexity reactors, the auger-type pyrolysis reactors allow a precise control of operating conditions such as pyrolysis temperature and residence time, also resulting in lower flue gas emissions. Nonetheless, if the quality of biochar is not compromised, the low-cost and low complexity reactors may constitute alternatives for the conversion of agro residues on each farm avoiding collection, transportation and even milling expenditures. In this regard, the properties of the biochar and PCM's along with the operating conditions disclosed in this study will serve for guidance and reference. Finally, the lack of local standards that regulate the production and use of biochar could make it difficult for local stakeholders as farmers' cooperatives, NGOs, the government, or quinoa/lupin exporting companies to advance with implementation models of TLUD's or flame curtain kilns at larger scales.

Data availability statement

The raw data supporting the conclusions of this article will be made available by the authors, without undue reservation.

Author contributions

MH provided funding, designed the experiments, collected samples, conducted the experiments, analyzed data, and wrote the original draft. JC conducted the experiments IS provided funding. IS and LT provided scientific guidance. AC, IS and LT reviewed the original draft.

Funding

This work was supported by the Humboldt University of Berlin and *Secretaría de Educación Superior, Ciencia, Tecnología e Innovación SENESCYT* of The Republic of Ecuador. Luís Tarelho declares the financial support from the Portuguese Foundation for Science and Technology (FCT)/Ministry of Science, Technology and Higher Education (MCTES) to Centre for Environmental and Marine Studies - CESAM (UIDP/50017/2020 + UIDB/50017/2020 + LA/P/0094/2020), through national funds, and to Project BioValChar - Sustainable valorisation of residual biomass for biochar, PCIF-GVB-0034-2019.

Acknowledgments

The authors acknowledge the *Gobierno Provincial del Chimborazo* that facilitated the contact with the community San Francisco de Bishud and thanks the farmers for the invitation that allowed our member to join the harvest season.

Conflict of interest

The authors declare that the research was conducted in the absence of any commercial or financial relationships that could be construed as a potential conflict of interest.

Publisher's note

References

Abbis, P., Benzenberg, C. P., Cerca, M., Anne De Boer, L., Ester, M., Frach, L., et al. (2017). *An analysis of the sustainability of the increasing consumption of Bolivian and Peruvian quinoa at university canteens in Berlin*. Berlin. Available at: edoc.hu-berlin.de/series/thesysdiscpapers.

Alarcon, M., Santos, C., Cevallos, M., Eyzaguirre, R., and Ponce, S. (2017). Study of the mechanical and energetic properties of pellets produce from agricultural biomass of quinoa, beans, oat, cattail and wheat. *Waste Biomass Valorization* 8, 2881–2888. doi:10.1007/s12649-017-9983-0

Aramideh, S., Xiong, Q., Kong, S. C., and Brown, R. C. (2015). Numerical simulation of biomass fast pyrolysis in an auger reactor. *Fuel* 156, 234–242. doi:10.1016/j.fuel.2015.04.038

Bedoya-Perales, N. S., Pumi, G., Mujica, A., Talamini, E., and Padula, A. D. (2018). Quinoa expansion in Peru and its implications for land use management. *Sustainability* 10, 532. doi:10.3390/su10020532

Bellemare, M. F., Fajardo-gonzalez, J., and Gitter, S. R. (2018). Foods and fads: The welfare impacts of rising quinoa prices in Peru. *World Dev.* 112, 163–179. doi:10.1016/j.worlddev.2018.07.012

Bier, H., Gerber, H., Huber, M., Junginger, H., Kray, D., Lange, J., et al. (2020). *Biochar-based carbon sinks to mitigate climate change*. Freiburg. Available at: http://www.biochar-industry.com/.

Bonifacio, A., Aroni, G., Villca, M., and Bentley, J. W. (2022). Recovering from quinoa: Regenerative agricultural research in Bolivia. *J. Crop Improv.* 00, 1–22. doi:10.1080/15427528.2022.2135155

Brassard, P., Godbout, S., and Raghavan, V. (2017). Pyrolysis in auger reactors for biochar and bio-oil production: A review. *Biosyst. Eng.* 161, 80–92. doi:10.1016/j.biosystemseng.2017.06.020

Bryant, L., Rangan, A., and Grafenauer, S. (2022). Lupins and health outcomes: A systematic literature review. *Nutrients* 14, 327. doi:10.3390/nu14020327

Caicedo, C., Peralta, E., Villacrés, E., and Rivera, M. (2001). *Poscosecha y mercado de chocho (Lupinus mutabilis Sweet) en Ecuador*. Quito. Available at: http://repositorio.iniap.gob.ec/handle/41000/2700.

Caicedo, V., and Peralta, E. (2000). *Zonificación potencial, sistemas de producción y procesamiento artesanal del chocho (lupinus mutabilis sweet) en Ecuador*. Quito. Available at: http://repositorio.iniap.gob.ec/jspui/handle/41000/441.

Campuzano, F., Brown, R. C., and Martínez, J. D. (2019). Auger reactors for pyrolysis of biomass and wastes. *Renew. Sustain. Energy Rev.* 102, 372–409. doi:10.1016/j.rser.2018.12.014

Chen, W.-H., Peng, J., and Bi, X. T. (2015). A state-of-the-art review of biomass torrefaction, densification and applications. *Renew. Sustain. Energy Rev.* 44, 847–866. doi:10.1016/j.rser.2014.12.039

Dai, J., Cui, H., and Grace, J. R. (2012). Biomass feeding for thermochemical reactors. *Prog. Energy Combust. Sci.* 38, 716–736. doi:10.1016/j.pecs.2012.04.002

Dunnigan, L., Ashman, P. J., Zhang, X., and Wai, C. (2018). Production of biochar from rice husk : Particulate emissions from the combustion of raw pyrolysis volatiles. *J. Clean. Prod.* 172, 1639–1645. doi:10.1016/j.jclepro.2016.11.107

Egamberdieva, D., Reckling, M., and Wirth, S. (2017). Biochar-based Bradyrhizobium inoculum improves growth of lupin (Lupinus angustifolius L.) under drought stress. *Eur. J. Soil Biol.* 78, 38–42. doi:10.1016/j.ejsobi.2016.11.007

European Biochar Foundation (2018). Guidelines for a sustainable production of biochar v4.5E. *Eur. Biochar Found.* v4.5, 1–22. doi:10.13140/RG.2.1.4658.7043

FAO and CIRAD (2015). *State of the art report on quinoa around the world*. Rome: FAO. Available at: https://www.fao.org/quinoa-2013/publications/detail/en/item/278923/icode/?no_mobile=1.

Fuentes, F. F., Bazile, D., Bhargava, A., and Martinez, E. A. (2012). Implications of farmers ' seed exchanges for on-farm conservation of quinoa , as revealed by its genetic diversity in Chile Terms of use : Click here Implications of farmers ' seed exchanges for on farm conservation of quinoa , as revealed by its geneti. *J. Agric. Sci.* 150, 702–716. doi:10.1017/S0021859612000056

Graf, B. L., Rojas-Silva, P., Rojo, L. E., Delatorre-Herrera, J., Baldeón, M. E., and Raskin, I. (2016). Innovations in health value and functional food development of quinoa (Chenopodium quinoa willd.) *Compr. Rev. Food Sci. Food Saf.* 14, 431–445. doi:10.1111/1541-4337.12135

Heredia, M. A., Tarelho, L. A. C., Matos, A., Robaina, M., Narváez, R., and Peralta, M. E. (2017). Thermoeconomic analysis of integrated production of biochar and process heat from quinoa and lupin residual biomass. *Energy Policy* 114, 332–341. doi:10.1016/j.jhep.2009.07.006

Heredia Salgado, M. A., Säumel, I., Cianferoni, A., and Tarelho, L. A. C. (2021). Potential for farmers' cooperatives to convert coffee husks into biochar and promote the bioeconomy in the north Ecuadorian amazon. *Appl. Sci. (Basel).* 11, 4747. doi:10.3390/app11114747

Heredia Salgado, M. A. (2020). Biomass thermochemical conversion in small scale facilities. Available at: https://ria.ua.pt/handle/10773/29518.

Heredia Salgado, M. A., Coba S, J. A., and Tarelho, L. A. C. (2020). Simultaneous production of biochar and thermal energy using palm oil residual biomass as feedstock in an auto-thermal prototype reactor. *J. Clean. Prod.* 266, 121804. doi:10.1016/j.jclepro.2020.121804

Heredia Salgado, M. A., Tarelho, L. A. C., Rivadeneira-Rivera, D. A., Ramirez, V., and Sinche, D. (2019b). Energetic valorization of the residual biomass produced during Jatropha curcas oil extraction. *Renew. Energy* 146, 1640–1648. doi:10.1016/j.renene.2019.07.154

Heredia Salgado, M. A., Tarelho, L. A. ., Matos, M. A. A., Rivadeneira, D., and Narváez C, R. A. (2019a). Palm oil kernel shell as solid fuel for the commercial and industrial sector in Ecuador: Tax incentive impact and performance of a prototype burner. *J. Clean. Prod.* 213, 104–113. doi:10.1016/j.jclepro.2018.12.133

Jacobsen, S. (2017). The scope for adaptation of quinoa in Northern Latitudes of Europe. *J. Agron. Crop Sci.* 203, 603–613. doi:10.1111/jac.12228

Jacobsen, S. (2011). The situation for quinoa and its production in southern Bolivia: From economic success to environmental disaster. *J. Agron. Crop Sci.* 197, 390–399. doi:10.1111/j.1439-037X.2011.00475.x

Kammann, C. I., Linsel, S., Gößling, J. W., and Koyro, H. W. (2011). Influence of biochar on drought tolerance of Chenopodium quinoa Willd and on soil-plant relations. *Plant Soil* 345, 195–210. doi:10.1007/s11104-011-0771-5

Kammann, C. I., Schmidt, H. P., Messerschmidt, N., Linsel, S., Steffens, D., Müller, C., et al. (2015). Plant growth improvement mediated by nitrate capture in co-composted biochar. *Sci. Rep.* 5, 11080–11113. doi:10.1038/srep11080

Kouris-Blazos, A., and Belski, R. (2016). Health benefits of legumes and pulses with a focus on Australian sweet lupins. *Asia Pac. J. Clin. Nutr.* 25, 1–17. doi:10.6133/apjcn.2016.25.1.23

López, J. E., Arroyave, C., Aristizábal, A., Almeida, B., Builes, S., and Chavez, E. (2022). Reducing cadmium bioaccumulation in theobroma cacao using biochar: Basis for scaling-up to field. *Heliyon* 8, e09790. doi:10.1016/j.heliyon.2022.e09790

López, J. E., Builes, S., Heredia Salgado, M. A., Tarelho, L. A. C., Arroyave, C., Aristizábal, A., et al. (2020). Adsorption of cadmium using biochars produced from agro-residues. *J. Phys. Chem. C* 124, 14592–14602. doi:10.1021/acs.jpcc.0c02216

Lyu, H., He, Y., Tang, J., Hecker, M., Liu, Q., Jones, P. D., et al. (2016). Effect of pyrolysis temperature on potential toxicity of biochar if applied to the environment. *Environ. Pollut.* 218, 1–7. doi:10.1016/j.envpol.2016.08.014

Maliro, M. F. ., Abang, M. ., Mukukankusi, C., Lung´aho, M., Fenta, B., Wanderu, S., et al. (2021). *Prospects for quinoa adaptation and utilization in eastern and southern Africa*. Addis Ababa: FAO. doi:10.4060/cb2351en

Man, K. Y., Chow, K. L., Man, Y. B., Mo, W. Y., and Wong, M. H. (2020). Use of biochar as feed supplements for animal farming. *Crit. Rev. Environ. Sci. Technol.* 51, 187–217. doi:10.1080/10643389.2020.1721980

Míguez, J. L., Morán, J. C., Granada, E., and Porteiro, J. (2012). Review of technology in small-scale biomass combustion systems in the European market. *Renew. Sustain. Energy Rev.* 16, 3867–3875. doi:10.1016/j.rser.2012.03.044

Neves, D., Thunman, H., Matos, A., Tarelho, L., and Gómez-Barea, A. (2011). Characterization and prediction of biomass pyrolysis products. *Prog. Energy Combust. Sci.* 37, 611–630. doi:10.1016/j.pecs.2011.01.001

Obi, O. F., Ezeoha, S. L., and Okorie, I. C. (2016). Energetic performance of a top-lit updraft (TLUD) cookstove. *Renew. Energy* 99, 730–737. doi:10.1016/j.renene.2016.07.060

Pandit, N. R., Mulder, J., Hale, S. E., Schmidt, H. P., and Cornelissen, G. (2017). Biochar from "Kon Tiki" flame curtain and other kilns: Effects of nutrient enrichment and kiln type on crop yield and soil chemistry. *PLoS One* 12, 01763788–e176418. doi:10.1371/journal.pone.0176378

Paniagua Bermejo, S., Prado-Guerra, A., García Pérez, A. I., and Calvo Prieto, L. F. (2020). Study of quinoa plant residues as a way to produce energy through thermogravimetric analysis and indexes estimation. *Renew. Energy* 146, 2224–2233. doi:10.1016/j.renene.2019.08.056

Paz-Ferreiro, J., Nieto, A., Méndez, A., Askeland, M. P. J., and Gascó, G. (2018). Biochar from biosolids pyrolysis: A review. *Int. J. Environ. Res. Public Health* 15, 956. doi:10.3390/ijerph15050956

Peralta, E., Mazon, N., Murillo, A., Rivera, M., Rodrígues, D., Lomas, L., et al. (2012). *Manual agrícola de granos andinos: Chocho, quinua, amaranto y ataco*. Quito: INIAP. *Cultivos, variedades y costos de producción*. 3rd ed. Available at: http://repositorio.iniap.gob.ec/jspui/handle/41000/833.

Polonini, L. F., Petrocelli, D., Parmigiani, S. P., and Lezzi, A. M. (2019). Influence on CO and PM emissions of an innovative burner pot for pellet stoves: An experimental study. *Energies* 12, 590–613. doi:10.3390/en12040590

Qiu, G. (2013). Testing of flue gas emissions of a biomass pellet boiler and abatement of particle emissions. *Renew. Energy* 50, 94–102. doi:10.1016/j.renene.2012.06.045

Rosas, G., Cara, J., Martínez, O., Martinez, O., Alburquerque, J. A., and Sanchez, M. E. (2014). Slow pyrolysis of relevant biomasses in the Mediterranean basin . Part 1 . Effect of temperature on process performance on a pilot scale. *J. Clean. Prod.* 120, 181–190. doi:10.1016/j.jclepro.2014.10.082

Schmidt, H., Kammann, C., and Hagemann, N. (2020). *Certification of the carbon sink potential of biochar*. Switzerland: Arbaz.

Scholz, S. M., Sembres, T., Roberts, K., Whitman, T., Wilson, K., and Lehmann, J. (2014). *Biochar systems for smallholders in developing countries:leveraging current knowledge and exploring future potential for climate-smart agriculture*. Washington, D.C: The World Bank. doi:10.1596/978-0-8213-9525-7

Silva, P. M., Massuela, D. C., Khan, M. W., Hamar, A., Khajehei, F., Grae, S., et al. (2020). Quinoa (Chenopodium quinoa willd.): An overview of the potentials of the "golden grain" and socio-economic and environmental aspects of its cultivation and marketization. *Foods* 9, 216. doi:10.3390/foods9020216

Stensrud, A. B. (2019). Safe milk and risky quinoa: The lottery and precarity of farming in Peru. *Focaal* 83, 72–84. doi:10.3167/fcl.2019.830108

Stubbs, J. J., Scott, S. E., and Duarte, C. (2018). Responding to food, environment and health challenges by changing meat consumption behaviours in consumers. *Nutr. Bull.* 43, 125–134. doi:10.1111/nbu.12318

The European Commission (2015). Commission regulation (eu) 2015/1189: Implementing directive 2009/125/EC of the European parliament and of the council with regard to ecodesign requirements for solid fuel burners. *Off. J. Eur. Union* L193/100, 8–15.

Tomczyk, A., Sokołowska, Z., and Boguta, P. (2020). Biochar physicochemical properties: Pyrolysis temperature and feedstock kind effects. *Rev. Environ. Sci. Biotechnol.* 19, 191–215. doi:10.1007/s11157-020-09523-3

Zheng, H., Liu, B., Liu, G., Cai, Z., and Zhang, C. (2019). *Potential toxic compounds in biochar : Knowledge gaps between biochar research and safety*. Elsevier. doi:10.1016/B978-0-12-811729-3.00019-4

frontiers | Frontiers in Bioengineering and Biotechnology

TYPE Review
PUBLISHED 07 December 2022
DOI 10.3389/fbioe.2022.1056804

OPEN ACCESS

EDITED BY
Benyamin Khoshnevisan,
University of Southern Denmark,
Denmark

REVIEWED BY
Mingfeng Cao,
Xiamen University, China
C. French,
University of Edinburgh,
United Kingdom

*CORRESPONDENCE
Fei Wang,
hgwf@njfu.edu.cn

SPECIALTY SECTION
This article was submitted to Bioprocess Engineering,
a section of the journal
Frontiers in Bioengineering and Biotechnology

RECEIVED 29 September 2022
ACCEPTED 25 November 2022
PUBLISHED 07 December 2022

CITATION
Zhang C, Chen H, Zhu Y, Zhang Y, Li X and Wang F (2022), *Saccharomyces cerevisiae* cell surface display technology: Strategies for improvement and applications.
Front. Bioeng. Biotechnol. 10:1056804.
doi: 10.3389/fbioe.2022.1056804

Saccharomyces cerevisiae cell surface display technology: Strategies for improvement and applications

Chenmeng Zhang[1,2,3], Hongyu Chen[1,2,3], Yiping Zhu[1,2,3], Yu Zhang[1,2,3], Xun Li[1,2,3] and Fei Wang[1,2,3]*

[1]Jiangsu Co Innovation Center of Efficient Processing and Utilization of Forest Resources, College of Chemical Engineering, Nanjing Forestry University, Nanjing, China, [2]Jiangsu Provincial Key Lab for Chemistry and Utilization of Agro Forest Biomass, Jiangsu Key Lab of Biomass Based Green Fuels and Chemicals, Nanjing, China, [3]International Innovation Center for Forest Chemicals and Materials, Nanjing Forestry University, Nanjing, China

Microbial cell surface display technology provides a powerful platform for engineering proteins/peptides with enhanced properties. Compared to the classical intracellular and extracellular expression (secretion) systems, this technology avoids enzyme purification, substrate transport processes, and is an effective solution to enzyme instability. *Saccharomyces cerevisiae* is well suited to cell surface display as a common cell factory for the production of various fuels and chemicals, with the advantages of large cell size, being a Generally Regarded As Safe (GRAS) organism, and post-translational processing of secreted proteins. In this review, we describe various strategies for constructing modified *S. cerevisiae* using cell surface display technology and outline various applications of this technology in industrial processes, such as biofuels and chemical products, environmental pollution treatment, and immunization processes. The approaches for enhancing the efficiency of cell surface display are also discussed.

KEYWORDS

***Saccharomyces cerevisiae*, cell-surface display technology, scaffoldin, bioconversion, cell factory**

1 Background

Cell surface display technology is an attractive method for immobilizing functional proteins/peptides and imparting specific functions to microbial cells. In the cell surface display system, functional proteins/peptides are fused with anchoring protein genes and expressed on the cell surface or plasma membrane under the guidance of signal peptides. The cell-surface display technology has unique advantages over intracellular expression and secretion: 1) Proteins displayed on the cell surface can maintain their functions and properties more stably under harsh temperature or pH conditions than free proteins. 2) The proteins immobilized on the cell surface can be recycled by filtration or centrifugation, avoiding the complicated process of lysing cells or purifying proteins

from the cultural liquid. 3) The multi-enzyme cell surface co-display system can shorten the substrate transfer distance, and the co-display of enzymes with synergistic effects can trigger synergistic proximity effects and improve catalytic efficiency. 4) Engineered yeast with functional proteins displayed on the surface can act on large molecular masses of substrates (e.g., cellulose, hemicellulose) that cannot enter the cell, and the resulting monomers (e.g., glucose) can be directly utilized by the cell to produce valuable products (e.g., bioethanol). This process contributes to the integrated bioprocessing process that combines hydrolysis, saccharification and fermentation. Cell surface display systems have many potential applications, including biocatalysts, high-throughput library screening, biological sorbents, oral vaccines, *etc.* (Teymennet-Ramírez et al., 2022).

Cell surface display systems have been successfully applied to various microbial cells. Among them, yeast cells are one of the most suitable host cells for cell surface display, with relatively large cell size, rigid cell walls, and allowing post-translational processing (including folding and glycosylation, *etc.*) of expressed heterologous eukaryotic proteins (Liu et al., 2016a). In yeast, cell surface display was first developed in *S. cerevisiae* with remarkable results. Subsequently, surface display systems using full-length or anchored structural domains of *S. cerevisiae* cell wall proteins were applied to other yeasts, including *Pichia pastoris* (Zhao N. et al., 2017; Yang et al., 2017; Ce et al., 2022) and *Yarrowia lipolytica* (An et al., 2016). *S. cerevisiae* is easy to manipulate genetically and has Generally Regarded As Safe (GRAS) status due to its widespread use in the food industry (Cha et al., 2022). In recent years, various applications of yeast surface display systems have been reported by many researchers, and there are also related review articles outlining strategies for improving yeast surface display systems (Teymennet-Ramírez et al., 2022). However, few have provided detailed overviews for one yeast alone. This paper focuses on the progress of research using *S. cerevisiae* as a cell surface display object and not only introduces strategies to improve cell surface display but also discusses in more detail the wide range of applications of surface-engineered *S. cerevisiae* and provides insights into the challenges of future commercialization.

2 Cell surface display systems in *S. cerevisiae*

Cell surface display is a powerful tool for endowing novel functions on *S. cerevisiae* cells by displaying functional proteins/peptides on the cell surface. The cell surface display system has been enriched by the research on cell wall structure of *S. cerevisiae*. Its inner layer consists mainly of β-linked glucans, which are cross-linked with chitin to maintain cell wall strength, and the outer layer consists mainly of mannoproteins, which are covalently linked to the inner layer, and heterologous proteins can be anchored to the mannoprotein layer to determine cell surface properties (Ye et al., 2021). In the cell surface display platform, different enzymes can be located on the same cell surface and the proximity could improve their synergism. This platform simplifies protein purification in some biocatalytic processes and promotes the construction and reuse of whole-cell catalysts.

2.1 Direct cell surface display

In cell surface display, the target protein fused with specific vector sequence is introduced into the yeast cell and then the fusion protein is expressed. The signal peptide guides the fusion protein to extracellular secretion, the anchor protein contained in the fusion protein can bind to the cell wall structure of yeast to immobilize the target protein on the surface of the yeast cell (Kondo & Ueda, 2004; Pepper et al., 2008). According to the different fusion modes of anchor proteins, cell surface display systems can be divided into glycosylphosphatidylinositol (Xing et al.) anchor system, FS/FL (truncated forms of Flo1p (Matsumoto et al., 2002), amino acids (FS) 1–1,099 and amino acids 1–1,417) anchor system and Pir protein anchor system (Figure 1). GPI anchor proteins such as Cwp1p, Cwp2p, Tip1p, Flo1p, Sed1p, YCR89w, and Tir1 link to β-1, 6-glucan of the cell wall by the C-terminal GPI-anchor structures, and the target gene is usually fused to the N- terminus (Van der Vaart et al., 1997). Particularly, the a-agglutinin, composed of Aga1 and Aga2, covalently binds to the cell wall by the C-terminal GPI-anchor structure of Aga1, the target protein gene fuses with the C-terminal or N-terminal of Aga2 and Aga2 is connected with Aga1 through a disulfide bond. The FL/FS gene encoding the Flo1p flocculation functional domain is located near the N- terminus of Flo1p and can adhere to mannans in the cell wall by non-covalent interaction, with the target protein generally fused at its C-terminus. Some proteins with active sites near the C-terminus have inhibitory activity when fused with GPI-anchored proteins, and this inhibition can be mitigated using the FL/FS display system (Matsumoto et al., 2002). In addition, the Pir protein display system is suitable for C-terminal fusion, N-terminal fusion and insertion fusion. The protein differs from the first two anchoring modes in that it can form an ester linkage with β-1, 3-glucose in the cell wall *via* N-terminal repeat sequences, or it can attach to specific components of the cell wall *via* disulfide bonds using C-terminal cysteine residues (Yang et al., 2014).

2.2 Scaffold-mediated cell surface display

Natural cellulosomes are often found in anaerobic bacteria (Felix and Ljungdahl, 1993) (such as *Clostridium thermocellum*,

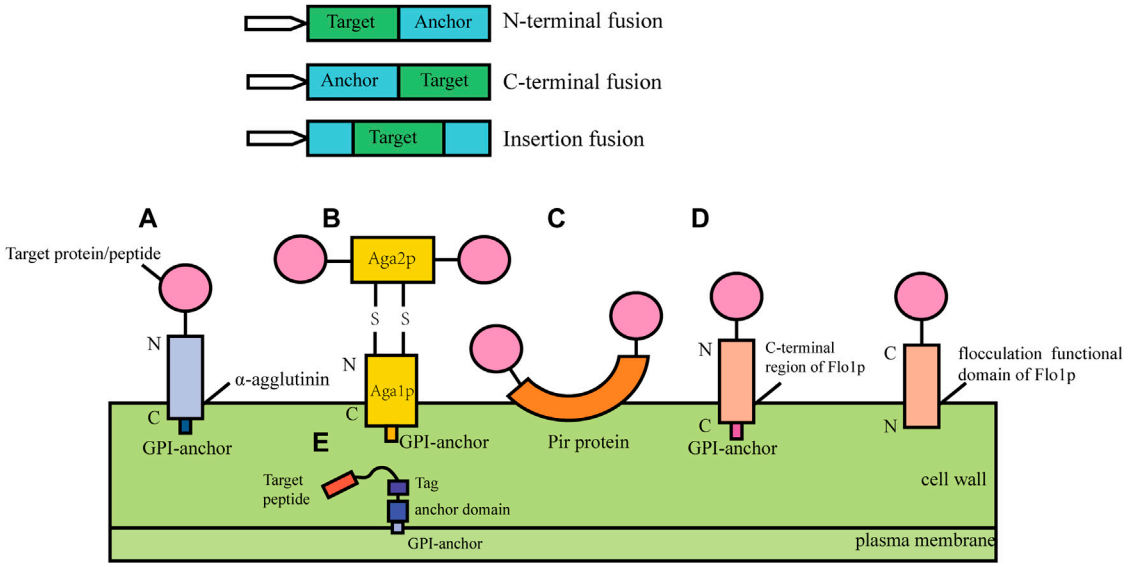

FIGURE 1
Cell surface display systems in *S. cerevisia*. **(A)** α-agglutinin-based display system; **(B)** a-agglutinin-based display system; **(C)** Pir-based display system; **(D)** Flo1p-based display system; **(E)** Membrane display system.

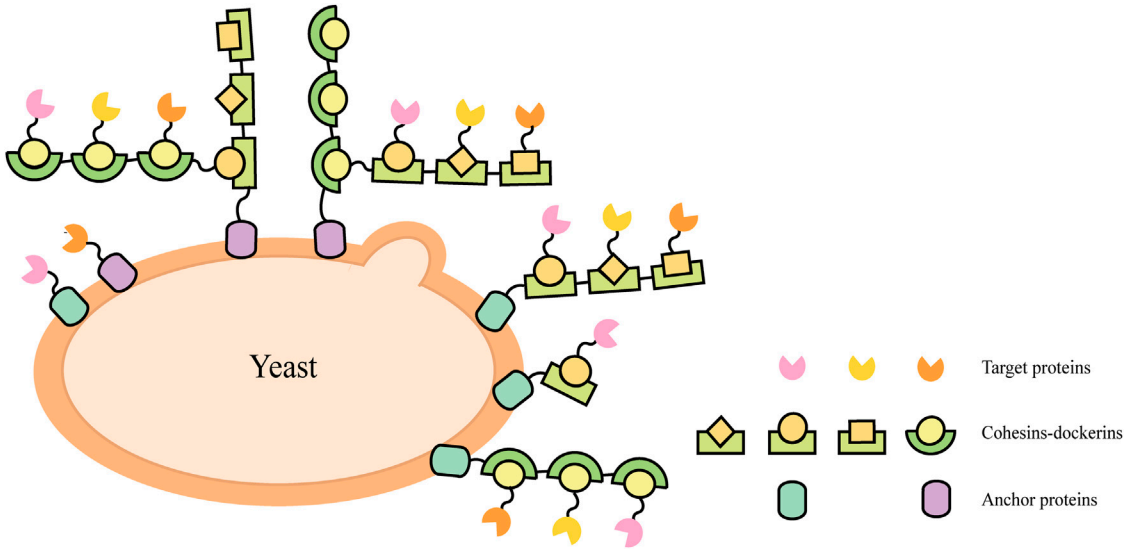

FIGURE 2
Schematic illustrations of direct and indirect cell-surface display strategies in *S. cerevisiae*.

C. cellulolyticum, *C. cellulovorans*, *Ruminococcus flavefaciens*, *etc.*) and the complex composed of scaffoldins, anchoring domains, cohesins, fiber binding domains, and catalytic units, which provides a novel scaffold-based strategy for cell surface display. This cell-surface display system usually triggers enzyme-enzyme proximity synergistic effects and enzyme-substrate-cell complex synergistic effects. A display method was described to allow the production of all cellulosomal components

TABLE 1 Advantages and disadvantages of each strategy.

Strategies	Advantage	Disadvantages	References
Direct cell surface display	Simple and effective	Not easy to control the ratio when multiple enzymes are co-displayed	Huang et al. (2020)
	High stability	Limited utilization of cell surface space	
	Reusable	Poor site-specificity	
	Easy downstream purification		
Scaffold-mediated cell surface display	Facilitate enzyme cascade reaction	High operational difficulty	Li et al. (2017)
	Improve cell surface space utilization	Complex assembly	
	Can control the proportion of displayed proteins	Poor control of binding stability of complex scaffolds	
	Shorten mass transfer distance	Easy downstream purification	

(miniscaffoldin CipA3 and enzymes) *in vivo*, avoiding the labor-intensive protein purification step (Wen et al., 2010). The complex composition of natural cellulosomes and the considerable molecular weight of scaffolding proteins create a metabolic burden for cell surface display. When multi-enzyme presentation is required, its specificity is not high and the efficiency of self-assembly is reduced. Therefore, the researchers selected cohesin domains and cellulose binding domain (CBD) from different strains to form artificial scaffolds, and selected the anchor proteins from the yeast cell wall as anchor elements to display the scaffolds on the yeast cell surface (Fierobe et al., 2005; Mingardon et al., 2007; Wieczorek and Martin, 2010). Target proteins fused with corresponding dockerins can bind to the scaffold through the interaction between the cohesin and dockerin (Figure 2). Cellulosomal components can be produced within the same cell and assembled on the cell surface, or they can be produced by cells of different strains and then co-incubated to assemble on the cell surface of the displayed scaffold. For example, cells displaying scaffoldins on the surface can be incubated directly with *Escherichia coli* cell lysates containing cellulases to form the cellulosome complex for ethanol production (Tsai S.-L. et al., 2009).

Direct cell surface display is a simple and effective strategy. The enzymes immobilized on the cell surface are stable, and the recycling of the whole cells shortens the purification process of the protein, but it cannot effectively use the cell surface space. When multiple enzymes with synergistic effects are co-displayed, the ratio of various enzymes cannot be well controlled. The scaffold-mediated surface display system can make up for the deficiency of the direct display system, shorten the transfer distance of the substrate and enhance the proximity effect between enzymes. However, the design is more complicated and the assembly stability on the cell surface cannot be guaranteed (Table 1). Therefore, a more appropriate design is needed to construct cell surface display engineering yeasts to make it more practical.

2.3 Improvement of cell-surface display efficiency

The improvement of cell surface display efficiency depends on the effective expression and secretion of target proteins and the activity of the displayed target proteins. To this end, many attempts have been made, such as selecting appropriate anchor proteins and expression vectors, constructing highly expressed gene cassettes, strengthening protein folding and post-translational modification, so as to improve the production and activity of proteins. However, further efforts are needed to achieve universal commercialization.

2.3.1 The important role and localization effect of anchoring domains

The display efficiency of enzymes on the cell surface is related to the anchoring proteins attached (Table 2). Attempts have been made to improve cell surface display efficiency by screening for contrasting new anchoring proteins. Phienluphon et al. (2019) selected 37 GPI-type anchor proteins from different sources by computational prediction, fused with yEGFP, pre-screened by comparing the fluorescence intensity, and further fused several vigorous fluorescence anchor proteins with β-glucosidase to determine the enzymatic activity. Finally, 6_Kl from *Kluyveromyces lactis* was found to have higher transcript levels and superior target protein display efficiency. By comparing the display efficiency and enzyme activity of several display systems, Yang et al. (2019) adapted the a-agglutinin anchoring system to develop a new surface display system by using α-galactosidase as the target enzyme and fusing it directly to Aga1p. The enzyme was also fused to conventional a-agglutinin and to six other anchoring proteins selected. A comparison of enzyme activity revealed that Aga1p, Dan4p, and Sed1p had high display efficiency and were promising anchoring systems for immobilizing recombinant proteins on the yeast surface. The display efficiency of the anchor protein domain varies with the molecular weight of the displayed protein. The localization effect of structural

TABLE 2 Comparison of anchoring efficiencies of different anchor proteins.

Enzyme origin	Anchor protein	Yeast host	Promoter	Activity	References
β-glucosidase (BGL1) from *Aspergillus aculeatus*	SAG1	*S. cerevisiae*	SED1	99 ± 10 U/g cell dry weight	Inokuma et al. (2014)
	SED1	*S. cerevisiae*	SED1	235 ± 28 U/g cell dry weight	Inokuma et al. (2014)
BGL1 from *Saccharomycopsis fbuligera*	DAN4	*S. cerevisiae*	TEF1	~785 U/g cell dry weight	Yang et al. (2019)
	AGA1	*S. cerevisiae*	TEF1	~920 U/g cell dry weight	Yang et al. (2019)
BGL from *Aspergillus niger*	Sag1	*S. cerevisiae*	GPD	~18 U/g cell dry weight	Zhang et al. (2019)
	Sed1	*S. cerevisiae*	GPD	25.22 ± 0.81 U/g cell dry weight	Zhang et al. (2019)
Lipase Lip2 from *Y. lipolytica*	Cwp2	*S. cerevisiae*	GPD	~8 U/g cell dry weight	Zhang et al. (2019)
	Cwp2	*S. cerevisiae*	PGK	7.6 ± 0.4 U/cell dry weight	Liu et al. (2010)
Lip7 from *Y. lipolytica*	a-agglutinin	*S. cerevisiae*	GAL1	283 U/g cell dry weight	Liu et al. (2010)
	Flo1	*P. pastoris*	AOX1	85 U/g cell dry weight	Jiang et al. (2007)
Rnizopus oryzae Lipase (ROL)	FLO1	*S. cerevisiae*	TRP1	61.3 IU/g cell dry weight	Matsumoto et al. (2002)
β-Glucuronidase from *Aspergillus oryzae*	Agα1	*P. pastoris*	GAP	24.32 U/g dry cell weight	Wang et al. (2019)
	Pir1	*P. pastoris*	GAP	28.89 U/g dry cell weight	Wang et al. (2019)

anchoring domains may also affect the display efficiency of target proteins on the cell surface. Inokuma et al. (2020) fused the anchored domains (Sed1p and Sag1p) with heterologous proteins and expressed them in *S. cerevisiae*. It was observed by fluorescence and immunoelectron microscopy that the two domains had different anchorings on the cell surface, with sed1p-anchoring domain mainly localized on the outer surface of the cell wall, while sag1p-anchoring domain was mainly localized inside the cell wall. The cell wall space can be effectively utilized by properly controlling the anchoring position, making the cell surface display technology more useful in various fields.

2.3.2 Improvement of protein secretion

Protein secretion is an essential factor in improving the efficiency of cell surface display. The main strategies to improve protein secretion include increasing protein expression levels and signal peptide engineering. The strength of the promoters often determines the expression level of heterologous proteins in *S. cerevisiae*. Different types of promoters differ in their strength. In addition, the strength of promoters can be influenced by other factors such as growth conditions (Sun et al., 2012a) (e.g., glucose concentration), introns (Hoshida et al., 2017) and other factors. Synthetic promoters were constructed using promoter engineering to further improve protein expression levels. The upstream activating sequences (UASs) of different promoters were combined with core promoters to construct a synthetic promoter library. Using this approach, galactose-inducible promoters stronger than P_{GAL1} were successfully constructed by fusing UAS_{GAL1} to the core promoters of TDH3 and TEF1 (Deng et al., 2021). The selection of efficient signal peptides helps to enhance protein secretion and increase the number of proteins displayed on the cell surface. A signal peptide from *S. cerevisiae* SED1 was shown to be an efficiently secreted *A. aculeatus* β-glucosidase (BGL1). The extracellular activity of BGL1 was 1.3-fold and 1.9-fold higher than that of the *Rhizopus oryzae* glucoamylase (GLUASP) and *S. cerevisiae* α-mating pheromone (MFα1SP), respectively (Inokuma et al., 2016). The design mutations of the a-factor preproleader of the MFα1SP have the opportunity to obtain enhanced signal peptides for the secretion of a variety of fungal enzymes (Aza et al., 2021). In addition, some researchers proposed that the fusion of the target protein with a secretion-enhancing peptide cassette and rational optimization of the original peptide could enhance the secretion of the heterologous proteins (Cho et al., 2022). The expression of the enzyme can be further improved by optimizing the combination of promoter and signal peptide. Different promoters and signal peptides constituting nine gene cassettes were selected for fusion expression with *Kluyveromyces marxianus* inulinase gene. The inulinase activity of *S. cerevisiae* carrying the PGK1 promoter and MFα1 signal sequence was the highest (Hong et al., 2015). Terminators affect gene expression by terminating transcription and controlling the half-life of mRNA. Synthetic terminators are short in sequence, easy to synthesize, and more functional. A panel of short (35–70 bp) synthetic terminators was reported to increase fluorescent protein output by 3.7-fold and transcript levels by 4.4-fold compared to the commonly used CYC1 terminator (Curran et al., 2015). The synthetic terminators might function better in *S. cerevisiae* compared to a native promoter.

Other strategies to improve protein secretion include: 1) Overexpression of related genes involved in protein transport or cell surface display (Wentz & Shusta, 2007; Hou et al., 2012; Van Zyl et al., 2016; Bao et al., 2017; Li et al., 2022) and combinatorial regulation of gene expression (Yang et al., 2022). 2) Point mutations and gene deletions (Matsuoka et al., 2014). Point mutation target genes identified from UV-mutagenized strains were analyzed to be involved in multiple intracellular biological processes. Detecting the effects of point mutations and gene deletions on the secretion of α-amylase could help to balance these biological processes and thus

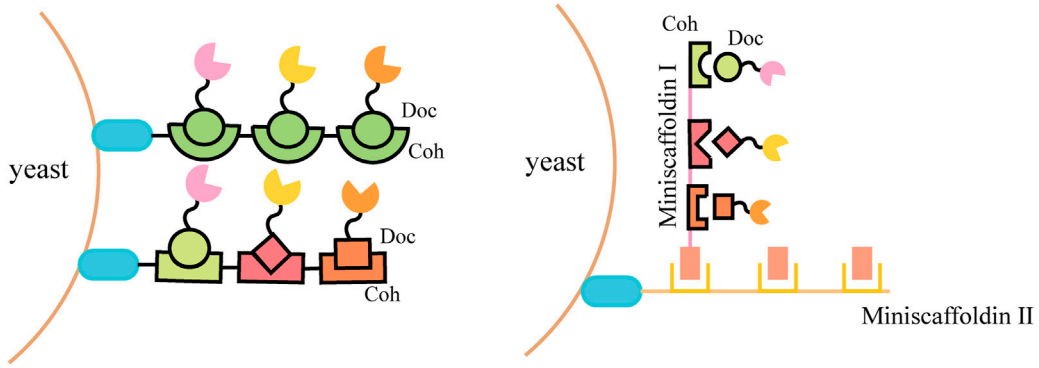

FIGURE 3
Schematic diagram of the assembly strategy on the yeast cell surface using scaffoldin.

improve protein secretion (Wang et al., 2022). 3) Optimization of secretion pathways (Tang et al., 2017; Huang et al., 2018; Besada-Lombana & Da Silva, 2019) and stress modulation (Lamour et al., 2019). 4) Co-overexpression of chaperones (Bae et al., 2016; Bae et al., 2022). 5) The choice of integration method. Auxotrophic integration, cocktail δ-integration (Yamada et al., 2010), CRISPR-δ-integration (Sasaki et al., 2019), and other integration methods (Zhang et al., 2021; Zheng et al., 2022) have been developed successively to increase the copy number of integrated genes, thereby enhancing protein secretory overexpression.

2.3.3 Reduction of steric hindrance and optimization of space utilization on the cell surface of *S. cerevisiae*

The activity of the target protein can be limited by the competition with other GPI proteins for the limited binding sites on the cell wall when displayed on the cell surface (Van der Vaart et al., 1997). For example, the β-Glucosidase activity of the SED1 disruptant was 22% higher than that of the Sed1-undisrupted strain (Bamba et al., 2018), the disruption of CWP2 and YGP1 could increase BGL activity by 63% and 24%, respectively, compared with the original strain (Arnthong et al., 2022), and CCW12 and CCW14 co-knockout resulted in increased cell wall thickness, which may increase the number of heterologous proteins displayed on the cell surface (Inokuma et al., 2021).

The addition of a suitable length of linker peptide between the anchor and target proteins seems to help to separate the active part of the protein from the cell wall, creating space for substrate access and improving the activity of the display enzyme (Washida et al., 2001; Ullah et al., 2017; Yang et al., 2019).

To further improve the space utilization and display efficiency of the cell surface, the introduction of scaffoldin is a potential strategy. Scaffoldin could be enhanced by increasing cohesion number and utilizing double-layered scaffoldins (Figure 3). The *ex vivo* assembly of a functional tetravalent designer cellulosome on the yeast cell surface was developed and exhibited a 4.2-fold enhancement in the hydrolysis of phosphoric acid swollen cellulose (PASC) compared with free enzymes (Tsai et al., 2013). Combining a two-scaffoldin-based cellulosome with an intracellular cellodextrin pathway in *S. cerevisiae* enabled the co-utilization of cellulose-mixed sugars (Fan et al., 2016; Li et al., 2017). A synthetic scaffoldin ScafAGA3 was constructed using the repeated N-terminus of Aga1p. In addition, the scaffoldin ScafCipA3 from *C. thermocellum* fused with Aga2p was attached to the scaffoldin ScafAGA3 *via* disulfide bonds, and the secreted cellulases assembled to ScafCipA3, allowing the formation of a complex cellulosome with two scaffoldins. The newly designed cellulosomes enabled yeast to ferment cellulose directly to ethanol (1.52 g/L) by regulating the ratio of scaffoldins and cellulases (Tang et al., 2018).

3 Applications of cell-surface display engineered *S. cerevisiae*

Cell-surface display technology can be used to produce biofuels and various chemicals from cheap sources rich in sugars, triglycerides and waste protein. In addition, it is also widely used in biological adsorbents and oral vaccines. Combined with metabolic engineering and synthetic biology methods, engineered yeast cells with desired functions can be constructed (Figure 4).

3.1 Applications in bioconversion of agricultural and forestry waste

Agricultural and forestry wastes are produced in large quantities worldwide, resulting in a certain amount of resource waste and environmental problems. From the

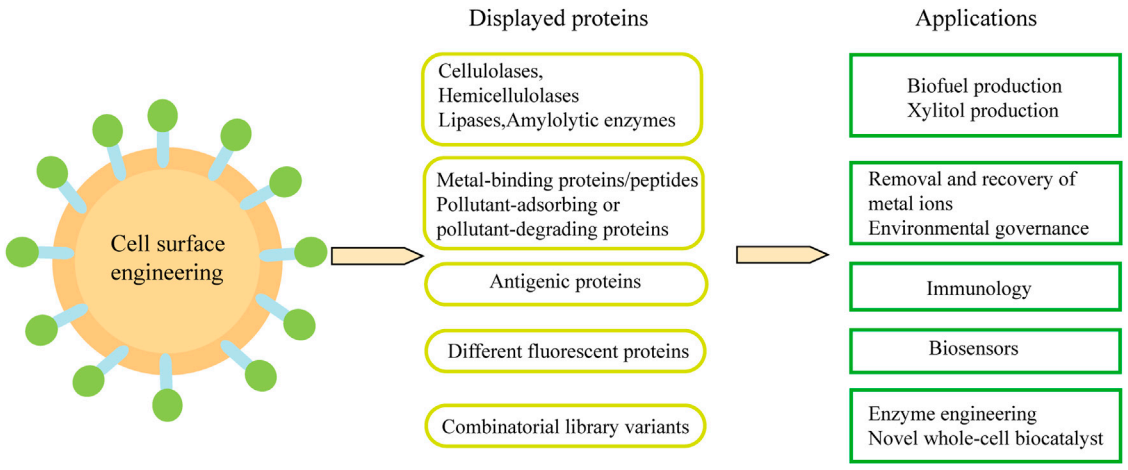

FIGURE 4
Applications of *S. cereviaiae* cell surface engineering.

perspective of the circular economy, the central task is to refine agricultural and forestry wastes to produce valuable energy and chemicals (Song et al., 2020). A variety of enzymes including cellulase, hemicellulases, lipase, amylase, cyclodextrin glucan invertase, amylase and other enzymes have been successfully expressed on the surface of yeast cells with biological activity. The successfully constructed engineered strains can not only effectively degrade agroforestry waste rich in lignocellulose and starch, but also lay the foundation for the simultaneous saccharification and fermentation (SSF)/consolidation bioprocessing (CBP) process.

3.1.1 Bioconversion of cellulose catalyzed by engineered *S. cerevisiae*

Cellulose, composed of glucose connected by β-1, 4-glycosidic bonds, is the most abundant macromolecular polysaccharide in nature. At least three cellulases are required to hydrolyze cellulose into glucose: endoglucanase (EG), cellobiohydrolase (CBH) and β-glucosidase (BGL). EG randomly hydrolyzes the β-1,4-glycosidic bonds by acting on amorphous regions of cellulose, and shortens the long-chain cellulose molecules to produce a larger number of shorter cellulose chains with reducing and non-reducing ends; CBH cuts off cellobiose units from the reducing/non-reducing ends of cellulose, and acts mainly on the crystalline region of cellulose (Hu et al., 2015); BGL hydrolyzes cellobiose into glucose. These three enzymes have been successfully displayed on the cell surface of *S. cerevisiae* to hydrolyze cellulose to glucose (Table 3). Placing EGII from *Trichoderma reesei* and CBHI from *Talaromyces emersonii* in the same space (on the cell surface or in the medium) facilitates the fermentation of amorphous cellulose-based ethanol (Liu et al., 2015). Engineering *S. cerevisia* demonstrated that these two enzymes, along with two others (CBH2 from *Chrysosporium lucknowense* and BGL from *Aspergillus aculeatus*) acted on amorphous cellulose and crystalline cellulose, exhibiting higher ethanol yields because CBH2 reduced the bumpy surface of the cellulose and facilitated the movement of CBH1 by enhanced synergistic hydrolysis (Liu et al., 2016b). Many attempts have been made to improve the fermentation process and introduce new lignocellulose-degrading enzymes (e.g., hydrolytic polysaccharide monooxygenases (LPMOs) and cellobiose dehydrogenases (CDHs)) to further enhance the degradation and product yield of cellulose (Quinlan et al., 2011; Horn et al., 2012; Matano et al., 2012; Nakatani et al., 2013; Bae et al., 2015; Cunha et al., 2021).

The development of multiple scaffoldins (e.g., CipA, ZZ-Coh-Coh, and ScafAGA3) can help to control the ratio of cell surface display proteins and improve ethanol production more effectively (Dong et al., 2020; Qi et al., 2021). A pentafunctional minicellulosome composed of LPMOs, CDHs, CBH, EG and BGL was generated and grown with phosphoric acid swollen cellulose as the sole carbon source (Liang et al., 2014). The delicate balance between the oxidative activity and classical hydrolyase is of importance for the degradation of cellulosic materials (Cannella and Jørgensen, 2014). Expression of all cellulosome components in a single strain may cause heavy metabolic burden and blockage of potential secretion mechanism, thus reducing enzyme activity (Wen et al., 2010). Therefore, displaying anchoring scaffoldins and secreting catalytic and non-catalytic units should be considered to be divided into two independent steps, which can decrease the metabolic burden of the yeast host (Tsai S. L. et al., 2009; Goyal et al., 2011). Researchers achieved an enhancement in the yield by increasing the complexity of the scaffold, that is, by constructing the cellulosome construction and its attachment by

TABLE 3 Applications of *S. cerevisiae* cell surface display in cellulose degradation.

Strains	Ethanol yield	Substrate	Enzymes	Anchor proteins	References
S. cerevisiae BY4741	EG-D-CBHI-D, 2.9 g/L; EG-S-CBHI-S, 2.6 g/L	10 g/L PASC	EG II, CBH I, BGL	Sed1	Liu et al. (2015)
S. cerevisiae BY4741	1.3 g/L	100 g/L MC6	EG, BGL, CBHI, CBHII	Sed1	Liu et al. (2016b)
S. cerevisiae MT8-1	3.4 g/L	20 g/L PASC	SWOI, EGII, CBHII, BGL1	α-agglutinin	Nakatani et al. (2013)
S. cerevisiae NBRC1440DHUWL	39.4 ± 2.3 g/L	200 g-DW/L cellulosic material	BGL1, CBH2, EG2	a-agglutinin	Matano et al. (2012)
S. cerevisiae CEN.PK102-5B	1.52 g/L	PASC	CBHI, CelA, BGL1	Aga1-Aga2	Tang et al. (2018)
S. cerevisiae EBY100	1.80 g/L	PASC	CelA, CBHII, BGLI	Aga1-Aga2	Kim et al. (2013)
S. cerevisiae EBY100	4.3 g/L	10 g/L CMC and batch fed sucrose	celcca (EG), CA_C0911 (CBH)	Aga1-Aga2	Li et al. (2017)
	2.9 g/L	xylose and 10 g/L CMC			
	1.2 g/L	xylose and 10 g/L PASC			
S. cerevisiae EBY100	1.8 g/L 94 h	PASC	CBHII, BGL1, CelA	Aga1-Aga2	Kim et al. (2013)
S. cerevisiae EBY100	2.7 g/L	PASC	GH61a (a LPMO), CDH, EGII, CBHII, BGL1	Aga1-Aga2	Liang et al. (2014)
S. cerevisiae EBY100	1,412 mg/L	Avicel	celCCA (EG), celCCE (CBH), Ccel_2454 (BGL)	Aga1-Aga2	Fan et al. (2012)
S. cerevisiae EBY100	1,138 mg/L	Avicel	celCCA, celCCE, Ccel_2454	Aga1-Aga2	Fan et al. (2013)
	1086 mg/L	PASC			
S. cerevisiae EBY100	8.61 g/L	20 g/L galactose and 10 g/L CMC	celcca, CA_C0911	Aga1-Aga2	Fan et al. (2016)
	9.97 g/L	20 g/L galactose and 10 g/L PASC			
S. cerevisiae L2612	0.95 g/L	10 g/L birchwood xylan	XynII, AbfB XlnD	Aga1-Aga2	Sun et al. (2012b)
S. cerevisiae BY4741	2.9 g/L	10 g/L Avicel	EG2, CBH1, CBH2, BGL	Sed1	Liu et al. (2017)
Commercial ethanol *S.cerevisiae*	(>50 g/L)	cheese whey and pretreated corn cob	BGL1, EG, CBH1, CBH2	Sed1 SAG1	Cunha et al. (2021)

S. cerevisiae, *Saccharomyces cerevisiae*. BGL, β-glucosidase; EG, CelA, endoglucanase; CBH, cellobiohydrolase; SWO I, expansin-like protein; LMPO, lytic polysaccharide monooxygenase; CDH, cellobiose dehydrogenase; xylosidase, Xln; endoxylanase, Xyn; α-L-arabinofuranosidases, AbfB.

two individual miniscaffoldins. The engineered *S. cerevisae* EBY100 could directly convert avicel to bioethanol (1,412 mg/L) (Fan et al., 2012). Others constructed novel cellulolytic yeast consortiums for cellulosic ethanol production (yield up to 1.87 g/L) (Tsai et al., 2010; Kim et al., 2013). The major drawbacks of hydrolyzing cellulose into glucose before cellular uptake are: 1) Inefficient cellulose hydrolysis caused by glucose inhibition on extracellular cellulases. 2) Glucose-induced carbon catabolite repression affects the co-utilization of other sugars. Reconstitution of the cellodextrin transport system in *S. cerevisiae* has been reported (Galazka Jonathan et al., 2010; Choi et al., 2022; Ylinen et al., 2022). This system promotes the efficient utilization of cellulose and mitigates the inhibitory effect of glucose (Fan et al., 2016; Li et al., 2017).

3.1.2 Bioconversion of hemicellulose catalyzed by engineered *S. cerevisiae*

Xylan, the main component of hemicellulose is the second-most polysaccharide in lignocellulosic materials. It is more easily degraded into monomers than cellulose through pretreatment processes, making it an attractive source of sugar for bioethanol fermentation. With the gradual maturity of cell surface display engineering and the heterologous expression of xylose metabolizing enzymes, a one-step process for xylan assimilation can be realized by engineered *S. cerevisiae*. Xylose-utilizing *S. cerevisiae* can be constructed by introducing the genes encoding enzymes related to the xylose assimilation pathway (Katahira et al., 2006). A series of multifunctional minihemicellulosomes were constructed for the hydrolysis of arabinoxylans. The D-xylose utilization pathway consisting of xylose reductase (XR), xylitol dehydrogenase (XDH), and D-xylose kinase (XK) from *Scheffersomyces stipitis* was integrated into the genome of *S. cerevisiae* L2612, combined with the display of bifunctional minihemicellulosome. Engineering *S. cerevisiae* could convert birchwood xylan directly to ethanol (Sun et al., 2012b). A strategy was proposed to efficiently degrade xylan for ethanol production by controlling the mixed cultures of xylose-utilizing engineered

yeast that displaying different hemicellulases (Tabañag et al., 2018). Industrial *S. cerevisiae* strains is considered to be a powerful host for displaying hemicellulose hydrolase on the cell surface and optimizing xylose assimilation because of its good heat resistance and high resistance to inhibitors. The use of industrial strains as gene recombination hosts may be more beneficial for the commercial production of ethanol. By introducing xylan-degrading enzymes and expressed xylose-assimilating enzymes into the recombinant yeast, hemicellulose substrates can be directly degraded to produce a variety of high-value-added products other than ethanol (Cunha et al., 2020).

Xylitol, a high-value-added pentose alcohol, can be produced by one-step reduction of xylose. Industrial production of xylitol from purified D-xylose requires an expensive catalytic hydrogenation process. A recombinant xylose-utilizing *S. cerevisiae* was constructed to directly degrade hemicellulose in rice straw hydrolysate to produce xylitol. The cell surface display technology combined with the incorporation of membrane separation technology further improved xylitol production, with a twofold increase in xylitol production by the multi-enzyme co-display engineered *S. cerevisiae* from the membrane separated hydrolysate (compared to the hydrolysate without membrane separation) (Guirimand et al., 2016). An engineered *S. cerevisiae* expressing cytosolic xylose reductase with β-D-glucosidase, xylosidase and xylanase co-displayed on the cell surface was constructed to produce xylitol from woody Kraft pulp (KP) (Guirimand et al., 2019). These results set the stage for large-scale xylitol production from lignocellulose.

3.1.3 Bioconversion of starch catalyzed by engineered *S. cerevisiae*

Starch, a polymer of α-D-glucose, is generally more easily degraded than cellulose and found in large quantities in many agricultural and industrial wastes. Using surface display engineering *S. cerevisiae* to degrade starch raw materials can not only produce biofuel but also improve the process quality of the food industry. Alpha-amylase and glucoamylase codisplayed *S. cerevisiae* was constructed to produce ethanol directly from corn starch with a yield of 86.5% of the theoretical value (Yamada et al., 2011). The activity of α-amylase was dependent on the anchor protein, and the activity of the strains based on flocculin system was 40 times higher than that based on agglutinin (Shigechi et al., 2002). Most of the insoluble starch is partially non-degradable (Shigechi et al., 2004), for which some attempts such as increasing enzyme activity to improve starch utilization efficiency have been reported. A diploid yeast strain displaying structurally optimized α-amylase and glucoamylase was successfully constructed. The modified yeast was used to ferment 100 g/L of raw starch with an average ethanol yield of up to 1.61 g/L/h over 23 successive cycles, yielding 76.6% of the theoretical value (Yamakawa et al., 2012). Cyclodextrin glucan transferase (CGTase) was demonstrated on *S. cerevisiae* cell surface to effectively hydrolyze starch to produce glucose and maltose for yeast fermentation and to enhance the bread-baking process (Shim et al., 2007).

3.1.4 Bioconversion of waste oil catalyzed by engineered *S. cerevisiae*

Lipases catalyze a variety of reactions and are widely used in industry, so the cell surface display of lipases is a potential way to construct whole cell catalysts. Biodiesel is a clean and renewable fuel that can be produced from waste rich in triglycerides. The production costs can be reduced by using engineered yeast cells that display lipases on the cell surface as recyclable biocatalysts. Through the flocculation function of Flo1p, the lipase ROL can be displayed on the cell surface of *S. cerevisae*, and the yield of synthesized methylesters from triglyceride and methanol reached 78.3% after 72 h of reaction (Matsumoto et al., 2002). Later *Candida antarctica* lipase B (CALB) and *Yarrowia lipolytica* lipases were also displayed on *S. cerevisae* by α-agglutinin- or Flo1p-display systems (Kato et al., 2007; Liu et al., 2010). *Pichia pastoris* can use methanol as the sole carbon source, and its promoter AOX1 is regulated by methanol and corresponding integrated vectors. The transformants have strong genetic stability and few native proteins are expressed extracellularly. *P. pastoris* lacks α-1, 3-mannosyltransferase, so lipase activity is not affected by excessive glycosylation. Compared with *S. cerevisiae*, *P. pastoris* displaying lipases on the cell surface is more suitable for the high-density culture and generally produce enzyme in higher yield. With the ability to utilize a variety of hydrophobic substrates as carbon sources, high resistance to adversity, and tolerance to high salinity and low temperatures, *Y. lipolytica* is an attractive host for cell surface display (Yuzbasheva et al., 2015; Qiao et al., 2018; Yang et al., 2020).

3.2 Applications in environmental control

Heavy metals are frequently detected in industrial wastewater, which are usually not biodegradable and can only be detoxified by means of absorption, enrichment and removal from wastewater (Fu and Wang, 2011). The recovery of rare metals can save resources and reduce environmental pollution. The cell wall of *S. cerevisiae* is mainly composed of mannoproteins, chitin, β-1, 6-glucan and β-1, 3- glucan (Kollár et al., 1995). These biomolecules consist of carboxylate, phosphate, hydroxyl group, amine, sulfhydryl group and other functional groups, which provide a range of different metal binding sites. Different metal-binding peptides combined with anchor systems can be displayed on the cell surface of *S. cerevisiae*. These engineered strains could recover metals from waste solutions and become useful tools for bioreremediation and bioadsorption of environmental pollutants (Mashangoane and Chirwa, 2022). Four types of

Solanum nigrum metallothionein (SMT) were displayed on *S. cerevisiae* cell surface by using an α-agglutinin-based display system to adsorb ultra-trace cadmium effectively (Qinguo et al., 2016). Similarly, by displaying MerR on the cell surface, the adsorption capacity of *S. cerevisiae* to Hg^{2+} was much higher than that of the original and the control strains, while the engineered yeast strain also exhibited higher tolerance to Hg^{2+} (Wei et al., 2018). In addition to heavy metals, there are many emerging environmental pollutants such as parabens with disruptive effects and ethyl carbamate (EC), a possible human carcinogen. The removal of parabens could be mediated by *Fusarium solani pisi* cutinase (FsC) expressed on the cell surface of *S. cerevisiae* (Zhu and Wei, 2019). The EC degradation could be improved by displaying urethanease (UreA) from *Micrococcus species* on the cell surface of *S. cerevisiae* (Han et al., 2022).

3.3 Applications in immunology

In view of the safety of *S. cerevisiae,* it is an excellent vector for vaccine production. An efficient antibody response can be obtained by displaying antigenic proteins on the yeast cell surface and then feeding the vaccine to animals. The antibody response can be enhanced by increasing the number of antigenic proteins displayed on the cell surface. Using the single-chain variable fragment (scFv) of the anti-infectious hematopoietic necrosis virus isolate Sn1203 antibody as a model protein, the a-agglutinin system was used to display *E. coli*-derived and yeast-derived ScFV on the cell surface of *S. cerevisiae*, which effectively increased the number of proteins displayed on the cell surface and enhanced the possibility of the engineered yeast as an oral vaccine (Zhao J.-Z. et al., 2017). VP28 is an envelope protein of White Spot Syndrome Virus (WSSV), which induces a high immune response in shrimp. Probiotics combined with VP28 anchored yeast cell extract could be used as an oral vaccine in shrimp aquaculture (Le Linh et al., 2021). VP24 is another important envelope protein of WSSV. When applied as an oral vaccine, the protective effect of *S. cerevisiae* with VP28 and VP24 fusion protein on cell surface against WSSV attack was more significant than that of with VP28 only, and the survival rate was up to 100% (Lei et al., 2021a). Vaccines made from recombinant viral proteins displayed on the surface of *S. cerevisiae* cells can be more easily recognized by the host mucosal immune system through oral administration, thus triggering protective immunity. This method is not only easy to operate and safe, but also has a short production cycle, which can be used to treat poultry in a short time. EBY100/PYD1-HA was developed as an oral vaccine against avian influenza A (H5N1) infected chickens (Lei et al., 2021b). Timely vaccination is the most effective solution to the outbreak epidemics. An engineered *S. cerevisiae* displaying the receptor binding domains (RBDs) of the spike protein of the initial strain of SARS-CoV-2 and its variants was constructed as a vaccine candidate against the coronavirus (COVID-19) (Xing et al., 2022). In view of the clear genetic background and easy genetic modification of *S. cerevisiae*, the vaccines constructed based on *S. cerevisiae* cell surface display are expected to achieve large-scale production to prevent various infectious diseases.

3.4 Applications in other areas

Cell surface engineering yeast can also be used in biosensors, protein library screening and other fields (Han et al., 2018; Zhao et al., 2021). Cell surface display of fluorescent proteins exerts less metabolic stress on cells than intracellular expression. Displaying a visible reporter on the cell surface may help characterize cells at the single-cell level. Under the control of different promoters, different fluorescent protein variants were displayed on the surface of *S. cerevisiae*, and the engineered yeast could be used as a reporting system to monitor environmental changes and the production of foreign proteins. The GFP cell surface display gene cassette controlled by GAPDH promoter and the BFP cell surface display gene cassette controlled by UPR-ICL promoter were both integrated into the genome of *S. cerevisiae*. The GAPDH promoter acted when the glucose concentration was high in the early stage of culture, and GFP was displayed on the cell surface emitting green fluorescence. When the glucose concentration was low, the UPR-ICL promoter acted and BFP was co-displayed on the cell surface emitting blue fluorescence. The fluorescence intensity and color on the cell surface changed with the intracellular and extracellular glucose concentrations, so the surface display system controlled by the promoters could be used to monitor the glucose concentration inside and outside the cell (Shibasaki et al., 2001). Furthermore, a system was constructed to monitor the production of foreign proteins in yeast by the same promoter controlling the production of foreign proteins and the surface display of reporter gene EGFP. This detection system is expected to be a powerful tool in the field of biological processes (Shibasaki et al., 2003).

Yeast display library technology is a powerful tool for isolation and identification of proteins with unique or modified properties or selection of specific substances (including functional antibodies, enzymes, active protein sites, and chemical probes, *etc.*), and further identification in combination with fluorescence-activated cell sorting (FACS) (Jeong et al., 2019; Bacon et al., 2020; Banach et al., 2022; Fiebig et al., 2022; Lerma Romero et al., 2022). *S. cerevisiae* surface display system could be designed using inefficient ribosomal skipping, and the protein of interest could be simultaneously displayed on the cell surface and secreted out of the cell (Cruz-Teran et al., 2017). A Multiple Navigation of Antibody Structures (MINAS) method that combines CRISPR/Cas9-based traceable editing and fluorescence-activated cell sorting (FACS) of yeast-display libraries has been successfully designed to act on any region of the antibody, introducing

hundreds of thousands of mutations and mapping the effect of these mutations on the desired phenotype (Oh et al., 2020). The optimization of the yeast surface display system is helpful in improving the application of the system in screening (Kajiwara et al., 2020).

In addition, cell surface display engineered *S. cerevisiae* encapsulated by biological materials can be used for protein purification. Taking advantage of the high affinity between *E. coli* vegetal E7 deoxyribonuclease (CL7) and its inhibitor immunoprotein 7 (IM7), calcium alginate beads encapsulated with *S. cerevisiae* cells displaying IM7 could be used as column filler materials to purify proteins fused with CL7 tags. Calcium alginate beads encapsulated with yeast cells displaying cellulosomes could act as a whole-cell catalyst to degrade cellulose substrates, which could be reused at least six times with very low activity reduction (Yin et al., 2022). This strategy of encapsulating cell surface displaying engineered bacteria will play an important role in pharmaceutical and bioengineering fields.

4 Current challenges and future prospects

Yeast cell surface display technology has developed rapidly in the past few decades, and different display systems have been designed. There are some bottlenecks in the development process of widely used *S. cerevisiae* cell surface display engineering: 1) Inefficient production of heterologous proteins leads to the lack of activity of engineered yeast strains; 2) with the increases in recycling times, the activity of engineered yeast may decrease more; 3) more attempts are needed in terms of improving the surface space utilization of yeast cells; 4) most of the current studies are mainly at the laboratory level, and further investigation are needed on the suitability of the constructed engineered strains for industrial mass production; 5) molecular and physiological knowledge on the tolerance of engineered yeast to many inhibitory compounds is limited.

To solve the above bottlenecks, future research can focus on the following aspects: 1) more novel anchoring proteins should be developed to extend the cell surface displayable sites and new gene editing systems combined with cell surface display should be designed to increase the copy number of target genes and simplify the process of plasmid transformation; 2) more biomaterials for encapsulating engineered yeasts should be developed to increase the times of reuses, maintain the activity of display proteins, and further expand the application areas. In addition, the system design to induce automatic flocculation of *S. cerevisiae* is also helpful to promote the yeast recovery; 3) constructing *S. cerevisiae* cell surface display systems by rational and systematic design, including the regulation of the location and ratio of multiple target proteins displayed on the cell surface and the way multifunctional scaffold proteins assembled on the cell surface. Exploring effective and versatile linkers is essential to improve the efficiency of cell surface display; 4) the combination of cell surface display technology, metabolic engineering and synthetic biology engineering is helpful to improve the ability of engineered yeast to utilize mixed substrates, reduce the production of by-products, and construct multifunctional "super yeast"; 5) to improve the tolerance of engineered strains to inhibitors or toxic substances in the fermentation process by means of strain mutagenesis, directed evolution, genetic engineering. The capability of engineered *S. cerevisiae* should be evaluated in a simulated industrial production environment.

5 Conclusion

In this paper, recent advances of cell-surface display engineering and the strategies to improve the display efficiency of *S. cerevisiae* are reviewed. In spite of the obvious requirement for increasing the amount of proteins that displayed on the cell surface and the efficient expression and secretion of target proteins, it is expected that more products using cell surface display will be commercialized in the future.

Author contributions

CZ: Drafted the manuscript. HC and YIZ: Illustration. YUZ and XL: Data curation. FW: Reviewing and Editing.

Funding

This work was financially supported by National Key Research & Development Program of China (No. 2019YFB1504002) and Topnotch Academic Programs Project (TAPP) Education Institutions.

Conflict of interest

The authors declare that the research was conducted in the absence of any commercial or financial relationships that could be construed as a potential conflict of interest.

Publisher's note

References

An, J., Zhang, L., Li, L., Liu, D., Cheng, H., Wang, H., et al. (2016). An alternative approach to synthesizing galactooligosaccharides by cell-surface display of β-galactosidase on Yarrowia lipolytica. *J. Agric. Food Chem.* 64 (19), 3819–3827. doi:10.1021/acs.jafc.5b06138

Arnthong, J., Ponjarat, J., Bussadee, P., Deenarn, P., Prommana, P., Phienluphon, A., et al. (2022). Enhanced surface display efficiency of β-glucosidase in *Saccharomyces cerevisiae* by disruption of cell wall protein-encoding genes YGP1 and CWP2. *Biochem. Eng. J.* 179, 108305. doi:10.1016/j.bej.2021.108305

Aza, P., Molpeceres, G., de Salas, F., and Camarero, S. (2021). Design of an improved universal signal peptide based on the α-factor mating secretion signal for enzyme production in yeast. *Cell. Mol. Life Sci.* 78 (7), 3691–3707. doi:10.1007/s00018-021-03793-y

Bacon, K., Blain, A., Burroughs, M., McArthur, N., Rao, B. M., and Menegatti, S. (2020). Isolation of chemically cyclized peptide binders using yeast surface display. *ACS Comb. Sci.* 22 (10), 519–532. doi:10.1021/acscombsci.0c00076

Bae, J.-H., Sung, B. H., Seo, J.-W., Kim, C. H., and Sohn, J.-H. (2016). A novel fusion partner for enhanced secretion of recombinant proteins in *Saccharomyces cerevisiae*. *Appl. Microbiol. Biotechnol.* 100 (24), 10453–10461. doi:10.1007/s00253-016-7722-2

Bae, J.-H., Yun, S.-H., Kim, M.-J., Kim, H.-J., Sung, B. H., Kim, S. I., et al. (2022). Secretome-based screening of fusion partners and their application in recombinant protein secretion in *Saccharomyces cerevisiae*. *Appl. Microbiol. Biotechnol.* 106 (2), 663–673. doi:10.1007/s00253-021-11750-9

Bae, J., Kuroda, K., and Ueda, M. (2015). Proximity effect among cellulose-degrading enzymes displayed on the *Saccharomyces cerevisiae* cell surface. *Appl. Environ. Microbiol.* 81 (1), 59–66. doi:10.1128/AEM.02864-14

Bamba, T., Inokuma, K., Hasunuma, T., and Kondo, A. (2018). Enhanced cell-surface display of a heterologous protein using SED1 anchoring system in SED1-disrupted *Saccharomyces cerevisiae* strain. *J. Biosci. Bioeng.* 125 (3), 306–310. doi:10.1016/j.jbiosc.2017.09.013

Banach, B. B., Tripathi, P., Da Silva Pereira, L., Gorman, J., Nguyen, T. D., Dillon, M., et al. (2022). Highly protective antimalarial antibodies via precision library generation and yeast display screening. *J. Exp. Med.* 219 (8), e20220323. doi:10.1084/jem.20220323

Bao, J., Huang, M., Petranovic, D., and Nielsen, J. (2017). Moderate expression of SEC16 increases protein secretion by *Saccharomyces cerevisiae*. *Appl. Environ. Microbiol.* 83 (14), e03400–e03416. doi:10.1128/AEM.03400-16

Besada-Lombana, P. B., and Da Silva, N. A. (2019). Engineering the early secretory pathway for increased protein secretion in *Saccharomyces cerevisiae*. *Metab. Eng.* 55, 142–151. doi:10.1016/j.ymben.2019.06.010

Cannella, D., and Jørgensen, H. (2014). Do new cellulolytic enzyme preparations affect the industrial strategies for high solids lignocellulosic ethanol production? *Biotechnol. Bioeng.* 111 (1), 59–68. doi:10.1002/bit.25098

Ce, D., Jie, Q., Xinping, W., Wenli, S., Lixia, C., Shuntang, L., et al. (2022). Engineering Pichia pastoris with surface-display minicellulosomes for carboxymethyl cellulose hydrolysis and ethonol production. *Biotechnol. Biofuels Bioprod*. doi:10.21203/rs.2.23317/v2

Cha, Y., Li, W., Wu, T., You, X., Chen, H., Zhu, C., et al. (2022). Probing the synergistic ratio of P450/CPR to improve (+)-Nootkatone production in *Saccharomyces cerevisiae*. *J. Agric. Food Chem.* 70 (3), 815–825. doi:10.1021/acs.jafc.1c07035

Cho, J. S., Oh, H. J., Jang, Y. E., Kim, H. J., Kim, A., Song, J.-A., et al. (2022). Synthetic pro-peptide design to enhance the secretion of heterologous proteins by *Saccharomyces cerevisiae*. *MicrobiologyOpen* 11 (3), e1300. doi:10.1002/mbo3.1300

Choi, H.-J., Jin, Y.-S., and Lee, W.-H. (2022). Effects of engineered *Saccharomyces cerevisiae* fermenting cellobiose through low-energy-consuming phosphorolytic pathway in simultaneous saccharification and fermentation. *J. Microbiol. Biotechnol.* 32 (1), 117–125. doi:10.4014/jmb.2111.11047

Cruz-Teran, C. A., Tiruthani, K., Mischler, A., and Rao, B. M. (2017). Inefficient ribosomal skipping enables simultaneous secretion and display of proteins in *Saccharomyces cerevisiae*. *ACS Synth. Biol.* 6 (11), 2096–2107. doi:10.1021/acssynbio.7b00144

Cunha, J. T., Gomes, D. G., Romaní, A., Inokuma, K., Hasunuma, T., Kondo, A., et al. (2021). Cell surface engineering of *Saccharomyces cerevisiae* for simultaneous valorization of corn cob and cheese whey via ethanol production. *Energy Convers. Manag.* 243, 114359. doi:10.1016/j.enconman.2021.114359

Cunha, J. T., Romaní, A., Inokuma, K., Johansson, B., Hasunuma, T., Kondo, A., et al. (2020). Consolidated bioprocessing of corn cob-derived hemicellulose: Engineered industrial *Saccharomyces cerevisiae* as efficient whole cell biocatalysts. *Biotechnol. Biofuels* 13 (1), 138. doi:10.1186/s13068-020-01780-2

Curran, K. A., Morse, N. J., Markham, K. A., Wagman, A. M., Gupta, A., and Alper, H. S. (2015). Short synthetic terminators for improved heterologous gene expression in yeast. *ACS Synth. Biol.* 4 (7), 824–832. doi:10.1021/sb5003357

Deng, J., Wu, Y., Zheng, Z., Chen, N., Luo, X., Tang, H., et al. (2021). A synthetic promoter system for well-controlled protein expression with different carbon sources in *Saccharomyces cerevisiae*. *Microb. Cell. Fact.* 20 (1), 202. doi:10.1186/s12934-021-01691-3

Dong, C., Qiao, J., Wang, X., Sun, W., Chen, L., Li, S., et al. (2020). Engineering Pichia pastoris with surface-display minicellulosomes for carboxymethyl cellulose hydrolysis and ethanol production. *Biotechnol. Biofuels* 13 (1), 108. doi:10.1186/s13068-020-01749-1

Fan, L.-H., Zhang, Z.-J., Mei, S., Lu, Y.-Y., Li, M., Wang, Z.-Y., et al. (2016). Engineering yeast with bifunctional minicellulosome and cellodextrin pathway for co-utilization of cellulose-mixed sugars. *Biotechnol. Biofuels* 9 (1), 137. doi:10.1186/s13068-016-0554-6

Fan, L.-H., Zhang, Z.-J., Yu, X.-Y., Xue, Y.-X., Wang, M.-M., and Tan, T.-W. (2013). *In vitro* assembly of minicellulosomes with two scaffoldins on the yeast cell surface for cellulose saccharification and bioethanol production. *Process Biochem.* 48 (3), 430–437. doi:10.1016/j.procbio.2013.01.012

Fan, L. H., Zhang, Z. J., Yu, X. Y., Xue, Y. X., and Tan, T. W. (2012). Self-surface assembly of cellulosomes with two miniscaffoldins on *Saccharomyces cerevisiae* for cellulosic ethanol production. *Proc. Natl. Acad. Sci. U. S. A.* 109 (33), 13260–13265. doi:10.1073/pnas.1209856109

Felix, C. R., and Ljungdahl, L. G. (1993). The cellulosome: The exocellular organelle of Clostridium. *Annu. Rev. Microbiol.* 47 (1), 791–819. doi:10.1146/annurev.mi.47.100193.004043

Fiebig, D., Bogen, J. P., Carrara, S. C., Deweid, L., Zielonka, S., Grzeschik, J., et al. (2022). Streamlining the transition from yeast surface display of antibody fragment immune libraries to the production as IgG format in mammalian cells. *Front. Bioeng. Biotechnol.* 10, 794389. doi:10.3389/fbioe.2022.794389

Fierobe, H.-P., Mingardon, F., Mechaly, A., Bélaïch, A., Rincon, M. T., Pagès, S., et al. (2005). Action of Designer Cellulosomes on Homogeneous versus Complex Substrates: Controlled incorporation of three distinct enzymes into a defined trifunctional scaffoldin. *J. Biol. Chem.* 280 (16), 16325–16334. doi:10.1074/jbc.M414449200

Fu, F., and Wang, Q. (2011). Removal of heavy metal ions from wastewaters: A review. *J. Environ. Manag.* 92 (3), 407–418. doi:10.1016/j.jenvman.2010.11.011

Galazka Jonathan, M., Tian, C., Beeson William, T., Martinez, B., Glass, N. L., and Cate Jamie, H. D. (2010). Cellodextrin transport in yeast for improved biofuel production. *Science* 330 (6000), 84–86. doi:10.1126/science.1192838

Goyal, G., Tsai, S. L., Madan, B., DaSilva, N. A., and Chen, W. (2011). Simultaneous cell growth and ethanol production from cellulose by an engineered yeast consortium displaying a functional mini-cellulosome. *Microb. Cell. Fact.* 10, 89. doi:10.1186/1475-2859-10-89

Guirimand, G., Inokuma, K., Bamba, T., Matsuda, M., Morita, K., Sasaki, K., et al. (2019). Cell-surface display technology and metabolic engineering of *Saccharomyces cerevisiae* for enhancing xylitol production from woody biomass. *Green Chem.* 21 (7), 1795–1808. doi:10.1039/C8GC03864C

Guirimand, G., Sasaki, K., Inokuma, K., Bamba, T., Hasunuma, T., and Kondo, A. (2016). Cell surface engineering of *Saccharomyces cerevisiae* combined with membrane separation technology for xylitol production from rice straw hydrolysate. *Appl. Microbiol. Biotechnol.* 100 (8), 3477–3487. doi:10.1007/s00253-015-7179-8

Han, K., Lee, H., Kang, T.-G., Lee, J., and Kim, S.-K. (2022). Direct and efficient elimination of ethyl carbamate by engineered *Saccharomyces cerevisiae* displaying urethanase. *Food control.* 142, 109236. doi:10.1016/j.foodcont.2022.109236

Han, L., Zhao, Y., Cui, S., and Liang, B. (2018). Redesigning of microbial cell surface and its application to whole-cell biocatalysis and biosensors. *Appl. Biochem. Biotechnol.* 185 (2), 396–418. doi:10.1007/s12010-017-2662-6

Hong, S.-J., Kim, H. J., Kim, J.-W., Lee, D.-H., and Seo, J.-H. (2015). Optimizing promoters and secretory signal sequences for producing ethanol from inulin by recombinant *Saccharomyces cerevisiae* carrying Kluyveromyces marxianus inulinase. *Bioprocess Biosyst. Eng.* 38 (2), 263–272. doi:10.1007/s00449-014-1265-7

Horn, S. J., Vaaje-Kolstad, G., Westereng, B., and Eijsink, V. (2012). Novel enzymes for the degradation of cellulose. *Biotechnol. Biofuels* 5 (1), 45. doi:10.1186/1754-6834-5-45

Hoshida, H., Kondo, M., Kobayashi, T., Yarimizu, T., and Akada, R. (2017). 5′-UTR introns enhance protein expression in the yeast *Saccharomyces cerevisiae*. *Appl. Microbiol. Biotechnol.* 101 (1), 241–251. doi:10.1007/s00253-016-7891-z

Hou, J., Tyo, K., Liu, Z., Petranovic, D., and Nielsen, J. (2012). Engineering of vesicle trafficking improves heterologous protein secretion in *Saccharomyces cerevisiae*. *Metab. Eng.* 14 (2), 120–127. doi:10.1016/j.ymben.2012.01.002

Hu, J., Gourlay, K., Arantes, V., Van Dyk, J. S., Pribowo, A., and Saddler, J. N. (2015). The accessible cellulose surface influences cellulase synergism during the hydrolysis of lignocellulosic substrates. *ChemSusChem* 8 (5), 901–907. doi:10.1002/cssc.201403335

Huang, M., Wang, G., Qin, J., Petranovic, D., and Nielsen, J. (2018). Engineering the protein secretory pathway of *Saccharomyces cerevisiae* enables improved protein production. *Proc. Natl. Acad. Sci. U. S. A.* 115 (47), E11025–E11032. doi:10.1073/pnas.1809921115

Huang, X., Bai, S., Liu, Z., Hasunuma, T., Kondo, A., and Ho, S.-H. (2020). Fermentation of pigment-extracted microalgal residue using yeast cell-surface display: Direct high-density ethanol production with competitive life cycle impacts. *Green Chem.* 22 (1), 153–162. doi:10.1039/C9GC02634G

Inokuma, K., Bamba, T., Ishii, J., Ito, Y., Hasunuma, T., and Kondo, A. (2016). Enhanced cell-surface display and secretory production of cellulolytic enzymes with *Saccharomyces cerevisiae* Sed1 signal peptide. *Biotechnol. Bioeng.* 113 (11), 2358–2366. doi:10.1002/bit.26008

Inokuma, K., Hasunuma, T., and Kondo, A. (2014). Efficient yeast cell-surface display of exo- and endo-cellulase using the SED1 anchoring region and its original promoter. *Biotechnol. Biofuels* 7 (1), 8. doi:10.1186/1754-6834-7-8

Inokuma, K., Kitada, Y., Bamba, T., Kobayashi, Y., Yukawa, T., den Haan, R., et al. (2021). Improving the functionality of surface-engineered yeast cells by altering the cell wall morphology of the host strain. *Appl. Microbiol. Biotechnol.* 105 (14), 5895–5904. doi:10.1007/s00253-021-11440-6

Inokuma, K., Kurono, H., den Haan, R., van Zyl, W. H., Hasunuma, T., and Kondo, A. (2020). Novel strategy for anchorage position control of GPI-attached proteins in the yeast cell wall using different GPI-anchoring domains. *Metab. Eng.* 57, 110–117. doi:10.1016/j.ymben.2019.11.004

Jeong, M.-Y., Rutter, J., and Chou, D. H.-C. (2019). Display of single-chain insulin-like peptides on a yeast surface. *Biochemistry* 58 (3), 182–188. doi:10.1021/acs.biochem.8b01094

Jiang, Z.-B., Song, H.-T., Gupta, N., Ma, L.-X., and Wu, Z.-B. (2007). Cell surface display of functionally active lipases from Yarrowia lipolytica in Pichia pastoris. *Protein Expr. Purif.* 56 (1), 35–39. doi:10.1016/j.pep.2007.07.003

Kajiwara, K., Aoki, W., and Ueda, M. (2020). Evaluation of the yeast surface display system for screening of functional nanobodies. *Amb. Expr.* 10 (1), 51. doi:10.1186/s13568-020-00983-y

Katahira, S., Mizuike, A., Fukuda, H., and Kondo, A. (2006). Ethanol fermentation from lignocellulosic hydrolysate by a recombinant xylose- and cellooligosaccharide-assimilating yeast strain. *Appl. Microbiol. Biotechnol.* 72 (6), 1136–1143. doi:10.1007/s00253-006-0402-x

Kato, M., Fuchimoto, J., Tanino, T., Kondo, A., Fukuda, H., and Ueda, M. (2007). Preparation of a whole-cell biocatalyst of mutated Candida Antarctica lipase B (mCALB) by a yeast molecular display system and its practical properties. *Appl. Microbiol. Biotechnol.* 75 (3), 549–555. doi:10.1007/s00253-006-0835-2

Kim, S., Baek, S.-H., Lee, K., and Hahn, J.-S. (2013). Cellulosic ethanol production using a yeast consortium displaying a minicellulosome and β-glucosidase. *Microb. Cell. Fact.* 12 (1), 14. doi:10.1186/1475-2859-12-14

Kollár, R., Petráková, E., Ashwell, G., Robbins, P. W., and Cabib, E. (1995). Architecture of the yeast cell wall: The linkage between chitin and β(1 →3)-glucan (∗). *J. Biol. Chem.* 270 (3), 1170–1178. doi:10.1074/jbc.270.3.1170

Kondo, A., and Ueda, M. (2004). Yeast cell-surface display-applications of molecular display. *Appl. Microbiol. Biotechnol.* 64 (1), 28–40. doi:10.1007/s00253-003-1492-3

Lamour, J., Wan, C., Zhang, M., Zhao, X., and Den Haan, R. (2019). Overexpression of endogenous stress-tolerance related genes in *Saccharomyces cerevisiae* improved strain robustness and production of heterologous cellobiohydrolase. *FEMS Yeast Res.* 19 (4), foz035. doi:10.1093/femsyr/foz035

Le Linh, H., Thu, N. P. A., Dung, T. T. X., Van Hau, N., Nghia, N. H., and Thao, D. T. P. (2021). Yeast cell surface displaying VP28 antigen and its potential application for shrimp farming. *Appl. Microbiol. Biotechnol.* 105 (16), 6345–6354. doi:10.1007/s00253-021-11493-7

Lei, H., Li, S., Lu, X., and Ren, Y. (2021a). Oral administration of *Saccharomyces cerevisiae* displaying VP28-VP24 confers protection against white spot syndrome virus in shrimp. *Virus Res.* 302, 198467. doi:10.1016/j.virusres.2021.198467

Lei, H., Lu, X., Li, S., and Ren, Y. (2021b). High immune efficacy against different avian influenza H5N1 viruses due to oral administration of a Saccharomyces cerevisiae-based vaccine in chickens. *Sci. Rep.* 11 (1), 8977. doi:10.1038/s41598-021-88413-2

Lerma Romero, J. A., Meyners, C., Christmann, A., Reinbold, L. M., Charalampidou, A., Hausch, F., et al. (2022). Binding pocket stabilization by high-throughput screening of yeast display libraries. *Front. Mol. Biosci.* 9, 1023131. doi:10.3389/fmolb.2022.1023131

Li, J., Zeng, Y., Wang, W.-B., Wan, Q.-Q., Liu, C.-G., den Haan, R., et al. (2022). Increasing extracellular cellulase activity of the recombinant *Saccharomyces cerevisiae* by engineering cell wall-related proteins for improved consolidated processing of carbon neutral lignocellulosic biomass. *Bioresour. Technol.* 365, 128132. doi:10.1016/j.biortech.2022.128132

Li, Y.-J., Lu, Y.-Y., Zhang, Z.-J., Mei, S., Tan, T.-W., and Fan, L.-H. (2017). Co-Fermentation of cellulose and sucrose/xylose by engineered yeasts for bioethanol production. *Energy fuels.* 31 (4), 4061–4067. doi:10.1021/acs.energyfuels.7b00032

Liang, Y., Si, T., Ang Ee, L., Zhao, H., and Kelly, R. M. (2014). Engineered pentafunctional minicellulosome for simultaneous saccharification and ethanol fermentation in *Saccharomyces cerevisiae*. *Appl. Environ. Microbiol.* 80 (21), 6677–6684. doi:10.1128/AEM.02070-14

Liu, W.-S., Pan, X.-X., Jia, B., Zhao, H.-Y., Xu, L., Liu, Y., et al. (2010). Surface display of active lipases Lip7 and Lip8 from Yarrowia lipolytica on Saccharomyces cerevisiae. *Appl. Microbiol. Biotechnol.* 88 (4), 885–891. doi:10.1007/s00253-010-2782-1

Liu, Z., Ho, S.-H., Hasunuma, T., Chang, J.-S., Ren, N.-Q., and Kondo, A. (2016a). Recent advances in yeast cell-surface display technologies for waste biorefineries. *Bioresour. Technol.* 215, 324–333. doi:10.1016/j.biortech.2016.03.132

Liu, Z., Ho, S.-H., Sasaki, K., den Haan, R., Inokuma, K., Ogino, C., et al. (2016b). Engineering of a novel cellulose-adherent cellulolytic *Saccharomyces cerevisiae* for cellulosic biofuel production. *Sci. Rep.* 6 (1), 24550. doi:10.1038/srep24550

Liu, Z., Inokuma, K., Ho, S.-H., den Haan, R., van Zyl, W. H., Hasunuma, T., et al. (2017). Improvement of ethanol production from crystalline cellulose via optimizing cellulase ratios in cellulolytic *Saccharomyces cerevisiae*. *Biotechnol. Bioeng.* 114 (6), 1201–1207. doi:10.1002/bit.26252

Liu, Z., Inokuma, K., Ho, S.-H., Haan, R. d., Hasunuma, T., van Zyl, W. H., et al. (2015). Combined cell-surface display- and secretion-based strategies for production of cellulosic ethanol with *Saccharomyces cerevisiae*. *Biotechnol. Biofuels* 8 (1), 162. doi:10.1186/s13068-015-0344-6

Mashangoane, B. F., and Chirwa, E. N. (2022). Cell surface display of palladium binding peptide on *Saccharomyces cerevisiae* EBY100 cells using the a-agglutinin anchor system developed for the biosorption of Pd (II). *Miner. Eng.* 176, 107325. doi:10.1016/j.mineng.2021.107325

Matano, Y., Hasunuma, T., and Kondo, A. (2012). Display of cellulases on the cell surface of *Saccharomyces cerevisiae* for high yield ethanol production from high-solid lignocellulosic biomass. *Bioresour. Technol.* 108, 128–133. doi:10.1016/j.biortech.2011.12.144

Matsumoto, T., Fukuda, H., Ueda, M., Tanaka, A., and Kondo, A. (2002). Construction of yeast strains with high cell surface lipase activity by using novel display systems based on the Flo1p flocculation functional domain. *Appl. Environ. Microbiol.* 68 (9), 4517–4522. doi:10.1128/AEM.68.9.4517-4522.2002

Matsuoka, H., Hashimoto, K., Saijo, A., Takada, Y., Kondo, A., Ueda, M., et al. (2014). Cell wall structure suitable for surface display of proteins in *Saccharomyces cerevisiae*. *Yeast* 31 (2), 67–76. doi:10.1002/yea.2995

Mingardon, F., Chanal, A., López-Contreras Ana, M., Dray, C., Bayer Edward, A., and Fierobe, H.-P. (2007). Incorporation of fungal cellulases in bacterial minicellulosomes yields viable, synergistically acting cellulolytic complexes. *Appl. Environ. Microbiol.* 73 (12), 3822–3832. doi:10.1128/AEM.00398-07

Nakatani, Y., Yamada, R., Ogino, C., and Kondo, A. (2013). Synergetic effect of yeast cell-surface expression of cellulase and expansin-like protein on direct ethanol production from cellulose. *Microb. Cell. Fact.* 12 (1), 66. doi:10.1186/1475-2859-12-66

Oh, E. J., Liu, R., Liang, L., Freed, E. F., Eckert, C. A., and Gill, R. T. (2020). Multiplex evolution of antibody fragments utilizing a yeast surface display platform. *ACS Synth. Biol.* 9 (8), 2197–2202. doi:10.1021/acssynbio.0c00159

Pepper, L. R., Cho, Y. K., Boder, E. T., and Shusta, E. V. (2008). A decade of yeast surface display technology: Where are we now? *Comb. Chem. high throughput Screen.* 11 (2), 127–134. doi:10.2174/138620708783744516

Phienluphon, A., Mhuantong, W., Boonyapakron, K., Deenarn, P., Champreda, V., Wichadakul, D., et al. (2019). Identification and evaluation of novel anchoring proteins for cell surface display on *Saccharomyces cerevisiae*. *Appl. Microbiol. Biotechnol.* 103 (7), 3085–3097. doi:10.1007/s00253-019-09667-5

Qi, K., Chen, C., Yan, F., Feng, Y., Bayer, E. A., Kosugi, A., et al. (2021). Coordinated β-glucosidase activity with the cellulosome is effective for enhanced lignocellulose saccharification. *Bioresour. Technol.* 337, 125441. doi:10.1016/j.biortech.2021.125441

Qiao, Y., Yang, K., Zhou, Q., Xu, Z., Yan, Y., Xu, L., et al. (2018). Engineering Yarrowia lipolytica for sustainable production of fatty acid methyl esters using *in situ* self-cycled glycerol as a carbon source. *ACS Sustain. Chem. Eng.* 6 (6), 7645–7651. doi:10.1021/acssuschemeng.8b00492

Qinguo, W., Honghai, Z., Dongge, G., and Ma, S. (2016). Cell surface display of four types of Solanum nigrum metallothionein on *Saccharomyces cerevisiae* for biosorption of cadmium. *J. Microbiol. Biotechnol.* 26 (5), 846–853. doi:10.4014/jmb.1512.12041

Quinlan, R. J., Sweeney, M. D., Lo Leggio, L., Otten, H., Poulsen, J. C., Johansen, K. S., et al. (2011). Insights into the oxidative degradation of cellulose by a copper metalloenzyme that exploits biomass components. *Proc. Natl. Acad. Sci. U. S. A.* 108 (37), 15079–15084. doi:10.1073/pnas.1105776108

Sasaki, Y., Mitsui, R., Yamada, R., and Ogino, H. (2019). Secretory overexpression of the endoglucanase by *Saccharomyces cerevisiae* via CRISPR-δ-integration and multiple promoter shuffling. *Enzyme Microb. Technol.* 121, 17–22. doi:10.1016/j.enzmictec.2018.10.014

Shibasaki, S., Tanaka, A., and Ueda, M. (2003). Development of combinatorial bioengineering using yeast cell surface display—Order-made design of cell and protein for bio-monitoring. *Biosens. Bioelectron.* 19 (2), 123–130. doi:10.1016/S0956-5663(03)00169-6

Shibasaki, S., Ueda, M., Ye, K., Shimizu, K., Kamasawa, N., Osumi, M., et al. (2001). Creation of cell surface-engineered yeast that display different fluorescent proteins in response to the glucose concentration. *Appl. Microbiol. Biotechnol.* 57 (4), 528–533. doi:10.1007/s002530100767

Shigechi, H., Fujita, Y., Koh, J., Ueda, M., Fukuda, H., and Kondo, A. (2004). Energy-saving direct ethanol production from low-temperature-cooked corn starch using a cell-surface engineered yeast strain co-displaying glucoamylase and α-amylase. *Biochem. Eng. J.* 18 (2), 149–153. doi:10.1016/j.bej.2003.08.003

Shigechi, H., Uyama, K., Fujita, Y., Matsumoto, T., Ueda, M., Tanaka, A., et al. (2002). Efficient ethanol production from starch through development of novel flocculent yeast strains displaying glucoamylase and co-displaying or secreting α-amylase. *J. Mol. Catal. B Enzym.* 17 (3), 179–187. doi:10.1016/S1381-1177(02)00026-7

Shim, J.-H., Seo, N.-S., Roh, S.-A., Kim, J.-W., Cha, H., and Park, K.-H. (2007). Improved bread-baking process using *Saccharomyces cerevisiae* displayed with engineered cyclodextrin glucanotransferase. *J. Agric. Food Chem.* 55 (12), 4735–4740. doi:10.1021/jf070217d

Song, C., Zhang, C., Zhang, S., Lin, H., Kim, Y., Ramakrishnan, M., et al. (2020). Thermochemical liquefaction of agricultural and forestry wastes into biofuels and chemicals from circular economy perspectives. *Sci. Total Environ.* 749, 141972. doi:10.1016/j.scitotenv.2020.141972

Sun, J., Shao, Z., Zhao, H., Nair, N., Wen, F., Xu, J.-H., et al. (2012a). Cloning and characterization of a panel of constitutive promoters for applications in pathway engineering in *Saccharomyces cerevisiae*. *Biotechnol. Bioeng.* 109 (8), 2082–2092. doi:10.1002/bit.24481

Sun, J., Wen, F., Si, T., Xu, J.-H., and Zhao, H. (2012b). Direct conversion of xylan to ethanol by recombinant *Saccharomyces cerevisiae* strains displaying an engineered minihemicellulosome. *Appl. Environ. Microbiol.* 78 (11), 3837–3845. doi:10.1128/AEM.07679-11

Tabañag, I. D. F., Chu, I. M., Wei, Y.-H., and Tsai, S.-L. (2018). Ethanol production from hemicellulose by a consortium of different genetically-modified sacharomyces cerevisiae. *J. Taiwan Inst. Chem. Eng.* 89, 15–25. doi:10.1016/j.jtice.2018.04.029

Tang, H., Song, M., He, Y., Wang, J., Wang, S., Shen, Y., et al. (2017). Engineering vesicle trafficking improves the extracellular activity and surface display efficiency of cellulases in *Saccharomyces cerevisiae*. *Biotechnol. Biofuels* 10 (1), 53. doi:10.1186/s13068-017-0738-8

Tang, H., Wang, J., Wang, S., Shen, Y., Petranovic, D., Hou, J., et al. (2018). Efficient yeast surface-display of novel complex synthetic cellulosomes. *Microb. Cell. Fact.* 17 (1), 122. doi:10.1186/s12934-018-0971-2

Teymennet-Ramírez, K. V., Martínez-Morales, F., and Trejo-Hernández, M. R. (2022). Yeast surface display system: Strategies for improvement and biotechnological applications. *Front. Bioeng. Biotechnol.* 9, 794742. doi:10.3389/fbioe.2021.794742

Tsai, S.-L., DaSilva, N. A., and Chen, W. (2013). Functional display of complex cellulosomes on the yeast surface via adaptive assembly. *ACS Synth. Biol.* 2 (1), 14–21. doi:10.1021/sb300047u

Tsai, S.-L., Oh, J., Singh, S., Chen, R., and Chen, W. (2009a). Functional assembly of minicellulosomes on the *Saccharomyces cerevisiae* cell surface for cellulose hydrolysis and ethanol production. *Appl. Environ. Microbiol.* 75 (19), 6087–6093. doi:10.1128/AEM.01538-09

Tsai, S. L., Goyal, G., and Chen, W. (2010). Surface display of a functional minicellulosome by intracellular complementation using a synthetic yeast consortium and its application to cellulose hydrolysis and ethanol production. *Appl. Environ. Microbiol.* 76 (22), 7514–7520. doi:10.1128/AEM.01777-10

Tsai, S. L., Oh, J., Singh, S., Chen, R., and Chen, W. (2009b). Functional assembly of minicellulosomes on the *Saccharomyces cerevisiae* cell surface for cellulose hydrolysis and ethanol production. *Appl. Environ. Microbiol.* 75 (19), 6087–6093. doi:10.1128/AEM.01538-09

Ullah, J., Chen, H., Vastermark, A., Jia, J., Wu, B., Ni, Z., et al. (2017). Impact of orientation and flexibility of peptide linkers on T. maritima lipase Tm1350 displayed on Bacillus subtilis spores surface using CotB as fusion partner. *World J. Microbiol. Biotechnol.* 33 (9), 166. doi:10.1007/s11274-017-2327-1

Van der Vaart, J. M., te Biesebeke, R., Chapman, J. W., Toschka, H. Y., Klis, F. M., and Verrips, C. T. (1997). Comparison of cell wall proteins of *Saccharomyces cerevisiae* as anchors for cell surface expression of heterologous proteins. *Appl. Environ. Microbiol.* 63 (2), 615–620. doi:10.1128/aem.63.2.615-620.1997

Van Zyl, J. H. D., Den Haan, R., and Van Zyl, W. H. (2016). Overexpression of native *Saccharomyces cerevisiae* ER-to-Golgi SNARE genes increased heterologous cellulase secretion. *Appl. Microbiol. Biotechnol.* 100 (1), 505–518. doi:10.1007/s00253-015-7022-2

Wang, X., Feng, X., Lv, B., Zhou, A., Hou, Y., and Li, C. (2019). Enhanced yeast surface display of β-glucuronidase using dual anchor motifs for high-temperature glycyrrhizin hydrolysis. *AIChE J.* 65 (9), e16629. doi:10.1002/aic.16629

Wang, Y., Li, X., Chen, X., and Siewers, V. (2022). CRISPR/Cas9-mediated point mutations improve α-amylase secretion in *Saccharomyces cerevisiae*. *FEMS Yeast Res.* 22 (1), foac033. doi:10.1093/femsyr/foac033

Washida, M., Takahashi, S., Ueda, M., and Tanaka, A. (2001). Spacer-mediated display of active lipase on the yeast cell surface. *Appl. Microbiol. Biotechnol.* 56 (5), 681–686. doi:10.1007/s002530100718

Wei, Q., Yan, J., Chen, Y., Zhang, L., Wu, X., Shang, S., et al. (2018). Cell surface display of MerR on *Saccharomyces cerevisiae* for biosorption of mercury. *Mol. Biotechnol.* 60 (1), 12–20. doi:10.1007/s12033-017-0039-2

Wen, F., Sun, J., and Zhao, H. (2010). Yeast surface display of trifunctional minicellulosomes for simultaneous saccharification and fermentation of cellulose to ethanol. *Appl. Environ. Microbiol.* 76 (4), 1251–1260. doi:10.1128/AEM.01687-09

Wentz, A. E., and Shusta, E. V. (2007). A novel high-throughput screen reveals yeast genes that increase secretion of heterologous proteins. *Appl. Environ. Microbiol.* 73 (4), 1189–1198. doi:10.1128/AEM.02427-06

Wieczorek, A. S., and Martin, V. J. J. (2010). Engineering the cell surface display of cohesins for assembly of cellulosome-inspired enzyme complexes on Lactococcus lactis. *Microb. Cell. Fact.* 9 (1), 69. doi:10.1186/1475-2859-9-69

Xing, H., Zhu, L., Wang, P., Zhao, G., Zhou, Z., Yang, Y., et al. (2022). Display of receptor-binding domain of SARS-CoV-2 Spike protein variants on the *Saccharomyces cerevisiae* cell surface. *Front. Immunol.* 13. doi:10.3389/fimmu.2022.935573

Yamada, R., Taniguchi, N., Tanaka, T., Ogino, C., Fukuda, H., and Kondo, A. (2010). Cocktail δ-integration: A novel method to construct cellulolytic enzyme expression ratio-optimized yeast strains. *Microb. Cell. Fact.* 9 (1), 32. doi:10.1186/1475-2859-9-32

Yamada, R., Yamakawa, S.-i., Tanaka, T., Ogino, C., Fukuda, H., and Kondo, A. (2011). Direct and efficient ethanol production from high-yielding rice using a *Saccharomyces cerevisiae* strain that express amylases. *Enzyme Microb. Technol.* 48 (4), 393–396. doi:10.1016/j.enzmictec.2011.01.002

Yamakawa, S.-i., Yamada, R., Tanaka, T., Ogino, C., and Kondo, A. (2012). Repeated fermentation from raw starch using *Saccharomyces cerevisiae* displaying both glucoamylase and α-amylase. *Enzyme Microb. Technol.* 50 (6), 343–347. doi:10.1016/j.enzmictec.2012.03.005

Yang, J., Huang, K., Xu, X., Miao, Y., Lin, Y., and Han, S. (2020). Cell surface display of thermomyces lanuginosus lipase in Pichia pastoris. *Front. Bioeng. Biotechnol.* 8, 544058. doi:10.3389/fbioe.2020.544058

Yang, N., Yu, Z., Jia, D., Xie, Z., Zhang, K., Xia, Z., et al. (2014). The contribution of Pir protein family to yeast cell surface display. *Appl. Microbiol. Biotechnol.* 98 (7), 2897–2905. doi:10.1007/s00253-014-5538-5

Yang, S., Lv, X., Wang, X., Wang, J., Wang, R., and Wang, T. (2017). Cell-surface displayed expression of trehalose synthase from Pseudomonas putida ATCC 47054 in Pichia pastoris using Pir1p as an anchor protein. *Front. Microbiol.* 8, 2583. doi:10.3389/fmicb.2017.02583

Yang, S., Shen, J., Deng, J., Li, H., Zhao, J., Tang, H., et al. (2022). Engineering cell polarization improves protein production in *Saccharomyces cerevisiae*. *Microorganisms* 10, 2005. doi:10.3390/microorganisms10102005

Yang, X., Tang, H., Song, M., Shen, Y., Hou, J., and Bao, X. (2019). Development of novel surface display platforms for anchoring heterologous proteins in *Saccharomyces cerevisiae*. *Microb. Cell. Fact.* 18 (1), 85. doi:10.1186/s12934-019-1133-x

Ye, M., Ye, Y., Du, Z., and Chen, G. (2021). Cell-surface engineering of yeasts for whole-cell biocatalysts. *Bioprocess Biosyst. Eng.* 44 (6), 1003–1019. doi:10.1007/s00449-020-02484-5

Yin, W., Wang, X., Liao, Y., Ma, L., Qiao, J., Liu, H., et al. (2022). Encapsulating IM7-displaying yeast cells in calcium alginate beads for one-step protein purification and multienzyme biocatalysis. *Front. Bioeng. Biotechnol.* 10, 849542. doi:10.3389/fbioe.2022.849542

Ylinen, A., de Ruijter, J. C., Jouhten, P., and Penttilä, M. (2022). PHB production from cellobiose with *Saccharomyces cerevisiae*. *Microb. Cell. Fact.* 21 (1), 124. doi:10.1186/s12934-022-01845-x

Yuzbasheva, E. Y., Yuzbashev, T. V., Perkovskaya, N. I., Mostova, E. B., Vybornaya, T. V., Sukhozhenko, A. V., et al. (2015). Cell surface display of Yarrowia lipolytica lipase Lip2p using the cell wall protein YlPir1p, its characterization, and application as a whole-cell biocatalyst. *Appl. Biochem. Biotechnol.* 175 (8), 3888–3900. doi:10.1007/s12010-015-1557-7

Zhang, Y., Min, Z., Qin, Y., Ye, D.-Q., Song, Y.-Y., and Liu, Y.-L. (2019). Efficient display of Aspergillus Niger β-glucosidase on *Saccharomyces cerevisiae* cell wall for aroma enhancement in wine. *J. Agric. Food Chem.* 67 (18), 5169–5176. doi:10.1021/acs.jafc.9b00863

Zhang, Z.-X., Wang, Y.-Z., Xu, Y.-S., Sun, X.-M., and Huang, H. (2021). Developing GDi-CRISPR system for multi-copy integration in *Saccharomyces cerevisiae*. *Appl. Biochem. Biotechnol.* 193 (7), 2379–2388. doi:10.1007/s12010-021-03532-w

Zhao, J.-Z., Xu, L.-M., Liu, M., Cao, Y.-S., LaPatra, S. E., Yin, J.-S., et al. (2017a). An efficient and simple method to increase the level of displayed protein on the yeast cell surface. *J. Microbiol. Methods* 135, 41–47. doi:10.1016/j.mimet.2017.02.002

Zhao, N., Xu, Y., Wang, K., and Zheng, S. (2017b). Synthesis of isomalto-oligosaccharides by Pichia pastoris displaying the Aspergillus Niger α-glucosidase. *J. Agric. Food Chem.* 65 (43), 9468–9474. doi:10.1021/acs.jafc.7b04140

Zhao, S., Guo, D., Zhu, Q., Dou, W., and Guan, W. (2021). Display of microbial glucose dehydrogenase and cholesterol oxidase on the yeast cell surface for the detection of blood biochemical parameters. *Biosensors* 11 (1), 13. doi:10.3390/bios11010013

Zheng, H., Wang, K., Xu, X., Pan, J., Sun, X., Hou, J., et al. (2022). Highly efficient rDNA-mediated multicopy integration based on the dynamic balance of rDNA in *Saccharomyces cerevisiae*. *Microb. Biotechnol.* 15 (5), 1511–1524. doi:10.1111/1751-7915.14010

Zhu, B., and Wei, N. (2019). Biocatalytic degradation of parabens mediated by cell surface displayed cutinase. *Environ. Sci. Technol.* 53 (1), 354–364. doi:10.1021/acs.est.8b05275

Frontiers in
Bioengineering and Biotechnology

Accelerates the development of therapies, devices, and technologies to improve our lives

A multidisciplinary journal that accelerates the development of biological therapies, devices, processes and technologies to improve our lives by bridging the gap between discoveries and their application.

Discover the latest Research Topics

See more →

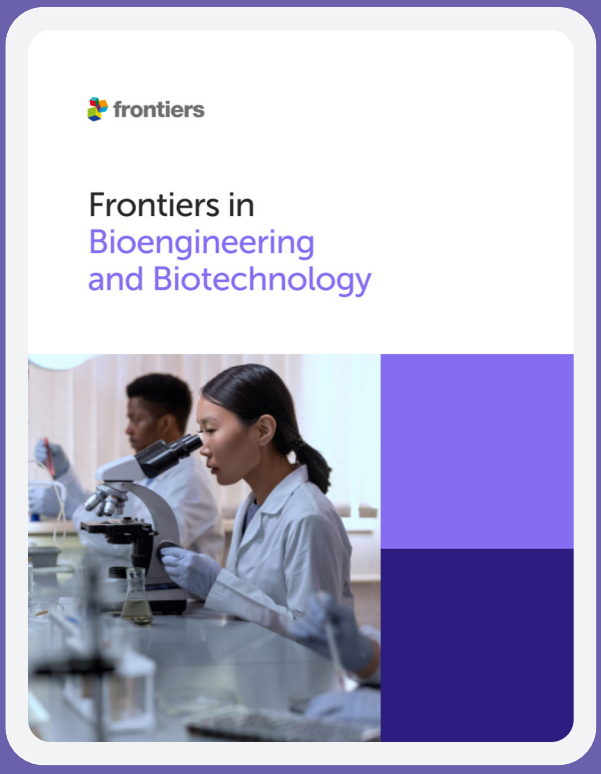

Frontiers

Avenue du Tribunal-Fédéral 34
1005 Lausanne, Switzerland
frontiersin.org

Contact us

+41 (0)21 510 17 00
frontiersin.org/about/contact